

**POLYMER MIXTURE THERMODYNAMICS AND APPLICATIONS FOR
FUNCTIONAL, MICROSTRUCTURED FILMS**

by

Jillian A. Emerson

A dissertation submitted to the Faculty of the University of Delaware in partial fulfillment of the requirements for the degree of Doctor of Philosophy in Chemical Engineering

Winter 2017

© 2017 Jillian A. Emerson
All Rights Reserved

ProQuest Number: 10256224

All rights reserved

INFORMATION TO ALL USERS

The quality of this reproduction is dependent upon the quality of the copy submitted.

In the unlikely event that the author did not send a complete manuscript and there are missing pages, these will be noted. Also, if material had to be removed, a note will indicate the deletion.



ProQuest 10256224

Published by ProQuest LLC (2017). Copyright of the Dissertation is held by the Author.

All rights reserved.

This work is protected against unauthorized copying under Title 17, United States Code
Microform Edition © ProQuest LLC.

ProQuest LLC.
789 East Eisenhower Parkway
P.O. Box 1346
Ann Arbor, MI 48106 – 1346

**POLYMER MIXTURE THERMODYNAMICS AND APPLICATIONS FOR
FUNCTIONAL, MICROSTRUCTURED FILMS**

by

Jillian A. Emerson

Approved:

Abraham M. Lenhoff, Ph.D.
Chair of the Department of Chemical and Biomolecular Engineering

Approved:

Babatunde A. Ogunnaike, Ph.D.
Dean of the College of Engineering

Approved:

Ann L. Ardis, Ph.D.
Senior Vice Provost for Graduate and Professional Education

I certify that I have read this dissertation and that in my opinion it meets the academic and professional standard required by the University as a dissertation for the degree of Doctor of Philosophy.

Signed:

Thomas H. Epps, III, Ph.D.
Professor in charge of dissertation

I certify that I have read this dissertation and that in my opinion it meets the academic and professional standard required by the University as a dissertation for the degree of Doctor of Philosophy.

Signed:

Eric M. Furst, Ph.D.
Professor in charge of dissertation

I certify that I have read this dissertation and that in my opinion it meets the academic and professional standard required by the University as a dissertation for the degree of Doctor of Philosophy.

Signed:

Michael E. Mackay, Ph.D.
Member of dissertation committee

I certify that I have read this dissertation and that in my opinion it meets the academic and professional standard required by the University as a dissertation for the degree of Doctor of Philosophy.

Signed:

Norman J. Wagner, Ph.D.
Member of dissertation committee

I certify that I have read this dissertation and that in my opinion it meets the academic and professional standard required by the University as a dissertation for the degree of Doctor of Philosophy.

Signed:

L. Pamela Cook, Ph.D.
Member of dissertation committee

ACKNOWLEDGMENTS

I'd like to start by thanking my two advisors, Thomas H. Epps, III and Eric M. Furst. For the past 6 years, they have provided keen insights, invaluable direction, and support. Additionally, I would not have been successful without their insistence on excellence. Not only have my advisors helped to steer my growth as a scientist but they also have aided in my development as a person. Although we didn't always agree on everything, I have benefited greatly under their direction.

In addition to my advisors, I would like to acknowledge my committee members: Norman Wagner, Michael Mackay, and Pamela Cook. Their helpful suggestions made my research stronger and provided new directions of study. I would also like to acknowledge the various collaborators that I've had the pleasure of working with during my time at Delaware: Jonathan Howse and Daniel Toolan, who provided the stroboscopic illumination data and continued collaboration throughout my time here; Antony Beris and Matthew Armstrong for their assistance in resolving early mathematical artifacts in the spin coating work; David Burriss in Mechanical Engineering at the University of Delaware and his students (Axel Moore, Nikolay Garabedian, and Diana Haidar) who taught me everything I know about tribology.

The support and equipment maintained by Chaoying Ni, Jennifer Sloppy, and Frank Kriss in the Keck Advanced Materials Characterization Lab made it possible to understand the structures studied in my work. Additionally, the NMR facilities run by Steve Bai provided key information in my studies.

None of this research would have been possible without the support of my research groups. I would like to acknowledge the members of the Epps and Furst research groups (past and present) for their contributions in both useful scientific discussions and friendship during my time here. In particular, I'd like to thank the thin films group: Jon Seppala, Julie Albert, Ming Luo, Cameron Shelton, Tom Gartner, Ron Lewis, Joey Kim, Doug Scott, and Jack Saltwick along with my undergraduate student, Eddie Sangern, and my high school interns, Victoria Muir and Will Esteves. Studies of sustainable polymers were made possible by Shu Wang, Angela Holmberg, and Michael Karavolias, who synthesized all of the materials. Additionally, Tiffany Suekama and Wei-Fan Kuan were instrumental in assisting with imaging of the polymer blend nanocomposites. I would also like to acknowledge Elizabeth Kelley and Sarah Mastroianni for teaching me the art of the BRAID and to Melody Morris for always being available to listen. I also want to acknowledge Kaleigh Reno for being my outreach partner-in-crime and to Mel Jurist and Janna Rhodes for constantly keeping me excited about science.

I would not have made it through graduate school without the help from my classmates and friends. In particular, I'd like to thank Kathy Whitaker and Benjamin Kremkow, my fellow musketeers, for dealing with me on a regular basis, and Devesh Radhakrishnan for being our (sometimes) fourth musketeer. Additionally, Alan Fast and Bryan Yonemoto were instrumental in keeping the mood light. I also want to acknowledge Jim, Laura, and Henry Swan for being amazing neighbors and wonderful friends. I owe a debt of gratitude to Kathie Young for keeping me sane and to Cinda Younce and Kristi Halberg for always being available to help out with the little things.

My family have all been key players along the road to this point. I want to start by acknowledging the furry family members who made grad school less stressful: to Rina, who reminded me to take long walks outside; to Asami for being a great work dog; and to Daisy, the craziest one of all. I'd like to thank my fiancé, Bryant, who put up with me during my entire Ph.D. (even/especially when I was busy and stressed) and for taking over the dog-walking duties as I wrote my dissertation. I also want to acknowledge his family, who kept me in their thoughts and prayers. Finally, I want to acknowledge my family who have dealt with all of the craziness of graduate school alongside of me: Lynne & Andy for checking in on me every once in a while; Patti & Dee for their support; Gran & Gramps and Donna & Norman for feeding a hungry graduate student and giving me an oasis to relax in; my sisters for putting up with last minute plan changes and work on the weekends; my dad for supporting me in my scientific endeavors; my mom for always being ready to goof off after a long day/week/month of work.

I would not have made it to this point without you all. This is for you.

TABLE OF CONTENTS

LIST OF TABLES.....	xiv
LIST OF FIGURES.....	xvi
ABSTRACT.....	xxxvi

Chapter

1 INTRODUCTION.....	1
1.1 Polymer Thermodynamics.....	3
1.1.1 Solubility Parameter.....	4
1.1.1.1 Hansen Solubility Parameters.....	5
1.1.1.2 Group Contribution Theory.....	6
1.1.2 Polymer-solvent Interactions.....	8
1.1.3 Polymer-polymer Interactions.....	12
1.1.4 Polymer-polymer-solvent Interactions.....	15
1.1.5 Polymer-polymer-nanoparticle Interactions.....	17
1.2 Kinetic Considerations.....	20
1.2.1 Phase Separation.....	21
1.2.1.1 Kinetics of Phase Separation: Theory.....	21
1.2.1.2 Kinetics of Phase Separation: Experimental Studies.....	23
1.2.2 Casting from Solution.....	24
1.3 Structure-property Relationships in Polymer Films.....	25
1.3.1 Homopolymer.....	25
1.3.2 Polymer Nanocomposites.....	25
1.3.3 Polymer Blends.....	27
1.3.4 Polymer Blend Nanocomposites.....	29
1.4 Dissertation Overview.....	31

REFERENCES	34
2 EXPERIMENTAL METHODS.....	54
2.1 Generation of Films	54
2.1.1 Substrate Preparation	54
2.1.2 Casting Methods	54
2.1.2.1 Spin Coating	55
2.1.2.2 Flow Coating.....	56
2.2 Characterization Techniques.....	56
2.2.1 Contact Angle	56
2.2.1.1 Static Sessile Contact Angle	57
2.2.1.2 Contact Angle Hysteresis.....	58
2.2.2 Nuclear Magnetic Resonance (NMR) Spectroscopy	59
2.2.3 Gel Permeation Chromatography (GPC).....	60
2.2.4 Atomic Force Microscopy (AFM).....	62
2.2.5 Spectral Reflectometry (SR).....	64
2.2.6 Solvent Vapor Swelling	66
2.2.7 Tribology.....	67
2.2.8 Transmission Electron Microscopy (TEM)	69
2.3 Seed-mediated Growth of Gold Nanoparticles	70
2.3.1 Synthesis of the Seed Solution.....	70
2.3.2 Synthesis of Gold Nanorods	70
2.3.3 Ligand Exchange Protocols	71
REFERENCES	72
3 INTERPLAY BETWEEN THERMODYNAMICS, PHASE SEPARATION KINETICS, AND FILM CASTING FROM POLYMER SOLUTIONS	76
3.1 Introduction.....	76
3.2 Materials & Methods	79
3.2.1 Materials	79
3.2.2 Blend Film Preparation	80
3.2.3 Solvent Vapor Swelling	80
3.2.4 Transmission.....	80

3.2.5	Tie Line Determination.....	81
3.2.6	Drying Curves.....	81
3.2.7	Stroboscopic Illumination.....	82
3.3	Results & Discussion.....	82
3.3.1	Polymer Solubility Parameters.....	82
3.3.1.1	Solvent Vapor Swelling of Polymer Films.....	83
3.3.1.2	Group Contribution Theory.....	88
3.3.2	Phase Diagram.....	89
3.3.2.1	Spinodal Curve.....	90
3.3.2.2	Binodal Curve.....	93
3.3.2.2.1	Transmission (PS/P3HT).....	94
3.3.2.2.2	¹ H NMR (PS/PI).....	96
3.4	Kinetics.....	98
3.4.1	Drying Curves.....	98
3.4.2	Stroboscopic Illumination.....	109
3.5	Conclusions.....	114
	REFERENCES.....	116
4	TUNING MORPHOLOGY IN POLYMER BLEND NANOCOMPOSITE FILMS <i>VIA</i> SOLVENT SELECTIVITY.....	125
4.1	Introduction.....	125
4.2	Materials & Methods.....	127
4.2.1	Materials.....	127
4.2.2	Gold Particle Synthesis & Characterization.....	127
4.2.2.1	UV-Vis Spectroscopy.....	128
4.2.2.2	Transmission Electron Microscopy (TEM).....	128
4.2.3	Blend Film Preparation.....	128
4.2.4	Film Characterization.....	129
4.2.4.1	Optical Microscopy (OM).....	129
4.2.4.2	Atomic Force Microscopy (AFM).....	129

4.2.4.3	Transmission Electron Microscopy (TEM)	130
4.3	Results & Discussion	130
4.3.1	Gold Particles.....	130
4.3.2	Drying Behavior.....	131
4.3.3	Morphology Changes.....	134
4.3.3.1	“Neutral” Solvent-cast Nanocomposites.....	135
4.3.3.2	PI-selective Solvent-cast Nanocomposites	141
4.3.4	Particle Location	143
4.4	Conclusions.....	147
REFERENCES	149
5	EFFECT OF MORPHOLOGY AND COMPOSITION ON FRICTION AND WEAR OF POLYMER BLEND FILMS.....	153
5.1	Introduction.....	153
5.2	Materials & Methods	156
5.2.1	Materials	156
5.2.2	Film Preparation.....	157
5.2.3	Annealing.....	158
5.2.4	Film Morphology and Domain Analysis	159
5.2.5	Tribology.....	160
5.3	Results & Discussion	162
5.3.1	Friction Coefficient of Blend Films: Varying Composition	162
5.3.2	Structure of As-cast Films	170
5.3.3	Effect of Microstructure on Friction Coefficient.....	174
5.3.4	Adhesion Break-up in PS/PI Blend Films	178
5.3.5	Effect of Domain Size on Friction Coefficient.....	182
5.4	Conclusions.....	188
REFERENCES	191
6	CHEMICAL AND FRICTION PROPERTIES OF SUSTAINABLE POLYMERS	194
6.1	Introduction.....	194

6.2	Materials & Methods	197
6.2.1	Solvents.....	197
6.2.2	Polymer Synthesis and Characterization	197
6.2.3	Glass Transition Temperature.....	197
6.2.4	Film Casting.....	198
6.2.5	Solvent Vapor Swelling	198
6.2.6	Atomic Force Microscopy	199
6.2.7	Contact Angle	199
6.3	Results & Discussion	200
6.3.1	Solvent Vapor Swelling	202
6.3.2	Surface Energy.....	211
6.3.2.1	Sessile Contact Angle	211
6.3.2.2	Contact Angle Hysteresis.....	213
6.3.3	Tribology.....	218
6.4	Conclusions.....	225
	REFERENCES	227
7	CONCLUSION & FUTURE DIRECTIONS	231
7.1	Dissertation Summary.....	231
7.1.1	Interplay Between Phase Behavior, Casting, and Film Morphology in Polymer Blends.....	231
7.1.2	Effect of Particles on Polymer Blend Morphology.....	233
7.1.3	Structure-property Relationships for Tribology.....	234
7.1.4	Chemical and Friction Properties of Sustainable Polymers.....	234
7.2	Recommendations for Future Work.....	235
7.2.1	Additional Considerations in Processing Effects.....	235
7.2.1.1	Glass Transition Temperatures.	235
7.2.1.2	Macro-micro Phase Separation Connection.....	238
7.2.1.3	Transitioning from Batch to Continuous Processes....	239
7.2.1.4	Effect of external fields on casting.	241
7.2.2	Functional Materials Generation.....	242

7.2.2.1	Pressure Sensitive Adhesives.....	242
7.2.2.2	Hierarchical Assemblies for Membranes.....	243
7.2.2.3	Hierarchical Assemblies for OPV Materials.....	244
7.3	Summary of Future Directions.....	247
REFERENCES		249
Appendix		
A	CASTING FROM POLYMER SOLUTIONS	256
B	SOLVENT VAPOR SWELLING OF POLYMER FILMS	258
B.1	Solvent Vapor Swelling	258
B.2	Bell Jar Solvent Vapor Swelling.....	258
B.3	Flow Solvent Vapor Swelling.....	259
B.4	Solvent Collection.....	261
C	SUPPORTING INFORMATION FOR CHAPTER 3	265
C.1	Drying Curves – Selecting $t = 0$ s	265
C.2	P3HT Refractive Index	266
C.3	Mathematica Code for Phase Diagram Calculation.....	268
C.4	Transmission Data	270
C.5	Gelation of P3HT in <i>o</i> -Xylene.....	272
C.6	Matlab Code for Fitting Spin Coating Data.....	273
C.7	PS/PMMA Film Characterization.....	279
C.8	Substituted Polystyrenes	281
REFERENCES		283
D	SUPPORTING INFORMATION FOR CHAPTER 6.....	285
D.1	Characterization of PSAM and PPM.....	285
D.2	Estimation of Polymer Refractive Index.....	286
D.3	Glass Transition Temperature Effects	287
D.4	Comparison of Swelling – PVM vs. PGM.....	288
E	SOLVENT SELECTIVITY AND POLYMER DISSOLUTION.....	290
E.1	PS/PI Selective Solvents.....	290
E.2	PS/PMMA Selective Solvents	293
F	PERMISSIONS	294

LIST OF TABLES

Table 3-1. Solubility parameters from literature, solvent vapor swelling, and group contribution theory.....	83
Table 3-2. Flory-Huggins solvent-polymer interaction parameters from solvent vapor swelling.....	87
Table 6-1. Sustainable polymer library. Chemical structures of sustainable polymers. All polymers share the same general backbone and repeat unit structures; each polymer differs at the functional groups <i>ortho</i> (R_1 , R_3) and <i>para</i> (R_2) to the methacrylate backbone.....	196
Table 6-2. Molecular weight and glass transition temperature of sustainable polymers used in the solvent vapor swelling experiments and the friction coefficient measurements.....	201
Table 6-3. Characterization data for the sustainable heteropolymers.....	201
Table 6-4. Flory-Huggins solvent-polymer interaction parameters for the homopolymers and heteropolymers with THF. As expected, the values of the heteropolymers fall between the interaction parameters of the homopolymers based on the same monomer constituents.....	208
Table 6-5. Flory-Huggins solvent-polymer interaction parameters for the homopolymers with CHCl_3	211
Table 6-6. Sessile contact angle measurements for the sustainable polymers with water. The static sessile contact angle (θ_s) is comparable to the advancing sessile contact angle (θ_A). The difference between the advancing and receding (θ_R) sessile contact angle is the contact angle hysteresis ($\Delta\theta$). The equilibrium contact angle (θ_0) is used to calculate the surface energy of the material.....	214
Table 6-7. Calculated probe-film adhesion for sustainable polymers.	222
Table 7-1. Properties of organic solvents	240
Table C-1. Solubility parameters from literature, solvent vapor swelling, and group contribution theory.....	282

Table E-1. Solvent selectivity for PS and PI. The selectivity was determined by literature values, experimentally, or solubility parameters. The color map indicates whether the solvent dissolved (blue) or didn't dissolve (red) the indicated component. Yellow boxes are placed for clear solutions that produced unstable films (films that partially dewet), which suggests solvent choice issues.....	291
Table E-2. Solvent selectivity for PS and PMMA. The selectivity was determined using literature values, experimentally, or solubility parameters. The color map indicates whether the polymer dissolved (blue) or partially dissolved (purple) in the solvent.....	293

LIST OF FIGURES

- Figure 1-1. Flow chart of factors that influence the solution processing-structure-property relationships in multicomponent films..... 1
- Figure 1-2. Schematic of morphologies produced by melt-mixed polymer blends. Reprinted with permission from Macosko, C. W. *Macromol. Symp.* 2000, 149, 171-184. Copyright 2000 John Wiley and Sons..... 2
- Figure 1-3: Schematic of lattice theory for a binary mixture of a) two solvents and b) solvent and polymer. 9
- Figure 1-4: Phase behavior of polymer-polymer blends. a) Phase diagram for a model A-B blend for which χ is the F-H interaction parameter, N is the degree of polymerization, and ϕ_A is the volume fraction of component A. The solid curve is the binodal line and the dashed curve is the spinodal line. Phase separation occurring between the binodal and spinodal curve (metastable) [e.g. B to B'] goes by nucleation and growth, shown in b). Phase separation within the unstable, spinodal envelope [e.g. A to A' in a)] occurs by spinodal decomposition, as shown in c). The arrows in b) and c) represent time evolution of structures. From Bates, F. S. *Science* 1991, 251, 898-905. Reprinted with permission from AAAS. 13
- Figure 1-5: Phase diagram (binodal curve and tie lines) for polymer-polymer-solvent system in the case of a symmetrically binary system ($m_2 = m_3 = m$) with a neutral solvent ($\chi_{12} = \chi_{13} = \chi$) with a combined $m\chi$ of 4, 8, and 20. S_0 represents the solvent (1) and P_1 (2) and P_2 (3) represent the polymer phases. Reprinted from Scott, R. L. *J. Chem. Phys.* 1949, 17, 279-284, with the permission of AIP Publishing..... 16
- Figure 1-6: Calculated spinodal curves for polymer/polymer blends with $N_1 = N_2 = 100$ containing spherical nanoparticles that have a preferential interaction with one of the polymers. ϕ_1 is the volume fraction of polymer 1 in the blend and ψ is the volume fraction of the nanoparticles. The radius of the nanoparticles, R_p , given in lattice units of the polymer (r_0) is a) 1, b) 5, and c) 10. Adapted with permission from Ginzburg, V. V., *Macromolecules* 2005, 38, 2362-2367. Copyright 2005 American Chemical Society..... 19

Figure 1-7. Spinodal curve for homopolymer blend (black) and the same blend filled with $\psi = 0.18$ (upper red & blue curves) or $\psi = 0.10$ (lower red & blue curves) for particle sizes $R_p = 3 r_0$ (red) and $R_p = 10 r_0$ (blue). The nanoparticles are “neutral”, meaning the interaction with A is the same as the interaction with B. Reprinted with permission from He, G., <i>et al. J. Polym. Sci., Part B: Polym. Phys.</i> 2006, 44, 2389-2403. Copyright 2006 John Wiley & Sons.....	20
Figure 1-8: Detailed flow chart of controllable factors that affect solution-processing-structure-property relationships in multi-component polymer films.....	32
Figure 2-1. Schematic of the casting behavior during a) spin coating and b) flow coating. During spin coating, the film thins by outflow and evaporation. In flow coating, the film thinning occurs by evaporation once the solution layer has been deposited by the blade.....	55
Figure 2-2. Schematic of a static sessile contact angle. The contact angle is determined by the balance of the interfacial tensions between the solid, liquid, and vapor phases.....	57
Figure 2-3. Schematic of contact angle hysteresis for a) receding, b) advancing and c) sliding. Sliding contact angle tests afford measurement of the advancing and receding contact angle simultaneously.....	58
Figure 2-4. Schematic of AFM operation.....	62
Figure 2-5. Height of the film relative to the substrate (film thickness, d) as a function of distance along the two scratch points shown in the inset. Inset is the AFM height image of the scratch and surrounding film. The height scale is 800 nm. The tall feature in the green curve is pushed up residual film and is not included in the height analysis.....	63
Figure 2-6. a) Schematic of light transmission in layered samples. b) Influence of thickness on measured spectra, for which $d_1 < d_2 < d_3$. With increasing thickness, the number of peaks in the reflectance increases. c) Effect of refractive index on spectra. Materials with higher refractive indices have spectra with larger amplitudes that are shifted upwards vertically in reflectance ($n_1 < n_2 < n_3$).....	65
Figure 2-7. Schematic of solvent vapor swelling.....	66

- Figure 2-8. Schematic of friction coefficient loops for tribology experiments with a) uniform, one phase, b) non-uniform, one phase, and c) uniform, two phase surfaces. The blue region represents the region over which the friction coefficient is measured. Oscillations in the negative and positive friction coefficient quadrants that are out of phase signify non-uniformity along the wear track, whereas the in-phase oscillations indicate structural differences between the two phases.68
- Figure 3-1. The polymer volume fraction, which is given by the ratio of the initial film thickness to the swollen film thickness, of PS is shown in time. Each of the four colors represents a different ratio of the flow rate of the solvent vapor stream to the diluent stream. The solvent concentration at equilibrium is shown as p/p_{sat} for each flow condition accessed. Once the film thickness equilibrated, the solvent vapor and dilution flow rates were changed, maintaining the same total flow rate. Reprinted with permission from Emerson, J. A., *et al.* *Macromolecules* 2013, 46 (16), 6533-6540. Copyright 2013 American Chemical Society.85
- Figure 3-2. Interaction parameter plots for PS (\blacktriangle) and P3HT (\blacksquare) with a) THF and b) CHCl_3 . For PS in CHCl_3 (b), the data were fit for $\phi_P < 0.6$ ($\phi_P^2 < 0.36$), for which χ_{i-j} was nearly constant over the concentration range. For $\phi_P^2 > 0.36$, χ_{i-j} decreased with increasing polymer composition. Reprinted with permission from Emerson, J. A., *et al.* *Macromolecules* 2013, 46 (16), 6533-6540. Copyright 2013 American Chemical Society.86
- Figure 3-3. Ternary phase diagram with spinodal curves for PS/polymer/*o*-xylene blends, for which the second polymer is P3HT (solid) or PI (dash). For ^{17}k PS/P3HT/*o*-xylene, the interaction parameters were: $\chi_{o-PS} = 0.34$, $\chi_{o-P3HT} = 0.84$, and $\chi_{PS-P3HT} = 0.48$. For ^{892}k PS/PI/*o*-xylene, the Flory-Huggins interactions were: $\chi_{o-PS} = 0.34$, $\chi_{o-PI} = 0.37$, and $\chi_{PS-PI} = 0.013$92
- Figure 3-4. Ternary phase diagram for PS/polymer/toluene, for which the second polymer is PI (solid: $\chi_{toluene-PS} = 0.340$, $\chi_{toluene-PI} = 0.342$, $\chi_{PS-PI} = 0.012$) or PMMA (dash: $\chi_{toluene-PMMA} = 0.45$, $\chi_{toluene-PS} = 0.38$, $\chi_{PS-PMMA} = 0.010$; dash dot: $\chi_{toluene-PMMA} = 0.43$, $\chi_{toluene-PS} = 0.36$, $\chi_{PS-PMMA} = 0.007$; dot: $\chi_{toluene-PMMA} = 0.40$, $\chi_{toluene-PS} = 0.34$, $\chi_{PS-PMMA} = 0.004$).93

- Figure 3-5. Phase diagram for blend of 17k PS/ 17k P3HT in *o*-xylene. Data points represent a discrete PS/P3HT/*o*-xylene solution through which transmission of a HeNe laser was measured. The color of the data point indicates the relative transmission (%) with respect to an *o*-xylene reference, in which white represents 100% transmission (no phase separation) and black indicates 0% transmission. Samples denoted by \times were gelled, and compositions indicated by $*$ were too viscous to transfer to the transmission cell. The dashed orange line represents the approximated binodal line, which connects the results from experimental data. The orange shaded region is the region in which the binodal line falls, determined by a decrease below 100% in the relative transmission. The purple solid line is the theoretical spinodal line and the purple shaded region represents the error in the spinodal line from the uncertainty in the solubility parameters.....95
- Figure 3-6: Processing phase diagram for PI/PS in a) *o*-xylene and b). Data points represent the composition of the binodal line determined gravimetrically and by ^1H NMR. The dashed line represents the approximated binodal line, which connects the results from experimental data. The solid line is the theoretical spinodal line calculated from Equations 1a-1c (also shown in Figure 3-3 and Figure 3-4). The parameters used to calculate the spinodal line were $M_{n,PS} = 892$ kg/mol, $M_{n,PI} = 541$ kg/mol, $\chi_{PS-PI} = 0.013$, $\rho_{PS} = 1.05$, $\rho_{PI} = 0.913$ with $\chi_{o-PS} = 0.342$, $\chi_{o-PI} = 0.372$, $\rho_o = 0.88$ for *o*-xylene (a) and $\chi_{toluene-PS} = 0.340$, $\chi_{toluene-PI} = 0.342$, $\rho_{tol} = 0.866$ for toluene (b).97
- Figure 3-7. a) Drying curves for 892k PS₅₀/PI₅₀ mixtures in *o*-xylene with an initial solution concentration of 0.0 wt. % (dot), 2.0 wt.% (dash), 2.2 wt.% (dot-dash), and 2.5 wt.% (solid) polymer with respect to *o*-xylene. b) Drying time (\bullet), initial solution viscosity (\blacktriangle) relative to the solvent viscosity, and evaporation rate (\square). The relative viscosity and evaporation rate increased with solution concentration. c) – e) optical micrographs of the resulting PS₅₀/PI₅₀ films cast from c) 2.0 wt.%, d) 2.2 wt.%, and e) 2.5 wt.% polymer. The scale bars represent 20 μm ... 100
- Figure 3-8. Effect of concentration on the drying and film morphology. a) Drying curves for 17k PS₅₀/ 33k PMMA₅₀ solutions cast at 1500 rpm with initial solution concentrations of 0 wt.% (dot), 0.9 wt.% (dash), 5 wt.% (dot-dash), and 9 wt.% (solid). b) Drying time (\bullet), relative viscosity (\blacktriangle), and evaporation rate (\square) as a function of polymer concentration. With increasing polymer concentration, the relative viscosity increased, and the evaporation rate decreased. As expected, the drying time increased with viscosity and solution concentration..... 101

Figure 3-9. Effect of molecular weight on the drying behavior and film morphology. The average degree of polymerization, $\langle N \rangle$ is calculated by the geometric mean of the individual degrees of polymerization of the homopolymers. a) Drying curves for *o*-xylene (dot, $\langle N \rangle = 1$), $\langle N \rangle = 230$ (dot dash), $\langle N \rangle = 1028$ (dash), and $\langle N \rangle = 2929$ (solid). b) Increasing the degree of polymerization increased the drying time (\bullet) and initial solution viscosity (\blacktriangle). The evaporation rate (\square) decreased with increasing $\langle N \rangle$. Optical micrographs of the films cast from c) $\langle N \rangle = 230$, d) $\langle N \rangle = 1028$, and e) $\langle N \rangle = 2929$ show the appearance of structure with the highest molecular weight combination. With increasing $\langle N \rangle$, the morphology evolved from stratified (bilayer, c) to droplet structures (e). 103

Figure 3-10. Effect of spin speed and concentration on drying behavior. The same initial solution is used to cast 17k PS/P3HT (1.75 wt.% in *o*-xylene) at 1500 rpm (dashed) and 2000 rpm (solid). A lower concentration solution (0.9 wt.% in *o*-xylene) is also cast at 800 rpm (dot) and 1500 rpm (dot-dash). Optical micrographs of the film morphologies are shown for the film cast from 1.75 wt.% 17k PS/P3HT in *o*-xylene at b) 1500 rpm and c) 2000 rpm. The scale bar represents 10 μ m. d) Drying time for *o*-xylene (\bullet), 0.9 wt.% 17k PS/P3HT (\bullet), and 1.75 wt.% 17k PS/P3HT (\bullet). The drying time decreased with increasing spin speed and decreasing solution concentration. e) The relative viscosity (\blacktriangle), η_r , calculated for the same initial solution concentration was independent of spin speed. η_r increased with concentration. The evaporation rates (\square) increased with spin speed and decreased with concentration..... 105

Figure 3-11. Drying curves for 17k PS/ 33k PMMA (\bullet) and 110k PS/ 100k PMMA (\bullet) compared to the spin coating model with a constant viscosity fit (solid lines). The lower molecular weight is fit well by a constant viscosity, which suggests that the viscosity does not increase appreciably during outflow. In comparison to 17k PS/ 33k PMMA, the drying behavior for 110k PS/ 100k PMMA is not well captured by a constant viscosity. Thus, the higher molecular weight blend has a significant increase in viscosity during casting, which could be due the earlier onset of phase separation..... 106

Figure 3-12. Drying curves for PS/P3HT films at various initial solution concentrations and relative polymer ratios. The black diamonds are the experimental data, the blue solid line is the spin coating model developed by Meyerhofer,⁶⁰ and the dotted gray line represents the onset of phase separation predicted by the phase diagram. 108

Figure 3-13. a) Spinodal (dashed line) curve for a 1.75 wt.% $^{17}\text{kPS}_{50}/\text{P3HT}_{50}$ blends in *o*-xylene plotted as volume fraction of solvent vs. the mass fraction of P3HT. The shaded region between the solid lines indicates the error in the calculated spinodal line, determined via error propagation from the interaction parameters. Time points indicate solvent volume fraction in the film during spin coating at 1500 rpm and are spaced temporally by 2 s. Reprinted with permission from Emerson, J. A., *et al. Macromolecules* 2013, 46 (16), 6533-6540. Copyright 2013 American Chemical Society. b) Full profile of solvent volume fraction vs. time during spin coating of PS/P3HT blend from *o*-xylene with critical volume fraction (dotted line) shown. The data points represent an average of the solvent volume fraction in the film from 4 drying curves based on the final film thickness, and the error bars indicate the standard deviation. c) Optical images from synchronized stroboscopic illumination after initial loading of solution (0.0 s), before visible onset of phase separation (6.0 s), during the onset of visible phase separation (12.5 s), throughout the blend phase separation (13.2 s, 13.5 s, 14.5 s), and of the final film (19.0 s). The dark regions are P3HT-rich, and the light regions are PS-rich. The scale bar represents 10 μm 111

Figure 3-14. a) Optical reflectance images recorded during bar-coating of a 5 wt.% $\text{PS}_{30}/\text{PMMA}_{70}$ blend in toluene (blade speed of 20 mm s^{-1}) from toluene. The 0 s frame is taken immediately after the bar has left the field of view (direction of travel was left to right). b) Drying curves and concentration changes in time for the bar spreading experiments. c) Spinodal curves for PMMA/PS in toluene determined from reported interaction parameters for $\chi_{\text{toluene-PMMA}}$, $\chi_{\text{toluene-PS}}$, and $\chi_{\text{PS-PMMA}}$ (dash: $\chi_{\text{toluene-PMMA}} = 0.45$, $\chi_{\text{toluene-PS}} = 0.38$, $\chi_{\text{PS-PMMA}} = 0.010$; dash-dot: $\chi_{\text{toluene-PMMA}} = 0.43$, $\chi_{\text{toluene-PS}} = 0.36$, $\chi_{\text{PS-PMMA}} = 0.007$; dot: $\chi_{\text{toluene-PMMA}} = 0.40$, $\chi_{\text{toluene-PS}} = 0.34$, and $\chi_{\text{PS-PMMA}} = 0.004$). The open and closed diamonds represent the composition for the initial bar-spread blend (5 wt.%) and the concentration at which phase separation began experimentally (7.3 wt.%), respectively. Reprinted with permission from Haq, E. U., *et al. J. Polym. Sci. Part B: Polym. Phys.* 2014, 52 (15), 985-992. Copyright 2014 Wiley Periodicals, Inc. 113

Figure 4-1. a) UV-Vis spectroscopy of gold nanorods (blue) and gold nanospheres (red). TEM micrographs of gold nanorods are shown in b) and c). The average particle size was $9 \pm 2 \text{ nm}$ by $27 \pm 5 \text{ nm}$ 131

- Figure 4-2. a)-c) Drying curves for PS₅₀/PI₅₀ films with in initial solution concentrations of a) 2.0 wt.%, b) 2.2 wt.%, and c) 2.5 wt.% polymer with respect to *o*-xylene. The neat samples (solid line) had the longest drying time. Solutions containing 1 vol.% (purple, dotted line), 2 vol.% (green, dashed line), and 9 vol.% (orange, dot-dashed line) PS-capped gold nanorods (PS-AuNR). In a) the short dashes represent the drying curve for 1 vol.% PS-capped gold nanospheres (PS-AuNS) with the same radius as the nanorods (see also Figure 4-1). d) Drying curve for PS₅₀/PI₅₀ film with an initial solution concentration of 1.0 wt.% (solid line) and with 2 vol.% PS-AuNR (dashed line). 132
- Figure 4-3. a) Summary of the drying behavior for PS₅₀/PI₅₀ in *o*-xylene (■) with 1 vol.% (◆), 2 vol.% (▲), and 9 vol.% (●) PS-AuNR or 1 vol.% (×) PS-AuNS. It took solutions with higher polymer contents longer to dry. Drying times for decalin cast films are not shown. The decalin cast films had a drying time of ~51 s at 1 wt.% PS₅₀/PI₅₀, which did not change with the 2 vol.% particle loading. At the same loading and initial polymer concentration, the nanorods reduced the drying time, whereas the nanospheres had the same drying time as the neat solution. In all cases, adding nanorods reduced the drying time. b) Ratio of the nanocomposite solution viscosity, η_{PBNC} , to the polymer blend solution viscosity η_{PB} from the same stock solution for *o*-xylene solutions with 2.0 wt.% (◆), 2.2 wt.%, (■) and 2.5 wt.% (▲) PS₅₀/PI₅₀. with PS-AuNR. 2.0 wt.% PS₅₀/PI₅₀. with PS-AuNS in *o*-xylene (×) and 1 wt.% PS₅₀/PI₅₀ with 2 vol.% PS-AuNR in *cis*-decalin (●). 134
- Figure 4-4. Optical micrographs of polymer blends and polymer blend nanocomposites on silicon wafers imaged using the Nikon microscope under bright field illumination operated in transmission mode. The color variation in the optical micrographs is related to both the film thickness and nanoparticle loading. The scale bar represents 20 μm . .. 135
- Figure 4-5. a, c, e) Chord length and b, d, f) circularity for PS₅₀/PI₅₀ (solid) with 1 vol.% (dotted), 2 vol.% (dashed), and 9 vol.% (dot-dashed line) gold nanoparticles. The initial polymer content was a, b) 2.0 wt.%, c, d) 2.2 wt.%, e, f) 2.5 wt.%. With nanoparticle loading, the chord length distribution became more uniform compared to the neat films. The peak domain circularity increased and the distribution narrowed with particle loading. 137

- Figure 4-6. AFM images of 2.0 wt.% (a-d), 2.2 wt.% (e-h), and 2.5 wt.% (i-l) for neat (a, e, f, i, j), 1 vol.% (b, g, k), 2 vol.% (c, h, l), and 9 vol.% (d). All micrographs are height images, with the exception of f) and j), which are phase images. The scale bars represent 10 μm . Note that a) depicts the inverted domain structure of PS₅₀/PI₅₀ cast from 2.0 wt.% solution. 138
- Figure 4-7. Chord length and circularity for 2.0 wt.% PS₅₀/PI₅₀ with the normal (blue, solid) and inverted (blue, dashed) phase structure. Chord length and circularity for 2.2 wt.% (purple, dashed) and 2.5 wt.% PS₅₀/PI₅₀ (red, dashed) films with inverted domain structure. 139
- Figure 4-8. Optical micrographs for a) 2.0 wt.% PS₅₀/PI₅₀ as-cast films and films washed with b) *n*-hexane (PI removed), c) PGMEA (PS removed). The film shown here had the inverted domain structure, for which the droplets were PS and the matrix was PI. Scale bars represent 20 μm . . 140
- Figure 4-9. Domain thickness for PS (closed symbols) and PI (open symbols) in films cast from 2.0 wt.% (◆), 2.2 wt.% (■), and 2.5 wt.% (▲) PS₅₀/PI₅₀ in *o*-xylene. 141
- Figure 4-10. Morphology of PS/PI films cast from decalin for the a) neat and b) 2 vol.% nanorods on silicon wafers. Distribution of the c) chord length ($\pi A/p$) and d) circularity ($4\pi A/p^2$) for the neat (solid) and 2 vol.% nanorod loading (dashed). The circularity increased slightly with increasing particle loading, but the chord length did not change. . 142
- Figure 4-11. Optical micrographs for PS₅₀/PI₅₀ films cast from *cis*-decalin washed with a) acetone and b) *n*-hexane washed films. The scale bars on the optical micrographs represent 20 μm . AFM height images for the c) acetone and d) *n*-hexane washed films. e) AFM height images of PS₅₀/PI₅₀ films cast from *cis*-decalin f) with 2 vol.% PS-AuNR. The scale bars on the AFM micrographs represent 5 μm 143
- Figure 4-12. Bright field optical microscopy (a-d) with the Nikon microscope operated in reflection mode. Bright field optical (e-h) with the Zeiss microscope operated in transmission mode. (i-l) Polarized light microscopy with the Zeiss microscope of the same spot of the films shown in (e-h). Polymers cast with 2.0 wt.% PS₅₀/PI₅₀ (a, e, i) with 1 vol.% (b, f, j), 2 vol.% (c, g, k), and 9 vol.% (d, h, l) gold nanorod loadings. The gold nanoparticles appear bright under cross polarizers.³⁵ The higher contrast in j, k, and l near the blend interfaces compared to i, indicate that particles are assembling at the polymer-polymer interface. 144

Figure 4-13. TEM micrographs of (a, b) neat PS/PI blend films and (c, d) PS/PI blends containing 2 vol.% gold nanorods cast from <i>o</i> -xylene. In the nanoparticle-laden samples, the particles are localized at/near the polymer/polymer interfaces as well as within the PS domain.	145
Figure 4-14. Bright field optical microscopy (a-d) with the Nikon microscope operated in reflection mode. Bright field optical (e-h) with the Zeiss microscope operated in transmission mode. (i-l) Polarized light microscopy with the Zeiss microscope of the same spot of the films shown in (e-h). Polymers cast with 2.0 wt.% PS ₅₀ /PI ₅₀ (a, e, i) with 2 vol.% (c, g, k) gold nanorod loading. There is no change in brightness between c) and f), suggesting that particles are not localized in these films.	147
Figure 5-1. a) Friction coefficient for the PEEK/PTFE composites plotted as a function of PEEK filler wt.% (calculated from the measured sample density). The friction coefficient was measured on 6.35 mm square sample surfaces under 250 N of normal load, 25.4 mm track length, and 50.8 mm/s. Reprinted with permission from Burris, D. L. and Sawyer, W. G. <i>Wear</i> 2006, 261, 410-418. Copyright 2006 Elsevier. b) Friction coefficient for PEEK/PTFE composites as a function of polymer composition at a velocity of 0.45 mm/s under 5 N (◐, ◑), 10 N (◒), 15 N (◓), and 20 N (◔). Reprinted with permission from Briscoe, B. J. <i>et al. Wear</i> 1986, 108, 357-374. Copyright 1986 Elsevier.	155
Figure 5-2. Cartoon depicting the tunability of the domain size of a homopolymer blend containing a glassy and rubbery polymer using composition and annealing. Composition affects both the domain size and shape, whereas the annealing time mostly changes the domain size.	156
Figure 5-3. Schematic of convection-assisted flow coating. The forced convection induced a directional drying front, which produced uniform films.	158
Figure 5-4. Schematic of experimental casting set-up. Convection and radiation were used to produce ~ 1 μm thick films. The temperature of the substrate was tuned by changing the position of the radiation source relative to the substrate.	159

- Figure 5-5. a) Front and b) side view digital photographs of the microtribometer used in friction coefficient measurements. A force is applied to the film using a 6.35 mm probe attached to a stainless steel beam. Two capacitance probes are used to measure the normal and friction forces. The linear reciprocating stage is controlled by a motor. The films are affixed to the stage before each experiment. The micrometer controls the position along the film. 161
- Figure 5-6. Friction coefficient of PS/PI films with varying composition PS (x_{PS}) measured with a) glass probe and b) HDPE probe. For both probe materials, the friction coefficient was non-monotonic with composition. The reported friction coefficients represent the average over the steady-state friction coefficient (see region II in Figure 5-7 and Figure 5-8). $\mu_{glass-PTFE}$ was measured at 4.6 mm/s as a comparison to the PS/PI blend films. Because μ_{PTFE} is independent of velocity at the speeds accessed herein,²⁰ the low friction coefficients measured for PS/PI are comparable to PTFE..... 163
- Figure 5-7. Sample time-dependent friction coefficient traces at 5 mN load for 100 cycles with a 6.35 mm diameter borosilicate glass probe. Region I represents a start-up regime, during which the friction coefficient varies in time. Region II is the steady-state friction coefficient. Reported friction coefficients represent an average over region II. For PI films, the probe breaks through the film within 100 cycles at all velocities. Region III of the PI plots indicate breakthrough (significant reduction in friction coefficient), which did not occur for the other films. See Figure 5-9a for an optical micrograph of wear through PI with glass. 165
- Figure 5-8. Time-dependent friction coefficient traces for PS/PI films with a 6.35 mm diameter HDPE probe. The load was constant at 5 mN in these linear reciprocating experiments along a 2 mm path. As for Figure 5-7, region I and II represent the start-up and steady-state friction coefficients, respectively. For HDPE, breakthrough was seen in the PI films (region III). Wear through the films was confirmed optically (see Figure 5-9b). At 0.5 mm/s, the black arrow indicates the point at which the experiments were stopped to prevent the HDPE bead from rubbing along the glass surface..... 166

- Figure 5-9. a) Wear through of a PI film with a glass probe at 0.5 mm/s and 5 mN for 100 cycles. b) Wear track widths for PI films after rastering across the film for 100 cycles at a 5 mN load with the HDPE probe at different velocities. The optical micrographs of the wear tracks at i) 0.5 mm/s, ii) 2.0 mm/s, iii) 4.6 mm/s, and iv) 7.8 mm/s are inset. The scale bars represent 200 μm 168
- Figure 5-10. Adhesion of PS and PI with a) glass and b) HDPE probes. Adhesion is characterized by the pull-off force upon immediate retraction from the set load. PS has a lower adhesion than PI with both probes. The pull-off force for PS with glass is within the noise of the measurement, whereas it is statistically significant with HDPE. The HDPE-PI pull-off force is lower than the glass-PI pull-off forces, suggesting lower adhesion. There was no strong trend between the approach/retraction velocity and the adhesion..... 169
- Figure 5-11. Domain assignment of PS/PI blend films. For $x_{PS} = 0.75$, the droplet phase was removed after washing with *n*-hexane; thus, the droplets are PI and the matrix is PS. Both $x_{PS} = 0.50$ and $x_{PS} = 0.25$ have a PI matrix with droplets of PI. The scale bars on the optical micrographs (reflection mode) represent 25 μm , and the scale bars on the atomic force micrographs (tapping mode) represent 10 μm 171
- Figure 5-12. Optical micrographs of PS/PI films for x_{PS} values of a) 0.9, b) 0.85, c) 0.8, d) 0.75, e) 0.7, f) 0.6, g) 0.5, and h) 0.25. The brightness and contrast have been artificially enhanced and the scale bars represent 10 μm . In some of the films, a full (c, d) or partial (f) wetting layer decreased the natural contrast at the domain interfaces. In f) the white arrows point to holes in the wetting layer, whereas the black arrows highlight the edge of the underlying domain. The domain size was characterized by the area-weighted chord length ($\pi A/p$). The droplet domain size as a function of x_{PS} is shown in i). The droplet size increases with x_{PS} , reaches a maximum value near the critical point, and then decreases with additional increases in x_{PS} 172

- Figure 5-13. Effect of the mass fraction of PS on the film thickness. The domain height is shown for PS (\blacktriangle) and PI (\blacklozenge) in the two component system and for PS height in the films, for which the PI domains have been removed by washing with *n*-hexane (\blacksquare). The film thickness was measured by atomic force microscopy using the scratch test method. In all cases, the PS domain is higher than the PI domain. The total film thicknesses increased with decreasing PS mass fraction due to the higher viscosity of the PI film. In the *n*-hexane washed films, the height of the PS agreed well with the two-component film heights..... 173
- Figure 5-14. Effect of the domain size on the friction coefficient for friction coefficients measured with the a) glass or b) HDPE probe. The domain size is represented by the average area-weighted chord length. The open symbols represent films for which the droplet phase is PI and the closed symbols represent films for which the droplet phase is PS. There is no direct correlation between domain size and friction coefficient in these composition-controlled films. The lines are to guide the eye and connect the data points in order of increasing or decreasing x_{PS} . The highest blend film friction coefficient occurred at the $x_{PS} = 0.25$, whereas the lowest blend film friction coefficient was measured for $0.60 > x_{PS} > 0.75$ (glass) or 0.85 (HDPE). 175
- Figure 5-15. Wear tracks for various composition films with the glass probe. As the PS content increases, the wear track width decreases, suggesting that a combination of reduced wear and contact radius exists for these samples. The scale bar represents 50 μm 176
- Figure 5-16. Atomic force micrographs of wear tracks on films after friction coefficient measurements with a 5 mN load after 100 cycles. For all micrographs, the phase image has higher contrast on the film that was exposed to the probe. The scale bars represent 10 μm 177
- Figure 5-17. Comparison of HDPE adhesion with PS, PI and blend films. The approach and retraction speed were 12.0 $\mu\text{m/s}$. The closed symbols represent immediate retraction, and open symbols represent results from experiments during which the probe was left in contact with the film (4 s, 16 s, or 80 s) or rastered across the film (5 mm/s for 5, 20, or 100 cycles). The $x_{PS} = 0.75$ blend film had lower pull-off forces than the neat PS. 179

- Figure 5-18. Ratio of the friction coefficient films for which the PI phase was removed (μ') to the friction coefficient of the neat polymer blend film (μ) produced under the same conditions. All films had an initial $x_{PS} = 0.75$. Optical micrographs of the b) as-cast film, c) as-cast film without the PI phase, d) film annealed for 24 h in *o*-xylene and d) 24 h annealed film without the PI phase. The PI was removed by soaking the films in *n*-hexane overnight. Compared to the friction coefficient of the film containing both PS and PI, the friction coefficients of the PI-removed films were always higher. Of particular interest was the spike in friction coefficient at 0.5 mm/s for both the as-cast and 24 h annealed films upon PI removal. This increase is likely due to the loss of the adhesion break-up in the film. 180
- Figure 5-19. Wear tracks in PI-removed films (casting $x_{PS} = 0.75$). The as-cast film with PI phase removed showed higher wear than the two-component as-cast film. In the 24 h anneal samples, the increase in wear upon PI removal is less pronounced due to the enhanced demixing of the PS and PI under the annealing conditions. 181
- Figure 5-20. a)-i) optical micrographs of annealed $x_{PS} = 0.75$ films. Films were annealed in *o*-xylene for a) 0 h (as-cast) b) 4 h, c) 8 h, d) 10 h, e) 14 h, f) 16 h, g) 24 h, h) 25 h, i) 48 h. The resulting increase in domain size with increasing annealing time is shown in j). Note: due to processing variabilities, there is not a strictly linear increase in domain size with annealing time. The scale bars represent 25 μm 183
- Figure 5-21. a) Friction coefficient of $x_{PS} = 0.75$ films with the glass probe measured at 0.5 mm/s (\blacklozenge), 4.6 mm/s (\blacksquare), and 7.8 mm/s (\blacktriangle). Replotting of the friction coefficient with chord length, b) shows a correlation between the domain size and friction coefficient at a constant composition for the two higher speeds. The lowest speed shows no dependence of friction coefficient on annealing time; this effect is likely due to the relaxation of PI during these experiments. 184
- Figure 5-22. Wear tracks for annealed $x_{PS} = 0.75$ films. Wear tracks are shown for 0.5 mm/s, 4.6 mm/s, and 7.8 mm/s for an as-cast film as well as films annealed in *o*-xylene for 4 h, 8 h, 10, h, 14 h, 16 h, and 25 h. 186

- Figure 5-23. Tuning domain size during casting with combined radiation and convection. Optical micrographs of films cast onto substrates at a) 24 °C, b) 26 °C, and c) 29 °C. The apparent domain size increased with increasing temperature. The brightness and contrast of the optical micrographs were artificially enhanced. The scale bars represent 50 μm . d) The friction coefficient as a function of substrate temperature during casting. Increases in temperature, which produced larger domain sizes, resulted in higher friction coefficients at 7.8 mm/s and 4.6 mm/s. At 0.5 mm/s, the friction coefficient remained independent of casting temperature, which is likely due to the lower De of the film under these experimental conditions. 187
- Figure 5-24. Effect of domain size on friction coefficient for varied composition films ($x_{PS} > 0.6$: ■, $x_{PS} \leq 0.6$: □) and annealed constant composition films (●). At a constant composition, the friction coefficient increases with domain size. For the varied composition films, the friction coefficient depends on both the composition and domain size. 189
- Figure 6-1. Sample swelling curves for polymers in THF. Increased compatibility occurs with decreasing polymer volume fraction. The solvent concentration is given by the ratio of the partial pressure to the saturated partial pressure, $p_i/p_{i,sat}$, for which the values are listed on the plots. The dashed line represents the non-swollen polymer (initial polymer volume fraction). a) Swelling of PSM (✕), PGM (+), PCM (□), PVM (◇), PEM (Δ). PSM had reduced swelling compared to the other polymers. This lack of swelling is likely due to the higher T_g of the material, which limits the mobility at insufficient solvent concentrations. b) Swelling of [PBOM] (●) and c) PES (▲), PCES (■), PVES (◆) in comparison to their homopolymer constituents. 203
- Figure 6-2. Effect of THF concentration on PEM mobility. The “rubbery” regime (●), in which the polymers have mobility, has a different slope than the “glassy” regime (●), in which the polymer is kinetically trapped. The closed symbols represent data from flow solvent vapor swelling experiments, whereas the open symbols represent data from THF/water bell jar experiments. 205
- Figure 6-3. a) Data points represent crossover polymer volume fraction for sustainable polymers. Shaded regions represent the estimated crossover from eq. 6.1 for each polymer. b) Crossover solvent concentration ($p_{i,c}/p_{i,sat}$) required to access the minimum polymer volume fraction for chain mobility. 206

- Figure 6-4. Replotting equilibrium swelling data for lignin-derived a) homopolymers and b) heteropolymers in THF. The solid lines represent the linear fit to the data, and the dashed lines represent the extrapolation of the fits. The homopolymers shown in a) in order of increasing compatibility with THF are PGM (+), PCM (■), PVM (◆), PEM (▲), PPM (●). The solubility of the heteropolymers in b) increases as expected based on the constituent make-up of the polymers: PCES (■) ~ PVES (◆) < PBOM (●) < PES(▲). The Flory-Huggins solvent-polymer interaction parameters are given in Table 6-4.207
- Figure 6-5. T_g and solvent quality for PSM. a) Polymer volume fractions of PSM swollen in saturated solvents. The gray shaded region represents the polymer volume fraction regime in which PSM has mobility, from eq. 6.1. b) Solubility parameters for solvents tested. PSM had the highest swelling (lowest polymer volume fraction) in chlorinated solvents (CHCl_3 , DCM). Due to the greater solvent uptake compared to the other solvents tested, CHCl_3 was selected for further experiments. c) Flow SVA of PSM in THF (top, ✕) and CHCl_3 (bottom, ✕). At similar solvent concentrations ($p_i/p_{i,sat}$), CHCl_3 swelled PSM more than THF. Additionally, the rubbery regime was accessible in the flow set-up with CHCl_3 (see Appendix D, Figure D-4)209
- Figure 6-6. a) Sample swelling curves for PSM (✕) and PSAM (●) in CHCl_3 . b) Replotted swelling data for PSM (✕), PSAM (●), and PVM (◆) in chloroform. PSM had the highest interaction parameter, whereas PVM had the lowest interaction parameter in CHCl_3210
- Figure 6-7. a) Contact angle with water (□) and diiodomethane (■). The water contact angle decreased with increasing oxygen content, whereas the diiodomethane contact angle increased slightly with aliphatic content and oxygen moieties. b) Calculated total (○), dispersive (■), and polar (◆) surface energy using the two-fluid contact angle method described in Chapter 2 as well as elsewhere.³³⁻³⁴ The PEM surface energy is the lowest, at 45 mJ/m^2 , which is higher than both polystyrene [40 mJ/m^2] and poly(methyl methacrylate) [41 mJ/m^2].³⁵ Aliphatic character decreased the polymer surface energy, whereas additional oxygen groups increased the surface energy.213

Figure 6-8. Comparison of surface energy calculated with static sessile contact angle measurements (\diamond) and advancing/receding contact angle measurements (\circ). The contact angles determined by the two-fluid static sessile method were higher than the angles calculated with the one-fluid equilibrium contact angle. The two-fluid Owens-Wendt formalism was used to calculate γ from θ for the static contact angle, whereas the Good-Girifalco method was used to calculate γ from θ_0 . It is worth noting that the trend in the surface energies is consistent for all of the polymers, which suggests that the static sessile method provides useful relative information about the polymer surface energies.216

Figure 6-9. Comparison of surface energy calculated using the two-fluid Owens-Wendt formula for static sessile contact angle measurements (\diamond) and Young's water contact angle measurements in conjunction with the static sessile diiodomethane contact angle measurements (\square). The two surface energies were in reasonable agreement; however, the surface energies calculated with the equilibrium contact angle were slightly higher than the static sessile method, as expected.217

Figure 6-10. Friction coefficient for a) PGM, b) PSM, c) PVM, d) PCM, e) PEM, and f) PPM with the glass (solid line) and HDPE (dotted line) probe. The friction coefficient was higher with HDPE than with glass for all polymers except PCM, likely owing to the higher adhesion between the neat materials and HDPE.218

Figure 6-11. Time-averages of sustainable polymer friction coefficients with the HDPE (\diamond) and glass (\blacklozenge) probes. The glass-polymer friction coefficient was within error for PGM, PSM, and PVM. PEM and PPM had similar glass-polymer friction coefficient, which was slightly smaller than the value for PGM, PSM, and PVM. PCM had a higher glass-polymer friction coefficient. The HDPE-polymer friction coefficient increased with oxygen content and decreased with aliphatic character. The error bars represent the standard deviation of the friction coefficient in time.219

Figure 6-12. Root mean squared roughness of sustainable polymer films measured using AFM.221

Figure 6-13. Pull-off forces for PSM (✕), PGM (+), PVM (◆), PCM (■), PEM (▲), and PPM (●) upon immediate retraction with approach and retraction velocities of a) 1.3 μm/s, b) 13 μm/s, and c) 26 μm/s. The pull-off forces for all of the polymers were low (< 0.5 mN), and there were no apparent trends with polymer structure. Thus, the adhesion alone cannot be causing the major shift in friction coefficient.....	224
Figure 7-1. Effect of casting solvent selectivity on height differences in polymer blend films. Phenetole is PS selective, <i>o</i> -xylene is nearly neutral for both PS and PI, and decalin is selective for PI. Atomic force microscopy height images are shown at the bottom; brighter colors represent higher regions. For all three solvents, the PS phase (which remains after <i>n</i> -hexane washes) is taller than the PI phase.....	237
Figure 7-2: Schematic of A/B-C polymer blends. The homopolymer, A, is shown in red, and the block polymer, B-C, is shown in blue and yellow, respectively. With increasing volume fraction A, the domain should shift from droplets of A in a B-C matrix to co-continuous A/B-C structures to matrix of A with droplets of B-C.....	244
Figure 7-3. Hierarchical organic photovoltaic (OPV) structure. Blue and green represent the two polymers and the gold capsules represent gold nanorods.....	246
Figure A-1. Common spin coating defects. The scale bar is 100 μm.....	257
Figure A-2. Non-uniformities in flow coated films.....	257
Figure B-1. Schematic of bell jar solvent vapor swelling setup. The films are placed in a chamber alongside a solvent reservoir. The solvent evaporates and produces a saturated solvent atmosphere inside the sealed chamber. The film thickness can be measured <i>in situ</i> using the spectral reflectometer through the quartz lid.....	259
Figure B-2. Flow solvent vapor annealing/swelling set-up. The nitrogen carrier gas is split into two streams; the first stream flows through the solvent bubblers, and the second stream acts as a diluent. The relative flow rates are controlled using mass flow controllers. Then, the solvent-rich vapor is delivered to the chamber, which is shown larger in Figure B-3. Changes in film thickness are monitored using a spectral reflectometer that is connected to a computer.....	260

- Figure B-3. Schematic of solvent vapor swelling chamber (not to scale). Solvent rich vapor in a nitrogen carrier gas is delivered to the sealed glass chamber. The quartz lid enables *in situ* film thickness measurements with a spectral reflectometer, which is moved using a motorized stage. The solvent vapor and N₂ gas exit the chamber *via* the exhaust port. Reprinted with permission from Emerson, J. A., *et al.* *Macromolecules* 2013, 46 (16), 6533-6540. Copyright 2013 American Chemical Society.261
- Figure B-4. Schematic of solvent collection experiments. After the N₂ passes through the solvent bubblers, the solvent rich vapor is condensed in a dry ice/isopropanol bath. The solvent condenses, and the N₂ is allowed to escape through the bleed needle to prevent pressurization. .262
- Figure B-5. Solvent uptake curves for chloroform (◆,▲), acetone (*), tetrahydrofuran (■,●), dimethylformamide (×). Manual (◆,*■) and automated (▲,●,×) flow controllers were used to flow N₂ through the solvent bubblers; there was not a significant difference between the two controller types with respect to the solvent uptake. The linear relationship between flow rate and solvent uptake suggests that the solvent-rich stream is saturated with respect to nitrogen.....263
- Figure B-6. Chloroform uptake with concentration. Between 24 °C and 28 °C, the solvent uptake is roughly linear with temperature. This 4 °C region has a ~30% difference in uptake values.....264
- Figure C-1. Time stamped spectra (reflectance [%] vs. wavelength [nm]) for drying curve experiments with 0.9 wt.% PS in *o*-xylene cast at 1500 rpm.266
- Figure C-2. a) Refractive index (n) and extinction coefficient (k) as a function of wavelength from Filmetrics (n: solid, k: dash dot) and literature (n: dash, k: dot).² b) Reflectance spectra (blue) fit for thickness using the Filmetrics model (red) produces a film thickness of 229 nm. c) The same spectra (blue) fit with the Campoy-Quiles refractive index profile (red) has a thickness of 216 nm. The thickness of this film from AFM was 222 nm ± 8 nm. Though both fits provide thicknesses within error of the AFM value, the Filmetrics fit is visually improved (lower residuals).267
- Figure C-3. Transmission experiment data at varying compositions of *o*-xylene (◆) and at varying mass fraction of P3HT (●). The dotted dashed line represents 100 % transmission (no phase separation). The solid red lines represent the spinodal fit to the data. The binodal region was determined by the deviation from 100 % transmission.271

Figure C-4. Digital photographs of PS/P3HT/ <i>o</i> -xylene solutions in the transmission cell. The volume fraction of each sample is indicated on the image. With increasing solvent concentration, the solutions change from opaque to optically transparent. Samples with higher P3HT content require more solvent to transition from the one phase (100% transmission) to the two phase (< 100% transmission) region. .	272
Figure C-5. Tilted vials containing PS ₉₀ /P3HT ₁₀ in <i>o</i> -xylene. For solution volume fractions less than or equal to 0.97, the mixture formed a gel-like state that was capable of suspending a stir bar when the vial was tilted 90°. Increasing the solvent concentration to 0.974 produced more liquid-like behavior; during the tilt test for this solution, the stir bar fell to the bottom of the vial.	273
Figure C-6. Morphology of ¹⁷ kPS/ ³³ kPMMA films cast from <i>o</i> -xylene. The scale bar represents 2 μm in all images, except for the bottom row of the optical micrographs, for which the scale bar is 5 μm. Although 0.9 wt.% 1:1 ¹⁷ kPS/ ³³ kPMMA in <i>o</i> -xylene cast into a film with microstructure, 5.0 wt.% and 9.0 wt.% solutions produced bilayer structure films. The color in the top row comes from height differences in the PS vs. PMMA domains, whereas it comes from thickness differences within a single polymer domain in the bottom rows.	280
Figure C-7. Replotting Eq. 3.2 for P4VV (●) in THF. The dashed line represents an extrapolation of the interaction parameter to higher polymer volume fractions.	281
Figure D-1. a) SEC of PPM (gray, solid) and PSAM (teal, dashed) in THF and CHCl ₃ , respectively. b) Second DSC trace on heating (endo up) of PPM (gray, solid) and PSAM (teal, dashed). The heating rate was 5 °C/min in N ₂	285
Figure D-2. Schematic of refractive index determination. First the reflectance spectrum is measured on the thin film. The position at which the spectra reflectance was captured is illustrated by the faded light spot. Note: the light spot does not burn in to the film. The film is then scratched using a razor blade, which does not damage the substrate surface at light loads. Atomic force microscopy is then used to measure the height of the scratch along a path shown schematically as the dashed black line. The resulting film thickness is then input into the fitting model for the spectrum, and the refractive index is varied until a good fit is achieved.	286

- Figure D-3. Effect of THF content on polymer mobility. The “rubbery” regime (●), in which the polymers have mobility, has a different slope than the “glassy” regime (●), in which the polymer is kinetically trapped. The closed symbols represent data from flow solvent vapor swelling experiments, whereas the open symbols represent data from THF/water bell jar experiments. For PES, the polymer remains rubbery across the THF content explored. PSM is glassy for the entirety of the experiments. The intersection of the glassy and rubbery lines provides the minimum polymer swelling to provide the polymer chains with sufficient mobility, called the crossover volume fraction, ϕ_c287
- Figure D-4. Effect of CHCl_3 on PSM T_g . In comparison to THF (shown in Figure D-3), CHCl_3 had a crossover between the glassy and rubbery regimes.288
- Figure D-5. Comparison of swelling of PGM (+) and PVM (◇) at the same CHCl_3 concentration. PGM swelled less than PVM at all CHCl_3 compositions, which suggests that CHCl_3 is a better solvent for PVM than PGM.289
- Figure E-1. Solvent selectivity for PS/PI mixtures. The $\phi_{\text{PS}} = \phi_{\text{PI}}$ line represents equal swelling under the same solvent conditions (neutral solvent). A solvent that falls below the line is PS selective, whereas a solvent that produces more swelling in PI is PI selective. *o*-Xylene and toluene are nearly neutral solvents for PS and PI. *cis*-Decalin is PI selective, and anisole is slightly PS selective.290
- Figure E-2. Various film instabilities formed during and after casting from initially clear solutions. In all cases, the PI films had evidence of dewetting (unstable).292

ABSTRACT

Polymer blend films are used in applications including organic optoelectronics and pressure sensitive adhesives. The film microstructure (domain size and composition) is a critical component that determines the material properties (*e.g.* friction coefficient). The morphology in these films is dictated by the thermodynamics and kinetics of phase separation in addition to the processing conditions, such as solvent evaporation, during film generation.

In this dissertation, the relationships between phase separation and casting conditions on microstructure and the effect of the resulting morphology on the friction coefficient were studied to produce targeted structures in multicomponent, hierarchical polymer blend films. First, a robust method was developed and implemented to measure polymer-solvent interaction parameters, which were used to predict the phase diagram in polymer blend solutions. The influence of the phase separation on the casting behavior was captured using *in situ* techniques. Second, the casting behavior and morphology of polymer blends was tuned through the addition of nanoparticles. The solvent quality, a parameter that has not previously been explored in polymer blend nanocomposites, was shown to impact the effect of the nanoparticles on the microstructure. Third, the relationships between the structure, composition, and friction coefficient were established to provide insight into rational design of tribologically-relevant materials like pressure sensitive adhesives. Finally, the techniques and methodologies developed in this dissertation were applied to renewable polymers to study the solvent-polymer interactions, surface energies, and

friction coefficients towards incorporating these sustainable materials into green, structured coatings.

Overall, this dissertation provides enhanced understanding and robust methods to characterize and control interactions in polymer blend films. These insights afford control over the final material properties through modifying the film morphology. The methods outlined in this work can be applied to polymer blend systems of interest for rational design of functional, hierarchical materials.

Chapter 1

INTRODUCTION

Polymer films are used in a variety of everyday items; food packaging, automotive coatings, organic photovoltaic devices, electronics, paint, among others contain at least one type of polymer coating. To produce these films, polymer solutions are often required. However, in multicomponent films, phase separation, which occurs as the result of inherent incompatibility between materials, can change the structure of the film drastically. In film applications, the morphology of the material influences the overall properties. Thus, understanding the relationship between the solution interactions, processing, and final morphology, both structurally and as it relates to material properties, is vital towards improved production of polymer films, as shown schematically in Figure 1-1.

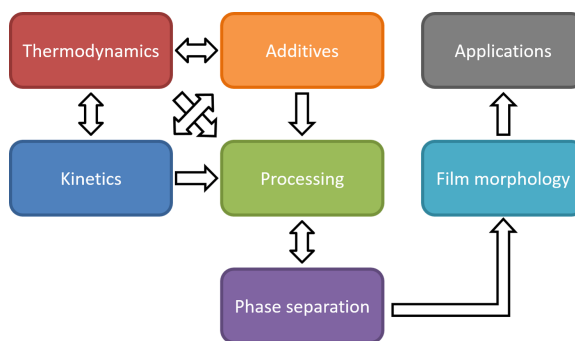


Figure 1-1. Flow chart of factors that influence the solution processing-structure-property relationships in multicomponent films.

First, the solution interactions largely are determined by the thermodynamics between the polymer and a second component including solvent, polymer, dispersed particles (pigments, fillers), surfactants, and other additives. Processing considerations and kinetics are most significantly influenced by casting method and solvent choice as well as the solution concentration. The thermodynamics, kinetics, and processing all lead to a particular film morphology; in polymer blends, there are two common structures: co-continuous domains and droplets of one polymer in the matrix of a second polymer. In the absence of solvent (melt-mixing), a variety of structures can be achieved in polymer blends due to deformation or further development of these initial structures, as shown in Figure 1-2, including the double emulsion, fiber, and lamellar morphologies.¹

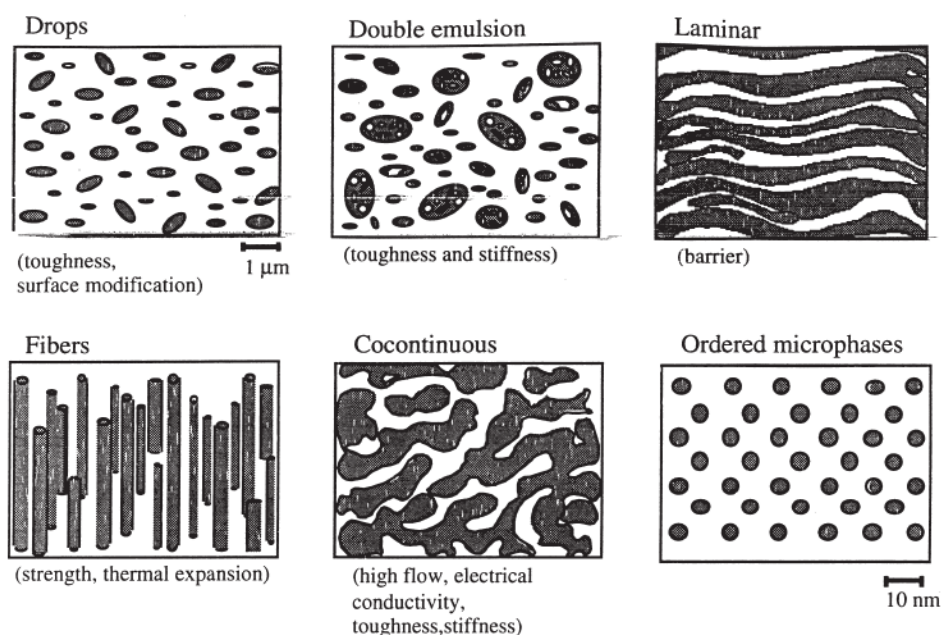


Figure 1-2. Schematic of morphologies produced by melt-mixed polymer blends. Reprinted with permission from Macosko, C. W. *Macromol. Symp.* 2000, 149, 171-184. Copyright 2000 John Wiley and Sons.

The resulting film properties influence the types of applications in which these blends can be used. For example, the droplet structures can impart toughness or stiffness, whereas the co-continuous structure promotes electrical conductivity; the lamellar film can be implemented in barrier applications. Therefore, controlling the morphology is key towards generating multicomponent, functional films. The next sections highlight the underlying thermodynamic and kinetic considerations in film generation, as well as the current structure-property relationships that have been determined in bulk and film geometries.

1.1 Polymer Thermodynamics

The polymer interactions with other components in a mixture affect the final morphology when a polymer film is cast from solution. Understanding the thermodynamics of polymer systems can be of great interest towards producing structures tuned for specific applications. One important thermodynamic property is the solubility parameter, δ . The solubility parameter can be applied to any mixture and provides *a priori* determination of the interaction between two materials. Starting with the simplest case of polymer-solvent interactions, the thermodynamics of polymer composite systems of varying complexity will be described by extension to polymer-polymer, polymer-polymer-solvent, and polymer-polymer-nanoparticle systems.

Thermodynamically, the free energy of mixing (ΔG_m) is given by the combination of enthalpic (ΔH_m) and entropic (ΔS_m) contributions:

$$\Delta G_m = \Delta H_m - T\Delta S_m \quad \text{Eq. 1.1}$$

for which T represents the absolute temperature. The entropy in the thermodynamics of polymer systems, which is discussed in the next sections, is taken to be solely the

result of configurational entropy, whereas the enthalpic contribution is affected by the constituents in the mixture by their direct and indirect molecular interactions.

1.1.1 Solubility Parameter

The solubility parameter, δ , provides quantification of the degree of interaction between materials. As such, it is an intrinsic material property and has units of $\text{MPa}^{1/2}$ [or $(\text{cal}/\text{cm}^3)^{1/2}$]. Hildebrand first proposed the solubility parameter, which is related to the cohesive energy density (the energy of vaporization per volume).² The solubility parameter is defined as the square root of the cohesive energy density,

$$\delta_i = \left(\frac{\Delta E_i^v}{V_i} \right)^{1/2} \quad \text{Eq. 1.2}$$

for which ΔE_i^v is the energy change of isothermal vaporization of species i and V_i is the molar volume of species i . Hildebrand and Scott related the solubility parameter to the enthalpy of mixing using regular solution theory,

$$\Delta H_m = V \left(\left[\frac{\Delta E_1^v}{V_1} \right]^{1/2} - \left[\frac{\Delta E_2^v}{V_2} \right]^{1/2} \right) \phi_1 \phi_2 \quad \text{Eq. 1.3}$$

in which V is the volume of the mixture and ϕ_i is the volume fraction of species i . Combining Eq. 1.2 with Eq. 1.3 allows the enthalpy (or heat) of mixing to be related to the solubility parameter,

$$\Delta H_m = \phi_1 \phi_2 V (\delta_1 - \delta_2)^2. \quad \text{Eq. 1.4}$$

From Eq. 1.4, the Hildebrand solubility parameter can be related to Flory-Huggins interaction parameters, which quantifies the interactions between two materials and will be discussed further in Section 1.1.2. The compatibility of any two components in a mixture can be determined using the solubility parameter. By this derivation, all of the interactions within the system are combined into a single

parameter. However, the Hildebrand model does not account for strong interactions such as polar and hydrogen bonding interactions. As such, it cannot accurately capture all types of interactions and applies best to systems containing only van der Waals interactions, which is applicable to many polymeric species.³

1.1.1.1 Hansen Solubility Parameters

To address the limitations of the Hildebrand solubility parameter in systems containing polar interactions and hydrogen bonding, Hansen proposed a modified model that accounts for the contributions of dispersive, polar, and hydrogen bonding forces between polymer subunits. Assuming that the cohesive energy density is the sum of the components ($E = E_d + E_p + E_h$), for which the subscripts d, p, and h represent the dispersive, polar, and hydrogen-bonding contributions, respectively; it follows that the solubility parameters are also a sum of their constituent components.

$$\delta^2 = \delta_d^2 + \delta_p^2 + \delta_h^2 \quad \text{Eq. 1.5}$$

Therefore, the influence of the individual forces can be accounted for in the total solubility parameter. The overall interaction under the Hansen solubility parameter is given as a solubility radius, R_2 . The solubility distance, D_{12} ,

$$D_{12} = \sqrt{4(\delta_{1,d} - \delta_{2,d})^2 + (\delta_{1,p} - \delta_{2,p})^2 + (\delta_{1,h} - \delta_{2,h})^2} \quad \text{Eq. 1.6}$$

represents the difference in solubility parameters of the polymer and solvent pair of interest, which allows for quantification of solvent quality. The ratio D_{12}/R_2 is called the “reduced energy density” (RED). Complete miscibility using the Hansen criterion occurs when $D_{12} < R_2$ (or $RED < 1$). RED values above 1 indicate a low affinity. However, R_2 must be measured experimentally, typically from solvent/non-solvent titration for a range of solvents, to determine solubility limits. The Hansen and Hildebrand solubility parameters also can be predicted by group contribution theory,

which will be discussed in the next section. These predictive methods provide *a priori* information about the solubility of a given material on the basis of its chemical constituents.

1.1.1.2 Group Contribution Theory

A number of group contribution theories have been introduced to predict the solubility parameter, molar volume, etc. of solvents and polymers.⁴⁻⁵ These group contribution theories largely have provided qualitative information about relative solubility; nonetheless, they are important to consider in design and application of materials, as they can estimate material properties solely on the basis of chemical structure. Group contribution theories rely on contributions from each of the molecular components to predict the properties of interest, commonly the solubility parameter.

Some of the most commonly used solubility parameter group contribution methods are Hoftyzer and van Krevelen,⁴ and Hoy.³ Hoftyzer and van Krevelen postulated relationships between the dispersive, polar, and hydrogen bonding solubility parameters and the respective molecular contributions, which are written in Eq. 1.7, Eq. 1.8, and Eq. 1.9,

$$\delta_d = \frac{\sum F_{d,i}}{V} \quad \text{Eq. 1.7}$$

$$\delta_p = \frac{\sqrt{\sum F_{p,i}^2}}{V} \quad \text{Eq. 1.8}$$

$$\delta_h = \frac{\sqrt{\sum E_{h,i}}}{V} \quad \text{Eq. 1.9}$$

for which $F_{d,i}$ is the dispersive energy contribution, $F_{p,i}$ is the polar energy contribution, and $E_{h,i}$ is the hydrogen bonding energy per structural group. For each structural unit, there is a corresponding group contribution, which is tabulated.⁴

The group contribution theory of Hoy differs from that of Hoftyzer and van Krevelen, but it follows the same principle. Hoy proposed the following series of equations to predict the solubility parameters based on a total solubility parameter, δ_t :

$$\delta_t = \frac{(F_t + B/\bar{n})}{V} \quad \text{Eq. 1.10}$$

The total solubility parameter is related to the molar attraction function, F_t , a constant “base value”, B , the number of repeat units per chain, \bar{n} is the number of repeat units per chain, and V is the molar volume of the structural unit of the polymer.

$$F_t = \sum N_i F_{t,i} \quad \text{Eq. 1.11}$$

$$B = 277 \quad \text{Eq. 1.12}$$

$$\bar{n} = \frac{0.5}{\Delta_T^{(P)}} \quad \text{Eq. 1.13}$$

in which $\Delta_T^{(P)}$ is a correction for non-ideality, given by

$$\Delta_T^{(P)} = \sum N_i \Delta_{T,i}^{(P)}. \quad \text{Eq. 1.14}$$

The polar component is related to the total contribution by the molecular aggregation number, α , the total (F_t) and polar (F_p) components of the molar attraction

$$\text{function, } B, \text{ and } \bar{n}. \delta_p = \delta_t \left(\frac{1}{\alpha^{(P)}} \frac{F_p}{F_t + B/\bar{n}} \right)^{1/2} \quad \text{Eq. 1.15}$$

for which

$$\alpha^{(P)} = \frac{777 \Delta_T^{(P)}}{V} \quad \text{Eq. 1.16}$$

and

$$F_p = \sum N_i F_{p,i}. \quad \text{Eq. 1.17}$$

The hydrogen bonding component is related to the total solubility parameter using the molecular aggregation number:

$$\delta_h = \delta_t \left(\frac{\alpha^{(P)} - 1}{\alpha^{(P)}} \right)^{1/2} \quad \text{Eq. 1.18}$$

and the dispersive component can be solved by Eq. 1.5, which has been rewritten in Eq. 1.19 to solve for the dispersive solubility parameter:

$$\delta_d = \left(\delta_t^2 - \delta_p^2 - \delta_h^2 \right)^{1/2} \quad \text{Eq. 1.19}$$

Both the Hoftyzer and van Krevelen and the Hoy methods provide qualitative information about changes in solubility with structural unit. However, group contribution theory typically overestimates the true material solubility parameter.⁴ Despite this limitation, it is often used to provide insight into the solubility of new and complex materials. To implement the solubility parameter relationships into energy of mixing, a thermodynamic model must first be known for the materials of interest.

1.1.2 Polymer-solvent Interactions

In the 1940's, Paul Flory and Maurice Huggins independently developed a theory that captured polymer-solvent interactions, which still is applied to a wide variety of systems. Their formalism comes from liquid lattice theory and assumes the solvent and repeat unit occupy the same segmental volume, as illustrated in Figure 1-3.

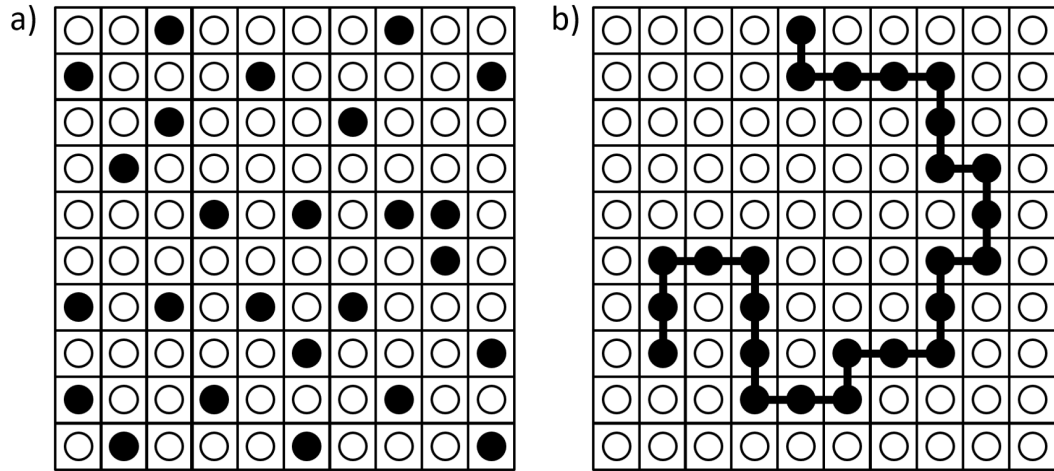


Figure 1-3: Schematic of lattice theory for a binary mixture of a) two solvents and b) solvent and polymer.

Using the derivative of Eq. 1.1 with respect to the number of solvent molecules and multiplication by Avogadro's number, N_{Av} , the free energy of mixing becomes the partial molar free energy, which is related to the chemical potential per mole. From lattice theory, Flory and Huggins determined the following relationship between solvents and polymers,⁶

$$\frac{\Delta\bar{G}_1}{RT} = \ln(1 - \phi_2) + \left(1 - \frac{V_1}{V_2}\right)\phi_2 + \chi_{12}\phi_2^2 \quad \text{Eq. 1.20}$$

for which $\Delta\bar{G}_i$ is the partial molar Gibbs free energy of component i , R is the universal gas constant, T is the temperature in K, ϕ_i is the volume fraction of component i with respect to total solution volume, V_i is the molar volume of component i , and χ_{ij} is the Flory-Huggins interaction parameter between components i and j , for which the solvent is written as 1 and the polymer is denoted as 2. A main limitation of the Flory-Huggins model is that it cannot account for preferential attractions between the

molecules, such as hydrogen bonding.⁶ Furthermore, at sufficiently low polymer concentrations, lattice theory cannot accurately describe the solution behavior.

By equating the chemical potential of two phases within the binary system, the equilibrium phase behavior may be determined. The conditions for equilibrium in a polymer-solvent system are given by

$$\mu_i = \mu_i' \quad \text{Eq. 1.21}$$

in which the prime designates the more concentrated of the two phases and i represents the material of interest (solvent = 1, polymer = 2). The critical conditions for the spinodal curve and critical point, respectively, are:

$$\left. \frac{\partial \mu_1}{\partial \phi_2} \right|_{T,P} = 0 \quad \text{Eq. 1.22}$$

and

$$\left. \frac{\partial^2 \mu_1}{\partial \phi_2^2} \right|_{T,P} = 0. \quad \text{Eq. 1.23}$$

Polymer-solvent interactions have been calculated with the Flory-Huggins theory using a variety of measurement techniques including scattering, osmosis, vapor pressure, inverse gas chromatography, melting or freezing point depression, intrinsic viscosity, and swelling equilibria.⁷ The phase behavior in polymer-solvent systems has also been determined experimentally. Furthermore, the polymer-solvent interactions can be related to the solubility parameter. The solubility parameter affords *a priori* assignment of solution behaviors, without measuring every polymer-solvent pair. As discussed in Section 1.1.1, the solubility parameter of component i , δ_i , is related to the enthalpy of mixing. From regular solution theory,

$$\chi_{12,H} = \frac{V_1}{RT} (\delta_1 - \delta_2)^2 \quad \text{Eq. 1.24}$$

for which V_1 is the molar volume of the solvent. One of the key limitations of regular solution theory is that only positive heats of mixing are possible. Thus, it works best for systems containing only dispersive forces and breaks down when hydrogen bonding contributes significantly to intermolecular forces. The Flory-Huggins interaction parameter can be modeled as the sum of entropic and enthalpic terms, as written in Eq. 1.25,

$$\chi_{12} = \chi_{12,H} + \chi_{12,S} . \quad \text{Eq. 1.25}$$

For polymer-solvent systems, the entropic contribution, $\chi_{12,S}$, is typically taken as 0.34. The criterion for polymer/solvent miscibility under the Flory-Huggins theory is $\chi_{12} < 0.5$. Combining Eq. 1.24 and Eq. 1.25 produces the commonly used relationship for the Flory-Huggins polymer-solvent interactions:

$$\chi_{12} = \frac{V_1}{RT} (\delta_1 - \delta_2)^2 + 0.34 . \quad \text{Eq. 1.26}$$

Given the entropic term in polymer-solvent systems, the difference between the solubility parameter of the pure solvent and the polymer must be less than 2 MPa^{1/2}. Generally, interaction parameters calculated with Eq. 1.26 are in good agreement with interaction parameters calculated from experimental data.⁷ To address the downfalls of the Hildebrand solubility parameters under strong association, the Hansen solubility parameters have also been related to the Flory-Huggins interaction parameter,⁸

$$\chi_{12} = \alpha \frac{V_1}{RT} \left([\delta_{1,d} - \delta_{2,d}]^2 + 0.25[\delta_{1,p} - \delta_{2,p}]^2 + 0.25[\delta_{1,h} - \delta_{2,h}]^2 \right) \quad \text{Eq. 1.27}$$

for which α is an empirical correction factor. However, even after optimization, Lindvig and coworkers only saw qualitative agreement between the calculated interaction parameter with experimental values.⁸ Furthermore, the error (~10%) was consistent with other approximations, such as group contribution theory. Though

these relationships provide *a priori* insight into the interactions, it is still important to validate the Flory-Huggins interaction parameter experimentally for polymer-solvent mixtures. Furthermore, although polymer-solution interactions play a key role in casting behavior, this binary mixture typically does not produce features. Thus, consideration of other additives is required to provide structures in polymer materials.

1.1.3 Polymer-polymer Interactions

In order to produce more complex architectures (see Figure 1-2 on pg. 2), it is relevant to consider the mixing of one polymer with another. From the initial polymer-solvent binary systems, the theory was extended to binary systems for which both components are polymer.

From the original Flory-Huggins theory, the free energy of mixing per segment for a polymer blend system is given by,

$$\frac{\Delta G_m}{k_B T} = \frac{\phi_1}{N_1} \ln \phi_1 + \frac{(1-\phi_1)}{N_2} \ln(1-\phi_1) + \phi_1(1-\phi_1)\chi_{12} \quad \text{Eq. 1.28}$$

for which ΔG_m is the change in free energy per segment upon mixing, ϕ_1 is the volume fraction of polymer 1 ($\phi_1 + \phi_2 = 1$), N_i is the number of segments in polymer i , and χ_{12} is the Flory-Huggins polymer-polymer interaction parameter. The phase behavior of such a system can be determined by the standard criteria for equilibrium (Eq. 1.29), stability (Eq. 1.30), and criticality (Eq. 1.31):

$$\frac{\partial \Delta G_m(\phi_1')}{\partial \phi_1} = \frac{\partial \Delta G_m(\phi_1'')}{\partial \phi_1} \quad \text{Eq. 1.29}$$

$$\frac{\partial^2 \Delta G_m}{\partial \phi_1^2} = 0 \quad \text{Eq. 1.30}$$

$$\frac{\partial^3 \Delta G_m}{\partial \phi_1^3} = 0 \quad \text{Eq. 1.31}$$

These equations can be solved to produce the polymer blend phase diagram, shown in Figure 1-4a.⁹ Eq. 1.29 describes the binodal line, also called the equilibrium curve. The binodal line represents the boundary between the one phase and two phase regions. Eq. 1.30 provides the spinodal curve, or the metastable line. Between the spinodal curve and binodal curve, phase separation occurs by nucleation and growth in the presence of a nucleation site (Figure 1-4b). Beneath the spinodal curve, phase separation evolves *via* spinodal decomposition (Figure 1-4c).

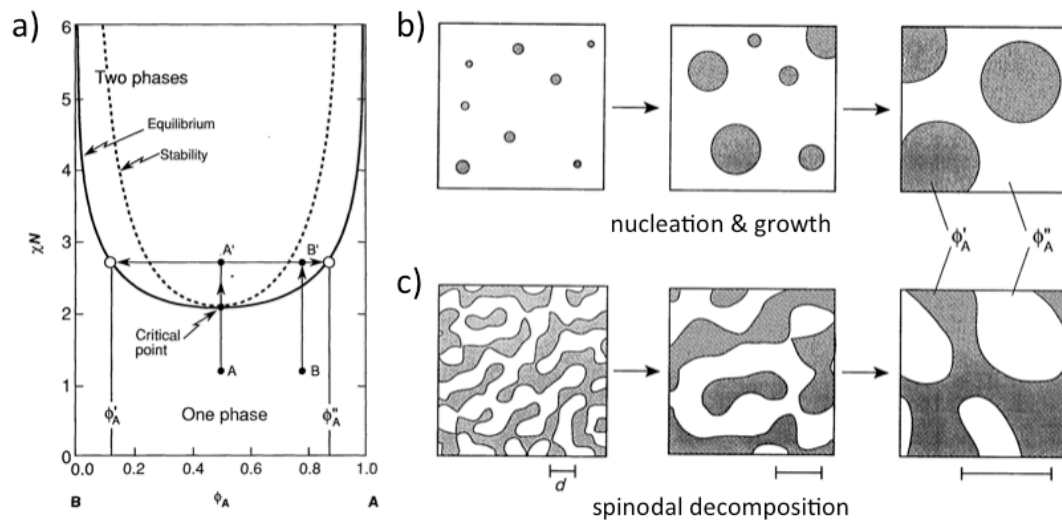


Figure 1-4: Phase behavior of polymer-polymer blends. a) Phase diagram for a model A-B blend for which χ is the F-H interaction parameter, N is the degree of polymerization, and ϕ_A is the volume fraction of component A. The solid curve is the binodal line and the dashed curve is the spinodal line. Phase separation occurring between the binodal and spinodal curve (metastable) [e.g. B to B'] goes by nucleation and growth, shown in b). Phase separation within the unstable, spinodal envelope [e.g. A to A' in a)] occurs by spinodal decomposition, as shown in c). The arrows in b) and c) represent time evolution of structures. From Bates, F. S. *Science* 1991, 251, 898-905. Reprinted with permission from AAAS.

The polymer-polymer interaction can also be captured using solubility parameter theories. The relationship described by Eq. 1.25 and Eq. 1.26 also apply to polymer/polymer blends. The key difference between polymer/solvent and polymer/polymer mixtures is the entropic contribution. For polymer/polymer blends, the entropic contribution (10^{-6} to 10^{-2}) to the Flory-Huggins interaction parameter is significantly smaller than the enthalpic contribution and can be neglected in this calculation.¹⁰⁻¹² The relationship between the solubility parameters and the interaction parameter for polymer/polymer blends is given by

$$\chi_{23} = \frac{V_0}{RT} (\delta_2 - \delta_3)^2 \quad \text{Eq. 1.32}$$

in which V_0 is the geometric mean of the polymer segment molar volumes, $V_0 = [V_2V_3]^{1/2}$. The criterion for miscibility is much smaller for polymer/polymer blends than for solvent/polymer mixtures, due to the increased number of contacts per molecule. In the presence of only dispersive forces, χ_{23} must be less than 0.002 ($\Delta\delta < 0.02$). If hydrogen bonding is present, the critical value of χ_{23} can span from 0.02 - 1.5, depending on the strength of the hydrogen bonding ($\Delta\delta < 0.2 - 6.0$).¹³ However, most polymer blend systems are immiscible, which produces phase separated architectures that can be of interest for applications.

Various researchers have worked towards measuring the phase boundary in polymer blends.¹⁴⁻¹⁷ A common method to determine phase behavior experimentally uses cloud point curves, for which turbidity or decreases in transmitted intensity indicates phase separation. For instance, Amis and coworkers made a gradient composition polymer film and heated on a gradient temperature stage to produce a visual representation of the phase behavior, which also agreed with the experimental cloud point curve.¹⁴ These experiments and others have been used to validate the

theoretical phase behavior expressions discussed in this section. The two-component mixture describes polymer-polymer interactions but lacks the solvent component required for most film processing techniques. Though these interactions can capture the behavior of blends in the melt phase, the contribution of solvent must be accounted for to better understand interaction-processing-structure-property relationships.

1.1.4 Polymer-polymer-solvent Interactions

Toward applications of polymer blends in films, it is often desirable to process in solution rather than the melt phase. Theoretically capturing the three-component phase behavior allows for insight into processing-structure relationships. The partial molar Gibbs free energy of each component (Equation 1.33 – 1.35), as described by R. L. Scott, can predict the phase behavior of polymer/polymer/solvent mixtures.¹⁸

$$\frac{\Delta\bar{G}_1}{RT} = \ln \phi_1 + \left(1 - \frac{1}{m_2}\right)\phi_2 + \left(1 - \frac{1}{m_3}\right)\phi_3 + \chi_{12}\phi_2^2 + \chi_{13}\phi_3^2 + (\chi_{12} + \chi_{13} - \chi_{23})\phi_2\phi_3 \quad \text{Eq. 1.33}$$

$$\frac{\Delta\bar{G}_2}{RT} = \ln \phi_2 + (1 - m_2)\phi_1 + \left(1 - \frac{m_2}{m_3}\right)\phi_3 + m_2[\chi_{12}\phi_1^2 + \chi_{23}\phi_3^2 + (\chi_{12} + \chi_{23} - \chi_{13})\phi_1\phi_3] \quad \text{Eq. 1.34}$$

$$\frac{\Delta\bar{G}_3}{RT} = \ln \phi_3 + (1 - m_3)\phi_1 + \left(1 - \frac{m_3}{m_2}\right)\phi_2 + m_3[\chi_{13}\phi_1^2 + \chi_{23}\phi_2^2 + (\chi_{13} + \chi_{23} - \chi_{12})\phi_1\phi_2] \quad \text{Eq. 1.35}$$

in which the solvent is written as 1, the two species of polymer are denoted as 2 and 3, and m_i is the ratio of the molar volume of component i to the solvent molar volume.

These equations can be combined and solved numerically to determine the phase diagram for a specific polymer/polymer/solvent system. For the symmetric case ($m_2 = m_3 = m$), the phase behavior diagrams are simplified and can be solved more readily, resulting phase diagram is shown in Figure 1-5. However, for asymmetric systems, these equations cannot be solved explicitly to produce the binodal curve. Instead, the

spinodal curve can be calculated using the secular determinant of the 3×3 matrix, as described by Scott.¹⁸⁻¹⁹

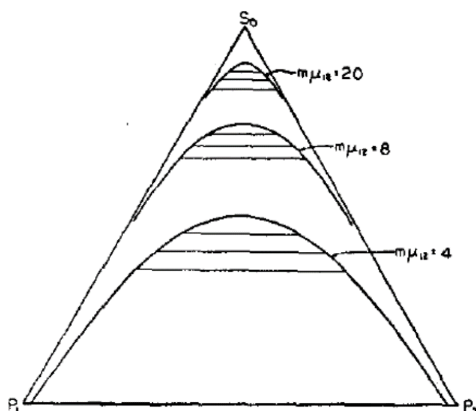


Figure 1-5: Phase diagram (binodal curve and tie lines) for polymer-polymer-solvent system in the case of a symmetrically binary system ($m_2 = m_3 = m$) with a neutral solvent ($\chi_{12} = \chi_{13} = \chi$) with a combined $m\chi$ of 4, 8, and 20. S_0 represents the solvent (1) and P_1 (2) and P_2 (3) represent the polymer phases. Reprinted from Scott, R. L. *J. Chem. Phys.* 1949, 17, 279-284, with the permission of AIP Publishing.

This theoretical treatment of thermodynamics of polymer-polymer-solvent mixtures has been validated by a number of studies.^{16, 20-25} Similar to polymer-polymer phase separation, light scattering can also be used to determine the binodal curve. In addition to light scattering, size exclusion chromatography has been utilized to locate the phase boundary. For example, Gómez and coworkers studied the phase separation of poly(vinylidene fluoride) with poly(styrene) in dimethylformamide with high performance liquid chromatography.²⁴ The agreement between theory and experiment is a promising step towards creating interaction-processing-structure-property relationships in polymer blends.

1.1.5 Polymer-polymer-nanoparticle Interactions

For many applications, it is desirable to include a nanoparticle filler to provide enhanced thermal, electrical, and mechanical properties. In comparison to the polymer/polymer/solvent system, there are additional nanoparticle-nanoparticle interactions to consider.²⁶

Ginzburg developed a theory to capture the thermodynamics of polymer/polymer/nanoparticle blends.²⁶ The free energy of such a system contains 3 main contributions from the polymer, particle, and interaction:

$$G = G_{pol} + G_{par} + G_{int} \quad \text{Eq. 1.36}$$

The polymer free energy is given by the Flory-Huggins theory with corrections to account for the volume occupied by the nanoparticle species,

$$G_{pol} = \frac{(1-\psi)\phi_1}{N} \ln \left[\frac{(1-\psi)\phi_1}{N} \right] + \frac{(1-\psi)(1-\phi_1)}{N} \ln \left[\frac{(1-\psi)(1-\phi_1)}{N} \right] + \chi_{12}(1-\psi)^2 \phi_1(1-\phi_1) \quad \text{Eq. 1.37}$$

for which ϕ_1 is the volume fraction of polymer 1 in the blend, ψ is the volume fraction of the nanoparticles, N is the degree of polymerization ($N_1 = N_2 = N$), and χ_{12} is the polymer-polymer interaction parameter.

The free energy of the particle, G_{part} , is described by the entropic free energy of hard spheres, for which the non-ideal term (second term) comes from the Carnahan-Starling equation of state.

$$G_{part} = \frac{\psi}{v_p} \left[\ln \psi + p \left(\frac{R_p}{r_0} \right) \frac{4\psi - 3\psi^2}{(1-\psi)^2} \right] \quad \text{Eq. 1.38}$$

G_{int} provides a mathematic description for the interaction between the polymers and the particles, and it consists of both an enthalpic and entropic contribution:

$$G_{int} = \frac{\psi}{v_p} (1-\psi) p \left(\frac{R_p}{r_0} \right) \frac{3R_p^2}{2Nr_0^2} + \chi \psi \left[\frac{r_0}{R_p} \right] (1-\psi)(1-\phi) \quad \text{Eq. 1.39}$$

The entropic term (first term) comes from chain stretching due to particle insertion, whereas the enthalpic contribution (second term) is proportional to the number of contact between the particles with polymer surfaces. In eq. 1.38 and eq. 1.39, there is an interpolating factor $p(R_p/r_0)$, for which p is given by the interpolating function $p(x) = \max[\tanh(x-1), 0]$, R_p is the radius of the particle, and r_0 is the radius of the monomer.

In the case of polymer nanocomposite blends, the stability conditions are

$$\frac{\partial^2 G}{\partial \phi^2} > 0,$$

$$\frac{\partial^2 G}{\partial \psi^2} > 0,$$

and

$$J = \det \begin{vmatrix} \frac{\partial^2 G}{\partial \phi^2} & \frac{\partial^2 G}{\partial \phi \psi} \\ \frac{\partial^2 G}{\partial \phi \psi} & \frac{\partial^2 G}{\partial \psi^2} \end{vmatrix} = \left[\frac{\partial^2 G}{\partial \phi^2} \right] \left[\frac{\partial^2 G}{\partial \psi^2} \right] - \left[\frac{\partial^2 G}{\partial \phi \psi} \right]^2 > 0.$$

This model has limitations at high nanoparticle volume fractions ($\psi > 0.3 - 0.4$), which can have positional ordering and crowding of particles. Because of these limits, it is not possible to analytically describe the full phase behavior of a polymer-polymer-nanoparticle system with high particle concentrations.

Next, consider that particles can have preferential interactions with one phase or have neutral interactions. With preferential interactions, the nanoparticles partition within that polymer phase and have incompatible interactions with the other phase.

The spinodal curves for the case for $\chi_{1-NP} = 0$ and $\chi_{2-NP} > 0$, for which 1 and 2 represent the different polymer types, and $N_1 = N_2 = 100$ are shown in Figure 1-6.²⁶ With increasing particle volume fraction (ψ), the spinodal curve is shifted to higher

compatibility (higher χN). The smallest particles (Figure 1-6a) act as compatibilizers. As the radius of the polymer increases, the spinodal curves become more asymmetric and the miscibility between the particles and polymer worsens.

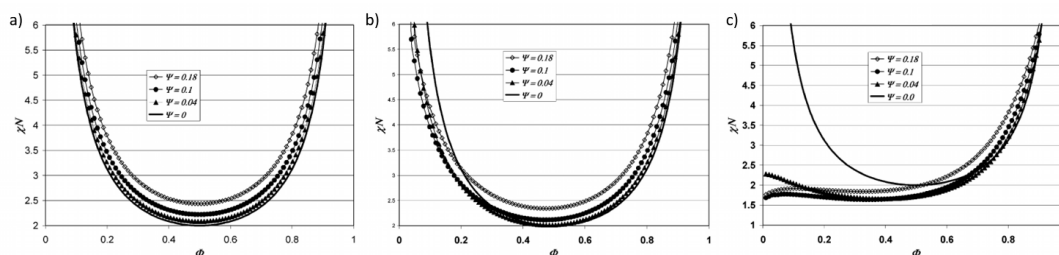


Figure 1-6: Calculated spinodal curves for polymer/polymer blends with $N_1 = N_2 = 100$ containing spherical nanoparticles that have a preferential interaction with one of the polymers. ϕ_1 is the volume fraction of polymer 1 in the blend and ψ is the volume fraction of the nanoparticles. The radius of the nanoparticles, R_p , given in lattice units of the polymer (r_0) is a) 1, b) 5, and c) 10. Adapted with permission from Ginzburg, V. V., *Macromolecules* 2005, 38, 2362-2367. Copyright 2005 American Chemical Society.

This theoretical approach was also solved for neutral particles ($\chi_{1-NP} = \chi_{2-NP} = 0$) in later work as shown in Figure 1-7.²⁷ The small particles ($R_p/r_0 = 3$, red) compatibilize the binary blends, as the spinodal curves lie inside and above the neat homopolymer system. Larger particles ($R_p/r_0 = 10$, blue) act as compatibilizers for symmetric and moderately asymmetric mixtures ($0.3 > \phi > 0.7$); however, for highly asymmetric mixtures of the two polymers, the particles act as destabilizing agents for the blend (wider region of instability). The thermodynamics of polymer blend nanocomposites have also been reported experimentally, which showed good agreement with the theoretical models.^{26, 28-30}

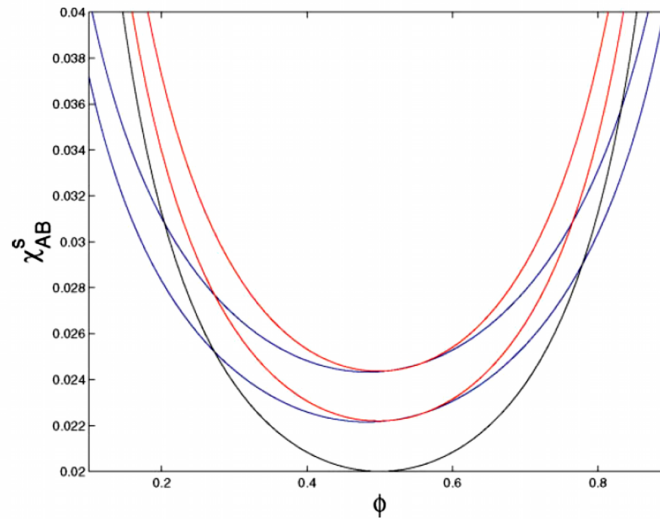


Figure 1-7. Spinodal curve for homopolymer blend (black) and the same blend filled with $\psi = 0.18$ (upper red & blue curves) or $\psi = 0.10$ (lower red & blue curves) for particle sizes $R_p = 3 r_0$ (red) and $R_p = 10 r_0$ (blue). The nanoparticles are “neutral”, meaning the interaction with A is the same as the interaction with B. Reprinted with permission from He, G., *et al. J. Polym. Sci., Part B: Polym. Phys.* 2006, 44, 2389-2403. Copyright 2006 John Wiley & Sons.

The thermodynamic behavior described in this section represent the equilibrium thermodynamics. However, these systems rarely are maintained at thermodynamic equilibrium, and they are often quenched or kinetically trapped. Thus, towards developing interaction-processing-structure-property relationships, it is important to also understand the kinetics involved in producing these phase separated structures.

1.2 Kinetic Considerations

In addition to the thermodynamics of phase separation, kinetics play a key role in various film preparation steps. There are two main contributions to the kinetics

during casting. The first effect comes from the thermodynamic incompatibility and depends on both the interactions and the depth of the quench during processing. The second factor is the result of kinetic trapping due to solvent removal.

1.2.1 Phase Separation

As discussed in the first sections, the Flory-Huggins interaction parameters have been utilized to describe the compatibility, with extensions to describe the phase behavior. Due to the large number of contacts between the polymers and other constituents, phase separation occurs in most systems. In binary systems, phase separation typically goes by nucleation and growth or spinodal decomposition. The thermodynamics of these transitions were discussed previously.

1.2.1.1 Kinetics of Phase Separation: Theory

Phase separation in binary systems occurs by two mechanisms (1) spinodal decomposition, or (2) nucleation and growth, illustrated in Figure 1-4 (pg. 13). Spinodal decomposition can produce co-continuous structures. The most common formalism to describe spinodal decomposition phase separation is that developed by Cahn and Hilliard for binary incompatible mixtures.

Spinodal decomposition occurs due to local density fluctuations. Cahn and Hilliard proposed that the free energy, F , of an inhomogeneous solution is given by

$$F = \int [f(c) + \kappa(\nabla c)^2] dV . \quad \text{Eq. 1.40}$$

in which $f(c)$ is the free energy density of a homogeneous material with composition c , κ is a positive constant (sometimes called the gradient energy coefficient)³¹, and ∇c is the concentration gradient. The product $\kappa(\nabla c)^2$ describes the free energy density contribution for a gradient in material composition. The difference in free energy

between the homogenous (of average concentration c_0) and inhomogeneous solution is then given by

$$\Delta F = \int \left[\frac{1}{2} \left(\frac{\partial^2 f}{\partial c^2} \right) (c - c_0) + \kappa (\nabla c)^2 \right] dV \quad \text{Eq. 1.41}$$

For $\partial^2 f / \partial c^2 > 0$, the free energy difference is stable to all fluctuations, whereas for $\partial^2 f / \partial c^2 < 0$, the solution is unstable to fluctuations for which the first term dominates.

At early times, the functional form of spinodal decomposition can be described by³²

$$\frac{\partial c}{\partial t} = M \left(\frac{\partial^2 f}{\partial c^2} \right) \nabla^2 c - 2M\kappa \nabla^2 c \quad \text{Eq. 1.42}$$

At long times, the co-continuous structures produced by spinodal decomposition become droplet-like in nature. For the late stage of spinodal decomposition in fluids, Siggia determined that domain growth during phase separation should transition from being proportional to the time, t , to following a $t^{1/3}$ behavior.³³ This early work by Cahn, Hilliard, and others was extended to polymers by de Gennes, Pincus, and Binder.³⁴⁻³⁶ In the early stages of phase separation, the fluctuations should have a wavelength on the order of the interfacial thickness (small compared to the ideal chain radius).³⁴ During the later stages of spinodal decomposition, when phase coarsening occurs by coalescence of droplets, de Gennes reported that the growth rate should transition from $t^{1/5}$ to $t^{1/3}$ as the domain size surpasses the chain radius.³⁴

Though the previous work was focused on bulk materials, there also have been simulation studies on phase separation with consideration of surface effects, which are important in supported films.³⁷⁻³⁸ Marko determined that the domain growth can be slowed in the presence of concentration oscillations near boundaries.³⁸ Work by Hore

and Laradji found that there were three stages during phase separation (1) the kinetics follow the bulk behavior of spinodal decomposition; (2) breakup of the co-continuous domain into droplets, for which droplets smaller than the film thickness grow and droplets larger than the film thickness shrink; and (3) backflow of polymer within the wetting layer into the film.³⁷ Thus, careful consideration of the geometry (bulk vs. thin film) is important to accurately determine the kinetics of the polymer-polymer-solvent phase separation process.

1.2.1.2 Kinetics of Phase Separation: Experimental Studies

In addition to the theoretical and simulation work on the kinetics of phase separation, a number of experimental studies have been reported for polymer solutions³⁹⁻⁴⁰ polymer blends,^{21, 41-60} and polymer blend nanocomposites.⁶¹ Most experimental studies found qualitative agreement with the kinetic theories proposed in the previous section. For example, Wang and Composto measured the morphological evolution in polymer blend films of deuterated poly(methyl methacrylate) [PMMA] and poly(styrene-*ran*-acrylonitrile) [SAN], using temperature to provide mobility.⁴⁴ They found at short times (> 15 min), the lateral domain growth is proportional to t , as described in the previous theories. As the domain size approached the film thickness, the growth slowed to $t^{1/3}$. For polymer blend nanocomposites, Chung and coworkers studied the effect of nanoparticles on the polymer blend kinetics during thermal annealing.⁶¹ At early times for nanoparticle loadings less than 5 wt.%, they also saw the domain size grow as $t^{1/3}$. The domain size decreased with increasing nanoparticle content, which they attributed to an increase in viscosity due to the nanoparticle incorporation. However, measuring real-time phase separation during casting, which

typically occurs on the order of seconds, remains a key challenge to understanding the relationship between the interactions, processing, and final material structure.

1.2.2 Casting from Solution

The kinetics in film casting largely come from the evaporation of solvent, which decreases the compatibility between the constituents in solution by increasing their concentration. Upon solvent removal, multicomponent solutions begin to phase separate, largely by mechanisms discussed in the previous section. The removal of solvent leads to an increase in incompatibility between materials, which drives phase separation, while simultaneously reducing the mobility. Thus, solvent removal is an important factor in understanding kinetic effects.

In homopolymer films, the solvent removal serves to quench the film at a specific thickness, as these materials typically are featureless. However, in multicomponent polymer systems, the evolution of the film morphology during casting (solvent removal) has been studied extensively.^{16, 62-68} These *in situ* studies can provide significant insight into the late stages of phase separation. However, to date, the onset and early stages of phase separation has not been reported for polymer blend systems during casting due to the small domain sizes and short time scales.

Howse and coworkers have studied the phase separation in polymer blend systems during casting (solvent removal) for both spin coating and blade coating geometries.^{16, 62, 64-65, 68} Using stroboscopic illumination, they captured the morphological evolution in thin films with sub-second resolution from the appearance of macroscopic structures through the final (dry) film structure. Though the structural development measured likely represents the late stages of phase separation once the film has begun to solidify, these studies provide key insights into the development of

structure during processing. The solvent evaporation and polymer interactions play a key role in determining the structure formed in these films.

1.3 Structure-property Relationships in Polymer Films

For decades, polymer films have been utilized for applications ranging from coatings, food & beverage, packaging, healthcare, energy, household goods, among many others. There are a number of different film architectures that have been demonstrated.

1.3.1 Homopolymer

Homopolymer films represent the simplest architecture of film. Homopolymer films have been used for coatings in a variety of fields, such as the pharmaceutical⁶⁹ and food/beverage⁷⁰ industries. However, the simplicity of these materials limits their use in many applications. Furthermore, homopolymer films typically do not have structure, and as such, do not require complex structure-property relationships. In many cases, improved properties are desired, such as electrical conductivity, which can be provided by additives.

1.3.2 Polymer Nanocomposites

To incorporate secondary function, such as mechanical strength, electrical conductivity, among others, nanoparticle fillers can be introduced.⁷¹⁻⁷² Though significant work has been done in the field of organic and clay-based nanofillers,⁷³⁻⁷⁴ we focus on metal-based fillers in this dissertation. These inorganic nanoparticles can impart thermal,⁷⁵⁻⁷⁷ optical,⁷⁸⁻⁸⁶ electrical,^{82, 87-98} magnetic,⁹⁹⁻¹⁰⁰ mechanical,^{76, 101-104} and other properties¹⁰⁵⁻¹¹³ as well as stability¹¹⁴⁻¹¹⁷ to the polymer composite.

Control of particle dispersion and development of structure-property relationships are key steps towards producing ideal material properties in polymer nanocomposites.^{71, 86, 118-130} Because the nanoparticle structure within the polymer nanocomposite plays a key role in the material properties, many studies have focused on tuning the interactions within the system to produce more ideal dispersion. One of the common recent applications for polymer nanocomposites is in organic optoelectronics, such as organic photovoltaics.^{85, 87-88} For example, Huynh and coworkers studied the effect of cadmium selenide (CdSe) nanorods in poly(3-hexylthiophene) [P3HT] for applications in organic photovoltaics (OPV)s.⁸⁸ They found improved dispersion of the nanoparticles by modification of the particle-polymer interaction through incorporation of a second solvent, which acted as a ligand for the particles. For OPVs, this dispersion is optimal, as it increases the polymer-particle interfacial area, which facilitates charge transport between the materials for enhanced conductivity. This work highlights the importance of understanding the desired polymer dispersion and the ability to control the aggregation of particles.

To augment the experimental work simulations have also helped to elucidate the factors and mechanisms underlying particle dispersion.¹³¹⁻¹³⁸

Polymer nanocomposites typically are produced by melt mixing or casting from solvent. In solvent, grafting a ligand to the particle surface improves dispersion with the polymer matrix.¹²⁶ In addition to the effects of brush-matrix interactions, the solvent quality and removal can affect the nanoparticle dispersion.¹³⁹

In polymer-grafted nanoparticle systems, the ratio of the graft chain length (P) to the matrix chain length (N), P/N , can be of particular importance.¹⁴⁰⁻¹⁴³ For spherical particles, Harton and coworkers used self-consistent mean-field model to

demonstrate the miscibility of grafted nanoparticles within a polymer matrix of the same material.¹⁴⁰ They found that miscibility increased with decreasing particle radius and increasing brush chain length (P). Frischknecht examined the miscibility of nanorods using self-consistent mean theory within a matrix and saw that the for $P/N > 1.5$, the particles were dispersed and P/N did not depend on the size of the particle.⁷⁹ For the corresponding experimental system, they reported that the P/N ratio depended on the size of the particle; however the critical P/N ranged from 2 to 6 for the systems modeled. The existence of a critical P/N ratio has also been elucidated experimentally elsewhere.^{84, 144-145} For gold nanorods of varying aspect ratio (2.5 - 6.3), Composto and coworkers found that a $P/N > 2$ resulted in aggregation.^{79, 84, 145} Though there is agreement between the simulation and experiment, these studies do not focus on the kinetic behaviors that also affect the dispersion.¹³⁹ Thus, the development of interaction-processing-structure-property relationships can benefit from further understanding of the effect of particles on processing.

1.3.3 Polymer Blends

Driving structures in polymer/nanoparticle blends can be difficult due to the inherent nature of the nanofiller. Polymer/polymer blends can be used to achieve enhanced material properties and are highly tunable, given that changing the formulation does not require additional synthetic steps. Though there are advantages in using miscible polymer blends, this work focuses on immiscible polymer blends, as the natural incompatibility between the polymers produces phase separation, which can be controlled into two microstructures. For immiscible binary polymer blends, there are two main morphologies that are produced upon phase separation: (1) dispersed phase or (2) co-continuous phases. The co-continuous phase morphology is

produced by spinodal decomposition, whereas the dispersed phase architecture commonly is the result of nucleation and growth. The phase separation mechanisms are discussed further in Section 1.2.1.

Polymer blends can be utilized in a variety of applications, such as organic optoelectronics,^{53, 146-158} membranes,¹⁵⁹⁻¹⁶⁰ and coatings.¹⁶¹⁻¹⁶² For each of these applications, a particular morphology is of interest to produce the desired material properties. For instance, in organic photovoltaics, a co-continuous structure with small domain sizes produces the highest efficiency.¹⁵⁷ Thus, characterizing the morphology of polymer blends and understanding the key parameters required to produce targeted structures are critical towards utilizing blends in applications.

A number of studies have examined the morphology in solvent-cast polymer blends and provided insight into the effect of various parameters on the film morphology.^{53, 146-185} One parameter that can be used to control the architecture is the blend composition.¹⁶³ To achieve a co-continuous structure, a composition near the critical blend concentration must be utilized to avoid phase separation by nucleation and growth. Droplet structures can be targeted by more asymmetric mixtures. In addition to the composition, the interactions can be tuned using molecular weight. Li and coworkers reported changes in the domain structure by varying the polymer molecular weight.^{172, 174} To further tune the thermodynamics (and morphology) of these blend systems, the solvent-polymer interaction or the preferential wetting can be controlled, as demonstrated by Walheim.¹⁸¹ Yamamura and coworkers studied the effect of solvent removal and found shorter drying times produced smaller droplets.¹⁸⁰ Though many factors were examined, a better connection of the thermodynamics, kinetics, and structure is required to target blend morphologies.

1.3.4 Polymer Blend Nanocomposites

Polymer blend nanocomposites are an extension of polymer blends and polymer nanocomposites. These materials benefit from the functionality of the nanoparticles as well as the tunability of the polymer blend. There are a few cases of miscible blend nanocomposites that have been reported in literature. Miscible blend nanocomposites are effectively an extension of polymer nanocomposites, but the second polymer affords additional tunability of interactions and functionalities.¹⁸⁶⁻¹⁸⁹ The key challenges facing miscible polymer blends is in tuning the interactions between the polymer and nanoparticle as well as controlling the dispersion, which was further discussed in Section 1.3.2.

Immiscible polymer blend nanocomposites further benefit from the phase separated structure of the polymer blend. Additionally, polymer blend nanocomposites typically have more stable morphologies, which are not affected by annealing due to the jammed or pinned structure, than the neat polymer blends. However, the phase separation itself is affected by the incorporation of nanoparticles. There has been a significant amount of research on the effect of particle incorporation on polymer blend morphology, both theoretical¹⁹⁰⁻¹⁹² and experimental^{61, 193-196}. However, the research on the interaction-processing-structure of these materials has been limited due to the wide and varied experimental parameter space.¹¹⁸

Similar to polymer nanocomposites, immiscible polymer blend nanocomposites are of interest in a variety of applications, such as radiation shielding,¹⁹⁷⁻¹⁹⁹ electronic devices,²⁰⁰⁻²⁰² and optical materials.²⁰³ In addition to affording new functionalities and strength, which are not otherwise accessible by polymers alone, nanofillers affect the morphology of the blend architecture.^{29, 204-209} Furthermore, nanoparticles can impart film stability by trapping the morphology.²¹⁰⁻²¹¹

Nanoparticles can localize in two main locations of interest within polymer blend nanocomposites (1) at the interface between the domains or (2) within one domain. Nanoparticles at the interface are typically considered compatibilizers, as they can reduce the domain size, and they work to stabilize (kinetically trap) the morphology by jamming the interface.¹⁹⁵ Nanoparticles within the domain are thought to slow domain growth during phase separation.¹⁹⁵

Nanoparticle compatibilizers are typically neutral to both polymers; in other words, these fillers lack a strong preferential association with either polymer. A spherical particle will be localized at the interface (act as a compatibilizer) if the difference in the surface tension between the particles and each phase is smaller than the surface tension between the two polymers²¹²

$$|\sigma_{A/NP} - \sigma_{B/NP}| < \sigma_{A/B} \quad \text{Eq. 1.43}$$

Work by Kwon and coworkers demonstrated the effect of nanofiller compatibilization of polymer blends; they found a three-fold reduction in domain size with 1 vol.% nanoparticle.²¹³ Simulation studies on the effect of Janus nanorods found that the surface geometry was a key parameter in the kinetics of polymer blend nanocomposites under shear.²¹⁴

In comparison to neutral nanoparticles, which assemble at the interface and act as compatibilizers between the polymers, nanofillers with preferential interactions will often partition into one of the polymer domains. The partitioning in polymer blend nanocomposites can be affected by brush length,²¹⁵ film thickness,¹⁹⁴ volume fraction,¹⁹⁴ and surface/brush chemistry.^{196, 215}

The nanoparticle partitioning within the polymer blend nanocomposite can also affect the properties. As such, knowing the position of the nanoparticles within the

domain is key to understanding the effect of the filler on the properties.²¹⁶⁻²¹⁸ Boiteux and coworkers found that iron particles dispersed into the poly(propylene) [PP] phase of a PP/polyamide/iron particle composite had a lower electrical percolation threshold than the homopolymers with the same conductivity.²¹⁷ Li and coworkers used the percolation of particles partitioned into one of the domains to kinetically trap the morphology evolution, demonstrating that particles are not required to localize at the interface to halt the phase separation.²¹⁸ Though there has been significant work towards understanding the effect of nanoparticles on the morphology and properties of polymer blend nanocomposites, most of these studies have been done on the final structure and are not related back to the processing.

1.4 Dissertation Overview

Modulating the microstructure of polymer blend films can be utilized to control functional properties, such as the friction coefficient. The thermodynamics and processing affect the overall microstructure. Control over microstructure of multi-component polymer blend systems can be achieved by developing insight into interaction-processing-structure-property relationships relevant to polymer films, as shown schematically in Figure 1-1 (pg. 1). However, there are a number of parameters that contribute to the thermodynamics, kinetics, and processing, which then control the morphology. A more detailed description of these factors is shown in Figure 1-8. Thus, understanding the individual contributions is not trivial.

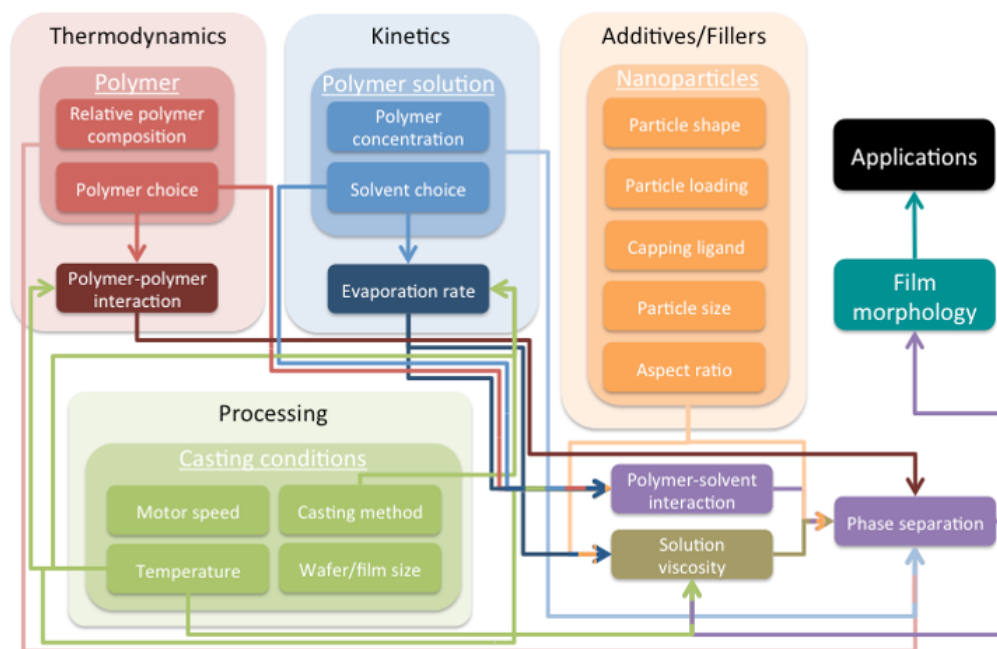


Figure 1-8: Detailed flow chart of controllable factors that affect solution-processing-structure-property relationships in multi-component polymer films.

Overall, this dissertation outlines methods to measure and control the interactions and processing to tune the morphology in films and tune the functional properties, in particular the friction coefficient, of blend films using the microstructure. Descriptions of film generation, characterization techniques, and particle synthesis used to develop interaction-processing-structure-property relationships are provided in Chapter 2.

The morphology in polymer blends is determined by the thermodynamics and processing. One of the key contributions made through this work, as described in Chapter 3, is the robust protocol for determining polymer thermodynamics and relating those parameters to the phase behavior. *In situ* characterization techniques, including stroboscopic illumination, were applied to demonstrate the importance of the

phase diagram (thermodynamics) and solvent removal (kinetics) on the film structure. The formation of hierarchical structures was studied in Chapter 4 using the phase separation of immiscible polymer blends to drive the assembly of nanoparticles. The importance of interactions and processing on the partitioning of the nanoparticles within the polymer blend is highlighted.

Due to their multi-component nature, polymer blend films have tunable friction and wear properties. The friction coefficient is dependent on the microstructure and composition of the polymer blend. Control over polymer blend film friction coefficients is afforded by modifying the blend film structure using composition and processing (solvent vapor annealing techniques), as described in Chapter 5. Building upon the insight gained in the previous sections, Chapter 6 contains the study of sustainable polymers towards developing new polymeric systems. In particular, the solvent-polymer interactions, surface energies, and friction coefficients were characterized and related to the chemical structure of these renewable materials, which can be developed into green, structured coatings. Finally, Chapter 7 contains a summary of the main results along with recommendations for future directions.

In this dissertation, we demonstrate effects of processing on materials starting from the thermodynamics and kinetics of the initial solutions. From the examples discussed in this chapter, it is obvious that there is a lack of understanding in polymer solutions concerning relating various processing parameters and conditions to the final film morphology. The goal of this dissertation is to provide key insight and guidance towards developing interaction-processing-structure-property relationships to target desired structures and properties.

REFERENCES

1. Macosko, C. W., Morphology development and control in immiscible polymer blends. *Macromolecular Symposia* **2000**, *149*, 171-184.
2. Hildebrand, J. H.; Scott, R. L., *Regular solutions*. Prentice-Hall: 1962.
3. Hansen, C. M., *Hansen Solubility Parameters: A User's Handbook, Second Edition*. CRC Press: 2007.
4. van Krevelen, D. W.; Nijenhuis, K. T., *Properties of Polymers - Their Correlation with Chemical Structure; Their Numerical Estimation and Prediction from Additive Group Contributions*. 4 ed.; Elsevier: Amsterdam, 2009.
5. Miller-Chou, B. A.; Koenig, J. L., A review of polymer dissolution. *Prog. Polym. Sci.* **2003**, *28*, 1223-1270.
6. Flory, P. J., *Principles of Polymer Chemistry*. Cornell University Press: Ithaca, 1953.
7. Brandrup, J.; Immergut, E. H.; Grulke, E. A., *Polymer Handbook*. 4th ed.; Wiley: New York, 1999.
8. Lindvig, T.; Michelsen, M. L.; Kontogeorgis, G. M., A Flory–Huggins model based on the Hansen solubility parameters. *Fluid Phase Equilib.* **2002**, *203*, 247-260.
9. Bates, F. S., Polymer-polymer phase behavior. *Science* **1991**, *251*, 898.
10. Graessley, W. W.; Krishnamoorti, R.; Reichart, G. C.; Balsara, N. P.; Fetters, L. J.; Lohse, D. J., Regular and irregular mixing in blends of saturated hydrocarbon polymers. *Macromolecules* **1995**, *28*, 1260-1270.
11. Maranas, J. K.; Mondello, M.; Grest, G. S.; Kumar, S. K.; Debenedetti, P. G.; Graessley, W. W., Liquid structure, thermodynamics, and mixing behavior of saturated hydrocarbon polymers. 1. Cohesive energy density and internal pressure. *Macromolecules* **1998**, *31*, 6991-6997.

12. Muller, M., Miscibility behavior and single chain properties in polymer blends: a bond fluctuation model study. *Macromol. Theory Simul.* **1999**, *8*, 343-374.
13. Coleman, M. M.; Serman, C. J.; Bhagwagar, D. E.; Painter, P. C., A practical guide to polymer miscibility. *Polymer* **1990**, *31*, 1187-1203.
14. Meredith, J. C.; Karim, A.; Amis, E. J., High-throughput measurement of polymer blend phase behavior. *Macromolecules* **2000**, *33*, 5760-5762.
15. Akpalu, Y. A.; Peng, P., Probing the melt miscibility of a commercial polyethylene blend by small-angle light scattering. *Mater. Manuf. Processes* **2008**, *23*, 269-276.
16. Emerson, J. A.; Toolan, D. T. W.; Howse, J. R.; Furst, E. M.; Epps, T. H., III, Determination of solvent-polymer and polymer-polymer Flory-Huggins interaction parameters for poly(3-hexylthiophene) via solvent vapor swelling. *Macromolecules* **2013**, *46*, 6533-6540.
17. Nedoma, A. J.; Lai, P.; Jackson, A.; Robertson, M. L.; Wanakule, N. S.; Balsara, N. P., Phase diagrams of blends of polyisobutylene and deuterated polybutadiene as a function of chain length. *Macromolecules* **2011**, *44*, 3077-3084.
18. Scott, R. L., The thermodynamics of high polymer solutions. V. Phase equilibria in the ternary system: polymer 1 – polymer 2 – solvent. *J. Chem. Phys.* **1949**, *17*, 279-284.
19. Scott, R. L., Thermodynamics of high polymer solutions. VI. The compatibility of copolymers. *J. Polym. Sci.* **1952**, *9*, 423-432.
20. Fukuda, T.; Nagata, M.; Inagaki, H., Light scattering from ternary solutions. 1. Dilute solutions of polystyrene and poly (methyl methacrylate). *Macromolecules* **1984**, *17*, 548-553.
21. Hashimoto, T.; Sasaki, K.; Kawai, H., Time-resolved light scattering studies on the kinetics of phase separation and phase dissolution of polymer blends. 2. Phase separation of ternary mixtures of polymer A, polymer B, and solvent. *Macromolecules* **1984**, *17*, 2812-2818.
22. Tong, Z.; Einaga, Y.; Miyashita, H.; Fujita, H., Phase equilibrium in polymer+ polymer+ solvent ternary systems. 2. Phase diagram of polystyrene+ polyisoprene+ cyclohexane. *Macromolecules* **1987**, *20*, 1888-1891.

23. Tseng, H. S.; Lloyd, D. R.; Ward, T. C., Interaction parameters of polystyrene-polyisoprene-toluene systems at 45° c from gel permeation chromatography. *J. Polym. Sci., Part B: Polym. Phys.* **1987**, *25*, 325-337.
24. Gómez, C. M.; Verdejo, E.; Figueruelo, J. E.; Campos, A.; Soria, V., On the thermodynamic treatment of poly(vinylidene fluoride)/polystyrene blend under liquid-liquid phase separation conditions *Polymer* **1995**, *36*, 1487-1498.
25. Campos, A.; Gómez, C. M.; García, R.; Figueruelo, J. E.; Soria, V., Extension of the Flory-Huggins theory to study incompatible polymer blends in solution from phase separation data. *Polymer* **1996**, *37*, 3361-3372.
26. Ginzburg, V. V., Influence of nanoparticles on miscibility of polymer blends. A simple theory. *Macromolecules* **2005**, *38*, 2362-2367.
27. He, G.; Ginzburg, V. V.; Balazs, A. C., Determining the phase behavior of nanoparticle-filled binary blends. *J. Polym. Sci., Part B: Polym. Phys.* **2006**, *44*, 2389-2403.
28. Nesterov, A. E.; Lipatov, Y. S., Compatibilizing effect of a filler in binary polymer mixtures. *Polymer* **1999**, *40*, 1347-1349.
29. Taguet, A.; Cassagnau, P.; Lopez-Cuesta, J. M., Structuration, selective dispersion and compatibilizing effect of (nano)fillers in polymer blends. *Prog. Polym. Sci.* **2014**, *39*, 1526-1563.
30. Lipatov, Y. S.; Nesterov, A. E.; Ignatova, T. D.; Nesterov, D. A., Effect of polymer-filler surface interactions on the phase separation in polymer blends. *Polymer* **2002**, *43*, 875-880.
31. Lee, D.; Huh, J.-Y.; Jeong, D.; Shin, J.; Yun, A.; Kim, J., Physical, mathematical, and numerical derivations of the Cahn–Hilliard equation. *Comput. Mater. Sci.* **2014**, *81*, 216-225.
32. Cahn, J. W., Phase separation by spinodal decomposition in isotropic systems. *J. Chem. Phys.* **1965**, *42*, 93.
33. Siggia, E. D., Late stages of spinodal decomposition in binary mixtures. *Phys. Rev. A* **1979**, *20*, 595.
34. De Gennes, P. G., Dynamics of fluctuations and spinodal decomposition in polymer blends. *J. Chem. Phys.* **1980**, *72*, 4756-4763.

35. Pincus, P., Dynamics of fluctuations and spinodal decomposition in polymer blends. II. *J. Chem. Phys.* **1981**, *75*, 1996-2000.
36. Binder, K., Collective diffusion, nucleation, and spinodal decomposition in polymer mixtures. *J. Chem. Phys.* **1983**, *79*, 6387.
37. Hore, M. J. A.; Laradji, M., Dissipative particle dynamics simulation of the interplay between spinodal decomposition and wetting in thin film binary fluids. *J. Chem. Phys.* **2010**, *132*, 024908.
38. Marko, J. F., Influence of surface interactions on spinodal decomposition. *Phys. Rev. E* **1993**, *48*, 2861.
39. Lal, J.; Bansil, R., Light-scattering study of kinetics of spinodal decomposition in a polymer solution. *Macromolecules* **1991**, *24*, 290-297.
40. Tanaka, H.; Lovinger, A. J.; Davis, D. D., Pattern evolution caused by dynamic coupling between wetting and phase-separation in binary-liquid mixture containing glass particles. *Phys. Rev. Lett.* **1994**, *72*, 2581-2584.
41. Bruder, F.; Brenn, R., Spinodal decomposition in thin films of a polymer blend. *Phys. Rev. Lett.* **1992**, *69*, 624.
42. Jones, R. A. L.; Norton, L. J.; Kramer, E. J.; Bates, F. S.; Wiltzius, P., Surface-directed spinodal decomposition. *Phys. Rev. Lett.* **1991**, *66*, 1326.
43. Li, L.; Shen, X.; Hong, S. W.; Hayward, R. C.; Russell, T. P., Fabrication of co-continuous nanostructured and porous polymer membranes: spinodal decomposition of homopolymer and random copolymer blends. *Angew. Chem. Int. Ed.* **2012**, *51*, 4089-4094.
44. Wang, H.; Composto, R. J., Thin film polymer blends undergoing phase separation and wetting: identification of early, intermediate, and late stages. *J. Chem. Phys.* **2000**, *113*, 10386-10397.
45. Wang, H.; Composto, R. J., Understanding morphology evolution and roughening in phase-separating thin-film polymer blends. *Europhys. Lett.* **2000**, *50*, 622-627.
46. Wang, H.; Composto, R. J., Hydrodynamic-flow-driven wetting in thin film polymer blends: growth kinetics and morphology. *Phys. Rev. E* **2000**, *61*, 1659-1663.

47. Yang, Y. P.; Xiao, Z. G.; Jiang, X.; Sheng, J., Light scattering studies on phase behavior of PP/PcBR blends during melt-mixing. *J. Macromol. Sci., Part B: Phys.* **2006**, *45*, 1083-1098.
48. Lefebvre, A. A.; Lee, J. H.; Balsara, N. P.; Vaidyanathan, C., Determination of critical length scales and the limit of metastability in phase separating polymer blends. *J. Chem. Phys.* **2002**, *117*, 9063-9073.
49. Lefebvre, A. A.; Lee, J. H.; Balsara, N. P.; Hammouda, B., Critical length and time scales during the initial stages of nucleation in polymer blends. *J. Chem. Phys.* **2002**, *116*, 4777-4781.
50. Wang, H.; Composto, R. J., Kinetics of surface and interfacial fluctuations in phase separating polymer blend films. *Macromolecules* **2002**, *35*, 2799-2809.
51. Chung, H.-J.; Composto, R. J., Breakdown of dynamic scaling in thin film binary liquids undergoing phase separation. *Phys. Rev. Lett.* **2004**, *92*, 185704.
52. Wang, Z.; Wang, H.; Shimizu, K.; Dong, J.-Y.; Hsiao, B. S.; Han, C. C., Structural and morphological development in poly (ethylene-co-hexene) and poly (ethylene-co-butylene) blends due to the competition between liquid-liquid phase separation and crystallization. *Polymer* **2005**, *46*, 2675-2684.
53. Jukes, P. C.; Heriot, S. Y.; Sharp, J. S.; Jones, R. A. L., Time-resolved light scattering studies of phase separation in thin film semiconducting polymer blends during spin-coating. *Macromolecules* **2005**, *38*, 2030-2032.
54. Ogawa, H.; Kanayac, T.; Nishida, K.; Matsuba, G., Phase separation and dewetting in polymer blend thin films. *Eur. Phys. J.: Spec. Top.* **2007**, *141*, 189-192.
55. Gelles, R.; Frank, C. W., Effect of molecular weight on polymer blend phase separation kinetics. *Macromolecules* **1983**, *16*, 1448-1456.
56. Krausch, G.; Dai, C. A.; Kramer, E. J.; Marko, J. F.; Bates, F. S., Interference of spinodal waves in thin polymer films. *Macromolecules* **1993**, *26*, 5566-5571.
57. Ermi, B. D.; Karim, A.; Douglas, J. F., Formation and dissolution of phase-separated structures in ultrathin blend films. *J. Polym. Sci., Part B: Polym. Phys.* **1998**, *36*, 191-200.

58. Sung, L.; Karim, A.; Douglas, J. F.; Han, C. C., Dimensional crossover in the phase separation kinetics of thin polymer blend films. *Phys. Rev. Lett.* **1996**, *76*, 4368-4371.
59. Wang, H.; Douglas, J. F.; Satija, S. K.; Composto, R. J.; Han, C. C., Early-stage compositional segregation in polymer-blend films. *Phys. Rev. E* **2003**, *67*, 061801.
60. Snyder, H. L.; Meakin, P.; Reich, S., Dynamical aspects of phase separation in polymer blends. *Macromolecules* **1983**, *16*, 757-762.
61. Chung, H. J.; Taubert, A.; Deshmukh, R. D.; Composto, R. J., Mobile nanoparticles and their effect on phase separation dynamics in thin-film polymer blends. *Europhys. Lett.* **2004**, *68*, 219-225.
62. Ebbens, S.; Hodgkinson, R.; Parnell, A. J.; Dunbar, A.; Martin, S. J.; Topham, P. D.; Clarke, N.; Howse, J. R., In situ imaging and height reconstruction of phase separation processes in polymer blends during spin coating. *ACS Nano* **2011**, *5*, 5124-5131.
63. Toolan, D. T. W.; Dunbar, A.; Ebbens, S.; Clarke, N.; Topham, P. D.; Howse, J. R., Direct observation of morphological development during the spin-coating of polystyrene–poly (methyl methacrylate) polymer blends. *J. Polym. Sci., Part B: Polym. Phys.* **2013**, *51*, 875-881.
64. Toolan, D. T. W.; Pullan, N.; Harvey, M. J.; Topham, P. D.; Howse, J. R., *In situ* studies of phase separation and crystallization directed by marangoni instabilities during spin-coating. *Adv. Mater.* **2013**, *25*, 7033-7037.
65. Toolan, D. T. W.; Howse, J. R., Development of in situ studies of spin coated polymer films. *J. Mater. Chem. C* **2013**, *1*, 603-616.
66. Heriot, S. Y.; Jones, R. A. L., An interfacial instability in a transient wetting layer leads to lateral phase separation in thin spin-cast polymer-blend films. *Nat. Mater.* **2005**, *4*, 782-786.
67. Zhang, H.; Takeoka, S., Morphological evolution within spin-cast ultrathin polymer blend films clarified by a freestanding method. *Macromolecules* **2012**, *45*, 4315-4321.
68. Haq, E. U.; Toolan, D. T. W.; Emerson, J. A.; Epps, T. H., III; Howse, J. R.; Dunbar, A. D. F.; Ebbens, S. J., Real time laser interference microscopy for bar-spread polystyrene/poly(methyl methacrylate) blends. *J. Polym. Sci., Part B: Polym. Phys.* **2014**, *52*, 985-992.

69. Banker, G. S., Film coating theory and practice. *J. Pharm. Sci.* **1966**, *55*, 81-89.
70. Siracusa, V.; Rocculi, P.; Romani, S.; Rosa, M. D., Biodegradable polymers for food packaging: a review. *Trends Food Sci. Technol.* **2008**, *19*, 634-643.
71. Vaia, R. A.; Maguire, J. F., Polymer nanocomposites with prescribed morphology: Going beyond nanoparticle-filled polymers. *Chem. Mater.* **2007**, *19*, 2736-2751.
72. Winey, K. I.; Vaia, R. A., Polymer nanocomposites. *MRS Bull.* **2007**, *32*, 314-319.
73. Paul, D. R.; Robeson, L. M., Polymer nanotechnology: nanocomposites. *Polymer* **2008**, *49*, 3187-3204.
74. Hussain, F.; Hojjati, M.; Okamoto, M.; Gorga, R. E., Review article: polymer-matrix nanocomposites, processing, manufacturing, and application: an overview. *J. Compos. Mater.* **2006**, *40*, 1511-1575.
75. Ash, B. J.; Siegel, R. W.; Schadler, L. S., Glass-transition temperature behavior of alumina/PMMA nanocomposites. *J. Polym. Sci., Part B: Polym. Phys.* **2004**, *42*, 4371-4383.
76. Lee, J.-Y.; Su, K. E.; Chan, E. P.; Zhang, Q.; Emrick, T.; Crosby, A. J., Impact of surface-modified nanoparticles on glass transition temperature and elastic modulus of polymer thin films. *Macromolecules* **2007**, *40*, 7755-7757.
77. Seyfi, J.; Jafari, S. H.; Khonakdar, H. A.; Sadeghi, G. M. M.; Zohuri, G.; Hejazi, I.; Simon, F., Fabrication of robust and thermally stable superhydrophobic nanocomposite coatings based on thermoplastic polyurethane and silica nanoparticles. *Appl. Surf. Sci.* **2015**, *347*, 224-230.
78. Jiang, G.; Hore, M. J. A.; Gam, S.; Composto, R. J., Gold nanorods dispersed in homopolymer films: optical properties controlled by self-assembly and percolation of nanorods. *ACS Nano* **2012**, *6*, 1578-1588.
79. Frischknecht, A. L.; Hore, M. J. A.; Ford, J.; Composto, R. J., Dispersion of polymer-grafted nanorods in homopolymer films: theory and experiment. *Macromolecules* **2013**, *46*, 2856-2869.
80. Hore, M. J. A.; Composto, R. J., Nanorod self-assembly for tuning optical absorption. *ACS Nano* **2010**, *4*, 6941-6949.

81. Liu, Y.; Mills, E. N.; Composto, R. J., Tuning optical properties of gold nanorods in polymer films through thermal reshaping. *J. Mater. Chem.* **2009**, *19*, 2704-2709.
82. Wang, C. C. D.; Choy, W. C. H.; Duan, C.; Fung, D. D. S.; Wei, E. I.; Xie, F.-X.; Huang, F.; Cao, Y., Optical and electrical effects of gold nanoparticles in the active layer of polymer solar cells. *J. Mater. Chem.* **2012**, *22*, 1206-1211.
83. Kim, J.; Yang, H.; Green, P. F., Tailoring the refractive indices of thin film polymer metallic nanoparticle nanocomposites. *Langmuir* **2012**, *28*, 9735-9741.
84. Wang, D. L.; Hore, M. J. A.; Ye, X. C.; Zheng, C.; Murray, C. B.; Composto, R. J., Gold nanorod length controls dispersion, local ordering, and optical absorption in polymer nanocomposite films. *Soft Matter* **2014**, *10*, 3404-3413.
85. Lopez-Haro, M.; Jiu, T. G.; Bayle-Guillemaud, P.; Jouneau, P. H.; Chandezon, F., Multiscale tomographic analysis of polymer-nanoparticle hybrid materials for solar cells. *Nanoscale* **2013**, *5*, 10945-10955.
86. Gao, B.; Rozin, M. J.; Tao, A. R., Plasmonic nanocomposites: polymer-guided strategies for assembling metal nanoparticles. *Nanoscale* **2013**, *5*, 5677-5691.
87. Huynh, W. U.; Dittmer, J. J.; Alivisatos, A. P., Hybrid nanorod-polymer solar cells. *Science* **2002**, *295*, 2425.
88. Huynh, W. U.; Dittmer, J. J.; Libby, W. C.; Whiting, G. L.; Alivisatos, A. P., Controlling the morphology of nanocrystal-polymer composites for solar cells. *Adv. Funct. Mater.* **2003**, *13*, 73-79.
89. Ginzburg, V. V.; Myers, K.; Malowinski, S.; Cieslinski, R.; Elwell, M.; Bernius, M., High-dielectric-constant self-assembled nodular structures in polymer/gold nanoparticle films. *Macromolecules* **2006**, *39*, 3901-3906.
90. Kim, J. M.; Shin, I. S.; Yoo, S. H.; Jeun, J. H.; Lee, J.; Kim, A.; Kim, H. S.; Ge, Z. Y.; Hong, J. I.; Bang, J. H.; Kim, Y. S., Effect of CdSe nanoparticles in polymethylmethacrylate tunneling layer on the performance of nonvolatile organic memory device. *Microelectron. Eng.* **2012**, *98*, 305-308.
91. Salaoru, I.; Paul, S., Non-volatile memory device- using a blend of polymer and ferroelectric nanoparticles. *J. Optoelectron. Adv. Mater.* **2008**, *10*, 3461-3464.

92. Verma, V. K.; Singh, Y.; Chauhan, R. N.; Anand, R. S.; Kumar, J., Characterization of CdSe nanocrystals for hybrid solar cells. *Integr. Ferroelectr.* **2010**, *120*, 1-5.
93. Geng, H. W.; Hill, C. M.; Pan, S. L.; Huang, L. B., Electrogenerated chemiluminescence and interfacial charge transfer dynamics of poly(3-hexylthiophene-2,5-diyl) (P3HT)-TiO₂ nanoparticle thin film. *Phys. Chem. Chem. Phys.* **2013**, *15*, 3504-3509.
94. Joge, P.; Kanchan, D. K.; Sharma, P.; Gondaliya, N., Effect of nano-filler on electrical properties of PVA-PEO blend polymer electrolyte. *Indian J. Pure Appl. Phys.* **2013**, *51*, 350-353.
95. Ulaganathan, M.; Nithya, R.; Rajendran, S.; Raghu, S., Li-ion conduction on nanofiller incorporated PVdF-co-HFP based composite polymer blend electrolytes for flexible battery applications. *Solid State Ionics* **2012**, *218*, 7-12.
96. Rajendran, S.; Kesavan, K.; Nithya, R.; Ulaganathan, M., Transport, structural and thermal studies on nanocomposite polymer blend electrolytes for Li-ion battery applications. *Curr. Appl. Phys.* **2012**, *12*, 789-793.
97. Jayanthi, S.; Sundaresan, B., Effect of ultrasonic irradiation and TiO₂ on the determination of electrical and dielectric properties of PEO-P(VdF-HFP)-LiClO₄-based nanocomposite polymer blend electrolytes. *Ionics* **2015**, *21*, 705-717.
98. Jayanthi, S.; Kulasekarapandian, K.; Arulsankar, A.; Sankaranarayanan, K.; Sundaresan, B., Influence of nano-sized TiO₂ on the structural, electrical, and morphological properties of polymer-blend electrolytes PEO-PVC-LiClO₄. *J. Compos. Mater.* **2015**, *49*, 1035-1045.
99. Xu, C.; Ohno, K.; Ladmiral, V.; Composto, R. J., Dispersion of polymer-grafted magnetic nanoparticles in homopolymers and block copolymers. *Polymer* **2008**, *49*, 3568-3577.
100. Robbes, A.-S.; Cousin, F.; Meneau, F.; Dalmas, F.; Schweins, R.; Gigmes, D.; Jestin, J., Polymer-grafted magnetic nanoparticles in nanocomposites: curvature effects, conformation of grafted chain, and bimodal nanotriggering of filler organization by combination of chain grafting and magnetic field. *Macromolecules* **2012**, *45*, 9220-9231.
101. Akcora, P.; Kumar, S. K.; García Sakai, V.; Li, Y.; Benicewicz, B. C.; Schadler, L. S., Segmental dynamics in PMMA-grafted nanoparticle composites. *Macromolecules* **2010**, *43*, 8275-8281.

102. Yin, B.; Hakkarainen, M., Flexible and strong ternary blends of poly(vinyl chloride), poly(butylene adipate) and nanoparticle-plasticizers. *Mater. Chem. Phys.* **2013**, *139*, 734-740.
103. Zhang, A. M.; Zhao, G. Q.; Guan, Y. J., Effects of mold cavity temperature on surface quality and mechanical properties of nanoparticle-filled polymer in rapid heat cycle molding. *J. Appl. Polym. Sci.* **2015**, *132*, 9.
104. Senses, E.; Isherwood, A.; Akcora, P., Reversible thermal stiffening in polymer nanocomposites. *ACS Appl. Mater. Interfaces* **2015**, *7*, 14682-14689.
105. Zou, H.; Wu, S.; Shen, J., Polymer/silica nanocomposites: preparation, characterization, properties, and applications. *Chem. Rev* **2008**, *108*, 3893-3957.
106. Ahuja, T.; Kumar, D., Recent progress in the development of nano-structured conducting polymers/nanocomposites for sensor applications. *Sens. Actuators, B* **2009**, *136*, 275-286.
107. Zhang, H.; Han, J.; Yang, B., Structural fabrication and functional modulation of nanoparticle-polymer composites. *Adv. Funct. Mater.* **2010**, *20*, 1533-1550.
108. Caporizzo, M. A.; Ezzibdeh, R. M.; Composto, R. J., Hierarchical nanoparticle topography in amphiphilic copolymer films controlled by thermodynamics and dynamics. *Langmuir* **2015**, *31*, 3027-3038.
109. Pihan, S. A.; Emmerling, S. G. J.; Butt, H.-J. r.; Berger, R. d.; Gutmann, J. S., Soft nanocomposites—from interface control to interphase formation. *ACS Appl. Mater. Interfaces* **2015**, *7*, 12380-12386.
110. Chen, Y. B.; Liu, X. J.; Liu, L. N.; Zhang, Y. F.; Wang, Z. Y.; Zhang, Q. L., Functional poly(vinylidene fluoride) membrane anchored with silver nanoparticle with antibacterial activity. *Synth. Met.* **2013**, *174*, 1-5.
111. Bhattacharya, M.; Chaudhry, S., High-performance silica nanoparticle reinforced poly (vinyl alcohol) as templates for bioactive nanocomposites. *Mater. Sci. Eng., C* **2013**, *33*, 2601-2610.
112. Yamamoto, Y.; Fujii, S.; Shitajima, K.; Fujiwara, K.; Hikasa, S.; Nakamura, Y., Soft polymer-silica nanocomposite particles as filler for pressure-sensitive adhesives. *Polymer* **2015**, *70*, 77-87.
113. Guo, L.; Yuan, W.; Lu, Z.; Li, C. M., Polymer/nanosilver composite coatings for antibacterial applications. *Colloids Surf., A* **2013**, *439*, 69-83.

114. Mukherjee, R.; Das, S.; Das, A.; Sharma, S. K.; Raychaudhuri, A. K.; Sharma, A., Stability and dewetting of metal nanoparticle filled thin polymer films: control of instability length scale and dynamics. *ACS Nano* **2010**, *4*, 3709-3724.
115. Amarandei, G.; O'Dwyer, C.; Arshak, A.; Thiele, U.; Steiner, U.; Corcoran, D., Effect of Au nanoparticle spatial distribution on the stability of thin polymer films. *Langmuir* **2013**, *29*, 6706-6714.
116. Amarandei, G.; Clancy, I.; O'Dwyer, C.; Arshak, A.; Corcoran, D., Stability of ultrathin nanocomposite polymer films controlled by the embedding of gold nanoparticles. *ACS Appl. Mater. Interfaces* **2014**, *6*, 20758-20767.
117. Vunain, E.; Mishra, A. K.; Krause, R. W., Fabrication, Characterization and Application of Polymer Nanocomposites for Arsenic(III) Removal from Water. *J. Inorg. Organomet. Polym. Mater.* **2013**, *23*, 293-305.
118. Balazs, A. C.; Emrick, T.; Russell, T. P., Nanoparticle polymer composites: where two small worlds meet. *Science* **2006**, *314*, 1107-1110.
119. Jancar, J.; Douglas, J. F.; Starr, F. W.; Kumar, S. K.; Cassagnau, P.; Lesser, A. J.; Sternstein, S. S.; Buehler, M. J., Current issues in research on structure-property relationships in polymer nanocomposites. *Polymer* **2010**, *51*, 3321-3343.
120. Kumar, S. K.; Krishnamoorti, R., Nanocomposites: structure, phase behavior, and properties. *Annu. Rev. Chem. Biomol. Eng.* **2010**, *1*, 37-58.
121. Meth, J. S.; Zane, S. G.; Chi, C.; Londono, J. D.; Wood, B. A.; Cotts, P.; Keating, M.; Guise, W.; Weigand, S., Development of filler structure in colloidal silica-polymer nanocomposites. *Macromolecules* **2011**, *44*, 8301-8313.
122. Sunday, D.; Ilavsky, J.; Green, D. L., A phase diagram for polymer-grafted nanoparticles in homopolymer matrices. *Macromolecules* **2012**, *45*, 4007-4011.
123. Srivastava, S.; Schaefer, J. L.; Yang, Z.; Tu, Z.; Archer, L. A., 25th anniversary article: polymer-particle composites: phase stability and applications in electrochemical energy storage. *Adv. Mater.* **2014**, *26*, 201-234.

124. Breneman, C. M.; Brinson, L. C.; Schadler, L. S.; Natarajan, B.; Krein, M.; Wu, K.; Morkowchuk, L.; Li, Y.; Deng, H.; Xu, H., Stalking the materials genome: a data-driven approach to the virtual design of nanostructured polymers. *Adv. Funct. Mater.* **2013**, *23*, 5746-5752.
125. Jordan, J.; Jacob, K. I.; Tannenbaum, R.; Sharaf, M. A.; Jasiuk, I., Experimental trends in polymer nanocomposites—a review. *Mater. Sci. Eng., A* **2005**, *393*, 1-11.
126. Krishnamoorti, R., Strategies for dispersing nanoparticles in polymers. *MRS Bull.* **2007**, *32*, 341-347.
127. Akcora, P.; Kumar, S. K.; Moll, J.; Lewis, S.; Schadler, L. S.; Li, Y.; Benicewicz, B. C.; Sandy, A.; Narayanan, S.; Ilavsky, J., “Gel-like” mechanical reinforcement in polymer nanocomposite melts. *Macromolecules* **2009**, *43*, 1003-1010.
128. Mackay, M. E.; Tuteja, A.; Duxbury, P. M.; Hawker, C. J.; Van Horn, B.; Guan, Z. B.; Chen, G. H.; Krishnan, R. S., General strategies for nanoparticle dispersion. *Science* **2006**, *311*, 1740-1743.
129. Kumar, S. K.; Jouault, N.; Benicewicz, B.; Neely, T., Nanocomposites with polymer grafted nanoparticles. *Macromolecules* **2013**, *46*, 3199-3214.
130. Jouault, N.; Zhao, D.; Kumar, S. K., Role of casting solvent on nanoparticle dispersion in polymer nanocomposites. *Macromolecules* **2014**, *47*, 5246-5255.
131. Zeng, Q. H.; Yu, A. B.; Lu, G. Q., Multiscale modeling and simulation of polymer nanocomposites. *Prog. Polym. Sci.* **2008**, *33*, 191-269.
132. Smith, G. D.; Bedrov, D., Dispersing nanoparticles in a polymer matrix: are long, dense polymer tethers really necessary? *Langmuir* **2009**, *25*, 11239-11243.
133. Jayaraman, A.; Schweizer, K. S., Effective interactions and self-assembly of hybrid polymer grafted nanoparticles in a homopolymer matrix. *Macromolecules* **2009**, *42*, 8423-8434.
134. Hall, L. M.; Jayaraman, A.; Schweizer, K. S., Molecular theories of polymer nanocomposites. *Curr. Opin. Solid State Mater. Sci.* **2010**, *14*, 38-48.
135. Liu, J.; Gao, Y.; Cao, D.; Zhang, L.; Guo, Z., Nanoparticle dispersion and aggregation in polymer nanocomposites: insights from molecular dynamics simulation. *Langmuir* **2011**, *27*, 7926-7933.

136. Jayaraman, A., Polymer grafted nanoparticles: Effect of chemical and physical heterogeneity in polymer grafts on particle assembly and dispersion. *J. Polym. Sci., Part B: Polym. Phys.* **2013**, *51*, 524-534.
137. Gao, Y. Y.; Liu, J.; Shen, J. X.; Zhang, L. Q.; Cao, D. P., Molecular dynamics simulation of dispersion and aggregation kinetics of nanorods in polymer nanocomposites. *Polymer* **2014**, *55*, 1273-1281.
138. Ganesan, V.; Jayaraman, A., Theory and simulation studies of effective interactions, phase behavior and morphology in polymer nanocomposites. *Soft Matter* **2014**, *10*, 13-38.
139. Cheng, S.; Grest, G. S., Dispersing nanoparticles in a polymer film via solvent evaporation. *ACS Macro Lett.* **2016**, *5*, 694-698.
140. Harton, S. E.; Kumar, S. K., Mean-field theoretical analysis of brush-coated nanoparticle dispersion in polymer matrices. *J. Polym. Sci., Part B: Polym. Phys.* **2008**, *46*, 351-358.
141. Xu, J.; Qiu, F.; Zhang, H.; Yang, Y., Morphology and interactions of polymer brush-coated spheres in a polymer matrix. *J. Polym. Sci., Part B: Polym. Phys.* **2006**, *44*, 2811-2820.
142. Kim, J. U.; Matsen, M. W., Interaction between polymer-grafted particles. *Macromolecules* **2008**, *41*, 4435-4443.
143. Trombly, D. M.; Ganesan, V., Curvature effects upon interactions of polymer-grafted nanoparticles in chemically identical polymer matrices. *J. Chem. Phys.* **2010**, *133*, 154904.
144. Kim, J.; Green, P. F., Phase behavior of thin film brush-coated nanoparticles/homopolymer mixtures. *Macromolecules* **2010**, *43*, 1524-1529.
145. Hore, M. J. A.; Frischknecht, A. L.; Composto, R. J., Nanorod assemblies in polymer films and their dispersion-dependent optical properties. *ACS Macro Lett.* **2012**, *1*, 115-121.
146. Arias, A. C.; Corcoran, N.; Banach, M.; Friend, R. H.; MacKenzie, J. D.; Huck, W. T. S., Vertically segregated polymer-blend photovoltaic thin-film structures through surface-mediated solution processing. *Appl. Phys. Lett.* **2002**, *80*, 1695-1697.
147. Arias, A. C.; Endicott, F.; Street, R. A., Surface-induced self-encapsulation of polymer thin-film transistors. *Adv. Mater.* **2006**, *18*, 2900-2904.

148. Qiu, L.; Lim, J. A.; Wang, X.; Lee, W. H.; Hwang, M.; Cho, K., Versatile use of vertical-phase-separation-induced bilayer structures in organic thin-film transistors. *Adv. Mater.* **2008**, *20*, 1141-1145.
149. Qiu, L.; Lee, W. H.; Wang, X.; Kim, J. S.; Lim, J. A.; Kwak, D.; Lee, S.; Cho, K., Organic thin-film transistors based on polythiophene nanowires embedded in insulating polymer. *Adv. Mater.* **2009**, *21*, 1349-1353.
150. Chen, F.-C.; Ko, C.-J.; Wu, J.-L.; Chen, W.-C., Morphological study of P3HT:PCBM blend films prepared through solvent annealing for solar cell applications. *Sol. Energy Mater. Sol. Cells* **2010**, *94*, 2426-2430.
151. Nicho, M. E.; García-Escobar, C. H.; Arenas, M. C.; Altuzar-Coello, P.; Cruz-Silva, R.; Güizado-Rodríguez, M., Influence of P3HT concentration on morphological, optical and electrical properties of P3HT/PS and P3HT/PMMA binary blends. *Mater. Sci. Eng., B* **2011**, *176*, 1393-1400.
152. Lee, J.; Jung, J. Y.; Kim, D. H.; Kim, J.-Y.; Lee, B.-L.; Park, J.-I.; Chung, J. W.; Park, J. S.; Koo, B.; Jin, Y. W., Enhanced electrical stability of organic thin-film transistors with polymer semiconductor-insulator blended active layers. *Appl. Phys. Lett.* **2012**, *100*, 083302.
153. Ruderer, M. A.; Wang, C.; Schaible, E.; Hexemer, A.; Xu, T.; Müller-Buschbaum, P., Morphology and optical properties of P3HT: MEH-CN-PPV blend films. *Macromolecules* **2013**, *46*, 4491-4501.
154. Moons, E., Conjugated polymer blends: linking film morphology to performance of light emitting diodes and photodiodes. *J. Phys.: Condens. Matter* **2002**, *14*, 12235.
155. Lee, Y.; Kim, J. K.; Chiu, C.-H.; Lan, Y.-K.; Huang, C.-I., Phase behavior of poly(3-alkylthiophene)/polystyrene blends. *Polymer* **2009**, *50*, 4944-4949.
156. Yin, C. L.; Liu, Z. Y.; Gao, Y. J.; Yang, M. B., Effect of compounding procedure on morphology and crystallization behavior of isotactic polypropylene/high-density polyethylene/carbon black ternary composites. *Polym. Adv. Technol.* **2012**, *23*, 1112-1120.
157. Fabiano, S.; Himmelberger, S.; Drees, M.; Chen, Z.; Altamimi, R. M.; Salleo, A.; Loi, M. A.; Facchetti, A. C., Charge transport orthogonality in all-polymer blend transistors, diodes, and solar cells. *Adv. Energy Mater.* **2014**, *4*, 1301409.

158. Yu, G.; Nishino, H.; Heeger, A. J.; Chen, T. A.; Rieke, R. D., Enhanced electroluminescence from semiconducting polymer blends. *Synth. Met.* **1995**, *72*, 249-252.
159. Esquirol, A.-L.; Sarazin, P.; Virgilio, N., Tunable porous hydrogels from cocontinuous polymer blends. *Macromolecules* **2014**, *47*, 3068-3075.
160. Riscanu, D.; Favis, B. D.; Feng, C.; Matsuura, T., Thin-film membranes derived from co-continuous polymer blends: preparation and performance. *Polymer* **2004**, *45*, 5597-5609.
161. Walheim, S.; Schäffer, E.; Mlynek, J.; Steiner, U., Nanophase-separated polymer films as high-performance antireflection coatings. *Science* **1999**, *283*, 520.
162. Müller-Buschbaum, P.; Ittner, T.; Maurer, E.; Körstgens, V.; Petry, W., Pressure-sensitive adhesive blend films for low-tack applications. *Macromol. Mater. Eng.* **2007**, *292*, 825-834.
163. Geoghegan, M.; Krausch, G., Wetting at polymer surfaces and interfaces. *Prog. Polym. Sci.* **2003**, *28*, 261-302.
164. Geoghegan, M.; Jones, R. A. L.; Payne, R. S.; Sakellariou, P.; Clough, A. S.; Penfold, J., Lamellar structure in a thin polymer blend film. *Polymer* **1994**, *35*, 2019-2027.
165. Müller-Buschbaum, P.; O'Neill, S. A.; Affrossman, S.; Stamm, M., Phase separation and dewetting of weakly incompatible polymer blend films. *Macromolecules* **1998**, *31*, 5003-5009.
166. Morin, C.; Ikeura-Sekiguchi, H.; Tyliczszak, T.; Cornelius, R.; Brash, J. L.; Hitchcock, A. P.; Scholl, A.; Nolting, F.; Appel, G.; Winesett, D. A., X-ray spectromicroscopy of immiscible polymer blends: polystyrene–poly (methyl methacrylate). *J. Electron. Spectrosc. Relat. Phenom.* **2001**, *121*, 203-224.
167. Sheng, J.; Qi, L. Y.; Yuan, X. B.; Shen, N. X.; Bian, D. C., Blends of polypropylene with poly (cis-butadiene) rubber. I. Phase structure and morphology of blends. *J. Appl. Polym. Sci.* **1997**, *64*, 2265-2272.
168. Ma, G. Q.; Yuan, X. B.; Sheng, J.; Bian, D. C., Blends of polypropylene with poly (cis-butadiene) rubber. II. Small-angle X-ray scattering studies of the phase structure of immiscible blends of polypropylene with poly (cis-butadiene) rubber. *J. Appl. Polym. Sci.* **2002**, *83*, 2088-2094.

169. Ma, G. Q.; Zhao, Y. H.; Yan, L. T.; Li, Y. Y.; Sheng, J., Blends of polypropylene with poly (cis-butadiene) rubber. III. Study on the phase structure and morphology of incompatible blends of polypropylene with poly (cis-butadiene) rubber. *J. Appl. Polym. Sci.* **2006**, *100*, 4900-4909.
170. Li, Y. y.; Wang, Y.; Sheng, J., Study on phase morphology of PP/PS blends by phase contrast micrographs. *J. Macromol. Sci., Part B: Phys.* **2005**, *44*, 665-676.
171. Sprenger, M.; Walheim, S.; Budkowski, A.; Steiner, U., Hierarchic structure formation in binary and ternary polymer blends. *Interface Sci.* **2003**, *11*, 225-235.
172. Li, X.; Han, Y.; An, L., Surface morphology control of immiscible polymer-blend thin films. *Polymer* **2003**, *44*, 8155-8165.
173. Harris, M.; Appel, G.; Ade, H., Surface morphology of annealed polystyrene and poly (methyl methacrylate) thin film blends and bilayers. *Macromolecules* **2003**, *36*, 3307-3314.
174. Li, X.; Xing, R.; Zhang, Y.; Han, Y.; An, L., Molecular weight effects on the phase morphology of PS/P4VP blend films on homogeneous SAM and heterogeneous SAM/Au substrates. *Polymer* **2004**, *45*, 1637-1646.
175. Wang, P.; Koberstein, J. T., Morphology of immiscible polymer blend thin films prepared by spin-coating. *Macromolecules* **2004**, *37*, 5671-5681.
176. Wei, J. H.; Coffey, D. C.; Ginger, D. S., Nucleating pattern formation in spin-coated polymer blend films with nanoscale surface templates. *J. Phys. Chem. B* **2006**, *110*, 24324-24330.
177. Leung, B. O.; Hitchcock, A. P.; Brash, J. L.; Scholl, A.; Doran, A., Phase segregation in polystyrene–polylactide blends. *Macromolecules* **2009**, *42*, 1679-1684.
178. Ruderer, M. A.; Metwalli, E.; Wang, W.; Kaune, G.; Roth, S. V.; Müller-Buschbaum, P., Thin films of photoactive polymer blends. *ChemPhysChem* **2009**, *10*, 664-671.
179. Karim, A.; Douglas, J. F.; Sung, L. P.; Ermi, B. D., Self-assembly by phase separation in polymer thin films. **2002**, 8319.

180. Yamamura, M.; Nishio, T.; Kajiwara, T.; Adachi, K., Effect of stepwise change of drying rate on microstructure evolution in polymer films. *Drying Technol.* **2001**, *19*, 1397-1410.
181. Walheim, S.; Boltau, M.; Mlynek, J.; Krausch, G.; Steiner, U., Structure formation via polymer demixing in spin-cast films. *Macromolecules* **1997**, *30*, 4995-5003.
182. Dalnoki-Veress, K.; Forrest, J. A.; Stevens, J. R.; Dutcher, J. R., Phase separation morphology of spin-coated polymer blend thin films. *Phys. A* **1997**, *239*, 87-94.
183. Walheim, S.; Ramstein, M.; Steiner, U., Morphologies in ternary polymer blends after spin-coating. *Langmuir* **1999**, *15*, 4828-4836.
184. Bergues, B.; Lekki, J.; Budkowski, A.; Cyganik, P.; Lekka, M.; Bernasik, A.; Rysz, J.; Postawa, Z., Phase decomposition in polymer blend films cast on homogeneous substrates modified by self-assembled monolayers. *Vacuum* **2001**, *63*, 297-305.
185. Jaczewska, J.; Budkowski, A.; Bernasik, A.; Moons, E.; Rysz, J., Polymer vs solvent diagram of film structures formed in spin-cast poly (3-alkylthiophene) blends. *Macromolecules* **2008**, *41*, 4802-4810.
186. Yuan, Y. X.; Fendler, J. H.; Cabasso, I., Photoelectron transfer mediated by size-quantized CdS particles in polymer-blend membranes. *Chem. Mater.* **1992**, *4*, 312-318.
187. Hore, M. J. A.; Composto, R. J., Using miscible polymer blends to control depletion-attraction forces between Au nanorods in nanocomposite films. *Macromolecules* **2012**, *45*, 6078-6086.
188. Kumar, A.; Bhushan, B., Effect of nanoparticles on nanomechanical and nanotribological properties of polyethylene blend films. *Macromol. React. Eng.* **2013**, *7*, 538-548.
189. Li, Y.; Chen, S.; Li, X.; Wu, M.; Sun, J., Highly transparent, nanofiller-reinforced scratch-resistant polymeric composite films capable of healing scratches. *ACS Nano* **2015**, *9*, 10055-10065.
190. Laradji, M.; Hore, M. J. A., Nanospheres in phase-separating multicomponent fluids: A three-dimensional dissipative particle dynamics simulation. *J. Chem. Phys.* **2004**, *121*, 10641-10647.

191. Hore, M. J. A.; Laradji, M., Microphase separation induced by interfacial segregation of isotropic, spherical nanoparticles. *J. Chem. Phys.* **2007**, *126*.
192. Hore, M. J. A.; Laradji, M., Prospects of nanorods as an emulsifying agent of immiscible blends. *J. Chem. Phys.* **2008**, *128*.
193. Composto, R. J.; Chung, H.-J.; Gam, S., Nanoparticle jamming to create discrete and bicontinuous polymer blend morphologies. *Abstracts of Papers of the American Chemical Society* **2009**, *237*.
194. Gam, S.; Corlu, A.; Chung, H.-J.; Ohno, K.; Hore, M. J. A.; Composto, R. J., A jamming morphology map of polymer blend nanocomposite films. *Soft Matter* **2011**, *7*, 7262-7268.
195. Chung, H.; Ohno, K.; Fukuda, T.; Composto, R. J., Self-regulated structures in nanocomposites by directed nanoparticle assembly. *Nano Lett.* **2005**, *5*, 1878-1882.
196. Wu, K. H.; Lu, S. Y., Preferential partition of nanowires in thin films of immiscible polymer blends. *Macromol. Rapid Commun.* **2006**, *27*, 424-429.
197. Bose, S.; Cardinaels, R.; Ozdilek, C.; Leys, J.; Seo, J. W.; Wubbenhorst, M.; Moldenaers, P., Effect of multiwall carbon nanotubes on the phase separation of concentrated blends of poly (alpha-methyl styrene)-co-acrylonitrile and poly(methyl methacrylate) as studied by melt rheology and conductivity spectroscopy. *Eur. Polym. J.* **2014**, *53*, 253-269.
198. Biswas, S.; Kar, G. P.; Bose, S., Engineering nanostructured polymer blends with controlled nanoparticle location for excellent microwave absorption: a compartmentalized approach. *Nanoscale* **2015**, *7*, 11334-11351.
199. Biswas, S.; Kar, G. P.; Bose, S., Attenuating microwave radiation by absorption through controlled nanoparticle localization in PC/PVDF blends. *Phys. Chem. Chem. Phys.* **2015**, *17*, 27698-27712.
200. Mamunya, Y. P.; Muzychenko, Y. V.; Pissis, P.; Lebedev, E. V.; Shut, M. I., Percolation phenomena in polymers containing dispersed iron. *Polym. Eng. Sci.* **2002**, *42*, 90-100.
201. Mamunya, Y. P.; Muzychenko, Y. V.; Pissis, P.; Lebedev, E. V.; Shut, M. I., Processing, structure, and electrical properties of metal-filled polymers. *J. Macromol. Sci., Part B: Phys.* **2001**, *B40*, 591-602.

202. Khutia, M.; Joshi, G. M.; Deshmukh, K.; Pandey, M., Preparation of modified polymer blend and electrical performance. *Compos. Interfaces* **2015**, *22*, 167-178.
203. Gurumurthy, S. C.; Pattabi, M.; Krishna, S.; Gaikwad, A. B., Preparation and characterization of silver particulate films on softened polystyrene and poly(4-vinylpyridine) blends. *J. Mater. Sci.: Mater. Electron.* **2014**, *25*, 2501-2506.
204. Guo, Y.; Moffitt, M. G., "Smart" self-assembled quantum dots regulate and stabilize structure in phase-separated polymer blends. *Chem. Mater.* **2007**, *19*, 6581-6587.
205. Causa, A.; Filippone, G.; Domingo, C.; Salerno, A., Study of the morphology and texture of poly (ϵ -caprolactone)/polyethylene oxide blend films as a function of composition and the addition of nanofillers with different functionalities. *RSC Adv.* **2015**, *5*, 59354-59363.
206. Thareja, P.; Velankar, S. S., Interfacial activity of particles at PI/PDMS and PI/PIB interfaces: analysis based on Girifalco-Good theory. *Colloid. Polym. Sci.* **2008**, *286*, 1257-1264.
207. Thareja, P.; Moritz, K.; Velankar, S. S., Interfacially active particles in droplet/matrix blends of model immiscible homopolymers: particles can increase or decrease drop size. *Rheol. Acta* **2010**, *49*, 285-298.
208. Nagarkar, S. P.; Velankar, S. S., Morphology and rheology of ternary fluid–fluid–solid systems. *Soft Matter* **2012**, *8*, 8464-8477.
209. Nagarkar, S.; Velankar, S. S., Rheology and morphology of model immiscible polymer blends with monodisperse spherical particles at the interface. *J. Rheol.* **2013**, *57*, 901-926.
210. Chung, H.-J.; Ohno, K.; Fukuda, T.; Composto, R. J., Internal phase separation drives dewetting in polymer blend and nanocomposite films. *Macromolecules* **2007**, *40*, 384-388.
211. Bai, L.; Fruehwirth, J.; Cheng, X.; Macosko, C. W., Interfacial silica nanoparticles stabilize cocontinuous polymer blends. **2015**, arXiv:1502.00165.
212. Lin, Y.; Skaff, H.; Emrick, T.; Dinsmore, A. D.; Russell, T. P., Nanoparticle assembly and transport at liquid-liquid interfaces. *Science* **2003**, *299*, 226-229.

213. Kwon, T.; Kim, T.; Ali, F. B.; Kang, D. J.; Yoo, M.; Bang, J.; Lee, W.; Kim, B. J., Size-controlled polymer-coated nanoparticles as efficient compatibilizers for polymer blends. *Macromolecules* **2011**, *44*, 9852-9862.
214. Li, W.; Dong, B.; Yan, L.-T., Janus nanorods in shearing-to-relaxing polymer blends. *Macromolecules* **2013**, *46*, 7465-7476.
215. Chung, H. J.; Kim, J.; Ohno, K.; Composto, R. J., Controlling the location of nanoparticles in polymer blends by tuning the length and end group of polymer brushes. *ACS Macro Lett.* **2012**, *1*, 252-256.
216. Cai, X.; Li, B.; Pan, Y.; Wu, G., Morphology evolution of immiscible polymer blends as directed by nanoparticle self-agglomeration. *Polymer* **2012**, *53*, 259-266.
217. Boiteux, G.; Mamuny, Y. P.; Lebedev, E. V.; Adamczewski, A.; Boullanger, C.; Cassagnau, P.; Seytre, G., From conductive polymer composites with controlled morphology to smart materials. *Synth. Met.* **2007**, *157*, 1071-1073.
218. Li, L.; Miesch, C.; Sudeep, P. K.; Balazs, A. C.; Emrick, T.; Russell, T. P.; Hayward, R. C., Kinetically trapped co-continuous polymer morphologies through intraphase gelation of nanoparticles. *Nano Lett.* **2011**, *11*, 1997-2003.

Chapter 2

EXPERIMENTAL METHODS

2.1 Generation of Films

2.1.1 Substrate Preparation

Silicon wafers were cleaned prior to use. First, the silicon wafers (Wafer World, N<100>) were cut into the desired size using a diamond tipped scribe. Glass slides were also pre-washed with acetone. Next, all substrates were triple rinsed with toluene and dried with compressed nitrogen. The substrates are then placed in an ultraviolet-ozone (UVO) cleaner (Jelight, model 342). The UVO cleaning reduces contaminants on the surface and also generates an oxide-rich layer on the wafer surface.¹ After cleaning with UVO, the substrates are triple rinsed again with toluene and used immediately.

2.1.2 Casting Methods

Two of the most commonly utilized lab-scale casting methods are spin coating and flow coating. Schematics of both casting methods are shown in Figure 2-1, below.

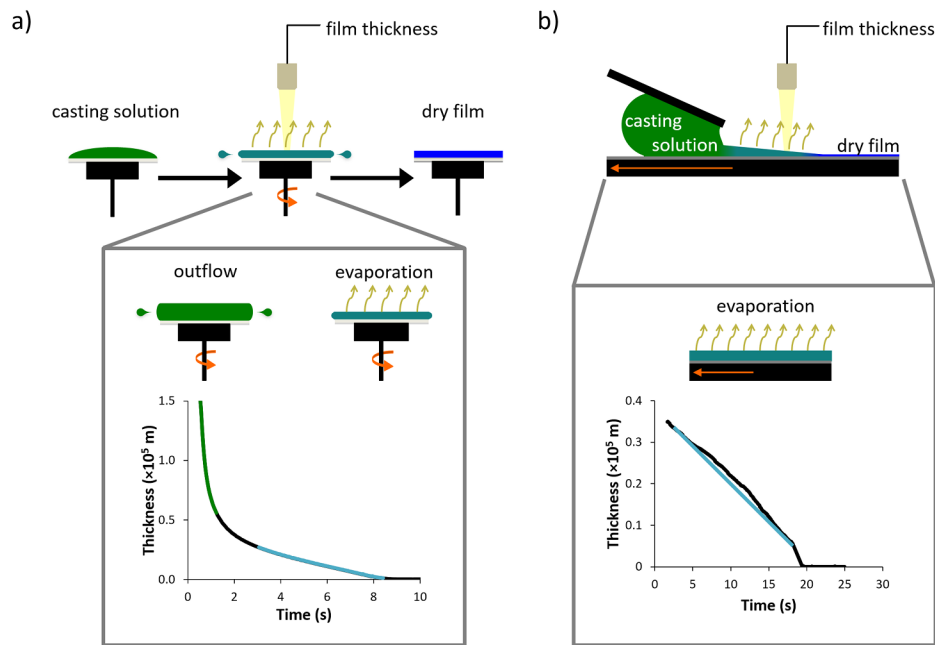


Figure 2-1. Schematic of the casting behavior during a) spin coating and b) flow coating. During spin coating, the film thins by outflow and evaporation. In flow coating, the film thinning occurs by evaporation once the solution layer has been deposited by the blade.

2.1.2.1 Spin Coating

Spin coating utilizes a rotating motor to thin the deposited solution (outflow) and allow for solvent removal (evaporation). Mathematically, spin coating can be modeled using the following equation, which was developed by D. Meyerhofer.²

$$\frac{dh}{dt} = -\frac{2\omega^2 h^3}{3\nu} - e \quad \text{Eq. 2-1}$$

For which h is the film thickness, t is time, ω is the rotational velocity, ν is the kinematic viscosity, and e is the evaporation rate. Thus, the film thickness is controlled by the competition between outflow and evaporation.

2.1.2.2 Flow Coating³

Flow coating is another method that can be used to generate thin films. A blade draws a solution layer across the substrate. The solvent then evaporates, leaving a dry film on the substrate. The thickness of flow coated films is controlled by the deposited solution layer height, and the drying time is determined by the evaporation rate. The solution layer is influenced by the polymer concentration, solution volume, blade speed (and acceleration), gap height, and solvent, whereas the evaporation rate is related to the solvent choice. Flow coating was used to produce uniform thickness films for solvent vapor swelling, contact angle, and tribology studies.

2.2 Characterization Techniques

2.2.1 Contact Angle

Contact angle affords quantification of the surface energy of a variety of materials. The contact angle, θ , of a surface is determined by the three-phase contact between solid (material of interest), liquid (contact angle fluid), and vapor (air).

Young's equation describes the force balance between these components.

$$\cos \theta = \frac{\gamma_{SV} - \gamma_{SL}}{\gamma_{LV}} \quad \text{Eq. 2-2}$$

γ_{ij} is the interfacial tension between phases i and j, for which the subscripts S, L, and V represent the solid, liquid, and vapor phases, respectively. The Good-Girifalco theory relates the Young's equation to contact angle data.⁴

$$(1 + \cos(\theta))\gamma_{LV} = 2\sqrt{\gamma_{SV}\gamma_{LV}} \quad \text{Eq. 2-3}$$

The Good-Girifalco model is commonly applied when only one contact angle fluid is used to measure the surface energy. With more contact angle fluids, the contact angle can be broken down further into dispersive (d) and polar (p)

components, as described by Owens-Wendt and Wu. The Owens-Wend two-fluid model uses a geometric mean of the polar and dispersive components,⁵

$$(1 + \cos(\theta))\gamma_{LV} = 2\left(\sqrt{\gamma_{SV}^D \gamma_{LV}^D} + \sqrt{\gamma_{SV}^P \gamma_{LV}^P}\right) \quad \text{Eq. 2-4}$$

Whereas the Wu method utilizes a harmonic mean.⁶

$$(1 + \cos(\theta))\gamma_{LV} = 4\left(\frac{\gamma_{SV}^D \gamma_{LV}^D}{\gamma_{SV}^D + \gamma_{LV}^D} + \frac{\gamma_{SV}^P \gamma_{LV}^P}{\gamma_{SV}^P + \gamma_{LV}^P}\right) \quad \text{Eq. 2-5}$$

The Owens-Wend method was selected for two fluid surface energy calculations. In the above equations, the contact angle is the equilibrium, or Young's contact angle. Two different contact angle methods were used to calculate the surface energy: static sessile (advancing) contact angles and contact angle hysteresis. The static sessile contact angle is commonly used to study polymer systems. However, contact angle hysteresis provides a more accurate surface energy than the static sessile method, as it accounts for surface heterogeneities (chemistry and topography).⁷

2.2.1.1 Static Sessile Contact Angle⁸⁻⁹

As described in the previous section, static sessile contact angles can be used to characterize the relative surface energies for a series of materials. The static sessile contact angle is considered an advancing contact angle and is shown schematically in Figure 2-2.



Figure 2-2. Schematic of a static sessile contact angle. The contact angle is determined by the balance of the interfacial tensions between the solid, liquid, and vapor phases.

Two fluids were used with the static sessile method: water ($\gamma_{LV} = 72.8$ mN/m, $\gamma_{LV}^D = 21.8$ mN/m, $\gamma_{LV}^P = 50.0$ mN/m) and diiodomethane ($\gamma_{LV} = 50.8$ mN/m, $\gamma_{LV}^D = 50.8$ mN/m, $\gamma_{LV}^P = 0.0$ mN/m). The surface energies of the polymers were characterized using the Owens-Wendt method.

2.2.1.2 Contact Angle Hysteresis^{7, 10-11}

In comparison to the static sessile contact angle, contact angle hysteresis provides the equilibrium surface energy of a material. Together, the advancing (θ_A) and receding (θ_R) contact angles provide information about surface heterogeneities that are not captured in the static sessile contact angle measurements. A schematic of advancing and receding contact angles is shown in Figure 2-3.

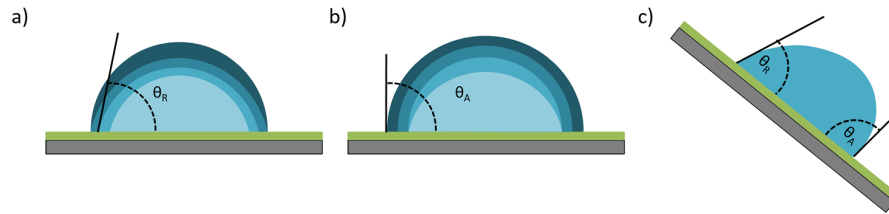


Figure 2-3. Schematic of contact angle hysteresis for a) receding, b) advancing and c) sliding. Sliding contact angle tests afford measurement of the advancing and receding contact angle simultaneously.

The contact angle hysteresis, CAH or $\Delta\theta$, is given by the difference between the advancing and receding contact angles.

$$CAH = \Delta\theta = \theta_A - \theta_R \quad \text{Eq. 2-6}$$

The equilibrium contact angle, θ_0 , is calculated with the advancing and receding values:^{10, 12}

$$\theta_0 = \cos^{-1} \left(\frac{\Gamma_A \cos \theta_A + \Gamma_R \cos \theta_R}{\Gamma_A + \Gamma_R} \right) \quad \text{Eq. 2-7}$$

and

$$\Gamma_i \equiv \left(\frac{\sin^3 \theta_i}{2 - 3 \cos \theta_i + \cos^3 \theta_i} \right)^{1/3} \quad \text{Eq. 2-8}$$

for which i represents either the advancing or receding contact angle. The equilibrium contact angle can then be used to calculate the surface energy using the Good-Girifalco, Young's, or Owens-Wendt methods.

2.2.2 Nuclear Magnetic Resonance (NMR) Spectroscopy¹³

Nuclear magnetic resonances (NMR) spectroscopy is commonly used to study the chemical constituents and the composition of polymers. NMR utilizes an external magnetic field (strength B at the nucleus) to promote alignment of specific nuclei, which have a spin quantum number of $1/2$ (e.g., ^1H , ^{13}C , ^{19}F), in a low-energy (parallel with the field) or high-energy (parallel against the field) state. The fundamental resonance frequency, ν_0 , required to flip the magnetic moment between the low- and high-energy states is related to the magnetogyric ratio, γ , of the nucleus and the strength of the applied external magnetic field (B_0).

$$\nu_0 = \frac{\gamma B_0}{2\pi} \quad \text{Eq. 2-9}$$

During a typical NMR experiment, the applied magnetic field is fixed at B_0 and the radiation absorption over a frequency range, ν , which is close to ν_0 in value, is measured. These absorptions are measured as chemical shifts (δ). The chemical shift is defined by

$$\delta = \frac{10^6 (\nu_0^{\text{sample}} - \nu_0^{\text{ref}})}{\nu_0} \quad \text{Eq. 2-10}$$

For which ν_0^{sample} and ν_0^{ref} are the characteristic frequencies of the sample and a reference, respectively. For polymers, ^1H NMR and ^{13}C NMR spectroscopy are commonly used. A trimethylsilane (TMS) standard is used as the reference compound with a chemical shift set to 0 ppm. The areas under the absorption peaks, or integrations, provide direct quantification of the relative composition of the components. In this dissertation, ^1H NMR was used with a TMS standard to characterize the relative polymer composition for phase diagram determination and ligand exchange on gold nanoparticles.

2.2.3 Gel Permeation Chromatography (GPC)¹³

Gel permeation chromatography (GPC) is a type of size exclusion chromatography. GPC can be used to determine the molecular weight and molecular weight distribution of a polymer. The molar mass of a polymer, M , is given by the product of the number of repeat units, N , with the molar mass of the repeat unit, M_0 ($M = N M_0$). The number-average molar mass, M_n , is given by the sum of the products of the molar mass of each fraction, M_i , with its mole fraction, x_i ($M_n = \sum M_i x_i$). Similarly, the weight-average molar mass, M_w , is the sum of the product of the M_i with weight fraction, w_i ($M_w = \sum M_i w_i$). The ratio of M_w to M_n is the dispersity of the polymer, \mathcal{D} , which provides information about the heterogeneity of the sample ($\mathcal{D} = M_w/M_n$). For example, a monodisperse system would have \mathcal{D} of 1. Thus, quantifying the molar mass and molar mass distribution is important towards understanding the range of molar masses in any given polymer sample. GPC works by flowing a solvent through columns containing porous beads. Polymer solution is injected into a column with void volume, V_0 , and a total internal volume, V_i . The volume of solvent required to

elute a polymer with a particular molar mass is the elution volume, V_e . V_e is related to the molecular size as follows,

$$V_e = V_0 + V_i \exp\left(\frac{-A_s \bar{L}}{2}\right) \quad \text{Eq. 2-11}$$

for which A_s is the surface area per unit pore volume and \bar{L} is the mean molecular projection of the molecule in solution. The path length a polymer takes through the columns depends on the chain dimensions relative to the pore size; larger polymers have shorter paths, which elute at shorter times. Thus, the polymers are separated by size. However, a calibration is required to determine the molar mass of the polymer instead of just the elution volume. The Mark-Houwink-Sakurada equation is used to relate the hydrodynamic volume, which provides the molecular size of polymer in solution, to the molar mass,

$$V_e \propto \log([\eta]M) = \log K + (1+a) \log M \quad \text{Eq. 2-12}$$

for which $[\eta]$ is the intrinsic viscosity, M is the molar mass, and K and a are constants for a given system. Values for K and a can be found in literature for a variety of polymer solutions. Polymers that elute at the same volume (time) have the same hydrodynamic volume. Therefore, the molar mass distribution can then be calculated using a polymer standard.

$$M(V_e) = \left[\frac{([\eta]M)_{V_e}}{K} \right]^{\frac{1}{1+a}} \quad \text{Eq. 2-13}$$

in which $([\eta]M)_{V_e}$ is from the calibration and K and a apply to the polymer studied under the condition used in the GPC operation.

2.2.4 Atomic Force Microscopy (AFM)¹⁴

Atomic force microscopy (AFM) was used to study the morphology and thickness of polymer blend and homopolymer films. In a typical AFM experiment, a cantilever with a sharp tip is used to scan the sample. There are two common modes in which the microscope can operate: tapping mode and contact mode. For polymer films, tapping mode is used more commonly, as contact mode can cause mechanical deformations and surface damage in soft materials. The tip oscillation is driven by a piezoelectric element. A laser beam reflects off of the cantilever onto the four-quadrant photodiode, which is used to detect bending deflection, bending oscillation, and cantilever torsion (see Figure 2-4).

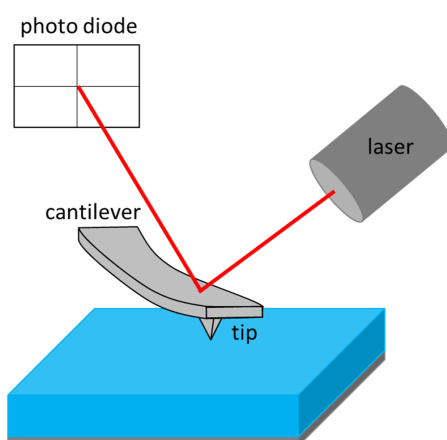


Figure 2-4. Schematic of AFM operation.

The tip is rastered across the stationary sample using the piezoelectric drive, whereas the vertical motion is controlled by a feedback mechanism. The oscillation amplitude is maintained at the set-point value using the piezoelectric drive (z-axis). Variations in the z-axis position during the scan are compiled to produce a height

image of the film. Phase lag between the frequency of the freely oscillating probe and the measured oscillation is used to generate the phase image. Phase images can be used to infer differences in material properties between the components of a structured film, as differences in interactions between the tip and film produce changes in the phase shift.

In addition to polymer contrast and domain height differences, AFM can also be used to measure the film thickness (within the z range of the instrument). The film is scratched using a sharp object, such as a razor blade. The scratching tool is selected such that minimal damage is done to the film substrate (i.e. the height difference reflects only the loss in film). A sample height image and scratch profile from a scratch test is shown in Figure 2-5. The film thickness is the difference in height between the film sample and the substrate.

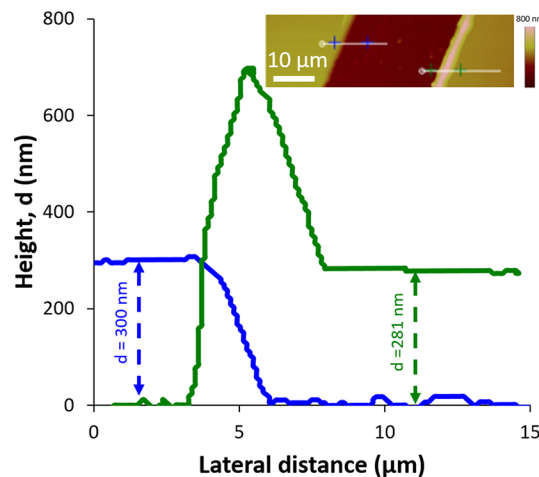


Figure 2-5. Height of the film relative to the substrate (film thickness, d) as a function of distance along the two scratch points shown in the inset. Inset is the AFM height image of the scratch and surrounding film. The height scale is 800 nm. The tall feature in the green curve is pushed up residual film and is not included in the height analysis.

2.2.5 Spectral Reflectometry (SR)¹⁵⁻¹⁶

Spectral reflectometry (SR) is used to measure the film thickness in supported films. Spectral reflectance is measured normal to the film surface over a range of wavelengths. The intensity of the reflected light is related to the number the film thickness, the optical properties (refractive index, n , and extinction coefficient, k), and the wavelength of light. For a single layer of a material in air, the reflectance, R , is given by

$$R = \frac{(n-1)^2 + k^2}{(n+1)^2 + k^2} \quad \text{Eq. 2-14}$$

If the material is non-adsorbing, Eq. 2-1 is further reduced to $R = |(n-1)/(n+1)|^2$, which can be solved at the wavelengths measured experimentally. n varies with wavelength. For the same non-adsorbing species, the Cauchy model relates the wavelength to the refractive index.

$$\begin{aligned} n(\lambda) &= A + \frac{B}{\lambda^2} + \frac{C}{\lambda^4} \\ k(\lambda) &= 0 \end{aligned} \quad \text{Eq. 2-15}$$

For which A , B , and C are fitting parameters. More complex equations between n and λ can be used, for which k is calculated with the Kramers-Kronig relationship. For materials with multiple interfaces, such as supported films, light is reflected off of both the top (air-film) and bottom (film-substrate) interfaces, as illustrated schematically in Figure 2-6. The sum of these reflected waves yields the total reflected light. Due to the phase relationship (Φ_1 vs. Φ_2) in normal incidence on a transparent film, the light may add constructively (in phase) or destructively (out of phase), which occurs at thickness, d , of $i\lambda/(2n)$ or $(i+1/2)\lambda/(2n)$, respectively, for which i is an integer and 2 accounts for light passing through the film twice. In these supported, non-absorbing ($k = 0$) films, the reflectance is modeled by

$$R \approx A + B \cos\left(\frac{4\pi}{\lambda} nd\right) \quad \text{Eq. 2-16}$$

The amplitude and periodicity are controlled by the thickness, optical constants, and interfacial roughness. Thus, films with greater thickness will have a larger number of oscillations over a particular wavelength range in comparison to films with a smaller thickness. Higher refractive index also leads to vertical shifts in the reflectance values as well as increases in the height of the oscillations. These effects are shown schematically in Figure 2-6.

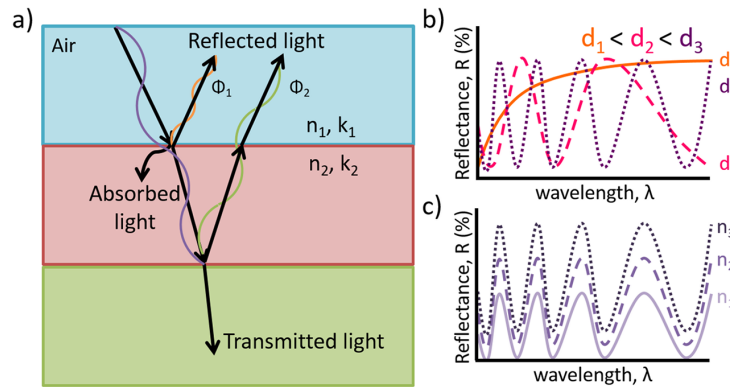


Figure 2-6. a) Schematic of light transmission in layered samples. b) Influence of thickness on measured spectra, for which $d_1 < d_2 < d_3$. With increasing thickness, the number of peaks in the reflectance increases. c) Effect of refractive index on spectra. Materials with higher refractive indices have spectra with larger amplitudes that are shifted upwards vertically in reflectance ($n_1 < n_2 < n_3$).

SR was used to provide film thicknesses of dry films and solvent swollen films both under solvent vapor annealing and casting from solution. The wavelength range studied depends on the light source used; the wavelength ranges used to measure film

thicknesses in this dissertation varied from 200 nm (deuterium lamp) or 400 nm (halogen lamp) to 1100 nm. In all work, only the film thickness was fit. The refractive indices were taken from literature or estimated *a priori*. During solvent vapor swelling, the refractive index was calculated using a linear mixing rule between the solvent refractive index and polymer refractive index. These values provided reasonable fits to the data (> 0.90 goodness of fit in all cases).

2.2.6 Solvent Vapor Swelling¹⁷⁻²⁰

Solvent vapor swelling can be used to determine solvent-polymer interactions, whereas solvent vapor annealing affords changes in the structure of films. Both techniques utilize a solvent-rich environment in a sealed chamber to provide polymer chain mobility. A schematic of solvent vapor swelling is shown in Figure 2-7. A dry polymer film is exposed to a solvent rich atmosphere. Then, the solvent diffuses into the film and swells the polymer chains.

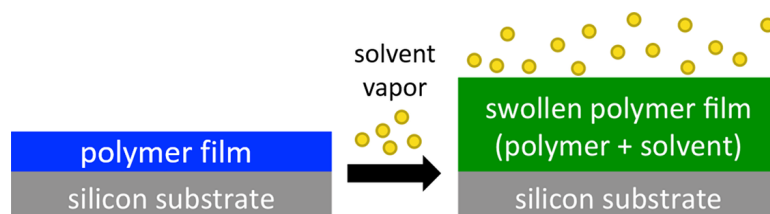


Figure 2-7. Schematic of solvent vapor swelling.

The amount of solvent that is incorporated into the film ($\phi_s = 1 - \phi_p$, for which ϕ_p is the polymer volume fraction) depends on the solvent concentration in the chamber and the polymer-solvent Flory-Huggins interaction parameter, χ_{s-p} . The solvent

concentration is given by the ratio of the pressure of solvent within the chamber, p_i , to the saturated partial pressure under the experimental temperatures, $p_{i,sat}$,

$$\ln\left(\frac{p_i}{p_{i,sat}}\right) = \chi_{i-p}\phi_p^2 + \ln(1 - \phi_p) + \left(1 - \frac{V_i}{V_p}\right)\phi_p \quad \text{Eq. 2-17}$$

For which V_s is the molar volume of solvent, and V_p is the molar volume of the polymer. Because $V_{poly} \gg V_i$, the last term in eq. 2-17 can be approximated as $(1-1/N)\phi_p$ or ϕ_p ,²¹⁻²² however, it is most accurate to use the actual molar volumes in place of these approximations, if these values are known.

2.2.7 Tribology²³

Tribology is the study of friction and wear. The friction coefficient, μ , is defined as the ratio of the friction force (F_F) to the normal force (F_N). In a tribology experiment, the friction coefficient is measured as a function of position along the film and time. These friction loops can be used to inform sample misalignment with the probe, surface non-uniformities, and structures on the surface. Figure 2-8 highlights different friction loops that can occur during a friction test.

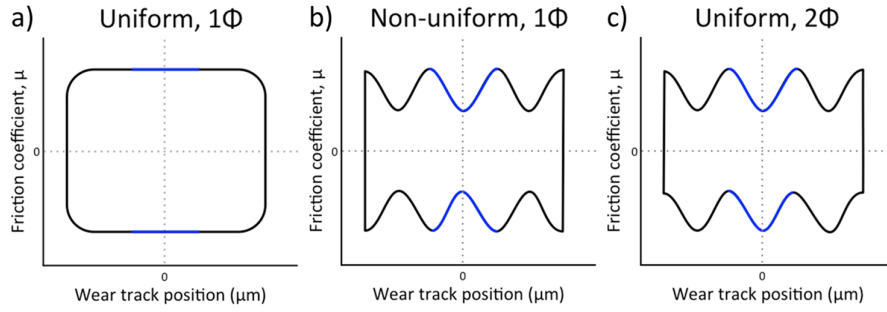


Figure 2-8. Schematic of friction coefficient loops for tribology experiments with a) uniform, one phase, b) non-uniform, one phase, and c) uniform, two phase surfaces. The blue region represents the region over which the friction coefficient is measured. Oscillations in the negative and positive friction coefficient quadrants that are out of phase signify non-uniformity along the wear track, whereas the in-phase oscillations indicate structural differences between the two phases.

The contact area plays a key role in the friction coefficient. For polymers, the contact radius follows the theory developed by Johnson, Kendall, and Roberts (JKR).²⁴

$$a_{JKR} = \left[\frac{3R}{4E^*} \left(F_N + 6W_{ad}\pi R + \sqrt{12W_{ad}RF_N + (6W_{ad}\pi R)^2} \right) \right]^{1/3} \quad \text{Eq. 2-18}$$

For which R is the bead radius, E^* is the composite modulus, F_N is the normal force, and W_{ad} is the work of adhesion. The composite modulus, E^* , is related to the Poisson ratio (ν_i) and the Young's modulus (E_i) of material i .

$$\frac{1}{E^*} = \frac{1-\nu_1^2}{E_1} + \frac{1-\nu_2^2}{E_2} \quad \text{Eq. 2-19}$$

In the absence of adhesion ($W_{ad} = 0 \text{ J/m}^2$), the JKR contact radius reduces to the Hertz contact radius ($a_{Hertz} = [(3R/4E^*)F_N]^{1/3}$).²⁴ However, most materials have some adhesion with the probe, which will increase the contact radius. The work of adhesion is given by²⁵

$$W_{ad} = \gamma_1 + \gamma_2 - \gamma_{12} \quad \text{Eq. 2-20}$$

for which the γ_i is the surface energy of material i and γ_{ij} is the interfacial tension between materials i and j . The interfacial tension can be determined from the geometric mean of the dispersive (γ^D) and polar (γ^P) surface energy contributions.^{6, 26}

$$\gamma_{12} = \gamma_1 + \gamma_2 - 2\sqrt{\gamma_1^D \gamma_2^D} - 2\sqrt{\gamma_1^P \gamma_2^P} \quad \text{Eq. 2-21}$$

2.2.8 Transmission Electron Microscopy (TEM)

Transmission electron microscopy was used to measure the size and aspect ratio of the gold nanorods as well as to characterize the nanorod partitioning in polymer blends.

An electron source, such as LaB₆ emits the electrons that travel through the column of the microscope, which is under vacuum. An electromagnetic lens focuses the electrons into a thin beam. The incident beam electron beam passes through the sample and is focused by the electromagnetic objective lens. The scattered beam then travels through an objective aperture and is focused onto the imaging plane, at which point the image can be captured and analyzed.

Contrast in TEM is provided by differences in atomic number (mass) and sample thickness, called mass-thickness or amplitude contrast. Thus, contrast can come from differences in mass, thickness, or a combination of the two. High-Z (high mass) materials should scatter more than low-Z materials of the same thickness. Additionally, thicker samples have higher scattering, as the electron passes through more material. In bright field mode, high mass and thick regions appear dark.

2.3 Seed-mediated Growth of Gold Nanoparticles²⁷⁻²⁹

Seed-mediated growth is a method to produce gold nanoparticles in an aqueous phase. First, a seed particle is synthesized. The seed particle can then be grown isotropically to form a larger spherical particle, or anisotropic growth can be promoted to produce gold nanorods using a surfactant, such as hexadecyltrimethylammonium bromide (CTAB). Nikoobakht and El-Sayed demonstrated the versatility of seed-mediated AuNR synthesis and formed NRs with aspect ratios ranging from 1.5 to 4.5.²⁷ Longer NRs (aspect ratio ranging from 4.6 to 10) are synthesized by adding a second surfactant. The CTAB stabilizing agent can then be replaced by other ligands, such as thiols.³⁰⁻³³

2.3.1 Synthesis of the Seed Solution.

5 mL of 0.2 M CTAB in water is mixed with 5 mL of 0.0005 M $\text{HAuCl}_4 \cdot 3\text{H}_2\text{O}$ and stirred. 0.6 mL of 0.01 M NaBH_4 is added to reduce the gold and form particles.

2.3.2 Synthesis of Gold Nanorods^{27-29, 34-35}

5 mL of 0.20 M CTAB is added to 0.25 mL of AgNO_3 . The silver, likely in the form of AgBr , helps to stabilize the nanorod surface, preventing the formation of spheres.²⁹ Furthermore, El-Sayed and coworkers postulated that the Ag ions assist packing of CTAB on the [110] facet, retarding growth of the particle width.²⁷ Over the course of particle growth, CTAB binds more strongly to the [110] facet (sides) than the other facets of the rod.³⁴ Next, 5.0 mL of 0.0010 M HAuCl_4 was added to the solution followed by 70 μL of 0.0788 M ascorbic acid, a mild reducing agent. The addition of ascorbic acid to the growth solution reduces the gold from Au^{3+} to Au^+ , changing the solution color from deep yellow to clear.³⁵ Finally, 12 μL of the seed solution is added to the growth solution. The color changed over ~ 30 minutes. All

solutions were kept at 28 °C in a water bath and stirred constantly. Vaia and coworkers detailed the growth mechanism of gold nanorods by seed-mediated growth synthesis.²⁸ Anisotropic growth along the [111] facet due to selective adsorption of CTAB on the higher energy ([110]/[100]) surfaces of the seed particle. The particles then become dumbbell shaped due to the addition of atoms from the end of the rod, followed by surface reconstruction to [120] and [250] facets. The particles were characterized by UV-Vis spectroscopy and transmission electron microscopy (TEM).

2.3.3 Ligand Exchange Protocols

There have been many reported methods for phase transferring gold nanoparticles from aqueous to organic solution.^{30, 32, 35-37} In these phase transfer methods, the ligand of interest is introduced to the gold solution either by itself (largely immiscible) followed by organic solvent addition^{30, 32, 35} or dissolved in a solvent that will mix with the aqueous particle solution,³⁶⁻³⁷ such as tetrahydrofuran (THF). PS-SH in THF (2 wt.%) was added to the aqueous reaction mixture in a 1:2 THF/water ratio by volume. The solution was stirred for 4 hours, after which the organic phase was extracted in a separatory funnel. Complete ligand exchange was characterized by the lack of CTAB evidenced in the ¹H NMR spectra. The particles were then dried down and stored prior to use.

REFERENCES

1. Vig, J. R., UV/ozone cleaning of surfaces. *J. Vac. Sci. Technol., A* **1985**, *3*, 1027-1034.
2. Meyerhofer, D., Characteristics of resist films produced by spinning. *J. Appl. Phys.* **1978**, *49*, 3993-3997.
3. Stafford, C. M.; Roskov, K. E.; Epps, T. H., III; Fasolka, M. J., Generating thickness gradients of thin polymer films via flow coating. *Rev. Sci. Instrum.* **2006**, *77*, 023908.
4. Good, R. J.; Girifalco, L. A., A theory for estimation of surface and interfacial energies. III. Estimation of surface energies of solids from contact angle data. *J. Phys. Chem.* **1960**, *64*, 561-565.
5. Owens, D. K.; Wendt, R. C., Estimation of the surface free energy of polymers. *J. Appl. Polym. Sci.* **1969**, *13*, 1741-1747.
6. Wu, S., Calculation of interfacial tension in polymer systems. *J. Polym. Sci., Part C: Polym. Symp.* **1971**, *34*, 19-30.
7. Gao, L.; McCarthy, T. J., Contact angle hysteresis explained. *Langmuir* **2006**, *22*, 6234-6237.
8. Albert, J. N. L.; Baney, M. J.; Stafford, C. M.; Kelly, J. Y.; Epps, T. H., III, Generation of monolayer gradients in surface energy and surface chemistry for block copolymer thin film studies. *ACS Nano* **2009**, *3*, 3977-3986.
9. Jańczuk, B.; Wójcik, W.; Zdziennicka, A., Determination of the components of the surface tension of some liquids from interfacial liquid-liquid tension measurements. *J. Colloid Interface Sci.* **1993**, *157*, 384-393.
10. Tadmor, R., Line energy and the relation between advancing, receding, and Young contact angles. *Langmuir* **2004**, *20*, 7659-7664.
11. Eral, H. B.; 't Mannetje, D. J. C. M.; Oh, J. M., Contact angle hysteresis: a review of fundamentals and applications. *Colloid. Polym. Sci.* **2013**, *291*, 247-260.

12. Chibowski, E.; Terpilowski, K., Surface free energy of sulfur—Revisited: I. Yellow and orange samples solidified against glass surface. *J. Colloid Interface Sci.* **2008**, *319*, 505-513.
13. Young, R. J.; Lovell, P. A., *Introduction to Polymers*. 3rd ed.; Taylor & Francis: 2011.
14. Magonov, S. N.; Reneker, D. H., Characterization of polymer surfaces with atomic force microscopy. *Annu. Rev. Mater. Sci.* **1997**, *27*, 175-222.
15. Taking the mystery out of thin-film measurements. Filmetrics, Inc.: San Diego, 2006.
16. Operations manual for the Filmetrics F20 thin-film analyzer, v. 4.81. Filmetrics, Inc.: San Diego, 2007.
17. Albert, J. N. L.; Bogart, T. D.; Lewis, R. L.; Beers, K. L.; Fasolka, M. J.; Hutchison, J. B.; Vogt, B. D.; Epps, T. H., III, Gradient solvent vapor annealing of block copolymer thin films using a microfluidic mixing device. *Nano Lett.* **2011**, *11*, 1351-1357.
18. Albert, J. N. L.; Young, W. S.; Lewis, R. L.; Bogart, T. D.; Smith, J. R.; Epps, T. H., III, Systematic study on the effect of solvent removal rate on the morphology of solvent vapor annealed ABA triblock copolymer thin films. *ACS Nano* **2012**, *6*, 459-466.
19. Albert, J. N. L.; Epps, T. H., III, Self-assembly of block copolymer thin films. *Mater. Today* **2010**, *13*, 24-33.
20. Emerson, J. A.; Toolan, D. T. W.; Howse, J. R.; Furst, E. M.; Epps, T. H., III, Determination of solvent-polymer and polymer-polymer Flory-Huggins interaction parameters for poly(3-hexylthiophene) via solvent vapor swelling. *Macromolecules* **2013**, *46*, 6533-6540.
21. Elbs, H.; Krausch, G., Ellipsometric determination of flory-huggins interaction parameters in solution. *Polymer* **2004**, *45*, 7935-7942.
22. Jaczewska, J.; Raptis, I.; Budkowski, A.; Goustouridis, D.; Raczowska, J.; Sanopoulou, A.; Pamula, E.; Bernasik, A.; Rysz, J., Swelling of poly(3-alkylthiophene) films exposed to solvent vapors and humidity: evaluation of solubility parameters. *Synth. Met.* **2007**, *157*, 726-732.
23. Burris, D. L.; Sawyer, W. G., Addressing practical challenges of low friction coefficient measurements. *Tribol. Lett.* **2009**, *35*, 17-23.

24. Johnson, K. L.; Kendall, K.; Roberts, A. D., Surface energy and the contact of elastic solids. *Proc. R. Soc. London, Ser. A* **1971**, *324*, 301.
25. Israelachvili, J. N., *Intermolecular and Surface Forces*. 3rd ed.; Academic Press: San Diego, 2011, p 415-467.
26. Fowkes, F. M., Attractive forces at interfaces. *Ind. Eng. Chem.* **1964**, *56*, 40-52.
27. Nikoobakht, B.; El-Sayed, M. A., Preparation and growth mechanism of gold nanorods (NRs) using seed-mediated growth method. *Chem. Mater.* **2003**, *15*, 1957-1962.
28. Park, K.; Drummy, L. F.; Wadams, R. C.; Koerner, H.; Nepal, D.; Fabris, L.; Vaia, R. A., Growth mechanism of gold nanorods. *Chemistry of Materials* **2013**, *25*, 555-563.
29. Jana, N. R.; Gearheart, L.; Murphy, C. J., Seed-mediated growth approach for shape-controlled synthesis of spheroidal and rod-like gold nanoparticles using a surfactant template. *Adv. Mater.* **2001**, *13*, 1389-1393.
30. Sahu, D.; Chu, H.-C.; Yang, P.-J.; Lin, H.-C., Surface modification of gold nanorods by grafting fluorene-based conjugated copolymers containing thiol-pendants. *Macromol. Chem. Phys.* **2012**, *213*, 1550-1558.
31. Hotchkiss, J. W.; Lowe, A. B.; Boyes, S. G., Surface modification of gold nanorods with polymers synthesized by reversible addition-fragmentation chain transfer polymerization. *Chem. Mater.* **2007**, *19*, 6-13.
32. Wijaya, A.; Hamad-Schifferli, K., Ligand customization and DNA functionalization of gold nanorods via round-trip phase transfer ligand exchange. *Langmuir* **2008**, *24*, 9966-9969.
33. Jebb, M.; Sudeep, P. K.; Pramod, P.; Thomas, K. G.; Kamat, P. V., Ruthenium(II) trisbipyridine functionalized gold nanorods. Morphological changes and excited-state interactions. *J. Phys. Chem. B* **2007**, *111*, 6839-6844.
34. Wang, Z. L.; Gao, R. P.; Nikoobakht, B.; El-Sayed, M. A., Surface reconstruction of the unstable {110} surface in gold nanorods. *J. Phys. Chem. B* **2000**, *104*, 5417-5420.
35. Jana, N. R.; Gearheart, L.; Murphy, C. J., Seeding growth for size control of 5-40 nm diameter gold nanoparticles. *Langmuir* **2001**, *17*, 6782-6786.

36. Liu, K.; Nie, Z.; Zhao, N.; Li, W.; Rubinstein, M.; Kumacheva, E., Step-growth polymerization of inorganic nanoparticles. *Science* **2010**, *329*, 197-200.
37. Wang, D. L.; Hore, M. J. A.; Ye, X. C.; Zheng, C.; Murray, C. B.; Composto, R. J., Gold nanorod length controls dispersion, local ordering, and optical absorption in polymer nanocomposite films. *Soft Matter* **2014**, *10*, 3404-3413.

Chapter 3

INTERPLAY BETWEEN THERMODYNAMICS, PHASE SEPARATION KINETICS, AND FILM CASTING FROM POLYMER SOLUTIONS

Portions of the text and figures were reproduced and adapted with permission from Emerson, J. A., *et al. Macromolecules* 2013, 46 (16), 6533-6540. Copyright 2013 American Chemical Society. Sections were also modified with permission from Haq, E. U.; Toolan, D. T. W.; Emerson, J. A. *et al. J. Polym. Sci. Part B: Polym. Phys.* 2014, 52 (15), 985-992. Copyright 2014 Wiley Periodicals, Inc.

3.1 Introduction

Polymer blend films have been utilized in a variety of applications including radiation shielding, organic optoelectronics, batteries, anti-reflection coatings, and pressure sensitive adhesives.¹⁻⁷ For these applications, morphology plays an important role in determining the material properties. Thus, understanding and controlling the phase behavior in complex mixtures is necessary to target property-driven hierarchical structures. The morphology is controlled by the thermodynamics and kinetics of phase separation along with the processing of the material.⁸⁻¹⁰ For linear polymer mixtures, the equilibrium phase behavior is governed by the interactions (monomer choice and degree of polymerization) and composition.⁹ In solution, the compatibility between the solvent and the two polymers also influences the phase behavior.¹¹ Additionally the processing parameters that affect the kinetics of phase separation, such as the evaporation rate and temperature influence the phase separation and morphological evolution.¹² Therefore, understanding the interactions between all

three components as well as the effect of casting is vital towards targeting morphologies in solution cast polymer blends.

The thermodynamics of polymer mixtures can be described using Flory-Huggins theory.^{8, 9, 11, 13-15} The Flory-Huggins interaction parameter (χ_{ij}) describes the compatibility of polymers with a second material (solvent or polymer). The phase behavior of multicomponent polymer blends is determined by the polymer molecular weight, molar volume, composition, and χ_{ij} .^{11, 14, 15} Using Flory-Huggins theory, χ_{ij} can be estimated from solubility parameters (δ) of the two materials, as discussed in Chapter 1. As δ 's for many solvents have been reported in literature, this method can provide *a priori* information about the phase behavior of polymer mixtures.

Solubility parameters can be determined by a variety of methods. Experimentally, δ can be calculated from the Flory-Huggins interaction parameters using regular solution theory. Scattering methods, osmosis, critical miscibility, vapor pressure methods, inverse gas chromatography, melting/freezing point depression, intrinsic viscosity, and swelling equilibria have been used to measure solvent-polymer Flory-Huggins interaction parameters (χ_{s-p}).¹⁶ Vapor pressure methods and swelling equilibria allow for measurement of a large composition range, which is important because the Flory-Huggins interaction parameter in solvent-polymer mixtures can vary widely with concentration.^{16, 17} This range is particularly relevant to relating χ_{s-p} to casting behavior, because the initially high solvent volume fraction ($\phi_s > 0.90$) is reduced primarily through evaporation to a dry film state ($\phi_s < 0.10$).^{17, 18} As the phase behavior in polymer mixtures depends on the interaction between all of the components, such a concentration dependence in the solvent-polymer interaction

parameters affects the onset of phase separation during casting. Solubility parameters can also be estimated using group contribution theory on the basis of the polymer structure. A variety of group contribution methods have been developed.^{19, 20} These solubility parameters enable *a priori* determination of the polymer blend phase behavior.

In addition to the thermodynamics of solution, the morphology in the film is controlled partially by the kinetics of phase separation, which is influenced by the processing dynamics.^{21, 22} The mechanisms of phase separation in polymer blend thin films have been reported in the literature, and they depend on the quench depth and rate as well as the concentration.²³⁻²⁸ At the same initial composition, changing the processing method (spin vs. flow coating) or the casting conditions (spin speed) can modify the film morphology.²² Therefore, connecting the equilibrium thermodynamics with processing insights can provide enhanced control over the final film morphology.

The effect of thermodynamics and processing were studied on solution-cast film morphologies using a variety of polymer blends. Solubility parameters were determined by solvent vapor swelling, using the experimental setup described by Albert *et al.* and others.^{17, 29, 30} From these experimentally determined solubility parameters, along with literature values and group contribution theory calculations, polymer/polymer/solvent phase diagrams were generated and validated experimentally. *In situ* analysis of spin-coated polymer blends provided better understanding of the relationship between the phase diagram and casting behavior. The insights developed through relating the processing and the thermodynamics

enable generation of targeted hierarchical structures for applications incorporating polymer blend films.

3.2 Materials & Methods

3.2.1 Materials

Polymers. Polystyrene ([PS], $M_n = 17.0$ kg/mol, $D = 1.04$; $M_n = 327.0$ kg/mol, $D = 1.05$) and poly(3-hexylthiophene) ([P3HT], $M_n = 17.4$ kg/mol, $D = 1.19$) were purchased from Polymer Source, Inc. Additional PS polymers ($M_n = 892$ kg/mol, $D = 1.04$; $M_n = 110$ kg/mol, $D = 1.04$) were acquired from Scientific Polymer Products. The different PS polymers are denoted as Xk PS, for which X is the molecular weight in units of kg/mol. Polyisoprene ([PI], $M_n = 541$ kg/mol, $D = 1.13$, 95% 1,4) was synthesized by anionic polymerization in cyclohexane using *sec*-butyllithium (*sec*-BuLi) as an initiator. Poly(methyl methacrylate)s [PMMA] of varying molecular weight ($M_n = 33$ kg/mol; $M_n = 100$ kg/mol; $M_n = 529$ kg/mol, $D = 1.11$) were purchased from Polysciences, Inc., Scientific Polymer Products, and Polymer Source, Inc., respectively. All polymers were used as received.

Solvents. *o*-xylene (puriss, p.a.) was obtained from Sigma-Aldrich. Toluene (certified ACS), chloroform (certified ACS) and tetrahydrofuran ([THF], optima) were purchased from Fisher Scientific. Chloroform-d (99.8+ atom% D, 0.03 v/v% TMS) from Acros Organics was used for proton nuclear magnetic resonance (^1H NMR) experiments. All solvents were used as received.

3.2.2 Blend Film Preparation

Polymer solutions were prepared gravimetrically at room temperature and stirred. ¹⁷kPS/P3HT solutions were dissolved in *o*-xylene and heated to 70 °C overnight. These solutions were cooled for 2 h, then reheated for 1 min (after opening briefly) before cooling to room temperature prior to use. Solutions were cast at a spin speed of 1500 rpm (unless noted otherwise) onto ultraviolet-ozone (Jelight, Model 342) cleaned silicon wafers (Wafer world, N-type, crystalline plane [100]).

3.2.3 Solvent Vapor Swelling

Solvent vapor swelling was used to determine the solvent-polymer interaction parameter using THF and CHCl₃, as described in Chapter 2 and Appendix B. The thin film pieces were placed in a sealed chamber alongside a cleaned silicon wafer, which allowed removal of chamber atmosphere effects from the swelling data. Nitrogen gas was flowed through fritted bubblers, which contained the solvent of choice, to carry solvent-rich vapor to the chamber. The solvent concentration was tuned by changing the relative flow rate between the solvent-rich stream and the nitrogen diluent, and the total nitrogen flow rate was maintained at 15 mL/min (PS, P3HT). All film thicknesses were greater than 100 nm to ensure the resulting swelling behavior was independent of film thickness.^{31, 32}

3.2.4 Transmission

The transmission of a HeNe laser (Melles Griot, 25-LHP-928-249, $\lambda = 632.8$ nm) was measured through PS/P3HT/*o*-xylene mixtures. The mass fraction of PS with respect to total polymer varied between 0 and 1, and the solvent volume fraction ranged from 0.94 to 1.00. Solutions of ¹⁷kPS/P3HT were dissolved in *o*-xylene by heating at 70 °C overnight. After cooling for 2 h, the initial solution was

sequentially diluted with *o*-xylene and used in subsequent transmission experiments. The solution was re-heated to 70 °C and held for ~1 min until the solution turned bright orange (P3HT solubilized) and cooled for 1 h before moving to the sample cell. The solution transmission did not change appreciably after 1 h of cooling, indicating that the solutions likely had reached an equilibrated state relevant to the time scales accessed during processing experiments. The polymer blend solutions were placed in a 1 mm path length glass sample cell, and the transmission was measured with a laser power meter (Newport Research Corporation, Model 820).

3.2.5 Tie Line Determination

Concentrated solutions of ^{892k}PS/PI in *o*-xylene and toluene were prepared and sealed until two clear phases formed. The top and bottom phases were extracted separately and weighed. After drying on a Schlenk line, the dry polymer mass was determined gravimetrically to calculate the polymer concentration in the phase. The top and bottom phases were then re-suspended in deuterated chloroform (CDCl₃) with an internal TMS standard to calculate the ratio of the two polymers. A Bruker AV-400 instrument was used to perform proton nuclear magnetic spectroscopy (¹H NMR).

3.2.6 Drying Curves

A spectral reflectometer was placed above the spin coater to measure the film thickness *in situ*. Spectra were captured every ~50 ms during casting using an automated recording software (Spincoater.py). The spectra were fit with a custom program (Spincoaterfitter.py). The data were shifted manually to the start time by setting the deviation from the initial state as $t = 0$ s (see Appendix D, Figure D-1).

3.2.7 Stroboscopic Illumination

The stroboscopic illumination set-up was used to capture phase separation during casting and is described in more detail elsewhere³³. For the PS/P3HT samples, a small DC motor acts as a spin-coater, which was mounted directly under a 60x objective. A 50 μ s pulse of red light (620 nm, LED Cree X lamp) and image collection were triggered once per revolution, which produced a set of static images of the same spot on the film. An Andor iXON 897+ detector, which has a field of view of $132 \times 132 \mu\text{m}$, was used in conjunction with an ELWD $\times 60$ objective. Cleaned silicon wafers (10 x 10 mm) were placed on the spin-coater, and the substrate surface was brought into focus using imperfections on the substrate surface. 50 μL of solution was dispensed onto the substrate and then spun at the 1500 rpm, during which the data was collected for 600 exposures (24 s).

3.3 Results & Discussion

3.3.1 Polymer Solubility Parameters

The solubility parameter is a measure of the cohesive energy density, which can be used to calculate the interaction parameter between two materials, such as two polymers or a polymer and a solvent. Polymer solubility parameters have been reported widely in literature for a variety of polymers.¹⁶ A summary of solubility parameters used to determine interactions (denoted by *) is given in Table 3-1. The solubility parameters are $19.5 \text{ MPa}^{1/2}$ and $19.0 \text{ MPa}^{1/2}$ for THF and CHCl_3 , respectively.

Table 3-1. Solubility parameters from literature, solvent vapor swelling, and group contribution theory.

Polymer	Literature	Solubility parameter, δ (MPa ^{1/2})	
		Solvent vapor swelling ^b	Group contribution theory ^c
PMMA	19.2*, 22.69 ^{16, 34}	N/A	19.3
PI	16.6*, ^{a, 16}	N/A	16.5
PS	18.2 ^{a, 16}	17.9 ± 0.2*	18.0
P3HT	12.8 – 20.0	14.8 ± 0.2*	16.0

*Value used to calculate $\chi_{\text{sol-poly}}$ and $\chi_{\text{poly-poly}}$. ^aSolubility parameters represent an average over the range of reported values for PS (17.4 MPa^{1/2} – 19.8 MPa^{1/2}) and PI (16.2 MPa^{1/2} – 17.1 MPa^{1/2}). ^bSolubility parameters (δ) were determined from regular solution theory calculations with solvent–polymer Flory–Huggins interaction parameters measured by solvent vapor swelling experiments with THF and CHCl₃. Error propagated from the uncertainties in the calculated Flory-Huggins interaction parameters. ^cSolubility parameters estimated from the van Krevelen and Hoftyzer group contribution method.¹⁹

Solubility parameters can be used to calculate solvent-polymer and polymer-polymer interaction parameters *via* regular solution theory. As discussed in Chapter 1 (Section 1.1.2, Eq. 1.19), these two-component mixtures are given by:

$$\chi_{ij} = \chi_H + \chi_S = \frac{V_{ref}}{RT} (\delta_i - \delta_j)^2 + \chi_S \quad \text{Eq. 4.1}$$

For which V_{ref} is a reference molar volume, R is the ideal gas constant (8.314 cm³ MPa mol⁻¹ K⁻¹), T is the temperature in K, δ is the solubility parameter, and χ_S is the entropic component to the Flory-Huggins interaction parameter. In solvent-polymer mixtures, V_{ref} is the molar volume of the solvent (THF: 81.7 cm³/mol; CHCl₃: 80.7 cm³/mol) and χ_S is taken to be 0.34.¹⁶ V_{ref} is calculated from the geometric mean of the polymer repeat unit molar volume ($V_{ref} = [V_i V_j]^{1/2}$) in the case of polymer-polymer mixtures. χ_S ranges from 10⁻⁶ to 10⁻² in polymer blends and is assumed to be negligible.³⁵⁻³⁷

3.3.1.1 Solvent Vapor Swelling of Polymer Films

The solubility parameters for polymers that have not been studied in literature can be calculated from the solvent-polymer interaction parameters measured by

solvent vapor swelling. According to lattice theory, the solvent vapor swelling can be used to measure solvent-polymer interaction parameter, as described in Chapter 1.

$$\ln\left(\frac{p_i}{p_{i,sat}}\right) = \chi_{i-poly}\phi_{poly}^2 + \ln(1 - \phi_{poly}) + \left(1 - \frac{V_i}{V_{poly}}\right)\phi_{poly} \quad \text{Eq. 4.2}$$

$p_i/p_{i,sat}$ is the ratio of the partial pressure of solvent to the saturated partial pressure, ϕ_{poly} is the volume fraction of polymer, V_i is the molar volume of solvent, and V_{poly} is the molar volume of the polymer. Typically, $V_{poly} \gg V_i$, so the last term in eq. 4.2 can be approximated as $(1-1/N)\phi_{poly}$ or ϕ_{poly} ,^{31, 38} however, to maintain a robust methodology, the ratio of the volumes was used in place of these approximations.

To perform swelling experiments, sections of thin films were placed alongside a cleaned silicon wafer in the solvent vapor annealing chamber (see Chapter 2 and Appendix B). Multiple films were sampled during each experiment by moving the motorized stage connected to the spectral reflectometer. A set of typical results for polymer swelling (volume fraction), given by the ratio of the initial to the swollen film thickness, is shown in Figure 3-1 for PS swelling in THF. Each of the four colors represents a different flow condition, for which the ratio of the pure N₂ to the N₂ through solvent flow rates were adjusted while maintaining a constant total flow rate. Solvent uptake as a function of N₂ flow rate and temperature is given in Appendix B.

The initial flow conditions had the highest solvent concentration, after which the solvent vapor composition was decreased (Figure 3-1). This procedure eliminated potential startup effects and ensured relaxation/mobility of otherwise glassy polymers.^{39, 40} Solvent vapor diffusion into the polymer film caused the film to swell from the initial thickness, d_0 . The films equilibrated rapidly with the solvent concentration in the chamber;^{31, 38} at any time, the film thickness was given by d_t . The ratio of the initial film thickness to the time-dependent film thickness yields the

polymer volume fraction ($\phi_p = d_0/d_t$). Once the solvent composition stopped changing in time, the film thickness remained constant at its equilibrated swollen film thickness, which decreased with solvent concentration.

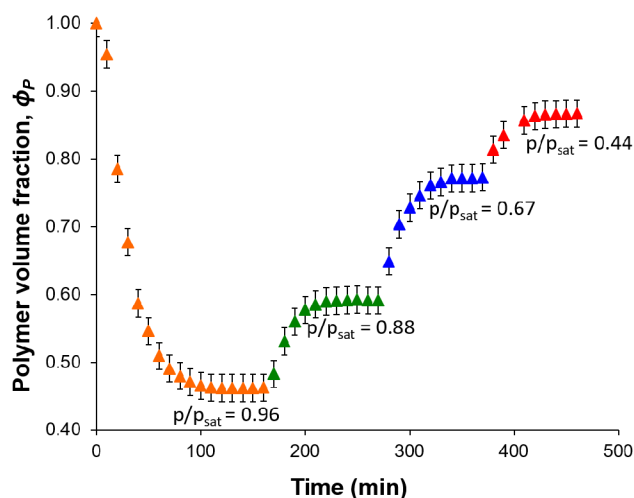


Figure 3-1. The polymer volume fraction, which is given by the ratio of the initial film thickness to the swollen film thickness, of PS is shown in time. Each of the four colors represents a different ratio of the flow rate of the solvent vapor stream to the diluent stream. The solvent concentration at equilibrium is shown as p/p_{sat} for each flow condition accessed. Once the film thickness equilibrated, the solvent vapor and dilution flow rates were changed, maintaining the same total flow rate. Reprinted with permission from Emerson, J. A., *et al. Macromolecules* 2013, 46 (16), 6533-6540. Copyright 2013 American Chemical Society.

Solvent vapor swelling was performed on PS, P3HT, and P4VV films in THF and CHCl_3 . The equilibrated polymer volume fractions in the swollen films were extracted from the plateaus of the swelling curves, such as those shown in Figure 3-1, and used to calculate the solvent-polymer Flory-Huggins interaction parameter, according to Eq. 4.2.

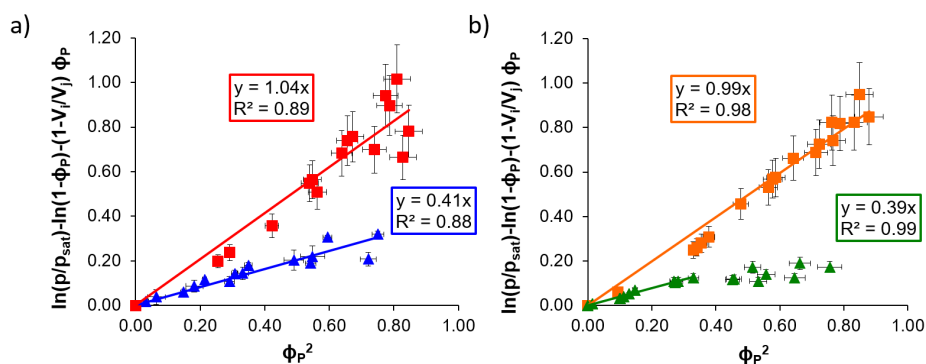


Figure 3-2. Interaction parameter plots for PS (\blacktriangle) and P3HT (\blacksquare) with a) THF and b) CHCl_3 . For PS in CHCl_3 (b), the data were fit for $\phi_P < 0.6$ ($\phi_P^2 < 0.36$), for which χ_{i-j} was nearly constant over the concentration range. For $\phi_P^2 > 0.36$, χ_{i-j} decreased with increasing polymer composition. Reprinted with permission from Emerson, J. A., *et al. Macromolecules* 2013, 46 (16), 6533-6540. Copyright 2013 American Chemical Society.

P3HT had the highest incompatibility with both THF and CHCl_3 , as evidenced by the larger slopes of the linear fits shown in Figure 3-2. In comparison to P3HT, PS has a significantly smaller interaction parameter (lower slope) with THF and CHCl_3 . $\chi_{\text{CHCl}_3\text{-PS}}$ was more favorable than $\chi_{\text{THF-PS}}$, as expected from the solubility parameter differences reported in literature ($\delta_{\text{PS}} = 18.2 \text{ MPa}^{1/2}$, $\delta_{\text{THF}} = 19.5 \text{ MPa}^{1/2}$, $\delta_{\text{CHCl}_3} = 19.0 \text{ MPa}^{1/2}$).¹⁶ From the original Flory–Huggins theory, the solvent-polymer interaction parameter should be independent of composition, although χ_{s-p} can vary with composition experimentally.¹⁶ A constant χ_{s-p} fits the film swelling data for P3HT with both THF and CHCl_3 as well as PS with THF. However, we found that the interaction parameter between PS and CHCl_3 was not constant over the entire proved composition range. This decrease in Flory–Huggins interaction parameter with increasing polymer concentration was consistent with data reported in the literature.^{41,}
⁴² Thus, only the swelling behavior for PS in CHCl_3 in the low polymer volume

fraction region ($\phi_P < 0.6$) was used, for which χ_{CHCl_3-PS} was independent of concentration, in conjunction with χ_{THF-PS} to generate a single solubility parameter for PS.

The Flory-Huggins solvent-polymer interaction parameters were extracted from the slopes of the lines in Figure 3-2 and are reported in Table 3-2. P3HT had similar solvent-polymer Flory-Huggins interaction parameters with both THF and $CHCl_3$, which agrees with the small difference between the solubility parameters of the two solvents. On the basis of the calculated interaction parameters, PS should dissolve more readily in either solvent than P3HT, which matches the experimental behavior. The χ_{s-PS} 's determined from this method ($\chi_{CHCl_3-PS} = 0.39 \pm 0.01$, $\chi_{THF-PS} = 0.41 \pm 0.02$) were in agreement with the values reported in literature ($\chi_{CHCl_3-PS} = 0.17-0.52$, $\chi_{THF-PS} = 0.16-0.70$), which supports the validity of these experimental measurements, setup and protocol.^{16, 31, 41, 42}

Table 3-2. Flory-Huggins solvent-polymer interaction parameters from solvent vapor swelling.

Polymer	$\chi_{THF-poly}$	χ_{CHCl_3-poly}
PS	0.41 ± 0.02	0.39 ± 0.01
P3HT	1.04 ± 0.04	0.99 ± 0.01

Using the Flory-Huggins solvent-polymer interaction parameters in Table 3-2 along with regular solution theory, the solubility parameters for PS and P3HT were calculated (Table 3-1). The experimental results (from literature & solvent vapor swelling) should agree reasonably well. The solubility parameter determined for PS from solvent vapor swelling is in excellent agreement with the values in literature. However, this is not the case for P3HT, for which the differences in solubility

parameter are more evident. The literature value for δ_{P3HT} varies widely ($12.8 \text{ MPa}^{1/2} - 20.0 \text{ MPa}^{1/2}$).^{38, 43-46} The upper limits of the solubility parameters were measured from solvent titration (dilute polymer solution), and the lower values were determined from solvent vapor swelling experiments with a polymer volume fraction range of $0.92 \leq \phi_{\text{poly}} \leq 0.97$ (very concentrated polymer “solutions”). Accessing a wider range of polymer volume fractions is important to evaluate the Flory-Huggins interaction parameter, which can vary with composition. From the solvent vapor swelling experiments, the P3HT solubility parameter was $14.8 \pm 0.2 \text{ MPa}^{1/2}$, which is within the range of literature values. For materials with preferential interactions (*e.g.* hydrogen bonding), the solvent vapor swelling technique in combination with Flory-Huggins theory cannot accurately capture the interaction. Thus, another approach must be used to produce the solubility parameter.

3.3.1.2 Group Contribution Theory

Group contribution theory enables the calculation of solubility parameters based on chemical structure and, as such, does not require experimental analysis of the material properties. A variety of group contribution methods have been developed.^{19, 20} One of the most commonly used formalisms was proposed by van Krevelen and Hoftyzer, in which the Hansen solubility parameter (comprised of polar, dispersive, and hydrogen bonding components) is calculated.¹⁹

Using this approach, the solubility parameters were estimated for PS, P3HT, PMMA, and PI. These results are listed in Table 3-1. As discussed in the previous section, the solvent vapor swelling data agree with other values reported in literature. For some polymers, group contribution theory provides a good estimate of the solubility parameter. For example, PS values are in agreement from all three sources.

PS has mostly dispersive interactions, which can be captured accurately using group contribution theory formalisms. δ_{PI} also is the same for group contribution in comparison to the literature values. Although PMMA has higher polar character, it is still described well by group contribution theory, likely due to the simple structure of the polymer. P3HT does not have strong polar interactions; however, group contribution theory does not accurately predict the solubility parameter. This disagreement between experiment and group contribution theory could be the result of the intermolecular interactions that produce π - π stacking and crystallization in these polymers. However, group contribution theory allows an estimation of the solubility parameters and affords approximation of material behavior for polymers that cannot be studied readily by other means. Although group contribution theory can provide *a priori* information about solubility, it produces, at best, an estimate and should be verified experimentally whenever possible, especially for systems with strong intermolecular bonding.

3.3.2 Phase Diagram

The phase diagram can be used to provide insight into the onset and mechanism of phase separation in polymer blend solutions upon quenching. Phase separation occurs by two mechanisms. In the metastable regime (between the binodal and spinodal curve), phase separation occurs *via* nucleation and growth in the presence of a nucleation site.⁸⁻¹⁰ Phase evolution undergoes spinodal decomposition in the unstable region of the phase diagram (spinodal curve). To determine the method of phase separation, the binodal and spinodal curves must be known, as well as the quench rate through the phase diagram.

The theoretical phase behavior in polymer/polymer/solvent blends have been described theoretically by R. L. Scott.^{11, 15}

$$\frac{\Delta\bar{G}_0}{RT} = \ln \phi_0 + \left(1 - \frac{1}{m_1}\right)\phi_1 + \left(1 - \frac{1}{m_2}\right)\phi_2 + \mu_{10}\phi_1^2 + \mu_{20}\phi_2^2 + (\mu_{10} + \mu_{20} - \mu_{12})\phi_1\phi_2 \quad \text{Eq. 4.3a}$$

$$\frac{\Delta\bar{G}_1}{RT} = \ln \phi_1 + (1 - m_1)\phi_0 + \left(1 - \frac{m_1}{m_2}\right)\phi_2 + m_1[\mu_{10}\phi_0^2 + \mu_{12}\phi_2^2 + (\mu_{10} + \mu_{12} - \mu_{20})\phi_0\phi_2] \quad \text{Eq. 4.3b}$$

$$\frac{\Delta\bar{G}_2}{RT} = \ln \phi_2 + (1 - m_2)\phi_0 + \left(1 - \frac{m_2}{m_1}\right)\phi_1 + m_2[\mu_{20}\phi_0^2 + \mu_{12}\phi_1^2 + (\mu_{20} + \mu_{12} - \mu_{10})\phi_0\phi_1] \quad \text{Eq. 4.3c}$$

For which $\Delta\bar{G}_i$ is the partial molar Gibbs free energy, R is the universal gas constant, T is the temperature in K, ϕ_i is the volume fraction of component i relative to total solution volume, m_i is the ratio of the molar volume of component i relative to solvent, and χ_{ij} is the Flory-Huggins interaction parameter between components i and j . The solution is denoted by 0 and the two polymers are indicated by the subscripts 1 and 2.

3.3.2.1 Spinodal Curve

The spinodal curve is the stability line and can be calculated from the determinant of the second derivative of the free energy with respect to the volume fraction.¹⁵ Solving these equations numerically in Mathematica (see Appendix C, Section C.2) produces the composition of the spinodal curves. In addition to the polymer molecular weight and density, these calculations require the solvent-polymer and polymer-polymer interactions. Because the solvent-polymer and polymer-polymer interactions between any two components can be calculated with the

solubility parameters, the phase behavior of polymer/polymer/solvent mixtures can be predicted using equations 4.3a-c *a priori*. For example, the interaction parameters between P3HT and CHCl_3 as well as THF were measured previously. However, these solvents are not commonly used in casting P3HT.

Recently, there has been interest in casting P3HT from *o*-xylene, which is less hazardous than other solvents used to process P3HT but also dissolves P3HT to a reasonable extent.⁴⁷ Mixing of insulating polymers, such as PS, with P3HT has been studied to produce diverse structures in the films for organic optoelectronic devices as well as to impart enhanced electrical conductivity due to the crystallization/self-assembly processes.^{48, 49} Insight into the phase behavior of PS/P3HT/*o*-xylene affords enhanced control of the structures developed during casting. For ^{17k}PS/P3HT/*o*-xylene, *o*-xylene is strongly PS-selective ($\chi_{o-PS} = 0.34$; $\chi_{o-P3HT} = 0.84$).⁵⁰ Because the PS-P3HT interaction parameter is very high ($\chi_{PS-P3HT} = 0.48$), the strength of these incompatibilities result in a narrow one-phase region and a highly asymmetric phase envelope, as shown in Figure 3-3.

For other applications, such as pressure sensitive adhesives, a rubbery second component (PI) may be of interest instead of the semi-crystalline P3HT.⁴ In comparison to these high P3HT-solvent interactions, *o*-xylene is a nearly neutral solvent for PS and PI. For ^{892k}PS/PI/*o*-xylene blend, the spinodal line occurs at a lower volume fraction and is more symmetric (Figure 3-3). Although the molecular weight of both components in the ^{892k}PS/PI blend is much higher, the phase boundary is shifted to lower solvent content due to the increased compatibility between the polymers and *o*-xylene.

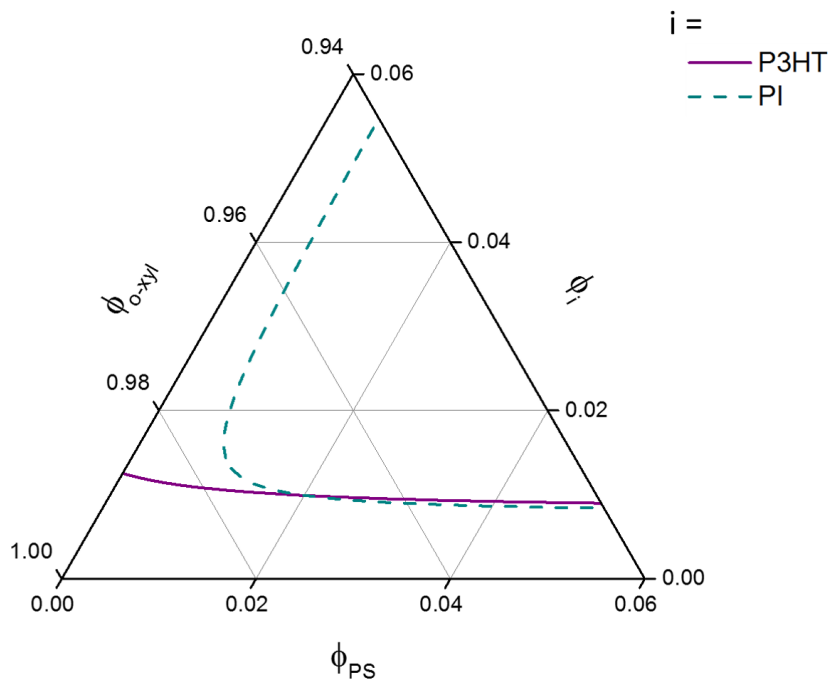


Figure 3-3. Ternary phase diagram with spinodal curves for PS/polymer/*o*-xylene blends, for which the second polymer is P3HT (solid) or PI (dash). For ^{17k}PS/P3HT/*o*-xylene, the interaction parameters were: $\chi_{o-PS} = 0.34$, $\chi_{o-P3HT} = 0.84$, and $\chi_{PS-P3HT} = 0.48$. For ^{892k}PS/PI/*o*-xylene, the Flory-Huggins interactions were: $\chi_{o-PS} = 0.34$, $\chi_{o-PI} = 0.37$, and $\chi_{PS-PI} = 0.013$

The phase behavior can be calculated for any combination of interaction parameters. Literature values can be used to predict the phase diagram of ^{327k}PS/^{529k}PMMA blends. In cases for which the solubility parameter varies, producing multiple spinodal curves can allow for estimates of the true solubility parameter, given known experimental conditions. For instance, examining whether PS/PMMA/*o*-xylene blends at different initial concentrations have phase separated can narrow down the solubility range of

the PMMA. These estimates can then provide information about the phase boundary *a priori* to ensure the blend formulation is initially homogenous.

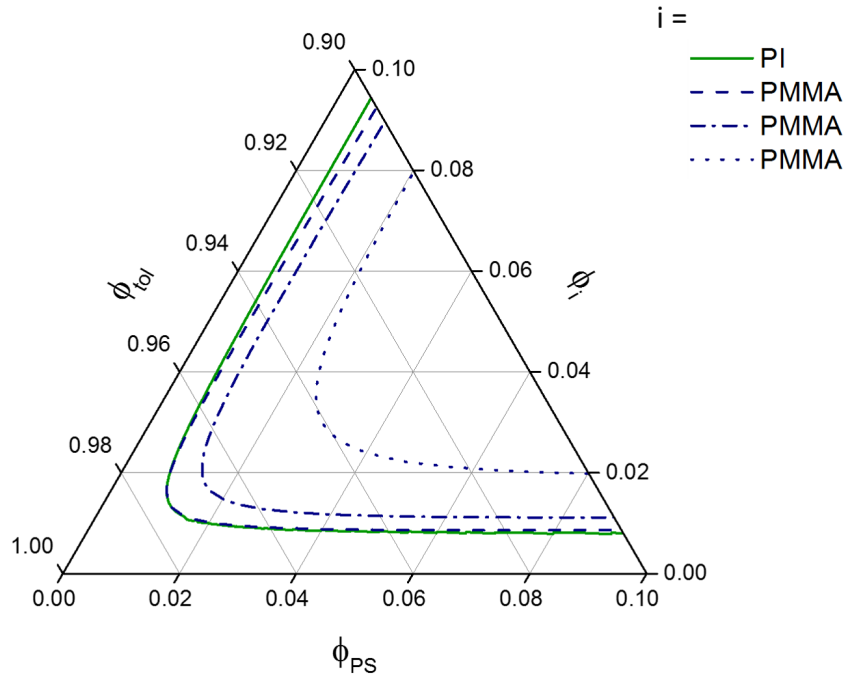


Figure 3-4. Ternary phase diagram for PS/polymer/toluene, for which the second polymer is PI (solid: $\chi_{\text{toluene-PS}} = 0.340$, $\chi_{\text{toluene-PI}} = 0.342$, $\chi_{\text{PS-PI}} = 0.012$) or PMMA (dash: $\chi_{\text{toluene-PMMA}} = 0.45$, $\chi_{\text{toluene-PS}} = 0.38$, $\chi_{\text{PS-PMMA}} = 0.010$; dash dot: $\chi_{\text{toluene-PMMA}} = 0.43$, $\chi_{\text{toluene-PS}} = 0.36$, $\chi_{\text{PS-PMMA}} = 0.007$; dot: $\chi_{\text{toluene-PMMA}} = 0.40$, $\chi_{\text{toluene-PS}} = 0.34$, $\chi_{\text{PS-PMMA}} = 0.004$).

3.3.2.2 Binodal Curve

Though the spinodal curve provides an estimate of the phase behavior, the binodal line is necessary to determine the onset of phase separation in off-critical compositions and to understand the mechanism by which phase separation will occur. Furthermore, an experimentally measured binodal curve can be used to validate the

theoretical phase diagram. Two methods were used to determine the binodal line: cloud point curves (transmission) and compositional analysis of phase separated layers.

The ternary phase diagrams reported in the previous section are replotted as pseudo-binary phase diagrams in this section. The concentration has been lumped into a combined term, x_i , which is the mass fraction of polymer i relative to the total polymer content. During processing, the relative composition of the two polymers is constant. Thus, information is not lost in generating these “processing” diagrams, which are less complex to extract information from.

3.3.2.2.1 Transmission (PS/P3HT)

Incorporating the transmission data onto the processing diagram provides insight into the boundary of the two phase region. The binodal line curve was determined from transmission measurements to validate the spinodal line for PS/P3HT/*o*-xylene. A HeNe laser was selected to measure transmission, as the wavelength ($\lambda = 632.8$ nm) was outside of the range over which P3HT absorbs strongly (400 nm – 600 nm). The deviation from 100% transmission marked the onset of phase separation and, thus, the boundary of the two phase region.⁵¹⁻⁵³ The relative transmission data and digital photographs of the PS/P3HT/*o*-xylene are shown in Appendix C, Figure C-3 and Figure C-4, respectively. The solvent volume fraction of the binodal line increased with P3HT volume fraction

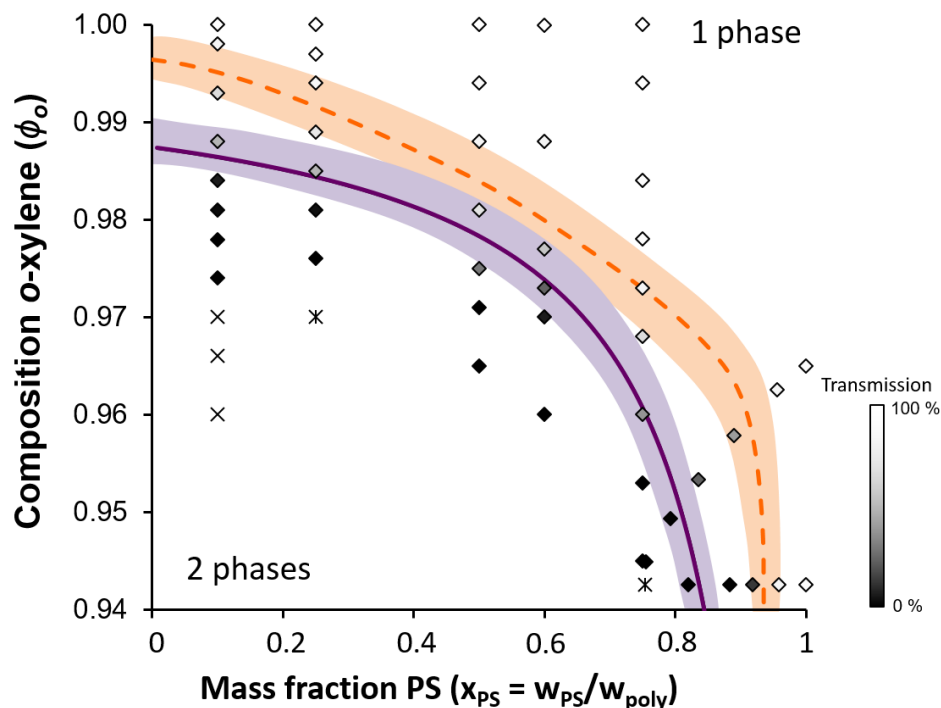


Figure 3-5. Phase diagram for blend of 17k PS/ 17k P3HT in *o*-xylene. Data points represent a discrete PS/P3HT/*o*-xylene solution through which transmission of a HeNe laser was measured. The color of the data point indicates the relative transmission (%) with respect to an *o*-xylene reference, in which white represents 100% transmission (no phase separation) and black indicates 0% transmission. Samples denoted by \times were gelled, and compositions indicated by $*$ were too viscous to transfer to the transmission cell. The dashed orange line represents the approximated binodal line, which connects the results from experimental data. The orange shaded region is the region in which the binodal line falls, determined by a decrease below 100% in the relative transmission. The purple solid line is the theoretical spinodal line and the purple shaded region represents the error in the spinodal line from the uncertainty in the solubility parameters.

The experimental binodal followed the theoretical spinodal curve with reasonable agreement. As such, the results in Figure 3-5 illustrate the synergy

between the experimental data and the calculated phase diagram, supporting the validity of this approach.

One interesting result that was found during the transmission tests was the gelation of the samples in *o*-xylene. These compositions are indicated by × in Figure 3-5. ¹⁷kFor PS₁₀/P3HT₉₀ mixtures, the gelled samples are shown in Figure C-5. Below solvent volume fractions of 0.970, the ¹⁷kPS₁₀/P3HT₉₀/*o*-xylene blends were able to suspend a Teflon stir bar when the vial was tilted 90°. A similar behavior was seen for ¹⁷kPS₇₅/P3HT₂₅ with solvent volume fractions less than 0.943. Gelation of P3HT has been studied in a variety of solvents.^{47, 54-59} The gelation of P3HT in aromatic organic solvents was previously studied by Pozzo and coworkers.⁵⁴⁻⁵⁷ With neat P3HT (M_w ~ 24 kg/mol) concentrations as low as 5 mg/mL (~0.5 wt.%), gelation occurred in *p*-xylene.⁵⁴ P3HT gelation occurs in three stages: (1) crystallization of P3HT chains into nanowhiskers, (2) formation of microgel clusters *via* fractal aggregation, and (3) merging of clusters into a 3D network.⁵⁸ As such the competition between crystallization, aggregation, and percolation drives the gelation. In comparison to the gelation threshold reported in literature, the onset of gelation was shifted in these ¹⁷kPS/P3HT/*o*-xylene solutions, likely due to the addition of a diluent (PS), which lowers the degree of P3HT aggregation.⁴⁷ Thus, due to the gelation, which occurs in addition to the phase separation, the kinetics may have a different effect on the casting behavior.

3.3.2.2.2 ¹H NMR (PS/PI)

¹H NMR is another valuable tool to measure the composition of phase separated systems and determine the binodal curve. At equilibrium, an incompatible mixture will bilayer phase separate to minimize the contact between the materials,

provided that there is sufficient mobility in the system. The compositions of these layers are in equilibrium and represent the composition of the binodal curve. The solvent concentration was determined gravimetrically after drying down the solution, and the relative polymer concentration was characterized for this dried polymer mixture using ^1H NMR in CDCl_3 . Binodal curves were produced for $^{892\text{k}}$ PS/PI/*o*-xylene and $^{892\text{k}}$ PS/PI/toluene mixtures. For both solutions, the spinodal curve and binodal curve were in reasonable agreement.

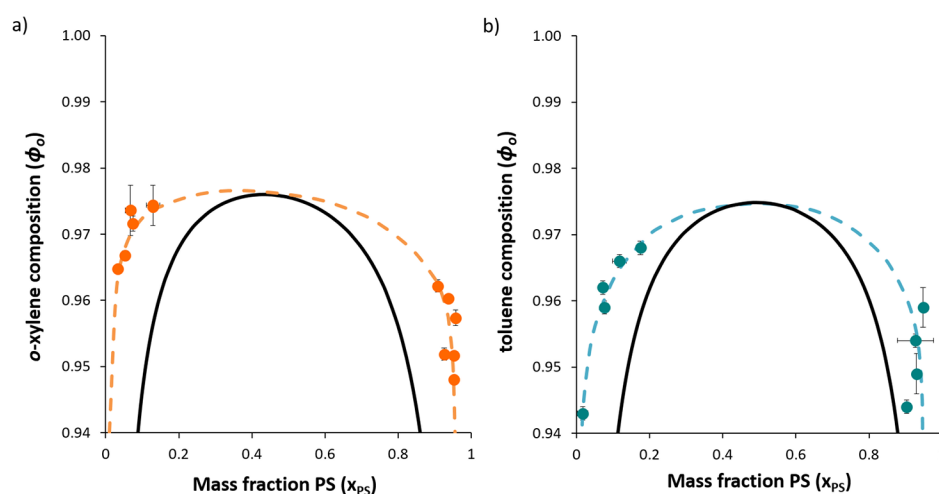


Figure 3-6: Processing phase diagram for PI/PS in a) *o*-xylene and b). Data points represent the composition of the binodal line determined gravimetrically and by ^1H NMR. The dashed line represents the approximated binodal line, which connects the results from experimental data. The solid line is the theoretical spinodal line calculated from Equations 1a-1c (also shown in Figure 3-3 and Figure 3-4). The parameters used to calculate the spinodal line were $M_{n,PS} = 892 \text{ kg/mol}$, $M_{n,PI} = 541 \text{ kg/mol}$, $\chi_{PS-PI} = 0.013$, $\rho_{PS} = 1.05$, $\rho_{PI} = 0.913$ with $\chi_{o-PS} = 0.342$, $\chi_{o-PI} = 0.372$, $\rho_o = 0.88$ for *o*-xylene (a) and $\chi_{toluene-PS} = 0.340$, $\chi_{toluene-PI} = 0.342$, $\rho_{tol} = 0.866$ for toluene (b).

As discussed for the spinodal curves, toluene and *o*-xylene have similar interactions with PS and PI. Additionally, both solvents are nearly neutral for PS and PI, which makes the processing diagram nearly symmetric for these materials. Thus, the phase diagram for *o*-xylene and toluene are very similar. However, the thermodynamics alone is not the only factor contributing to the final film morphology. Thus, it is also relevant to study the processing and kinetics of phase evolution.

3.4 Kinetics

The final film morphology is a product of the thermodynamics and kinetics of phase separation during film casting. Thus, in addition to understanding the phase behavior in polymer/polymer/solvent mixtures, the kinetic effects in processing must also be studied. Though it is possible to examine the film morphology *ex situ*, the dry films do not provide insight into the processing. To this end, two *in situ* techniques were implemented to provide insight into the drying behavior and casting process. The first technique utilized film thickness measurements during casting. These drying curves were related to the state of the solution using a simple casting model. The second technique, called stroboscopic illumination, allowed for direct visualization of phase separation.

3.4.1 Drying Curves

A useful tool to determine the effect of phase separation on the casting behavior is through modeling the drying behavior. Meyerhofer developed a model to describe the change in film thickness during spin casting.⁶⁰

$$\frac{dh}{dt} = -\frac{2\omega^2 h^3}{3\nu} - e$$

For which h is the film thickness, t is time, ω is the rotational velocity, ν is the kinematic viscosity, and e is the evaporation rate. The film thickness can be directly measured during casting. Thus, drying curves can be used to understand changes in viscosity of solutions during casting and to relate differences in drying behavior to the final film morphology. The evaporation rate can be extracted from the slope toward the end of the drying process, and the viscosity can be determined from the slope of the drying curve at early times.

The drying curves for ^{892k}PS/PI/*o*-xylene blends of various concentrations are shown in Figure 3-7. The relative viscosity, given by the ratio of the solution viscosity to the solvent viscosity, evaporation rate, and the drying time increased with polymer concentration. Changes in drying time were influenced by a shift in the balance between the viscosity and evaporation. Increasing the viscosity results in less solution loss during outflow. Thus, the film thickness increased with concentration. The domain size also increased with solution concentration, likely resulting in the proximity to the two phase region.

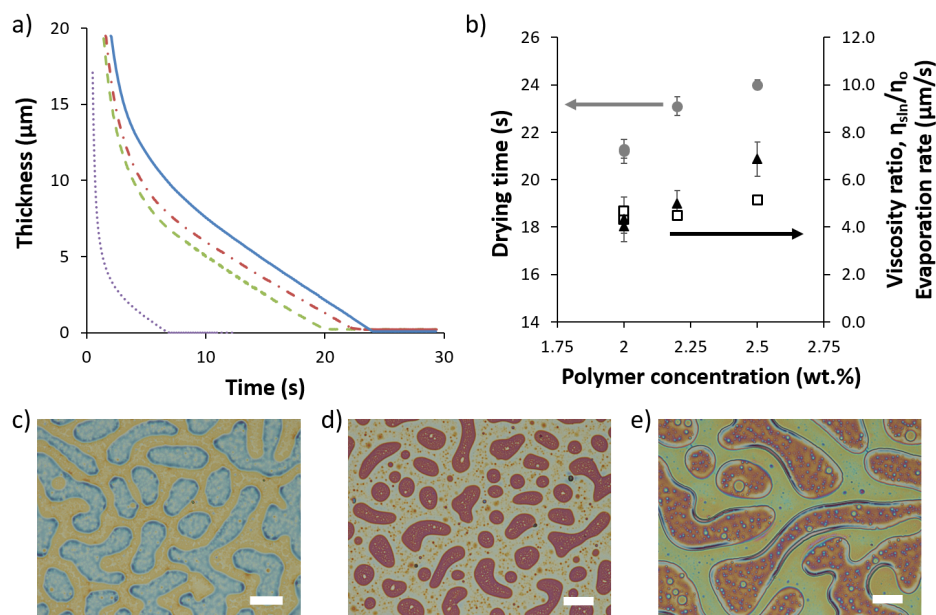


Figure 3-7. a) Drying curves for $^{892k}\text{PS}_{50}/\text{PI}_{50}$ mixtures in *o*-xylene with an initial solution concentration of 0.0 wt. % (dot), 2.0 wt.% (dash), 2.2 wt.% (dot-dash), and 2.5 wt.% (solid) polymer with respect to *o*-xylene. b) Drying time (●), initial solution viscosity (▲) relative to the solvent viscosity, and evaporation rate (□). The relative viscosity and evaporation rate increased with solution concentration. c) – e) optical micrographs of the resulting PS₅₀/PI₅₀ films cast from c) 2.0 wt.%, d) 2.2 wt.%, and e) 2.5 wt.% polymer. The scale bars represent 20 μm.

Similarly, the changes in $^{17k}\text{PS}/^{33k}\text{PMMA}$ films can be monitored using the drying behavior. As with the $^{892k}\text{PS}/\text{PI}$ films, the relative viscosity increased with the polymer concentration in solution. The drying time also increased with increasing wt.% polymer. In comparison to $^{892k}\text{PS}/\text{PI}$, which had a droplet/co-continuous morphology, the $^{17k}\text{PS}/^{33k}\text{PMMA}$ films formed a bilayer (see also Appendix C, Figure C-5) when cast from 5.0 wt.% or 9.0 wt.% solution. The films cast from 0.9 wt.% $^{17k}\text{PS}/^{33k}\text{PMMA}$ in *o*-xylene had a droplet type structure; however, the films were very thin at this concentration (~30 nm). Although *o*-xylene is a nearly neutral solvent for

PS/PI, it is selective for PS in PS/PMMA blends. Thus, during casting, the free surface is preferential to PS, which produces a top PS layer over the PMMA. This result is consistent with the selectivity of the silicon substrate for.⁶¹ The evaporation rate for $^{17}\text{kPS}/^{33}\text{kPMMA}$ also decreased with concentration, whereas it increased with polymer concentration in the PS/PI system. The morphology evolution could be contributing to the differences in the evaporation rates.

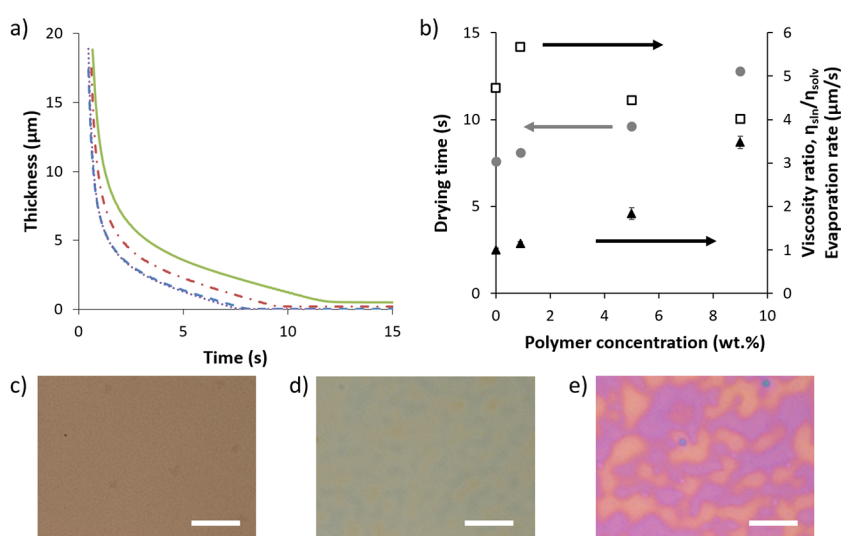


Figure 3-8. Effect of concentration on the drying and film morphology. a) Drying curves for $^{17}\text{kPS}_{50}/^{33}\text{kPMMA}_{50}$ solutions cast at 1500 rpm with initial solution concentrations of 0 wt.% (dot), 0.9 wt.% (dash), 5 wt.% (dot-dash), and 9 wt.% (solid). b) Drying time (●), relative viscosity (▲), and evaporation rate (□) as a function of polymer concentration. With increasing polymer concentration, the relative viscosity increased, and the evaporation rate decreased. As expected, the drying time increased with viscosity and solution concentration.

In addition to the concentration, the molecular weight of the polymers can be modified to change the structure in the films. Increasing the molecular weight should

produce more incompatibility in the polymer/polymer/solvent mixture. Thus, at the same initial concentration, a higher molecular weight mixture will be closer to the two phase region. The average degree of polymerization in these mixtures, $\langle N \rangle$ is given by the geometric mean of the homopolymer degrees of polymerization ($\langle N \rangle = [N_{PS}N_{PMMA}]^{1/2}$). Blends with higher $\langle N \rangle$ had increased viscosity relative to *o*-xylene and increased drying time. The evaporation rate decreased with increasing $\langle N \rangle$, regardless of the structure that formed in the film. This suggests that the change in evaporation rate is independent of morphology and is more related to the material (PMMA vs. PI).

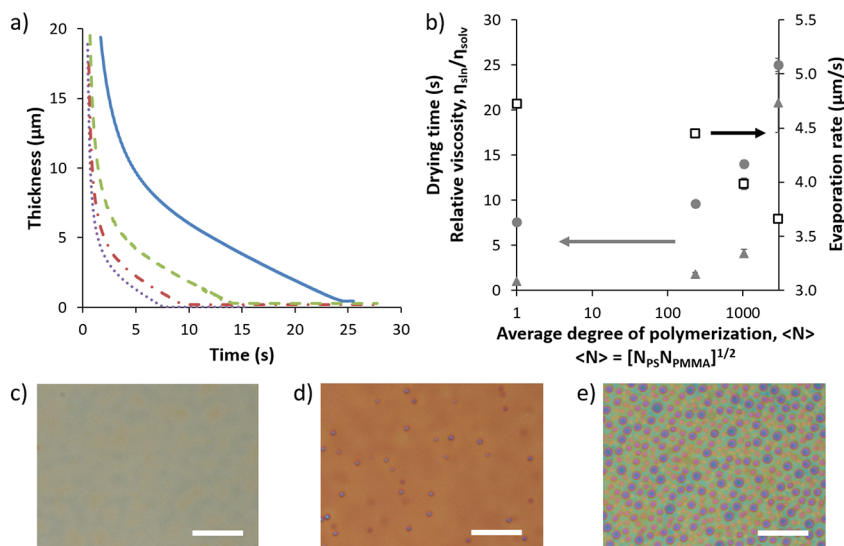


Figure 3-9. Effect of molecular weight on the drying behavior and film morphology. The average degree of polymerization, $\langle N \rangle$ is calculated by the geometric mean of the individual degrees of polymerization of the homopolymers. a) Drying curves for *o*-xylene (dot, $\langle N \rangle = 1$), $\langle N \rangle = 230$ (dot dash), $\langle N \rangle = 1028$ (dash), and $\langle N \rangle = 2929$ (solid). b) Increasing the degree of polymerization increased the drying time (●) and initial solution viscosity (▲). The evaporation rate (□) decreased with increasing $\langle N \rangle$. Optical micrographs of the films cast from c) $\langle N \rangle = 230$, d) $\langle N \rangle = 1028$, and e) $\langle N \rangle = 2929$ show the appearance of structure with the highest molecular weight combination. With increasing $\langle N \rangle$, the morphology evolved from stratified (bilayer, c) to droplet structures (e).

A third polymer mixture was studied to determine the relationship between evaporation rate and initial solution viscosity. The effect of concentration is shown in Figure 3-10 for 17k PS/P3HT blends. Three different solution concentrations (0.0 wt.%, 0.9 wt.%, and 1.75 wt.% 17k PS₅₀/P3HT₅₀ with respect to *o*-xylene) were tested with three spin speeds (800 rpm, 1500 rpm, and 2000 rpm). The spin speed range was selected to independently change the evaporation rate and the solution viscosity. The evaporation rate is proportional to the square root of the angular velocity, $\omega^{1/2}$.⁶⁰ Thus,

increasing the spin speed [$\omega = \text{spin speed } (2\pi)/60$] increases the evaporation rate. Increasing the solution concentration (viscosity) at the same spin speed produced a longer drying time and decreased the evaporation rate. It is important to note that the relative viscosity for 0.9 wt.% was less than 1; this effect could be the result of temperature variation in the lab between experimental days. Increasing the spin speed (evaporation rate) reduced the drying time and had no effect on the measured relative viscosity. Thus, the evaporation rate does not directly affect the viscosity, but the concentration controls both viscosity and evaporation rate. Additionally, it is evident that the differences in polymer type can influence the evaporation rate (for P3HT and PI, $e \sim \eta_r$; for PMMA, $e \sim 1/\eta_r$). It is possible that these differences come from the glass transition temperature, T_g , of the materials. Both PI and P3HT have T_g 's around or below ambient temperature ($T_{g,\text{PI}} = -72 \text{ }^\circ\text{C}$;¹⁶ $T_{g,\text{P3HT}} \sim 10 \text{ }^\circ\text{C}$ ⁶²), whereas the T_g for PMMA is much higher ($\sim 100 \text{ }^\circ\text{C}$).¹⁶ Thus, the solvent likely becomes trapped in the PMMA at the higher concentrations, which would reduce the apparent evaporation rate compared to the rubbery materials.

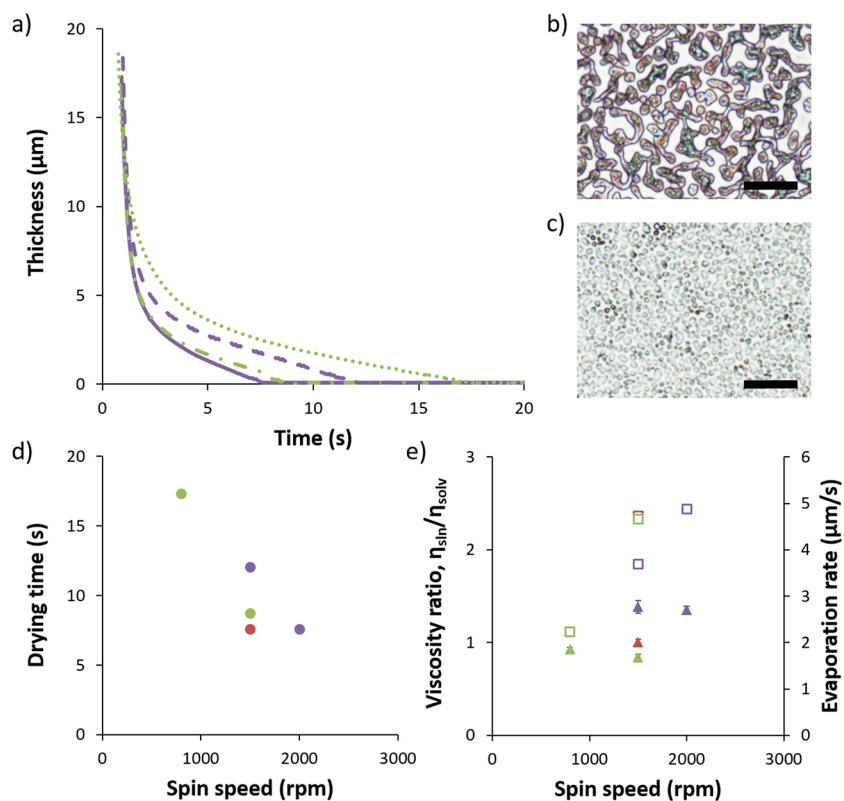


Figure 3-10. Effect of spin speed and concentration on drying behavior. The same initial solution is used to cast 17k PS/P3HT (1.75 wt.% in *o*-xylene) at 1500 rpm (dashed) and 2000 rpm (solid). A lower concentration solution (0.9 wt.% in *o*-xylene) is also cast at 800 rpm (dot) and 1500 rpm (dot-dash). Optical micrographs of the film morphologies are shown for the film cast from 1.75 wt.% 17k PS/P3HT in *o*-xylene at b) 1500 rpm and c) 2000 rpm. The scale bar represents 10 μm. d) Drying time for *o*-xylene (●), 0.9 wt.% 17k PS/P3HT (●), and 1.75 wt.% 17k PS/P3HT (●). The drying time decreased with increasing spin speed and decreasing solution concentration. e) The relative viscosity (\blacktriangle), η_r , calculated for the same initial solution concentration was independent of spin speed. η_r increased with concentration. The evaporation rates (\square) increased with spin speed and decreased with concentration.

In addition to extracting the viscosity and evaporation rate, the spin coating model can also be used to compare the predicted evolution to the physical drying

behavior. At short times, the concentration does not change significantly. Additionally, because the viscosity only plays a role in the drying behavior during outflow, during which film loss is due to flow of solution off of the wafer (the first few seconds of drying), assuming a constant composition is reasonable. This model accurately captures the drying behavior for $^{17k}\text{PS}/^{33k}\text{PMMA}$, but fails to describe the change in film thickness for $^{110k}\text{PS}/^{100k}\text{PMMA}$. The higher molecular weight blend should phase separate at a lower concentration (earlier time). Upon phase separation, if it occurs during outflow, deviation from the spin coating model would be expected, as the viscosity increases due the formation of structure.^{63, 64}

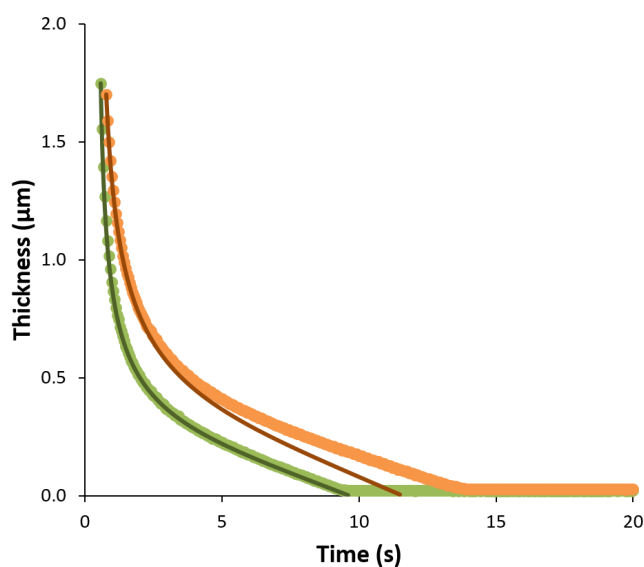


Figure 3-11. Drying curves for $^{17k}\text{PS}/^{33k}\text{PMMA}$ (●) and $^{110k}\text{PS}/^{100k}\text{PMMA}$ (●) compared to the spin coating model with a constant viscosity fit (solid lines). The lower molecular weight is fit well by a constant viscosity, which suggests that the viscosity does not increase appreciably during outflow. In comparison to $^{17k}\text{PS}/^{33k}\text{PMMA}$, the drying behavior for $^{110k}\text{PS}/^{100k}\text{PMMA}$ is not well captured by a constant viscosity. Thus, the higher molecular weight blend has a significant increase in viscosity during casting, which could be due the earlier onset of phase separation.

Because differences can be seen in systems for which the viscosity changes, it was of interest to study a more complex blend. For ^{17k}PS/P3HT, the drying behavior relative to the model is shown in Figure 3-12. The expected time (concentration) at which phase separation should occur is indicated by the dotted lines. In comparison to the ^{17k}PS/PMMA films, the spin coating model does not agree with experimental results, even at low concentrations. This result suggests that the viscosity increases significantly for this low molecular weight mixture.

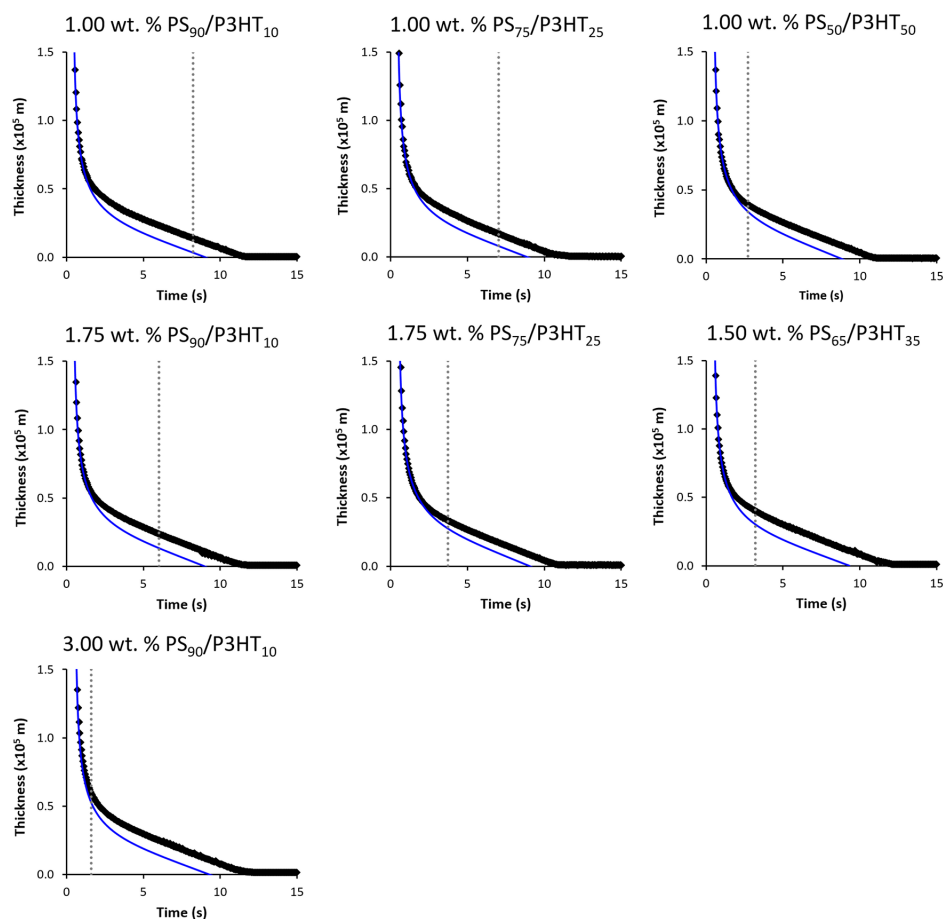


Figure 3-12. Drying curves for PS/P3HT films at various initial solution concentrations and relative polymer ratios. The black diamonds are the experimental data, the blue solid line is the spin coating model developed by Meyerhofer,⁶⁰ and the dotted gray line represents the onset of phase separation predicted by the phase diagram.

In all cases, the predicted onset of phase separation occurs after the model deviates from the measured drying behavior. This is likely due to the crystallization/gelation phenomena of P3HT, which would give rise to a rapid increase in viscosity.^{47, 54, 58, 59} Because P3HT gelation has multiple steps, the timescales of gelation are important. Huang and coworkers measured the gelation of various P3HT

($M_n \sim 41$ kg/mol) solutions in *o*-xylene and found the gelation time was on the order of weeks at room temperature for concentrations below 2 wt.% P3HT.⁵⁹ Whether gelation occurs and the time scales for gelation are strongly dependent on molecular weight; for a 1 wt.% lower molecular weight P3HT ($M_n \sim 13.0$ kg/mol) solution prepared with *o*-xylene, gelation did not occur within 24 h, whereas the same concentrations of higher molecular weight P3HTs gelled within minutes ($M_n \sim 34.4$ kg/mol) and too quickly to measure ($M_n \sim 62.5$ kg/mol).⁴⁷ The gelation time also decreases with concentration.⁵⁹ In the transmission study (Section 3.3.2.2.1), gelation in ¹⁷kPS/P3HT occurred within an hour at higher solution concentrations. The earlier gelation during casting suggests that the processing influences this gelation mechanism. Thus, understanding what happens to the solution during these time scales can provide valuable insight into the evolution of structure during casting.

3.4.2 Stroboscopic Illumination

Measuring the morphological evolution in time can provide insight into the phase behavior in multicomponent mixtures. For polymer blend films being quenched into the two-phase region, the size scales of the structures can be determined using light scattering, x-ray scattering, and optical microscopy techniques.^{21-23, 25, 26, 28, 33, 50, 65-85} Many of these studies were focused on thermal quenches; however, processing in thin films typically uses solution deposition methods. The evolution of the film morphology during casting (solvent removal) in polymer blend solutions has been studied using stroboscopic illumination, which provides visualization of the morphology evolution during casting with optical microscopy.^{21, 22, 33, 50, 82-84} Howse and coworkers have studied the phase separation in polymer blend systems during casting (solvent removal) for both spin coating and blade coating geometries.^{21, 22, 33, 50,}

⁸³ Using stroboscopic illumination, they were able to capture the morphological evolution in thin films with sub-second resolution. Though the phase separation likely represents the late stages of phase separation, once the film has begun to solidify, these studies provide key insights into the development of structure during processing.

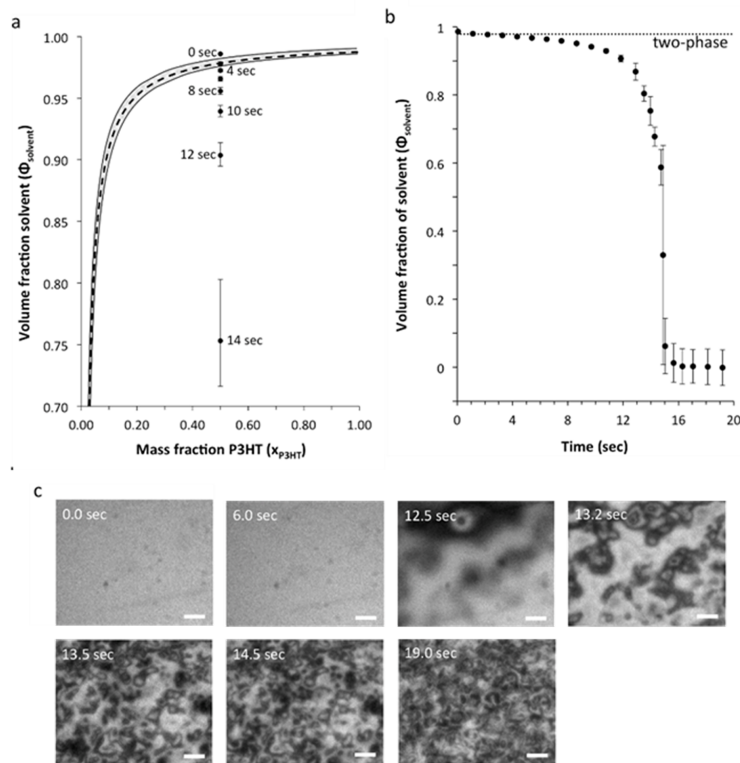


Figure 3-13. a) Spinodal (dashed line) curve for a 1.75 wt.% $^{17k}\text{PS}_{50}/\text{P3HT}_{50}$ blends in *o*-xylene plotted as volume fraction of solvent vs. the mass fraction of P3HT. The shaded region between the solid lines indicates the error in the calculated spinodal line, determined via error propagation from the interaction parameters. Time points indicate solvent volume fraction in the film during spin coating at 1500 rpm and are spaced temporally by 2 s. Reprinted with permission from Emerson, J. A., *et al. Macromolecules* 2013, 46 (16), 6533-6540. Copyright 2013 American Chemical Society. b) Full profile of solvent volume fraction vs. time during spin coating of PS/P3HT blend from *o*-xylene with critical volume fraction (dotted line) shown. The data points represent an average of the solvent volume fraction in the film from 4 drying curves based on the final film thickness, and the error bars indicate the standard deviation. c) Optical images from synchronized stroboscopic illumination after initial loading of solution (0.0 s), before visible onset of phase separation (6.0 s), during the onset of visible phase separation (12.5 s), throughout the blend phase separation (13.2 s, 13.5 s, 14.5 s), and of the final film (19.0 s). The dark regions are P3HT-rich, and the light regions are PS-rich. The scale bar represents 10 μm .

Though much of this work has been focused on spin coating, these techniques can be extended readily to blade and bar coating methods. Once the initial solution layer is deposited by the bar (or blade), the film drying occurs by evaporation only. Thus, the change in film thickness is constant with time. Figure 3-14 shows a series of microscopy images obtained at various times during bar coating from a 5 wt.% ^{327k}PS₃₀/^{529k}PMMA₇₀ solution along with the change in film thickness and concentration in time. The spreading bar moved from left to right aligned vertically with the blade. The macroscopic onset of phase separation occurred at 3.1 s (7.3 wt.%). Using the mid-range parameter values reported in literature ($\chi_{toluene-PMMA} = 0.43$, $\chi_{toluene-PS} = 0.36$, $\chi_{PS-PMMA} = 0.007$) gave the best agreement with the experimental onset of phase separation.

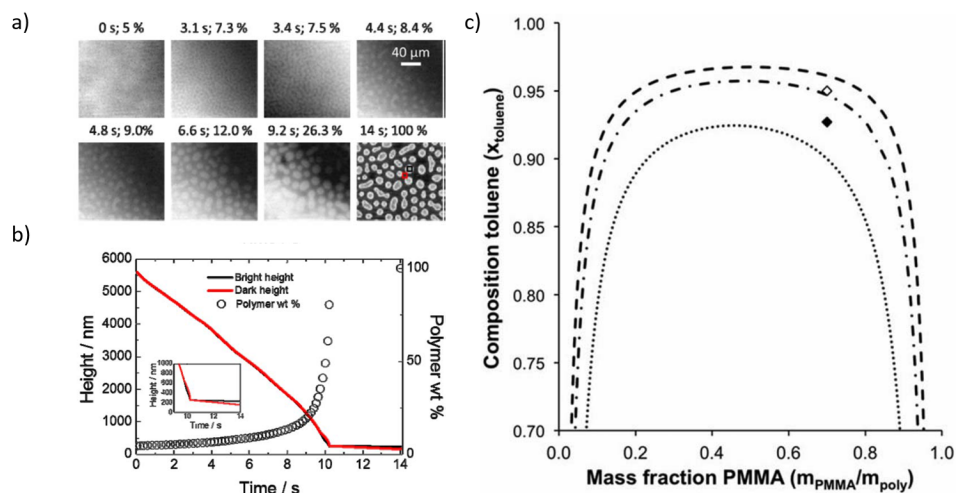


Figure 3-14. a) Optical reflectance images recorded during bar-coating of a 5 wt.% PS₃₀/PMMA₇₀ blend in toluene (blade speed of 20 mm s⁻¹) from toluene. The 0 s frame is taken immediately after the bar has left the field of view (direction of travel was left to right). b) Drying curves and concentration changes in time for the bar spreading experiments. c) Spinodal curves for PMMA/PS in toluene determined from reported interaction parameters for $\chi_{\text{toluene-PMMA}}$, $\chi_{\text{toluene-PS}}$, and $\chi_{\text{PS-PMMA}}$ (dash: $\chi_{\text{toluene-PMMA}} = 0.45$, $\chi_{\text{toluene-PS}} = 0.38$, $\chi_{\text{PS-PMMA}} = 0.010$; dash-dot: $\chi_{\text{toluene-PMMA}} = 0.43$, $\chi_{\text{toluene-PS}} = 0.36$, $\chi_{\text{PS-PMMA}} = 0.007$; dot: $\chi_{\text{toluene-PMMA}} = 0.40$, $\chi_{\text{toluene-PS}} = 0.34$, and $\chi_{\text{PS-PMMA}} = 0.004$). The open and closed diamonds represent the composition for the initial bar-spread blend (5 wt.%) and the concentration at which phase separation began experimentally (7.3 wt.%), respectively. Reprinted with permission from Haq, E. U., *et al. J. Polym. Sci. Part B: Polym. Phys.* 2014, 52 (15), 985-992. Copyright 2014 Wiley Periodicals, Inc.

Stroboscopic illumination can provide valuable insights into the phase separation process; however, it requires custom equipment to capture the images. Additionally, the structures detected by stroboscopic illumination must be visible under the set magnification. As discussed for PS/P3HT, these smaller structures may contribute to deviations from the spin coating model. Thus, further understanding of the nano- and microstructure during casting is necessary to fully elucidate the

relationship between thermodynamics, kinetics, and processing of polymer blend films.

3.5 Conclusions

Polymer blends are of interest in a plethora of functional coatings, which are produced by solution deposition methods. The morphology of the resulting film impacts the material performance. Thus, controlling the structure in polymer blend films allows for targeting desired structures in these multicomponent systems. In this chapter, the relationship between the equilibrium phase diagram and phase evolution during processing of polymer blend solutions was explored.

A robust protocol was developed to measure the solvent-polymer Flory-Huggins interaction parameters. These χ_{s-p} values were used to determine the solubility parameters. PS was used to validate the experimental setup and procedure; the experimentally determined χ_{s-p} and δ were in good agreement with literature values. The methodology was applied to measure the interactions and solubility parameters for P3HT. δ was then used to predict the phase behavior in polymer/polymer/solvent mixtures. The resulting phase diagrams were validated experimentally by determining the binodal curve, which supported the theoretical spinodal curve.

Insights into the drying behavior also were developed. From the drying curves, viscosity, evaporation rate, and drying time could be extracted for various polymer blend solutions during casting. In particular, these parameters can be used to model the drying behavior and determine deviations from the predicted film thinning. Increases in viscosity due to gelation or phase separation manifested as differences between the spin coating model and experimental drying behavior. These results

demonstrate that drying curves can be a useful tool to inform the initial solution conditions and phase separation behaviors during casting.

Stroboscopic illumination was applied to track the morphological evolution during casting. These results allow for understanding of the structural development at the later stages of phase separation and the solidification and kinetic trapping of the polymer films. The methods described in this chapter can be applied to a variety of polymer systems. However, further understanding of the development of nano- and microstructure is required to relate the thermodynamics, kinetics, and processing of polymer blend films, which is discussed in more detail in Chapter 7.

REFERENCES

1. Fabiano, S.; Himmelberger, S.; Drees, M.; Chen, Z.; Altamimi, R. M.; Salleo, A.; Loi, M. A.; Facchetti, A. C., Charge transport orthogonality in all-polymer blend transistors, diodes, and solar cells. *Adv. Energy Mater.* **2014**, *4* (6), 1301409.
2. Yu, G.; Nishino, H.; Heeger, A. J.; Chen, T. A.; Rieke, R. D., Enhanced electroluminescence from semiconducting polymer blends. *Synth. Met.* **1995**, *72* (3), 249-252.
3. Javier, A. E.; Patel, S. N.; Hallinan, D. T.; Srinivasan, V.; Balsara, N. P., Simultaneous electronic and ionic conduction in a block copolymer: application in lithium battery electrodes. *Angew. Chem. Int. Ed.* **2011**, *50* (42), 9848-9851.
4. Müller-Buschbaum, P.; Ittner, T.; Maurer, E.; Körstgens, V.; Petry, W., Pressure-sensitive adhesive blend films for low-tack applications. *Macromol. Mater. Eng.* **2007**, *292* (7), 825-834.
5. Nunes-Pereira, J.; Costa, C. M.; Lanceros-Mendez, S., Polymer composites and blends for battery separators: state of the art, challenges and future trends. *J. Power Sources* **2015**, *281*, 378 - 398.
6. Colaneri, N. F.; Schacklette, L. W., EMI shielding measurements of conductive polymer blends. *IEEE Trans. Instrum. Meas.* **1992**, *41* (2), 291-297.
7. Walheim, S.; Schäffer, E.; Mlynek, J.; Steiner, U., Nanophase-separated polymer films as high-performance antireflection coatings. *Science* **1999**, *283* (5401), 520.
8. Rubinstein, M.; Colby, R. H., *Polymer Physics*. Oxford University Press: New York, 2003.
9. Bates, F. S., Polymer-polymer phase behavior. *Science* **1991**, *251* (4996), 898.
10. Bansil, R., Phase separation in polymer solutions and gels. *J. Phys. IV France* **1993**, *03* (C1), C1-225-C1-235.

11. Scott, R. L., The thermodynamics of high polymer solutions. V. Phase equilibria in the ternary system: polymer 1 – polymer 2 – solvent. *J. Chem. Phys.* **1949**, *17* (3), 279-284.
12. Toolan, D. T. W.; Haq, E. u.; Dunbar, A.; Ebbens, S.; Clarke, N.; Topham, P. D.; Howse, J. R., Direct observation of morphological development during the spin-coating of polystyrene–poly(methyl methacrylate) polymer blends. *J. Polym. Sci., Part B: Polym. Phys.* **2013**, *51* (11), 875-881.
13. Flory, P. J., *Principles of Polymer Chemistry*. Cornell University Press: Ithaca, 1953.
14. Scott, R. L., The thermodynamics of high polymer solutions. IV. Phase equilibria in the ternary system: polymer-liquid 1-liquid 2. *J. Chem. Phys.* **1949**, *17* (3), 268-279.
15. Scott, R. L., Thermodynamics of high polymer solutions. VI. The compatibility of copolymers. *J. Polym. Sci.* **1952**, *9* (5), 423-432.
16. Brandrup, J.; Immergut, E. H.; Grulke, E. A., *Polymer Handbook*. 4th ed.; Wiley: New York, 1999.
17. Emerson, J. A.; Toolan, D. T. W.; Howse, J. R.; Furst, E. M.; Epps, T. H., III, Determination of solvent-polymer and polymer-polymer Flory-Huggins interaction parameters for poly(3-hexylthiophene) via solvent vapor swelling. *Macromolecules* **2013**, *46* (16), 6533-6540.
18. Bornside, D. E.; Macosko, C. W.; Scriven, L. E., On the modeling of spin coating. *Journal of Imaging Technology* **1987**, *13* (4), 122-130.
19. van Krevelen, D. W.; Nijenhuis, K. T., *Properties of Polymers - Their Correlation with Chemical Structure; Their Numerical Estimation and Prediction from Additive Group Contributions*. 4 ed.; Elsevier: Amsterdam, 2009.
20. Miller-Chou, B. A.; Koenig, J. L., A review of polymer dissolution. *Prog. Polym. Sci.* **2003**, *28* (8), 1223-1270.
21. Toolan, D. T. W.; Howse, J. R., Development of in situ studies of spin coated polymer films. *J. Mater. Chem. C* **2013**, *1* (4), 603-616.

22. Haq, E. U.; Toolan, D. T. W.; Emerson, J. A.; Epps, T. H., III; Howse, J. R.; Dunbar, A. D. F.; Ebbens, S. J., Real time laser interference microscopy for bar-spread polystyrene/poly(methyl methacrylate) blends. *J. Polym. Sci., Part B: Polym. Phys.* **2014**, *52* (15), 985-992.
23. Sung, L.; Karim, A.; Douglas, J. F.; Han, C. C., Dimensional crossover in the phase separation kinetics of thin polymer blend films. *Phys. Rev. Lett.* **1996**, *76* (23), 4368-4371.
24. Karim, A.; Slawacki, T. M.; Kumar, S. K.; Douglas, J. F.; Satija, S. K.; Han, C. C.; Russell, T. P.; Liu, Y.; Overney, R.; Sokolov, O.; Rafailovich, M. H., Phase-separation-induced surface patterns in thin polymer blend films. *Macromolecules* **1998**, *31* (3), 857-862.
25. Wang, H.; Composto, R. J., Hydrodynamic-flow-driven wetting in thin film polymer blends: growth kinetics and morphology. *Phys. Rev. E* **2000**, *61* (2), 1659-1663.
26. Wang, H.; Composto, R. J., Thin film polymer blends undergoing phase separation and wetting: identification of early, intermediate, and late stages. *J. Chem. Phys.* **2000**, *113* (22), 10386-10397.
27. Walheim, S.; Boltau, M.; Mlynek, J.; Krausch, G.; Steiner, U., Structure formation via polymer demixing in spin-cast films. *Macromolecules* **1997**, *30* (17), 4995-5003.
28. Hashimoto, T.; Sasaki, K.; Kawai, H., Time-resolved light scattering studies on the kinetics of phase separation and phase dissolution of polymer blends. 2. Phase separation of ternary mixtures of polymer A, polymer B, and solvent. *Macromolecules* **1984**, *17* (12), 2812-2818.
29. Albert, J. N. L.; Young, W. S.; Lewis, R. L.; Bogart, T. D.; Smith, J. R.; Epps, T. H., III, Systematic study on the effect of solvent removal rate on the morphology of solvent vapor annealed ABA triblock copolymer thin films. *ACS Nano* **2012**, *6* (1), 459-466.
30. Cavicchi, K. A.; Russell, T. P., Solvent annealed thin films of asymmetric polyisoprene-poly(lactide) diblock copolymers. *Macromolecules* **2007**, *40* (4), 1181-1186.
31. Elbs, H.; Krausch, G., Ellipsometric determination of flory-huggins interaction parameters in solution. *Polymer* **2004**, *45* (23), 7935-7942.

32. Manoli, K.; Goustouridis, D.; Chatzandroulis, S.; Raptis, I.; Valamontes, E. S.; Sanopoulou, M., Vapor sorption in thin supported polymer films studied by white light interferometry. *Polymer* **2006**, *47* (17), 6117-6122.
33. Ebbens, S.; Hodgkinson, R.; Parnell, A. J.; Dunbar, A.; Martin, S. J.; Topham, P. D.; Clarke, N.; Howse, J. R., In situ imaging and height reconstruction of phase separation processes in polymer blends during spin coating. *ACS Nano* **2011**, *5* (6), 5124-5131.
34. Barton, A. F. M., *Handbook of Polymer-Liquid Interaction Parameters and Solubility Parameters*. Taylor & Francis: 1990.
35. Maranas, J. K.; Mondello, M.; Grest, G. S.; Kumar, S. K.; Debenedetti, P. G.; Graessley, W. W., Liquid structure, thermodynamics, and mixing behavior of saturated hydrocarbon polymers. 1. Cohesive energy density and internal pressure. *Macromolecules* **1998**, *31* (20), 6991-6997.
36. Graessley, W. W.; Krishnamoorti, R.; Reichart, G. C.; Balsara, N. P.; Fetters, L. J.; Lohse, D. J., Regular and irregular mixing in blends of saturated hydrocarbon polymers. *Macromolecules* **1995**, *28* (4), 1260-1270.
37. Muller, M., Miscibility behavior and single chain properties in polymer blends: a bond fluctuation model study. *Macromol. Theory Simul.* **1999**, *8* (4), 343-374.
38. Jaczewska, J.; Raptis, I.; Budkowski, A.; Goustouridis, D.; Raczowska, J.; Sanopoulou, A.; Pamula, E.; Bernasik, A.; Rysz, J., Swelling of poly(3-alkylthiophene) films exposed to solvent vapors and humidity: evaluation of solubility parameters. *Synth. Met.* **2007**, *157* (18-20), 726-732.
39. Albert, J. N. L.; Bogart, T. D.; Lewis, R. L.; Beers, K. L.; Fasolka, M. J.; Hutchison, J. B.; Vogt, B. D.; Epps, T. H., III, Gradient solvent vapor annealing of block copolymer thin films using a microfluidic mixing device. *Nano Lett.* **2011**, *11* (3), 1351-1357.
40. Stamatialis, D. F.; Wessling, M.; Sanopoulou, M.; Strathmann, H.; Petropoulos, J. H., Optical vs. direct sorption and swelling measurements for the study of stiff-chain polymer-penetrant interactions. *J. Membr. Sci.* **1997**, *130* (1-2), 75-83.
41. Bawn, C. E. H.; Wajid, M. A., High polymer solutions part 7.-Vapour pressure of polystyrene solutions in acetone, chloroform, and propyl acetate. *Trans. Faraday Soc.* **1956**, *52* (12), 1658-1664.

42. Scholte, T. G., Determination of thermodynamic parameters of polymer-solvent systems by light scattering. *Eur. Polym. J.* **1970**, *6* (8), 1063-1074.
43. Machui, F.; Abbott, S.; Waller, D.; Koppe, M.; Brabec, C. J., Determination of solubility parameters for organic semiconductor formulations. *Macromol. Chem. Phys.* **2011**, *212* (19), 2159-2165.
44. Zen, A.; Saphiannikova, M.; Neher, D.; Asawapirom, U.; Scherf, U., Comparative study of the field-effect mobility of a copolymer and a binary blend based on poly(3-alkylthiophene)s. *Chem. Mater.* **2005**, *17* (4), 781-786.
45. Kim, J. Y.; Noh, S.; Nam, Y. M.; Kim, J. Y.; Roh, J.; Park, M.; Amsden, J. J.; Yoon, D. Y.; Lee, C.; Jo, W. H., Effect of nanoscale SubPc interfacial layer on the performance of inverted polymer solar cells based on P3HT/PC71BM. *ACS Appl. Mater. Interfaces* **2011**, *3* (11), 4279-4285.
46. Heffner, G. W.; Pearson, D. S., Molecular characterization of poly(3-hexylthiophene). *Macromolecules* **1991**, *24* (23), 6295-6299.
47. Koppe, M.; Brabec, C. J.; Heiml, S.; Schausberger, A.; Duffy, W.; Heeney, M.; McCulloch, I., Influence of molecular weight distribution on the gelation of P3HT and its impact on the photovoltaic performance. *Macromolecules* **2009**, *42* (13), 4661-4666.
48. Jaczewska, J.; Budkowski, A.; Bernasik, A.; Moons, E.; Rysz, J., Polymer vs solvent diagram of film structures formed in spin-cast poly(3-alkylthiophene) blends. *Macromolecules* **2008**, *41* (13), 4802-4810.
49. Lu, G.; Tang, H.; Qu, Y.; Li, L.; Yang, X., Enhanced electrical conductivity of highly crystalline polythiophene/insulating-polymer composite. *Macromolecules* **2007**, *40* (18), 6579-6584.
50. Emerson, J. A.; Toolan, D. T. W.; Howse, J. R.; Furst, E. M.; Epps, T. H., III, Determination of solvent-polymer and polymer-polymer Flory-Huggins interaction parameters for poly(3-hexylthiophene) via solvent vapor swelling. *Macromolecules* **2013**, *46* (16), 6533-6540.
51. Kapnistos, M.; Hinrichs, A.; Vlassopoulos, D.; Anastasiadis, S. H.; Stammer, A.; Wolf, B. A., Rheology of a lower critical solution temperature binary polymer blend in the homogeneous, phase-separated, and transitional regimes. *Macromolecules* **1996**, *29* (22), 7155-7163.

52. Bae, Y. C.; Lambert, S. M.; Soane, D. S.; Prausnitz, J. M., Cloud-point curves of polymer solutions from thermo-optic measurements. *Macromolecules* **1991**, *24* (15), 4403-4407.
53. Boutris, C.; Chatzi, E. G.; Kiparissides, C., Characterization of the LCST behaviour of aqueous poly(N-isopropylacrylamide) solutions by thermal and cloud point techniques. *Polymer* **1997**, *38* (10), 2567-2570.
54. Newbloom, G. M.; Weigandt, K. M.; Pozzo, D. C., Electrical, mechanical, and structural characterization of self-assembly in poly(3-hexylthiophene) organogel networks. *Macromolecules* **2012**, *45* (8), 3452-3462.
55. Newbloom, G. M.; de la Iglesia, P.; Pozzo, L. D., Controlled gelation of poly(3-alkylthiophene)s in bulk and in thin-films using low volatility solvent/poor-solvent mixtures. *Soft Matter* **2014**, *10* (44), 8945-8954.
56. Newbloom, G. M.; Kim, F. S.; Jenekhe, S. A.; Pozzo, D. C., Mesoscale morphology and charge transport in colloidal networks of poly(3-hexylthiophene). *Macromolecules* **2011**, *44* (10), 3801-3809.
57. Newbloom, G. M.; Weigandt, K. M.; Pozzo, D. C., Structure and property development of poly(3-hexylthiophene) organogels probed with combined rheology, conductivity and small angle neutron scattering. *Soft Matter* **2012**, *8* (34), 8854-8864.
58. Xu, W. T.; Tang, H. W.; Lv, H. Y.; Li, J.; Zhao, X. L.; Li, H.; Wang, N.; Yang, X. N., Sol-gel transition of poly(3-hexylthiophene) revealed by capillary measurements: phase behaviors, gelation kinetics and the formation mechanism. *Soft Matter* **2012**, *8* (3), 726-733.
59. Huang, W. Y.; Lee, C. C.; Hsieh, T. L., The role of conformational transitions on the performance of poly(3-hexylthiophene)/fullerene solar cells. *Sol. Energy Mater. Sol. Cells* **2009**, *93* (3), 382-386.
60. Meyerhofer, D., Characteristics of resist films produced by spinning. *J. Appl. Phys.* **1978**, *49* (7), 3993-3997.
61. Albert, J. N. L.; Baney, M. J.; Stafford, C. M.; Kelly, J. Y.; Epps, T. H., III, Generation of monolayer gradients in surface energy and surface chemistry for block copolymer thin film studies. *ACS Nano* **2009**, *3* (12), 3977-3986.
62. Trinh Tung Ngo and Duc Nghia Nguyen and Van Tuyen, N., Glass transition of PCBM, P3HT and their blends in quenched state. *Adv. Nat. Sci.: Nanosci. Nanotechnol.* **2012**, *3* (4), 045001.

63. Dondos, A.; Skondras, P.; Pierri, E.; Benoît, H., Hydrodynamic crossover in two-polymer mixtures from viscosity measurements. *Die Makromolekulare Chemie* **1983**, *184* (10), 2153-2158.
64. Qiu, Y.-R.; Ouyang, W., Rheological behavior of poly(vinyl butyral)/polyethylene glycol binary systems. *Materials Science and Engineering: C* **2012**, *32* (2), 167-171.
65. Bruder, F.; Brenn, R., Spinodal decomposition in thin films of a polymer blend. *Phys. Rev. Lett.* **1992**, *69* (4), 624.
66. Jones, R. A. L.; Norton, L. J.; Kramer, E. J.; Bates, F. S.; Wiltzius, P., Surface-directed spinodal decomposition. *Phys. Rev. Lett.* **1991**, *66* (10), 1326.
67. Li, L.; Shen, X.; Hong, S. W.; Hayward, R. C.; Russell, T. P., Fabrication of co-continuous nanostructured and porous polymer membranes: spinodal decomposition of homopolymer and random copolymer blends. *Angew. Chem. Int. Ed.* **2012**, *51* (17), 4089-4094.
68. Wang, H.; Composto, R. J., Understanding morphology evolution and roughening in phase-separating thin-film polymer blends. *Europhys. Lett.* **2000**, *50* (5), 622-627.
69. Yang, Y. P.; Xiao, Z. G.; Jiang, X.; Sheng, J., Light scattering studies on phase behavior of PP/PcBR blends during melt-mixing. *J. Macromol. Sci., Part B: Phys.* **2006**, *45* (6), 1083-1098.
70. Lefebvre, A. A.; Lee, J. H.; Balsara, N. P.; Vaidyanathan, C., Determination of critical length scales and the limit of metastability in phase separating polymer blends. *J. Chem. Phys.* **2002**, *117* (19), 9063-9073.
71. Lefebvre, A. A.; Lee, J. H.; Balsara, N. P.; Hammouda, B., Critical length and time scales during the initial stages of nucleation in polymer blends. *J. Chem. Phys.* **2002**, *116* (12), 4777-4781.
72. Wang, H.; Composto, R. J., Kinetics of surface and interfacial fluctuations in phase separating polymer blend films. *Macromolecules* **2002**, *35* (7), 2799-2809.
73. Chung, H.-J.; Composto, R. J., Breakdown of dynamic scaling in thin film binary liquids undergoing phase separation. *Phys. Rev. Lett.* **2004**, *92* (18), 185704.

74. Wang, Z.; Wang, H.; Shimizu, K.; Dong, J.-Y.; Hsiao, B. S.; Han, C. C., Structural and morphological development in poly (ethylene-co-hexene) and poly (ethylene-co-butylene) blends due to the competition between liquid–liquid phase separation and crystallization. *Polymer* **2005**, *46* (8), 2675-2684.
75. Jukes, P. C.; Heriot, S. Y.; Sharp, J. S.; Jones, R. A. L., Time-resolved light scattering studies of phase separation in thin film semiconducting polymer blends during spin-coating. *Macromolecules* **2005**, *38* (6), 2030-2032.
76. Ogawa, H.; Kanayac, T.; Nishida, K.; Matsuba, G., Phase separation and dewetting in polymer blend thin films. *Eur. Phys. J.: Spec. Top.* **2007**, *141* (1), 189-192.
77. Gelles, R.; Frank, C. W., Effect of molecular weight on polymer blend phase separation kinetics. *Macromolecules* **1983**, *16* (9), 1448-1456.
78. Krausch, G.; Dai, C. A.; Kramer, E. J.; Marko, J. F.; Bates, F. S., Interference of spinodal waves in thin polymer films. *Macromolecules* **1993**, *26* (21), 5566-5571.
79. Ermi, B. D.; Karim, A.; Douglas, J. F., Formation and dissolution of phase-separated structures in ultrathin blend films. *J. Polym. Sci., Part B: Polym. Phys.* **1998**, *36* (1), 191-200.
80. Wang, H.; Douglas, J. F.; Satija, S. K.; Composto, R. J.; Han, C. C., Early-stage compositional segregation in polymer-blend films. *Phys. Rev. E* **2003**, *67* (6), 061801.
81. Snyder, H. L.; Meakin, P.; Reich, S., Dynamical aspects of phase separation in polymer blends. *Macromolecules* **1983**, *16* (5), 757-762.
82. Toolan, D. T. W.; Dunbar, A.; Ebbens, S.; Clarke, N.; Topham, P. D.; Howse, J. R., Direct observation of morphological development during the spin-coating of polystyrene–poly (methyl methacrylate) polymer blends. *J. Polym. Sci., Part B: Polym. Phys.* **2013**, *51* (11), 875-881.
83. Toolan, D. T. W.; Pullan, N.; Harvey, M. J.; Topham, P. D.; Howse, J. R., *In situ* studies of phase separation and crystallization directed by marangoni instabilities during spin-coating. *Adv. Mater.* **2013**, *25* (48), 7033-7037.
84. Heriot, S. Y.; Jones, R. A. L., An interfacial instability in a transient wetting layer leads to lateral phase separation in thin spin-cast polymer-blend films. *Nat. Mater.* **2005**, *4* (10), 782-786.

85. Zhang, H.; Takeoka, S., Morphological evolution within spin-cast ultrathin polymer blend films clarified by a freestanding method. *Macromolecules* **2012**, *45* (10), 4315-4321.

Chapter 4

TUNING MORPHOLOGY IN POLYMER BLEND NANOCOMPOSITE FILMS *VIA* SOLVENT SELECTIVITY

4.1 Introduction

Polymer blend nanocomposites (PBNC) are of interest for a variety of applications, such as optical materials,¹ electronic devices,²⁻⁴ and radiation shielding.⁵⁻⁷ These materials benefit from the hierarchical structure provided by the polymer blend as well as the functionality of the nanoparticles. Additionally, PBNCs typically have more stable morphologies than the neat polymer blends, due the jammed or pinned structure, which makes them less affected by further processing (annealing).⁸⁻⁹ However the polymer blend phase separation is affected by the incorporation of nanoparticles.¹⁰⁻¹⁶ The effect of particle incorporation on polymer blend morphology has been studied by experiment,¹⁷⁻²¹ simulation,²²⁻²⁴ and theory.²⁵⁻²⁶ The nanoparticle partitioning within the polymer blend nanocomposites has an effect on the material properties, such as the electrical conductivity. Boiteux and coworkers found that iron particles dispersed into the poly(propylene) [PP] phase of a PP/polyamide composite had a lower electrical percolation threshold with the same total conductivity than iron in either homopolymer.²⁷ As such, the position of the nanoparticles within the domain is key to understanding the effect of the filler on the properties. The relationship between the particle loading, processing, and resulting morphology in these PBNCs is not well-studied due to the wide and varied experimental parameter space.²⁸

Within the polymer blend nanocomposites, nanoparticles can localize in two regions: (1) at the polymer-polymer interface or (2) in the polymer domain. Nanoparticles at the interface stabilize (kinetically trap) the morphology by jamming the interface, which can reduce the domain size; nanoparticles within the domain slow domain growth during phase separation.¹⁹ Additionally, percolation of nanoparticles within a domain can also cause jamming.^{27, 29-30} Researchers have studied the effect of surface/brush chemistry^{21, 31} and brush length³¹ on nanoparticle partitioning in polymer blend nanocomposites. Using deuterated poly(methyl methacrylate) [dPMMA]/poly(styrene-*ran*-acrylonitrile) [SAN] blends, Composto and coworkers found that modifying the end group (Cl vs. H terminated PMMA) on the particle ligand (PMMA) changed the preference of the location of the silica nanospheres from within the PMMA domain to the PMMA/SAN interface.³¹ Regardless of the surface chemistry, the nanoparticles were initially dispersed in the composites, and the PBNCs required annealing to produce the more energetically favorable structures. This work demonstrated that the particle-polymer interactions and the processing of the films influenced the nanoparticle partitioning. However, processing was only used to produce the more energetically favorable structures and was not considered explicitly.

The studies described above were focused on the effect of loading and ligand on the PBNC morphology in the dry state. The influence of processing on polymer blend nanocomposites has not been studied previously. To produce PBNCs in film geometries, solvent deposition is required. In this chapter, the effect of processing on polymer blend nanocomposites will be explored using the drying time and solvent selectivity to modify the casting behavior.

4.2 Materials & Methods

4.2.1 Materials

Polymers. Polystyrene ([PS], $M_n = 892$ kg/mol, $\bar{D} = 1.04$) was purchased from Scientific Polymer Products. Polyisoprene ([PI], $M_n = 541$ kg/mol, $\bar{D} = 1.13$, 95% 1,4) was synthesized by anionic polymerization in cyclohexane using *sec*-butyllithium (*sec*-BuLi) as an initiator. PS-thiol ([PS-SH], $M_n = 1.6$ kg/mol, $\bar{D} = 1.04$, ~20 % -SH) also was synthesized anionically in cyclohexane with *sec*-BuLi initiator; ethylene sulfide was used to end-cap the PS with a thiol group. Poly(acrylic acid) [PAA] (25 wt.% in water) with an approximate molecular weight of 240 kg/mol was purchased from Acros Organics.

Solvents. *o*-xylene (puriss, p.a.), propylene glycol monomethyl ether acetate [PGMEA] (> 99.5%), and anisole were obtained from Sigma-Aldrich. Toluene (certified ACS), *n*-hexane (optima), isopropanol (certified ACS), and methanol (certified ACS) were purchased from Fisher Scientific. *cis*-Decalin (> 98%) was purchased from TCI America. Chloroform-*d* (99.8+ atom% D, 0.03 v/v% TMS) from Acros Organics was used for proton nuclear magnetic resonance (^1H NMR) experiments. All solvents were used as received.

Gold Particles. Hydrogen tetrachloroaurate trihydrate ($\geq 99.9\%$) and sodium borohydride were purchased from Fisher Scientific. Cetyl trimethyl ammonium bromide ([CTAB], $\geq 99.9\%$) was purchased from Sigma. MilliQ water (18 Ω) was obtained from a Millipore Direct Q5 system.

4.2.2 Gold Particle Synthesis & Characterization

The gold particles were synthesized using the seed-mediated growth method developed by El-Sayed and coworkers.³² The specific protocol is described in detail

in Chapter 2. The particles were characterized with UV-Vis Spectroscopy and transmission electron microscopy. As-synthesized gold particles were stabilized with CTAB in water. This ligand was replaced with PS-SH to transfer the particles to organic solutions, following the procedure outlined in Chapter 2. Complete ligand exchange was confirmed using proton nuclear magnetic resonance spectroscopy (^1H NMR); after transferring the particles to the organic phase, there was no evidence of CTAB in the ^1H NMR. Particles were stored in toluene at room temperature and dried down using rotary evaporation before use. Note: the PS-AuNPs re-suspended readily in organic solvents after drying.

4.2.2.1 UV-Vis Spectroscopy

UV-Vis spectroscopy was performed on the gold nanoparticle reaction mixtures in water using an Agilent 8453 UV-Vis spectrophotometer equipped with a diode array detector (190 nm - 1100 nm). The gold concentration in solution was ~ 1 mM.

4.2.2.2 Transmission Electron Microscopy (TEM)

Transmission electron microscopy (TEM) was used to image the gold nanoparticles. Gold nanoparticle samples were prepared on lacey carbon 300 mesh Cu grids (Ted Pella). ~ 0.03 mL of the nanoparticle reaction mixture were placed on the grid surface, left for 5 s, and removed through the bottom of the grid. A JEOL 3010 TEM was operated at 300 kV to collect the micrographs.

4.2.3 Blend Film Preparation

Stock solutions of the polymer blend in *o*-xylene were made at 2.0 wt.%, 2.2 wt.%, and 2.5 wt.% polymer with respect to solvent with 1:1 ratio of PS to PI,

hereafter denoted as PS₅₀/PI₅₀. To create PBNCs, the stock solutions were added to dried PS-AuNPs to reach a target loading (1 vol.%, 2 vol.%, 9 vol.%). Films were cast onto pre-cleaned silicon wafer pieces by spin coating. All films were cast at 1500 rpm for 60 s. Drying curves were collected as described in Chapter 2.

4.2.4 Film Characterization

The structure of the polymer blend and PBNC films was determined by optical microscopy and atomic force microscopy. From optical microscopy, the domain size was characterized using Image J's "Analyze particle" routine on binary images.

4.2.4.1 Optical Microscopy (OM)

Bright field microscopy (reflection and transmission mode) and polarized light microscopy (transmission mode) were used to image the films on silicon wafers and glass substrates. Bright field optical micrographs were captured using a Nikon Eclipse LV100 microscope with a Prioroptiscan II control box and a Nikon DS-Fi1 connected to a Nikon Digital Sight in transmission and reflection mode. Polarized light microscopy images were captured using a high-speed camera (Phantom v5.1, Vision Research) attached to an inverted microscope (Axiovert 200, Zeiss) with 585 ± 20 nm bandpass filter (Chroma Technology Corp., Bellows Falls, VT). The cross-polarizer setup is described elsewhere.³³

4.2.4.2 Atomic Force Microscopy (AFM)

Atomic force micrographs were captured with a Veeco Nanoscope V Dimension 3100 operated in tapping mode. The film morphologies were imaged using silicon probes (tap150) with a force constant of 5 N/m and resonant frequencies between 120 kHz and 180 kHz.

4.2.4.3 Transmission Electron Microscopy (TEM)

Polymer blend and polymer blend nanocomposite films were peeled off of the silicon wafer substrate using PAA. Immediately prior to peeling, the films were submerged in liquid nitrogen. The peeled films were floated in water, which dissolves the PAA, and collected onto a lacey carbon TEM grid. The films were imaged at 300 kV.

4.3 Results & Discussion

The goal of this work is to elucidate the effect of processing on polymer blend nanocomposites. A model PS/PI blend with gold nanorods was used. The processing is characterized by the drying behavior during casting will be explored using the drying time and solvent selectivity to modify the casting behavior.

4.3.1 Gold Particles

Gold nanoparticles were characterized by UV-Vis and TEM. The UV-Vis traces for the gold nanoparticles are shown in Figure 4-1. The spherical particles have a single peak at 520 nm, which corresponds to a radius of ~ 15 nm. The nanorods have two peaks: one for the transverse plasmon resonance (520 nm), which corresponds to the diameter of the particle, and the second for the longitudinal plasmon absorption (765 nm), which is related to the aspect ratio of the particle.^{32, 34} The plasmon resonances for the gold nanorods correspond to a diameter of ~ 15 nm and an aspect ratio of ~ 3 . These values are in agreement with the average diameter and aspect ratio from TEM, which are 9 ± 2 nm \times 27 ± 5 nm, respectively.

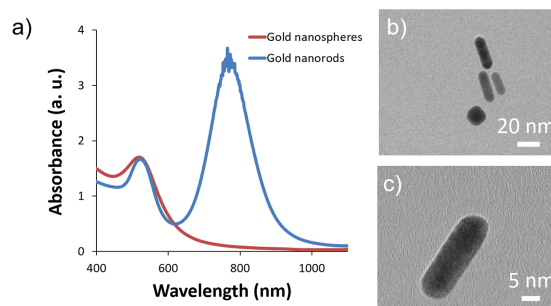


Figure 4-1. a) UV-Vis spectroscopy of gold nanorods (blue) and gold nanospheres (red). TEM micrographs of gold nanorods are shown in b) and c). The average particle size was 9 ± 2 nm by 27 ± 5 nm.

4.3.2 Drying Behavior

The effect of processing was characterized using the drying curves, as described in Chapter 3, section 3.4.1. Sample drying curves for the polymer blend nanocomposites cast from *o*-xylene (neutral) and *cis*-decalin (PI-selective) solutions are shown in Figure 4-2. For films cast from three different initial polymer concentration solutions in *o*-xylene (2.0 wt.%, 2.2 wt.%, 2.5 wt.%), the drying time decreased with the addition of polystyrene-capped gold nanorods (PS-AuNR). The films cast from *cis*-decalin had the same drying behavior without and with nanorods.

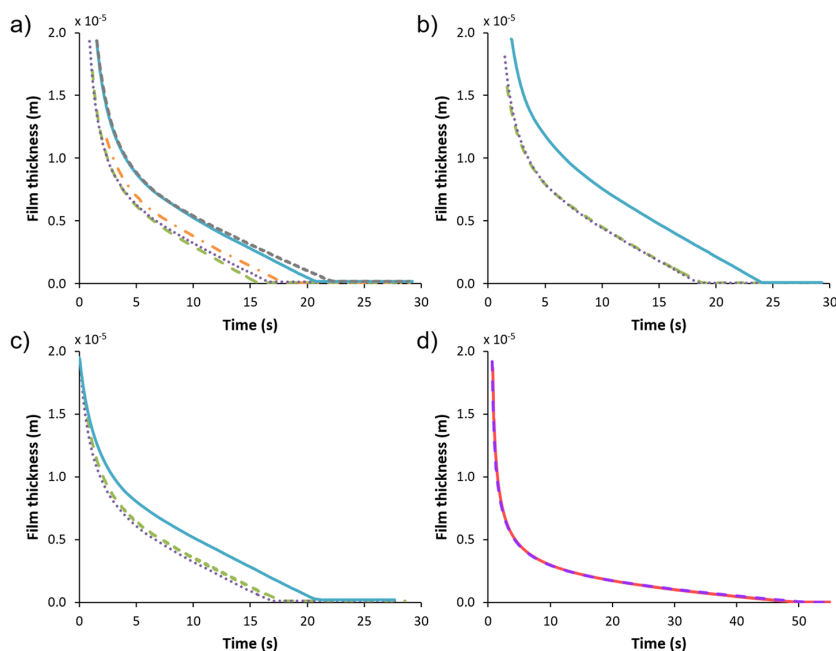


Figure 4-2. a)-c) Drying curves for PS₅₀/PI₅₀ films with in initial solution concentrations of a) 2.0 wt.%, b) 2.2 wt.%, and c) 2.5 wt.% polymer with respect to *o*-xylene. The neat samples (solid line) had the longest drying time. Solutions containing 1 vol.% (purple, dotted line), 2 vol.% (green, dashed line), and 9 vol.% (orange, dot-dashed line) PS-capped gold nanorods (PS-AuNR). In a) the short dashes represent the drying curve for 1 vol.% PS-capped gold nanospheres (PS-AuNS) with the same radius as the nanorods (see also Figure 4-1). d) Drying curve for PS₅₀/PI₅₀ film with an initial solution concentration of 1.0 wt.% (solid line) and with 2 vol.% PS-AuNR (dashed line).

As discussed in Chapter 3, the drying curves can provide valuable insight into the viscosity of the mixture. The drying time, which is a product of the competition between outflow (viscosity) and evaporation (solvent choice) can be determined from the drying curves. A summary of the drying times can be found in Figure 4-3a. The drying time increased with polymer concentration in *o*-xylene. Additionally, adding nanoparticles decreased the drying time. This effect is partially due to changes in

solution viscosity upon particle addition, which shifted the balance between the outflow and evaporation regimes. As described in Chapter 2, the initial solution viscosity can be estimated from the slope of the drying curve at short times, during which the concentration does not change appreciably. The ratio of the PBNC solution viscosity to the PB solution viscosity is shown in Figure 4-3b. Adding PS-AuNR to solutions of PS₅₀/PI₅₀ in *o*-xylene decreased the viscosity at all polymer concentrations by ~40%. However, the PS-AuNS drying behavior was consistent with the neat blend casting for both the drying time and relative viscosity. In comparison to the *o*-xylene drying behavior, the drying time for *cis*-decalin did not change with 2 vol.% PS-AuNR loading. This behavior also is evidenced in the viscosity – there was no change in the estimated viscosity upon particle loading. Thus, the casting behavior of PS₅₀/PI₅₀ in *cis*-decalin was not influenced significantly by the particle addition.

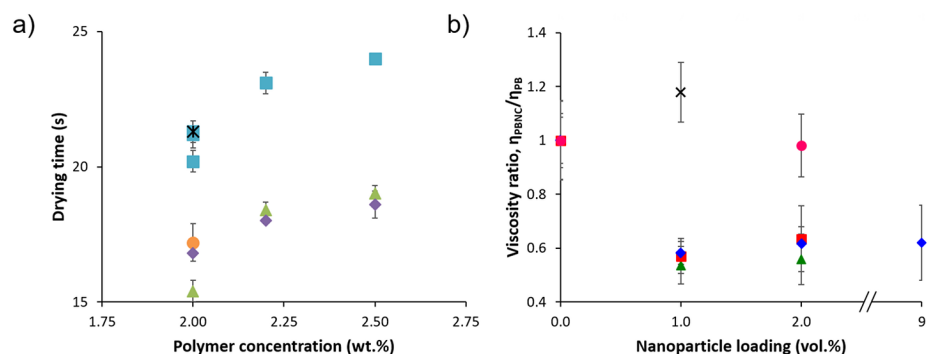


Figure 4-3. a) Summary of the drying behavior for PS₅₀/PI₅₀ in *o*-xylene (■) with 1 vol.% (◆), 2 vol.% (▲), and 9 vol.% (●) PS-AuNR or 1 vol.% (×) PS-AuNS. It took solutions with higher polymer contents longer to dry. Drying times for decalin cast films are not shown. The decalin cast films had a drying time of ~51 s at 1 wt.% PS₅₀/PI₅₀, which did not change with the 2 vol.% particle loading. At the same loading and initial polymer concentration, the nanorods reduced the drying time, whereas the nanospheres had the same drying time as the neat solution. In all cases, adding nanorods reduced the drying time. b) Ratio of the nanocomposite solution viscosity, η_{PBNC} , to the polymer blend solution viscosity η_{PB} from the same stock solution for *o*-xylene solutions with 2.0 wt.% (◆), 2.2 wt.%, (■) and 2.5 wt.% (▲) PS₅₀/PI₅₀. with PS-AuNR. 2.0 wt.% PS₅₀/PI₅₀. with PS-AuNS in *o*-xylene (×) and 1 wt.% PS₅₀/PI₅₀ with 2 vol.% PS-AuNR in *cis*-decalin (●).

4.3.3 Morphology Changes

As discussed in the previous sections, the processing is impacted by the incorporation of nanoparticles into the polymer blend. For most films, the drying time and the solution viscosities decreased upon PS-AuNR addition (see Figure 4-3). Decreasing the viscosity shifts the balance between the outflow and evaporation regime, producing changes the drying time (quench rate). The slowing of phase evolution with nanoparticle addition has been reported in literature, which can also affect the morphology.^{19, 27, 29-30} Thus, it is of interest to study these effects on the film morphology.

4.3.3.1 “Neutral” Solvent-cast Nanocomposites

Films cast from *o*-xylene, which is a nearly neutral solvent for PS and PI, were strongly influenced by the nanoparticle loading. The optical morphology of these films at the concentrations and loadings tested are shown in Figure 4-4. From the optical micrographs, the apparent domain size decreased with particle loading.

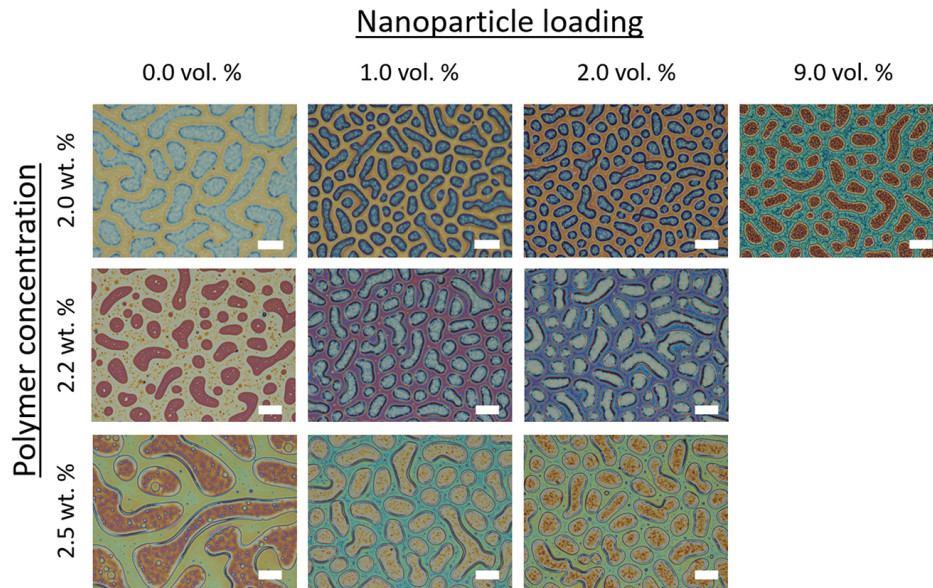


Figure 4-4. Optical micrographs of polymer blends and polymer blend nanocomposites on silicon wafers imaged using the Nikon microscope under bright field illumination operated in transmission mode. The color variation in the optical micrographs is related to both the film thickness and nanoparticle loading. The scale bar represents 20 μm .

The chord length distributions for the films shown in Figure 4-4 are plotted in Figure 4-5. Comparing the neat polymer blends, the chord length distribution broadened with increasing initial polymer concentration. As discussed in Chapter 3, Section 4.4.1 (Figure 4.7), the viscosity increased with polymer concentration, which

would provide slower phase separation dynamics and increase the drying time. However, increasing the concentration brings the initial composition closer to the two phase region, which would produce phase separation earlier in the drying process. The competition between these two effects produced larger domain structures. Due to the increase in solids content, the film thickness also increased with polymer concentration.

The distribution of chord length narrows with particle loading. In comparison to the neat films, an addition of PS-AuNR significantly shifts the size distribution to smaller domains. In the 2.0 wt.% PS/PI blends with 9 vol.% PS-AuNR, the chord length is slightly greater than the 1 vol.% or 2 vol.% loadings. This effect is likely due to a slight reduction in the solution viscosity, despite the increased solids content.

The domain circularity also increased with particle loading. Because the domain shapes in all of the films were asymmetric, it is unlikely that the particles provided a nucleation site by which nucleation and growth was supported. Thus, the structural evolution likely progressed to later stages, during which the domains were pinched off into droplet structures. Future studies on the evolution of the morphology during casting could elucidate the exact mechanism.

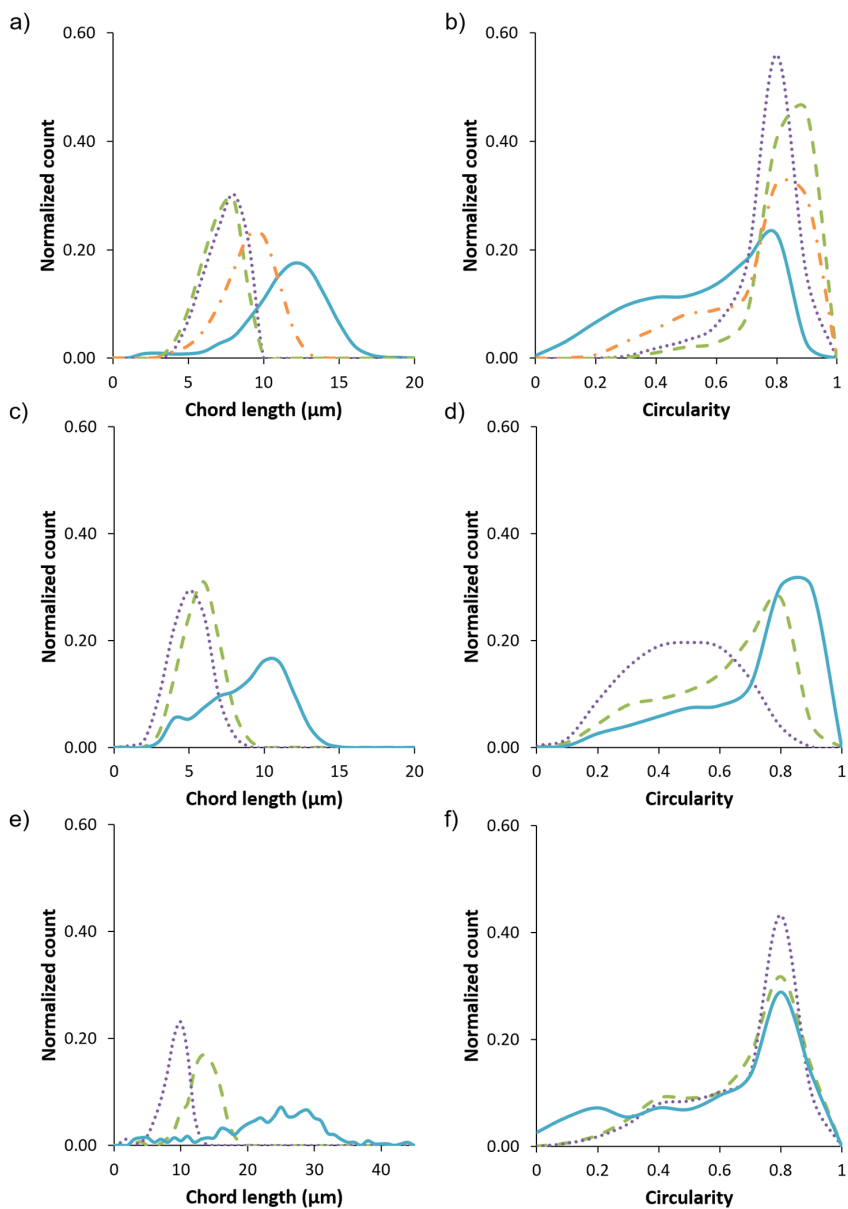


Figure 4-5. a, c, e) Chord length and b, d, f) circularity for PS₅₀/PI₅₀ (solid) with 1 vol.% (dotted), 2 vol.% (dashed), and 9 vol.% (dot-dashed line) gold nanoparticles. The initial polymer content was a, b) 2.0 wt.%, c, d) 2.2 wt.%, e, f) 2.5 wt.%. With nanoparticle loading, the chord length distribution became more uniform compared to the neat films. The peak domain circularity increased and the distribution narrowed with particle loading.

From the optical micrographs and domain characterization, it is evident that nanoparticles produce a change in the domain size and shape. However, the change in chord length and circularity for the blend films can only be directly compared in materials for which the droplet phase is the same polymer for quantification of the shape change. To confirm the domain assignment in these films, the AFM height images were used, shown in Figure 4-6.

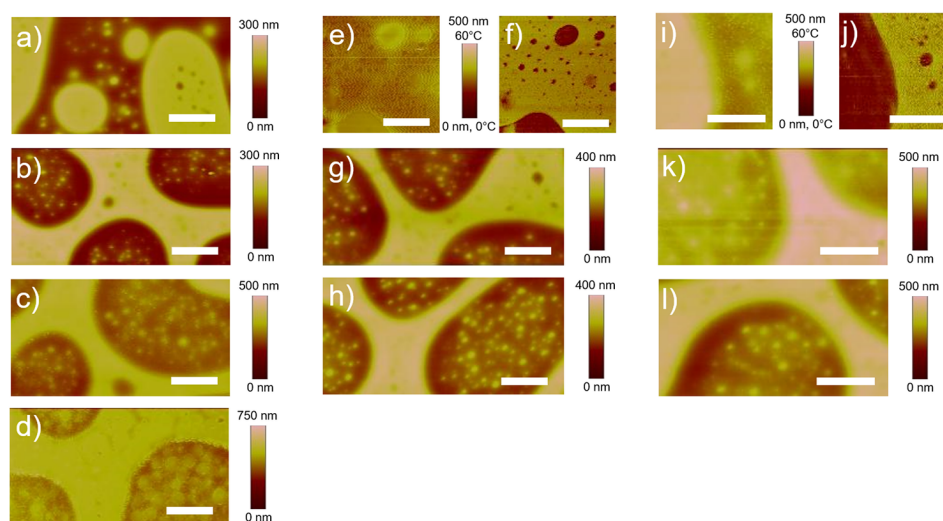


Figure 4-6. AFM images of 2.0 wt.% (a-d), 2.2 wt.% (e-h), and 2.5 wt.% (i-l) for neat (a, e, f, i, j), 1 vol.% (b, g, k), 2 vol.% (c, h, l), and 9 vol.% (d). All micrographs are height images, with the exception of f) and j), which are phase images. The scale bars represent 10 μm . Note that a) depicts the inverted domain structure of PS₅₀/PI₅₀ cast from 2.0 wt.% solution.

From the AFM height micrographs, PS should be the taller phase (lighter in color), as it will solidify first during casting. All of the nanoparticle-containing films had PS matrix and PI droplets. The neat films shown in Figure 4-6 all had an inverted phase structure (PS droplets in PI matrix). It is worth noting that the 2.0 wt.%

PS₅₀/PI₅₀ films in Figure 4-6 had an inverted phase structure, whereas other films cast at the same concentration and spin speed, such as the films shown in Figure 4-4, had the same structure as the nanoparticle-containing film (PS droplets in PI matrix). Chapter 3. Briefly, the phase inversion in the polymer systems occurs due to the progression of phase separation. The shift in chord length and circularity for the normal and inverted phase structure in films cast from the same initial concentration in the absence of nanoparticles can be seen in Figure 4-7. As such, the changes in domain size and circularity do not fully reflect the effect of the nanoparticles on the film if the droplet phases are not composed of the same polymer (the area coverage of PS and PI are unequal due to the relative height differences).

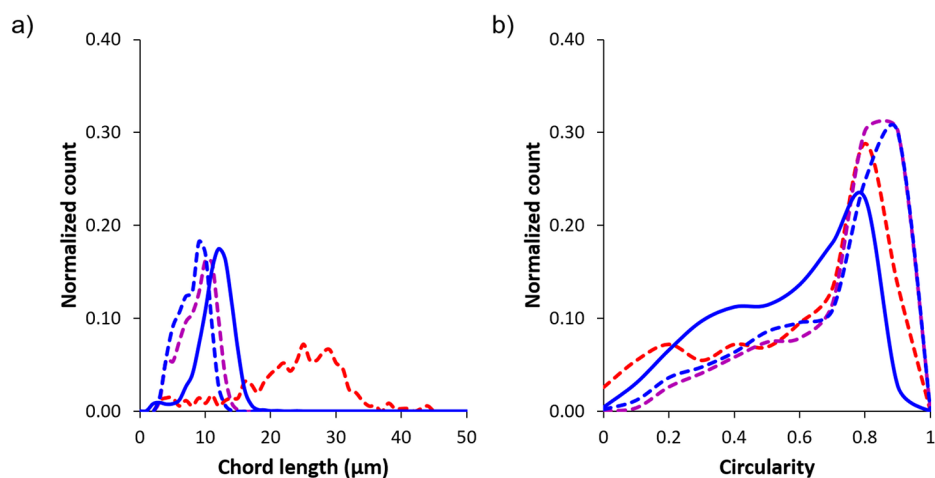


Figure 4-7. Chord length and circularity for 2.0 wt.% PS₅₀/PI₅₀ with the normal (blue, solid) and inverted (blue, dashed) phase structure. Chord length and circularity for 2.2 wt.% (purple, dashed) and 2.5 wt.% PS₅₀/PI₅₀ (red, dashed) films with inverted domain structure.

Comparing the solid and dashed blue lines, which correspond to normal and inverse phase structure, respectively, for films cast from 2.0 wt.% PS₅₀/PI₅₀ solution, the chord length and circularity are shifted based on the film structure. However, the chord length distributions still shift to larger sizes with increased polymer concentration. Thus, despite the discrepancy in the droplet phase material in the inverted structures of the neat polymer films in comparison to the nanocomposite films, it is evident that the domain size is still changed upon particle addition. Selective washing with *n*-hexane and PGMEA was used to confirm the domain assignment for the films cast from 2.0 wt.% PS₅₀/PI₅₀ solutions. *n*-Hexane was used to remove the PI phase and PGMEA was used to remove the PS phase.

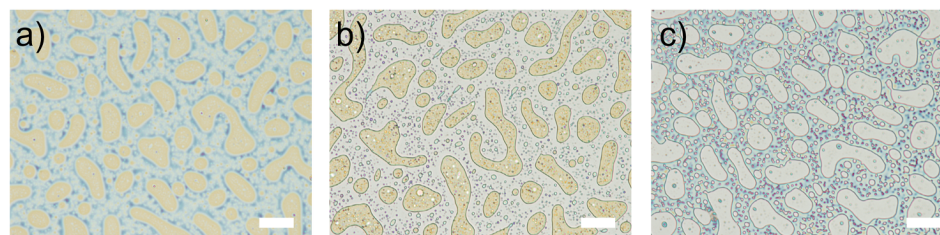


Figure 4-8. Optical micrographs for a) 2.0 wt.% PS₅₀/PI₅₀ as-cast films and films washed with b) *n*-hexane (PI removed), c) PGMEA (PS removed). The film shown here had the inverted domain structure, for which the droplets were PS and the matrix was PI. Scale bars represent 20 μm .

The film thickness was determined by AFM scratch testing. The heights of the PS and PI domains to the substrate were measured and are shown in Figure 4-9. Film thickness increased with polymer concentration. Low particle loadings did not significantly change the film thickness, regardless of the initial polymer concentration.

Films containing 9 vol.% particle loading (only for 2.0 wt.% polymer) were thicker than the other films.

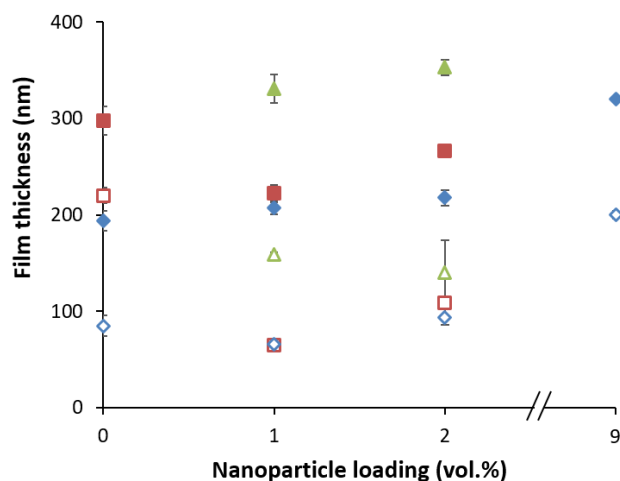


Figure 4-9. Domain thickness for PS (closed symbols) and PI (open symbols) in films cast from 2.0 wt.% (◆), 2.2 wt.% (■), and 2.5 wt.% (▲) PS₅₀/PI₅₀ in *o*-xylene.

4.3.3.2 PI-selective Solvent-cast Nanocomposites

cis-Decalin was used as the PI selective solvent (see Appendix E, Figure E-1 for the relative swelling behavior of PS and PI). In comparison to the *o*-xylene cast films, the drying behavior (see Figure 4-2 and Figure 4-3) of films cast from *cis*-decalin was not influenced by the addition of 2 vol.% PS-AuNR. The lack of sensitivity in the film drying to particle addition suggests that the morphology should not appreciably change unless the particle significantly compatibilizes the blend, given that the solution viscosity, drying time, and concentration are the same. The optical micrographs, chord length distributions, and circularity distributions are shown in Figure 4-10. The chord length remained unchanged upon particle loading, and the

domain circularity increased slightly. This effect suggests that the nanoparticles did not significantly influence the drying behavior in the PS/PI/*cis*-decalin solution.

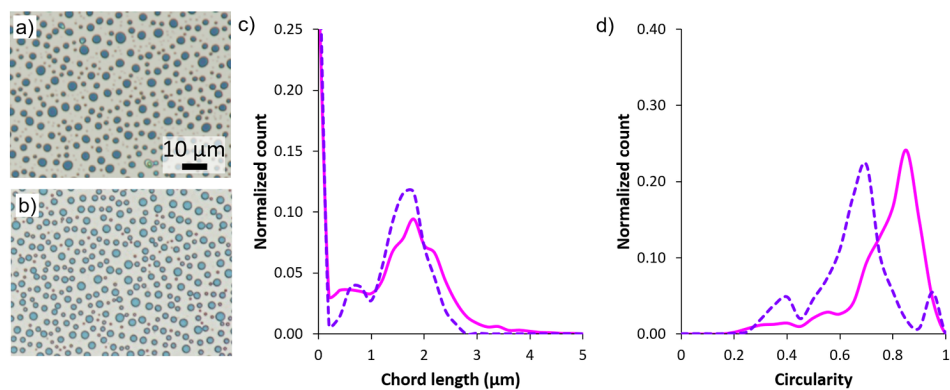


Figure 4-10. Morphology of PS/PI films cast from decalin for the a) neat and b) 2 vol.% nanorods on silicon wafers. Distribution of the c) chord length ($\pi A/p$) and d) circularity ($4\pi A/p^2$) for the neat (solid) and 2 vol.% nanorod loading (dashed). The circularity increased slightly with increasing particle loading, but the chord length did not change.

The domain assignment in the films cast from *cis*-decalin was confirmed with AFM height images before and after washing with *n*-hexane (remove PI) or acetone (remove PS). The droplet phase is PS in both samples. The thickness of the PI layer was on the order of 10 nm, whereas the PS domain height was greater than 100 nm

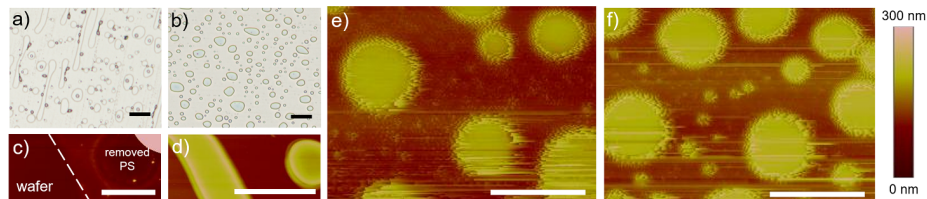


Figure 4-11. Optical micrographs for PS₅₀/PI₅₀ films cast from *cis*-decalin washed with a) acetone and b) *n*-hexane washed films. The scale bars on the optical micrographs represent 20 μm. AFM height images for the c) acetone and d) *n*-hexane washed films. e) AFM height images of PS₅₀/PI₅₀ films cast from *cis*-decalin f) with 2 vol.% PS-AuNR. The scale bars on the AFM micrographs represent 5 μm.

The drying behavior and film morphology of *cis*-decalin is the same regardless of whether nanoparticles were added to the solution. Therefore, the particle location within these films is such that the overall structure was not influenced. To better understand the effect of processing and solvent choice on the morphology of polymer blend nanocomposites, the partitioning of the nanoparticles in these solvents must be studied and related to the final film structure.

4.3.4 Particle Location

To fully elucidate the effect of the particles on the blend morphology and processing, the nanoparticle partitioning within the polymer blend must be characterized. Due to plasmonic resonance effects, gold nanoparticles can appear bright under polarized light optical microscopy.³⁵ A comparison between bright field (reflection mode), bright field (transmission mode), and polarized light (transmission mode) is given in Figure 4-12. The transmission mode micrographs (bright field and polarized) are taken on the same spot.

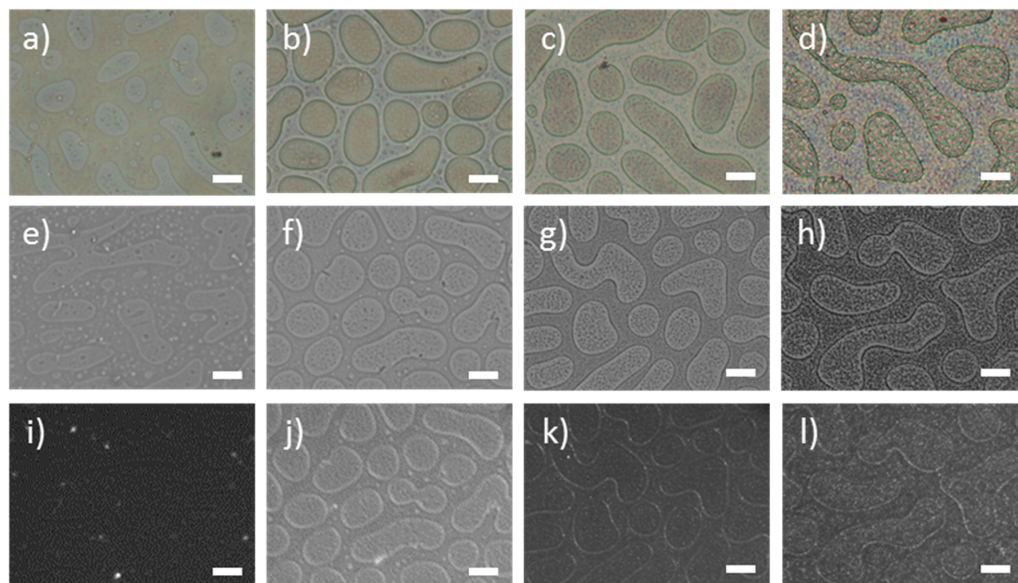


Figure 4-12. Bright field optical microscopy (a-d) with the Nikon microscope operated in reflection mode. Bright field optical (e-h) with the Zeiss microscope operated in transmission mode. (i-l) Polarized light microscopy with the Zeiss microscope of the same spot of the films shown in (e-h). Polymers cast with 2.0 wt.% PS₅₀/PI₅₀ (a, e, i) with 1 vol.% (b, f, j), 2 vol.% (c, g, k), and 9 vol.% (d, h, l) gold nanorod loadings. The gold nanoparticles appear bright under cross polarizers.³⁵ The higher contrast in j, k, and l near the blend interfaces compared to i, indicate that particles are assembling at the polymer-polymer interface.

For the neat sample, the polarized light microscopy image is dark. However, for the films containing nanoparticles, the polarized light microscopy images have illuminated interfaces, suggesting the nanoparticles are localized in this region. To confirm the hypothesis that the gold nanorods had a higher concentration at the interface, the films were peeled and imaged. Submerging the films in liquid nitrogen was required to efficiently separate the film from the substrate. The resulting TEM micrographs are shown in Figure 4-13.

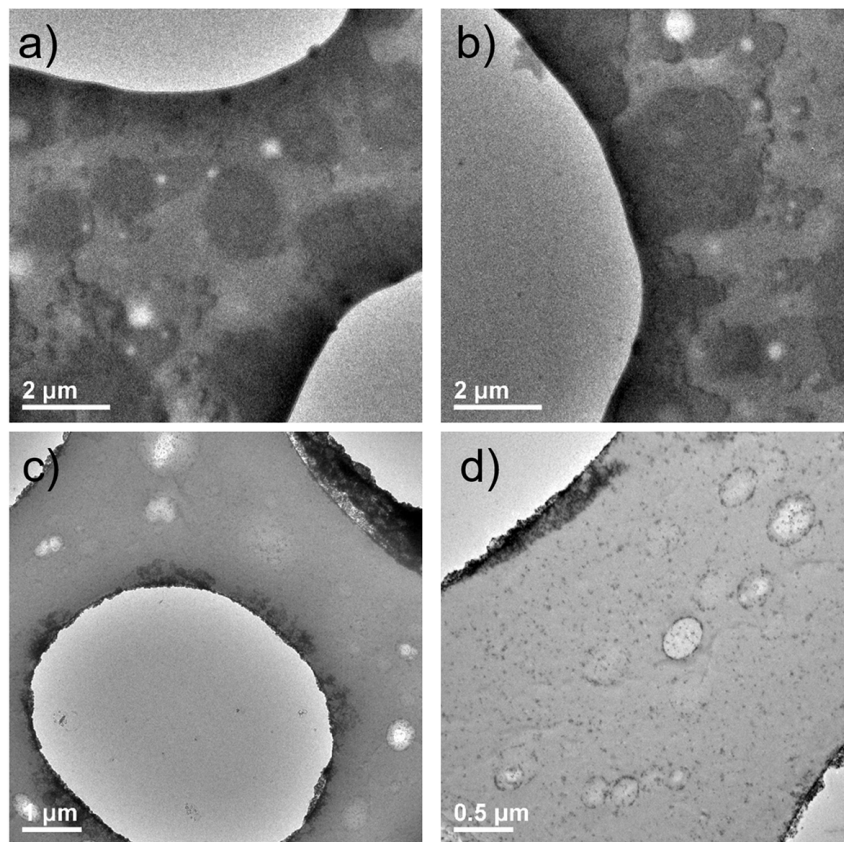


Figure 4-13. TEM micrographs of (a, b) neat PS/PI blend films and (c, d) PS/PI blends containing 2 vol.% gold nanorods cast from *o*-xylene. In the nanoparticle-laden samples, the particles are localized at/near the polymer/polymer interfaces as well as within the PS domain.

The top images of the neat blend film were used as a standard to which the nanocomposite films may be compared. Both films had similar contrast between the domains. The droplet phase in both cases is the PI (lighter in color). The polymer blend nanocomposites had particles at the interfaces between the two macroscopic domains as well as around droplets of microdomains of PI within the PS matrix. In addition to segregating to the interface, particles also were found within the domain. For the capsule geometry, maximum packing is 73.1 vol.%.³⁶ Using the perimeter of

the domains and the relative domain height, along with the nanoparticle dimensions and maximum packing, only ~ 0.05 vol.% - 0.20 vol.% particle is required to saturate the interface. Thus, at 2 vol.%, more than 10 times the number of particles are in the film compared to the amount needed to produce a monolayer at the interfaces.

The neutral solvent cast samples resulted in nanoparticles at the interface. However, by changing the solvent selectivity, the effect of adding particles to the solution on the drying behavior can be modified. For instance, in comparison to *o*-xylene, *cis*-decalin is highly selective for PI. In addition to the reduction in polymer blend compatibility with *cis*-decalin, the interaction between *cis*-decalin and PS is significantly lower than *o*-xylene and PS. Thus, during casting, the PS will solidify at a higher solvent concentration, which may affect the particle localization due to kinetic trapping.

Polarized light microscopy for the *cis*-decalin films are shown in Figure 4-14. Both films have the same contrast under polarized light, which suggests that the particles are not localized within the polymer blend film. Instead, this lack of contrast indicates that the particles are dispersed within the polymer phase or at the substrate/free surface interfaces. Thus, the selectivity of the *cis*-decalin provided a kinetic trap to prevent the particles from migrating to the polymer/polymer interfaces.

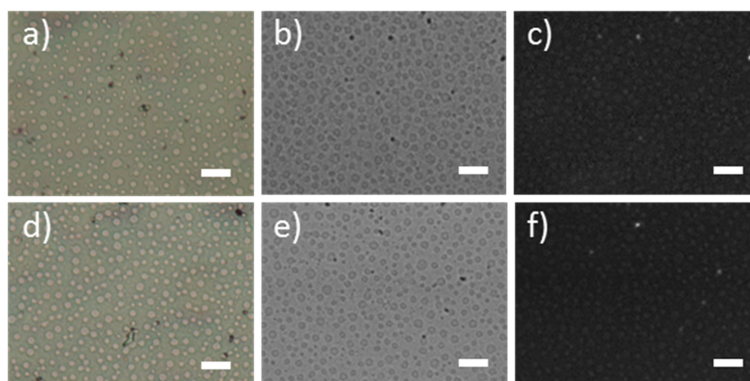


Figure 4-14. Bright field optical microscopy (a-d) with the Nikon microscope operated in reflection mode. Bright field optical (e-h) with the Zeiss microscope operated in transmission mode. (i-l) Polarized light microscopy with the Zeiss microscope of the same spot of the films shown in (e-h). Polymers cast with 2.0 wt.% PS₅₀/PI₅₀ (a, e, i) with 2 vol.% (c, g, k) gold nanorod loading. There is no change in brightness between c) and f), suggesting that particles are not localized in these films.

Attempts to remove the *cis*-decalin cast films from the silicon wafer substrate were unsuccessful due to the thin PI layer. Though the PS domains have ~100 nm - 200 nm height, the PI domain is on the order of ~5 nm. When performing the peeling technique, the PAA droplet shattered in the liquid nitrogen, whereas it remained intact for the *o*-xylene cast samples (minimum PI thickness ~ 70 nm - 100 nm). Thus, characterizing the *cis*-decalin cast films requires more complex preparation and imaging techniques than those described in this dissertation and remains a challenge to be solved in future work.

4.4 Conclusions

PBNCs have versatile properties that make them well-suited for applications in hierarchical coatings. However, to produce these coatings, solvent casting is required.

The effect of processing on polymer blend nanocomposites during solvent casting has not been well-studied. The goal of this work was to study the effects of polymer concentration, nanoparticle loading, and solvent selectivity on the processing and morphology of PBNCs with PS-selective nanoparticles. The drying behavior of PBNCs was studied using *in situ* measurements of the film thickness (drying curves). These drying curves were influenced by the addition of nanoparticles in a neutral solvent. The morphologies of the resulting films revealed the domain size was reduced upon the addition of nanofillers. Polarized light microscopy and transmission electron microscopy demonstrated that the particles localized at the polymer-polymer interface. In comparison to the neutral solvent, nanoparticles did not influence the drying behavior or morphology of films cast from a PI-selective solvent. The insensitivity to particle loading likely stems from the higher incompatibility of the blend with *cis*-decalin, which would drive the phase behavior and solidification of PS during casting. Earlier PS solidification could trap the nanoparticles in a dispersed state within the domain.

These results demonstrate that processing (drying behavior and solvent selectivity) significantly impacts the particle partitioning and, therefore, the effect of particles on the domain size. As such, the influence of casting represents another important factor to consider in the production of hierarchical coatings from polymer blend nanocomposites.

REFERENCES

1. Gurumurthy, S. C.; Patabi, M.; Krishna, S.; Gaikwad, A. B., Preparation and characterization of silver particulate films on softened polystyrene and poly(4-vinylpyridine) blends. *J. Mater. Sci.: Mater. Electron.* **2014**, *25*, 2501-2506.
2. Mamunya, Y. P.; Muzychenko, Y. V.; Pissis, P.; Lebedev, E. V.; Shut, M. I., Percolation phenomena in polymers containing dispersed iron. *Polym. Eng. Sci.* **2002**, *42*, 90-100.
3. Mamunya, Y. P.; Muzychenko, Y. V.; Pissis, P.; Lebedev, E. V.; Shut, M. I., Processing, structure, and electrical properties of metal-filled polymers. *J. Macromol. Sci., Part B: Phys.* **2001**, *B40*, 591-602.
4. Khutia, M.; Joshi, G. M.; Deshmukh, K.; Pandey, M., Preparation of modified polymer blend and electrical performance. *Compos. Interfaces* **2015**, *22*, 167-178.
5. Bose, S.; Cardinaels, R.; Ozdilek, C.; Leys, J.; Seo, J. W.; Wubbenhorst, M.; Moldenaers, P., Effect of multiwall carbon nanotubes on the phase separation of concentrated blends of poly (alpha-methyl styrene)-co-acrylonitrile and poly(methyl methacrylate) as studied by melt rheology and conductivity spectroscopy. *Eur. Polym. J.* **2014**, *53*, 253-269.
6. Biswas, S.; Kar, G. P.; Bose, S., Engineering nanostructured polymer blends with controlled nanoparticle location for excellent microwave absorption: a compartmentalized approach. *Nanoscale* **2015**, *7*, 11334-11351.
7. Biswas, S.; Kar, G. P.; Bose, S., Attenuating microwave radiation by absorption through controlled nanoparticle localization in PC/PVDF blends. *Phys. Chem. Chem. Phys.* **2015**, *17*, 27698-27712.
8. Chung, H.-J.; Ohno, K.; Fukuda, T.; Composto, R. J., Internal phase separation drives dewetting in polymer blend and nanocomposite films. *Macromolecules* **2007**, *40*, 384-388.
9. Bai, L.; Fruehwirth, J.; Cheng, X.; Macosko, C. W., Interfacial silica nanoparticles stabilize cocontinuous polymer blends. **2015**, arXiv:1502.00165.

10. Guo, Y.; Moffitt, M. G., "Smart" self-assembled quantum dots regulate and stabilize structure in phase-separated polymer blends. *Chem. Mater.* **2007**, *19*, 6581-6587.
11. Causa, A.; Filippone, G.; Domingo, C.; Salerno, A., Study of the morphology and texture of poly (ϵ -caprolactone)/polyethylene oxide blend films as a function of composition and the addition of nanofillers with different functionalities. *RSC Adv.* **2015**, *5*, 59354-59363.
12. Thareja, P.; Velankar, S. S., Interfacial activity of particles at PI/PDMS and PI/PIB interfaces: analysis based on Girifalco-Good theory. *Colloid. Polym. Sci.* **2008**, *286*, 1257-1264.
13. Thareja, P.; Moritz, K.; Velankar, S. S., Interfacially active particles in droplet/matrix blends of model immiscible homopolymers: particles can increase or decrease drop size. *Rheol. Acta* **2010**, *49*, 285-298.
14. Nagarkar, S. P.; Velankar, S. S., Morphology and rheology of ternary fluid–fluid–solid systems. *Soft Matter* **2012**, *8*, 8464-8477.
15. Nagarkar, S.; Velankar, S. S., Rheology and morphology of model immiscible polymer blends with monodisperse spherical particles at the interface. *J. Rheol.* **2013**, *57*, 901-926.
16. Taguet, A.; Cassagnau, P.; Lopez-Cuesta, J. M., Structuration, selective dispersion and compatibilizing effect of (nano)fillers in polymer blends. *Prog. Polym. Sci.* **2014**, *39*, 1526-1563.
17. Composto, R. J.; Chung, H.-J.; Gam, S., Nanoparticle jamming to create discrete and bicontinuous polymer blend morphologies. *Abstracts of Papers of the American Chemical Society* **2009**, 237.
18. Gam, S.; Corlu, A.; Chung, H.-J.; Ohno, K.; Hore, M. J. A.; Composto, R. J., A jamming morphology map of polymer blend nanocomposite films. *Soft Matter* **2011**, *7*, 7262-7268.
19. Chung, H.; Ohno, K.; Fukuda, T.; Composto, R. J., Self-regulated structures in nanocomposites by directed nanoparticle assembly. *Nano Lett.* **2005**, *5*, 1878-1882.
20. Chung, H. J.; Taubert, A.; Deshmukh, R. D.; Composto, R. J., Mobile nanoparticles and their effect on phase separation dynamics in thin-film polymer blends. *Europhys. Lett.* **2004**, *68*, 219-225.

21. Wu, K. H.; Lu, S. Y., Preferential partition of nanowires in thin films of immiscible polymer blends. *Macromol. Rapid Commun.* **2006**, *27*, 424-429.
22. Laradji, M.; Hore, M. J. A., Nanospheres in phase-separating multicomponent fluids: A three-dimensional dissipative particle dynamics simulation. *J. Chem. Phys.* **2004**, *121*, 10641-10647.
23. Hore, M. J. A.; Laradji, M., Microphase separation induced by interfacial segregation of isotropic, spherical nanoparticles. *J. Chem. Phys.* **2007**, *126*.
24. Hore, M. J. A.; Laradji, M., Prospects of nanorods as an emulsifying agent of immiscible blends. *J. Chem. Phys.* **2008**, *128*.
25. Ginzburg, V. V., Influence of nanoparticles on miscibility of polymer blends. A simple theory. *Macromolecules* **2005**, *38*, 2362-2367.
26. He, G.; Ginzburg, V. V.; Balazs, A. C., Determining the phase behavior of nanoparticle-filled binary blends. *J. Polym. Sci., Part B: Polym. Phys.* **2006**, *44*, 2389-2403.
27. Boiteux, G.; Mamuny, Y. P.; Lebedev, E. V.; Adamczewski, A.; Boullanger, C.; Cassagnau, P.; Seytre, G., From conductive polymer composites with controlled morphology to smart materials. *Synth. Met.* **2007**, *157*, 1071-1073.
28. Balazs, A. C.; Emrick, T.; Russell, T. P., Nanoparticle polymer composites: where two small worlds meet. *Science* **2006**, *314*, 1107-1110.
29. Cai, X.; Li, B.; Pan, Y.; Wu, G., Morphology evolution of immiscible polymer blends as directed by nanoparticle self-agglomeration. *Polymer* **2012**, *53*, 259-266.
30. Li, L.; Miesch, C.; Sudeep, P. K.; Balazs, A. C.; Emrick, T.; Russell, T. P.; Hayward, R. C., Kinetically trapped co-continuous polymer morphologies through intraphase gelation of nanoparticles. *Nano Lett.* **2011**, *11*, 1997-2003.
31. Chung, H. J.; Kim, J.; Ohno, K.; Composto, R. J., Controlling the location of nanoparticles in polymer blends by tuning the length and end group of polymer brushes. *ACS Macro Lett.* **2012**, *1*, 252-256.
32. Nikoobakht, B.; El-Sayed, M. A., Preparation and growth mechanism of gold nanorods (NRs) using seed-mediated growth method. *Chem. Mater.* **2003**, *15*, 1957-1962.

33. Prileszky, T. A.; Furst, E. M., Crystallization kinetics of partially crystalline emulsion droplets in a microfluidic device. *Langmuir* **2016**, *32*, 5141-5146.
34. Link, S.; Mohamed, M. B.; El-Sayed, M. A., Simulation of the optical absorption spectra of gold nanorods as a function of their aspect ratio and the effect of the medium dielectric constant. *J. Phys. Chem. B* **1999**, *103*, 3073-3077.
35. Sönnichsen, C.; Alivisatos, A. P., Gold nanorods as novel nonbleaching plasmon-based orientation sensors for polarized single-particle microscopy. *Nano Lett.* **2005**, *5*, 301-304.
36. Baule, A.; Mari, R.; Bo, L.; Portal, L.; Makse, H. A., Mean-field theory of random close packings of axisymmetric particles. *Nat. Commun.* **2013**, *4*, 2194.

Chapter 5

EFFECT OF MORPHOLOGY AND COMPOSITION ON FRICTION AND WEAR OF POLYMER BLEND FILMS

5.1 Introduction

Polymer blend films have been utilized in a variety of applications including organic optoelectronics, pressure sensitive adhesives, batteries, radiation shielding, and anti-reflection coatings.¹⁻⁷ In comparison to their base constituents, polymer blends have enhanced optical, electrical, thermal, and mechanical properties.⁸⁻⁹ To produce polymer blend coatings for applications cost-effectively and rapidly require the use of continuous processing techniques. However, the microstructure, including the domain size and composition, strongly influences the material properties.¹⁰ For instance, anti-reflection coatings require a domain spacing that is significantly smaller than the wavelength of visible light and a maximized volume ratio of pore space after one domain removal; balancing these two effects produce transparent anti-reflection materials.⁷

Tribology, or the friction and wear of materials, is one such property that is influenced by the microstructure. The friction coefficient and wear is important in applications such as bearings, solid lubricants, and functional coatings. Going back to the anti-reflection coating example, the wear of the material is important as scratches increase the specular reflections and light scattering. A material with low wear is desirable to enhance the lifetime of the coating. Therefore, understanding the

relationship between microstructure and friction coefficient is vital for utilizing polymer blends in coatings applications.

The tribology of variety of polymer blends have been studied, for which the blend is comprised of polyamides,¹¹⁻¹³ polyethylene,^{12, 14} poly(tetrafluoroethylene) [PTFE],¹⁵⁻¹⁹ and/or poly(ether ether ketone) [PEEK].^{15-16, 18-19} A benefit of using blends for tribology applications is that they can impart both low friction and low wear, which may not be readily accessible for the neat polymers. However, in comparison to the neat films that are typically featureless, these multi-component materials have surface structures. Thus, it is important to understand the relationship between the composition, structure, and friction coefficient. A common polymer blend used in friction and wear studies is PEEK/PTFE.^{15-16, 19} Burriss and coworkers reported a non-monotonic trend in friction coefficient (decreasing, then increasing) with increasing PEEK composition, which is shown in Figure 5-1a.¹⁶ These results agreed with a previous study by Bijwe and coworkers on the same polymer blend system.¹⁵ However, Briscoe and coworkers previously reported an increase in friction coefficient with PEEK concentration over a wide composition range, shown in Figure 5-1b.¹⁹ Burriss and coworkers hypothesized that processing and preparation protocols, which can have a strong influence on domain size, contributed to these experimental differences. However, the domain size is affected by the film composition and was not characterized in these works.

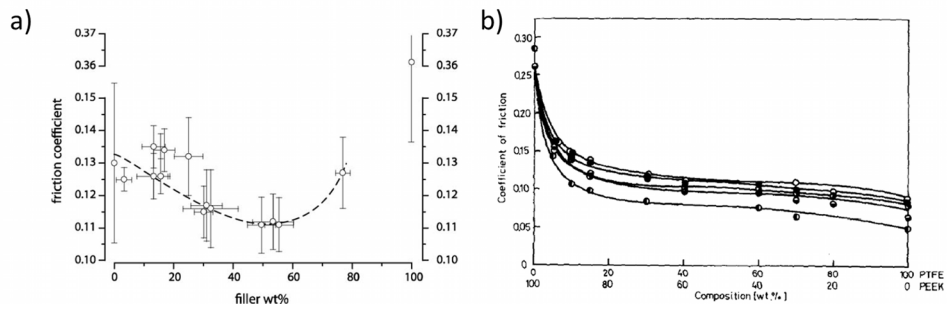


Figure 5-1. a) Friction coefficient for the PEEK/PTFE composites plotted as a function of PEEK filler wt.% (calculated from the measured sample density). The friction coefficient was measured on 6.35 mm square sample surfaces under 250 N of normal load, 25.4 mm track length, and 50.8 mm/s. Reprinted with permission from Burris, D. L. and Sawyer, W. G. *Wear* 2006, 261, 410-418. Copyright 2006 Elsevier. b) Friction coefficient for PEEK/PTFE composites as a function of polymer composition at a velocity of 0.45 mm/s under 5 N (◻, ◐), 10 N (◑), 15 N (●), and 20 N (○). Reprinted with permission from Briscoe, B. J. *et al. Wear* 1986, 108, 357-374. Copyright 1986 Elsevier.

In addition to the coupling of the composition and domain size, these studies focused on bulk materials, which are typically heated and then extruded or melt-pressed. For coatings applications, blend films commonly are generated by solution casting. The effect of polymer blend morphology and composition on the friction and wear of blend films is not well understood. Thus, developing these structure-property relationships in films is vital towards producing advanced low friction and wear-resistant polymer coatings. The purpose of this work is to establish a relationship between microstructure (composition and domain size) and friction coefficient. The effect of microstructure on friction coefficient and the influence domain size at a single composition were studied, as shown schematically in Figure 5-2.

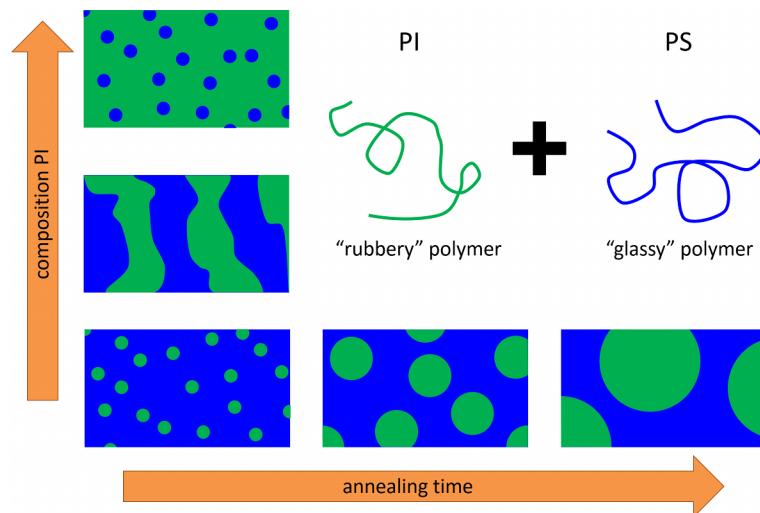


Figure 5-2. Cartoon depicting the tunability of the domain size of a homopolymer blend containing a glassy and rubbery polymer using composition and annealing. Composition affects both the domain size and shape, whereas the annealing time mostly changes the domain size.

A polystyrene [PS] and polyisoprene [PI] polymer blend system was selected. Although PS and PI are not commonly used materials for typical tribological applications, their friction coefficients are known.²⁰⁻²¹ Additionally, these materials have been well-characterized with respect to their interactions, phase behavior, and material properties, making them a robust blend to control the film microstructure (composition and domain size). The protocols reported herein can be applied to other polymer blend systems and polymer composites of interest for tribology.

5.2 Materials & Methods

5.2.1 Materials

Polystyrene [$M_n = 892$ kg/mol, $D = 1.04$] was purchased from Scientific Polymer Products. Polyisoprene [$M_n = 541$ kg/mol, $D = 1.13$, 95% 1,4] was

synthesized in cyclohexane by anionic polymerization with a *sec*-butyllithium initiator. Toluene (certified ACS) and *o*-xylene (puriss. p.a.) were purchased from Fischer Scientific and Sigma-Aldrich, respectively. The purchased materials were used as received. Glass microscope slides (25 mm × 75 mm, pre-cleaned) were obtained from Fisher Scientific and silicon wafers (N-type, crystallographic plane [100]) were purchased from Wafer World (product number 1196). Glass slides and silicon wafers were cleaned immediately prior to use.

5.2.2 Film Preparation

Solutions of 2.5 wt.% polymer in toluene were prepared gravimetrically. The relative ratio of PS to total polymer ($x_{PS} = m_{PS}/[m_{PS}+m_{PI}]$) was changed while maintaining a constant total polymer concentration. For blend films, 2.5 wt.% was the maximum concentration at $x_{PS} = 0.50$ in a homogenous solution, based on the thermodynamic incompatibility of the polymers. Solutions were cast on cleaned glass microscope slides or silicon wafers using flow coating.²² All substrates were triple rinsed with toluene before and after cleaning with ultraviolet-ozone (Jelight, Model 342).

The flow coating apparatus was operated with a velocity of 15 mm/s, acceleration of 2 mm/s², gap height of 70 μm, and a blade width of 20 mm. 100-110 μL of solution were deposited under the blade. Due to the thicker layer of solution deposited on the wafer required to produce ~1 μm thick films, the solvent evaporation did not follow a directional drying front induced by the blade motion. The resulting films had variable thicknesses (see also Appendix A). More uniform films were produced with additional convection applied during casting to induce directional drying (shown schematically in Figure 5-3). The convection was introduced using a

fan (Radio Shack, product number 273-241C), which was rated at an air velocity of ~ 3.8 m/s.

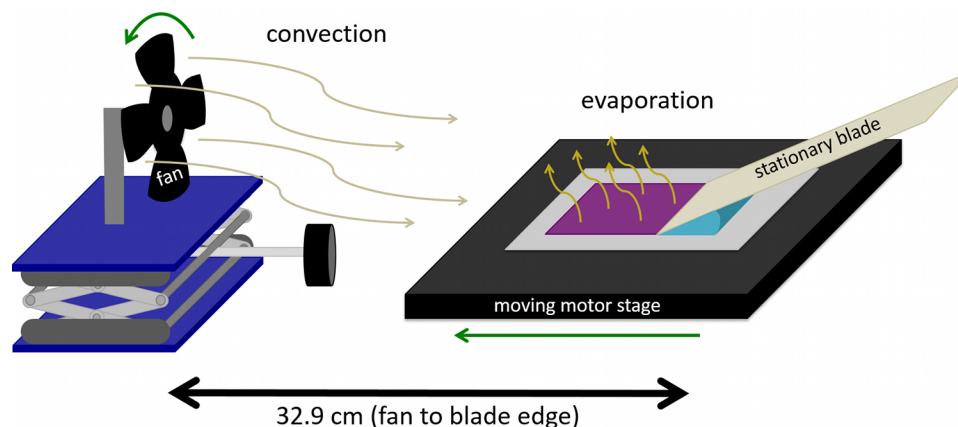


Figure 5-3. Schematic of convection-assisted flow coating. The forced convection induced a directional drying front, which produced uniform films.

5.2.3 Annealing

Two annealing methods were used to modify the domain structure in the polymer blend films. In the first, films were placed in a sealed chamber containing a solvent (*o*-xylene) reservoir. This process is called a bell jar anneal. *o*-Xylene was selected as a solvent, as it did not change the polymer-solvent interaction parameters significantly (see Chapter 3, Figure 3.6) but had a higher boiling point (evaporates more slowly), which afforded enhanced temporal control over the annealing process. The bell jar anneals were run for various lengths of time to tune the film morphology. The second method annealed the films during casting, as shown schematically in Figure 5-4. This *in situ* method combined radiation and convection during coating. The radiative energy was controlled by changing the distance between a heating lamp

(Dazor, model p-2324, 30 W) and the substrate. The temperature was measured using a thermocouple placed on the substrate surface. Using this method, a narrow temperature range was achieved (24 °C – 29 °C) for distances between the lamp and substrate corresponding to 29.4 cm and 3.8 cm, respectively.

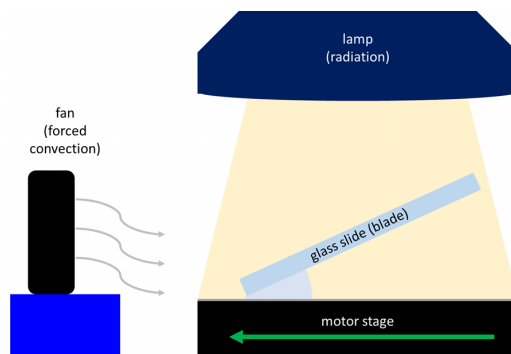


Figure 5-4. Schematic of experimental casting set-up. Convection and radiation were used to produce $\sim 1 \mu\text{m}$ thick films. The temperature of the substrate was tuned by changing the position of the radiation source relative to the substrate.

5.2.4 Film Morphology and Domain Analysis

Optical micrographs were captured using a bright field Nikon microscope (Eclipse L100) equipped with a CCD camera (Nikon DS-Fi1, 5 Mp) operated in reflection mode at $5\times$, $20\times$, or $100\times$ magnification. The images were thresholded in ImageJ to make binary images, which were used to analyze the domain size with ImageJ's "Analyze particle" routine. The "Analyze particles" routine counts and measures objects in binary or thresholded images.²³ First, the image is scanned until the edge of an object is located. Second, the object is then outlined and measured. Third, the selected object is made invisible to the program to prevent double counting. Finally, once all of the objects have been located, measured, and counted, the results

are summarized. Atomic force micrographs were captured with a Veeco Nanoscope V Dimension 3100 operated in tapping mode. The film morphologies were imaged using silicon probes (tap150) with a force constant of 5 N/m and resonant frequencies between 120 kHz and 180 kHz.

5.2.5 Tribology

The friction coefficient and adhesion of the polymer films were measured using a custom-built, linear reciprocating microtribometer with a sphere-on-flat geometry. Digital photographs of the tribometer are shown in Figure 5-5. The microtribometer uses two capacitance probes, which are located perpendicular to each other, to measure the normal and friction forces. The load is applied to a stainless steel beam to which a spherical probe is affixed. The probe diameter was 6.35 mm and made of either borosilicate glass or high-density polyethylene (HDPE), depending on the experiment. The film of interest is attached to a motor stage, which reciprocates linearly during the experiments at the set speed. Finally, the micrometer is used to control the lateral position along the film to ensure all friction coefficient and adhesion measurements are taken from different spots on the film.

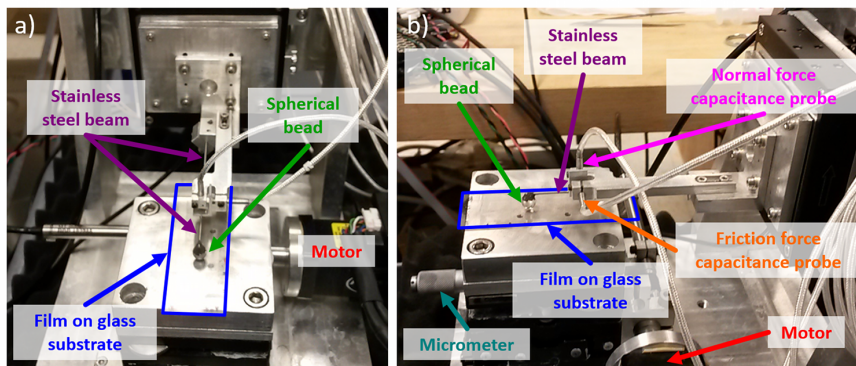


Figure 5-5. a) Front and b) side view digital photographs of the microtribometer used in friction coefficient measurements. A force is applied to the film using a 6.35 mm probe attached to a stainless steel beam. Two capacitance probes are used to measure the normal and friction forces. The linear reciprocating stage is controlled by a motor. The films are affixed to the stage before each experiment. The micrometer controls the position along the film.

The tribometer was operated at a load of 5 mN for 100 cycles with a path length of 2 mm for all friction coefficient tests, unless noted otherwise. A range of velocities between 0.5 mm/s and 7.8 mm/s were used. Low velocities were selected to reduce the effect of frictional heating.²⁰⁻²¹ The adhesion tests were performed using the same tribometer. The normal load was varied from 0.3 mN to 15.8 mN (controlled by distance) with approach/retraction velocities ranging from 1.2 $\mu\text{m/s}$ to 24.1 $\mu\text{m/s}$. For simplicity, the approach and retraction velocity were the same within a given adhesion test. The adhesion was characterized using pull-off forces upon retraction. There were three adhesion test protocols: (1) immediate retraction of the probe upon reaching the set distance; (2) leaving the probe in contact with the surface for 4 s, 16 s, or 80s before retraction; and (3) rastering the probe across the sample at 4.6 mm/s for 5, 20, or 100 cycles.

5.3 Results & Discussion

5.3.1 Friction Coefficient of Blend Films: Varying Composition

The friction coefficients were measured for $0.00 \leq x_{PS} \leq 1.00$ with the glass and HDPE probes are plotted in Figure 5-6a and Figure 5-6b. The friction coefficient did not follow the naively predicted behavior (linear mixing rule between the neat homopolymer values). Instead, the friction coefficient was non-monotonic with composition and featured a minimum around the same composition. The minimum $\mu_{glass-film}$ is 0.11 ± 0.03 ($x_{PS} = 0.70$, $v = 0.5$ mm/s), and the minimum $\mu_{HDPE-film}$ is 0.24 ± 0.06 ($x_{PS} = 0.75$, $v = 0.5$ mm/s). For both probes, PI had a larger friction coefficient than PS. However, there are a few key differences between the friction coefficients measured with both probes. For the glass probe, the friction coefficient decreased in a nearly linear fashion as x_{PS} increased from 0.0 to 0.5, whereas the HDPE-film friction coefficient remained nearly constant over the same composition range. Further increases in PS content, between $0.5 > x_{PS} > 1.0$, produced non-monotonic changes in the friction coefficient with both probes. At higher x_{PS} , ($x_{PS} > 0.8$), the glass-film friction coefficient was independent of composition and has a value similar to neat PS. The reported friction coefficients represent the time averages over the steady-state regime (region II in Figure 5-7 and Figure 5-8) for multiple films. With the glass probe, the neat PS film had average friction coefficients between 0.46 and 0.52, which are in agreement with the values reported in literature for steel contact on PS, for which the friction coefficient ranged from 0.4 to 0.6 for velocities between 0.5 cm/s and 500 cm/s.²⁰ For the HDPE probe, the friction coefficient of PS was no longer independent of velocity but instead ranged from 0.51 to 0.63. The dependence of friction coefficient on velocity likely was due to the increased probe-film adhesion.

However, these values still fell within the reported friction coefficients for PS. In comparison to the PS, the neat PI friction coefficient varied more with velocity, regardless of probe type, which is partially caused by the increase in adhesion between the probes and the PI films. Depending on the velocity and probe, the PI friction coefficient ranged from 1.3 to 2.1 for glass and 0.64 to 0.93 for HDPE, which fall below the maximum rubber friction coefficient between 2.5 and 3 for a smooth surface.²¹

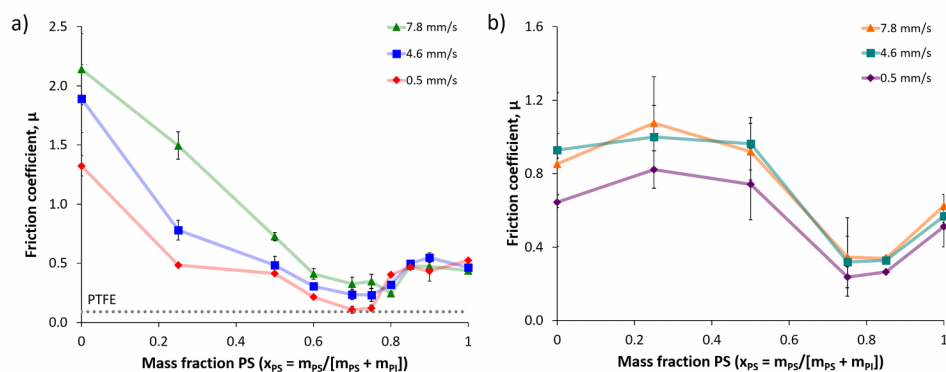


Figure 5-6. Friction coefficient of PS/PI films with varying composition PS (x_{PS}) measured with a) glass probe and b) HDPE probe. For both probe materials, the friction coefficient was non-monotonic with composition. The reported friction coefficients represent the average over the steady-state friction coefficient (see region II in Figure 5-7 and Figure 5-8). $\mu_{glass-PTFE}$ was measured at 4.6 mm/s as a comparison to the PS/PI blend films. Because μ_{PTFE} is independent of velocity at the speeds accessed herein,²⁰ the low friction coefficients measured for PS/PI are comparable to PTFE.

The friction coefficient of polymer blend films with PS mass fractions, x_{PS} , from 0 to 1 are measured as a function of time. The time-dependent friction coefficients for the 6.35 mm borosilicate glass probe and 6.35 mm HDPE probe are

shown in Figure 5-7 and Figure 5-8, respectively. PTFE was used as a standard to which the friction coefficients of the PS/PI blend films could be compared. At the velocities accessed in these studies, the PTFE friction coefficient has been reported to be independent of speed.²⁰ Thus, only the intermediate speed (4.6 mm/s) was used to measure the friction coefficient for PTFE. Note that the PTFE sample was not a deposited film, but a piece of bulk material (McMaster-Carr, 8735K12).

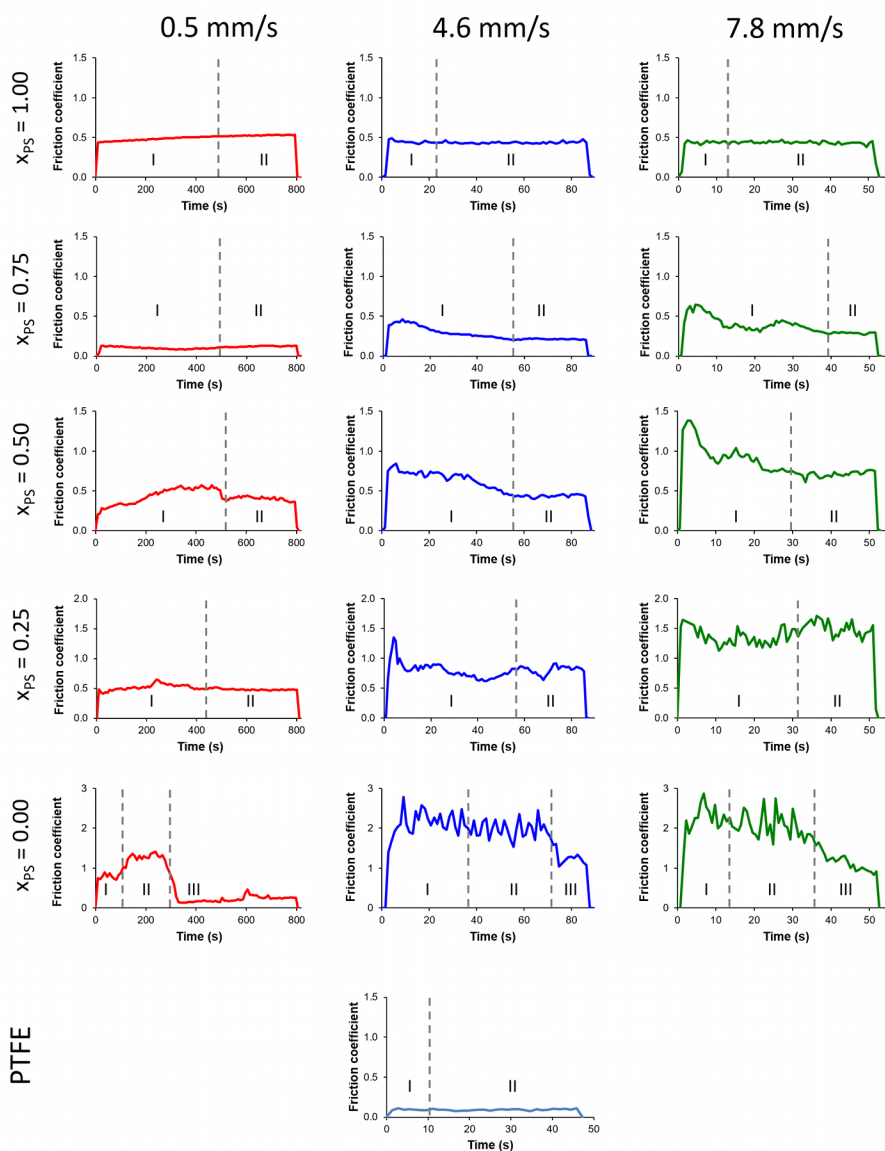


Figure 5-7. Sample time-dependent friction coefficient traces at 5 mN load for 100 cycles with a 6.35 mm diameter borosilicate glass probe. Region I represents a start-up regime, during which the friction coefficient varies in time. Region II is the steady-state friction coefficient. Reported friction coefficients represent an average over region II. For PI films, the probe breaks through the film within 100 cycles at all velocities. Region III of the PI plots indicate breakthrough (significant reduction in friction coefficient), which did not occur for the other films. See Figure 5-9a for an optical micrograph of wear through PI with glass.

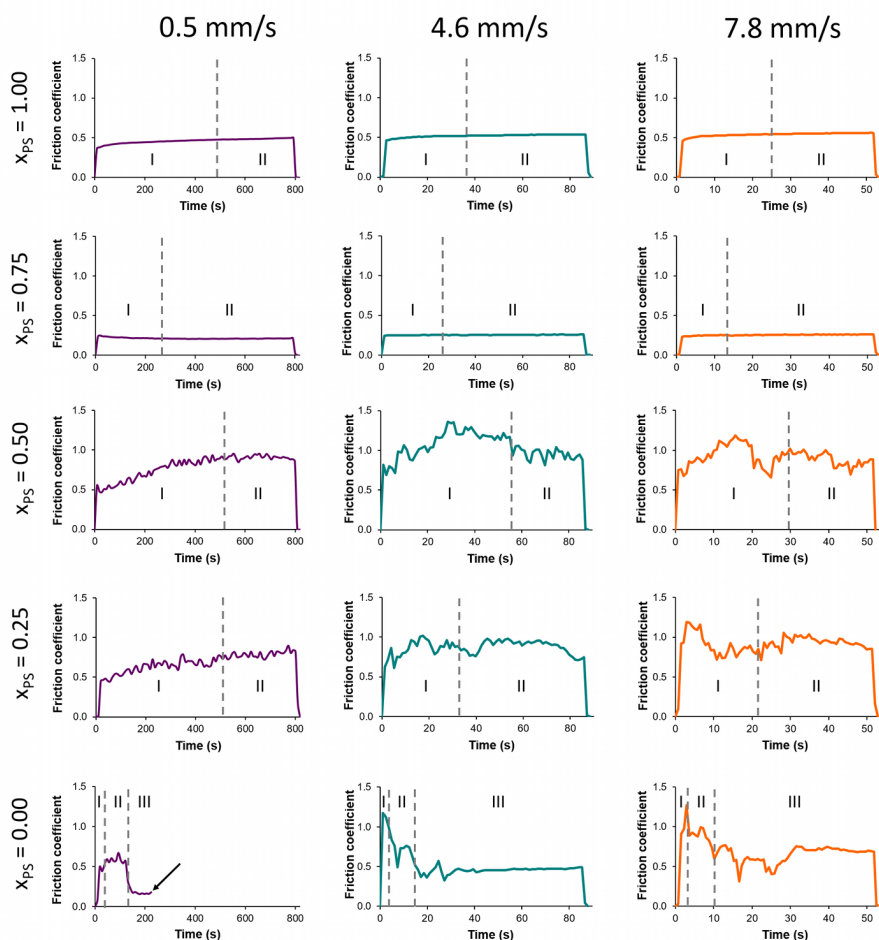


Figure 5-8. Time-dependent friction coefficient traces for PS/PI films with a 6.35 mm diameter HDPE probe. The load was constant at 5 mN in these linear reciprocating experiments along a 2 mm path. As for Figure 5-7, region I and II represent the start-up and steady-state friction coefficients, respectively. For HDPE, breakthrough was seen in the PI films (region III). Wear through the films was confirmed optically (see Figure 5-9b). At 0.5 mm/s, the black arrow indicates the point at which the experiments were stopped to prevent the HDPE bead from rubbing along the glass surface.

For most films, there are two main friction regimes in these plots. First, the friction coefficient changes with time (region I), which resulted from startup effects.

These startup effects included removing low-energy surface contaminants from the probe or film and wearing through the PI wetting layer (see also Figure 5-16), of which the latter was more significant. Thus, the startup effects were not as pronounced in PS-rich films in comparison to majority PI films. Next, the friction coefficient reaches a plateau value and is independent of time (steady-state, region II). The plateau region is truncated in the PI films due to wear and breakthrough during the friction coefficient tests. This third region is breakthrough of the PI film, during which the probe has destroyed the film and is rastering across the substrate surface (see also Figure 5-9), which occurred with both probes.

The breakthrough of the probe through the film only occurred for neat PI; regardless of velocity or probe type, the PI film was completely removed after 100 cycles with a 5 mN load. Optical micrographs of the PI film after the friction coefficient tests is shown in Figure 5-9a for the glass probe and Figure 5-9b for the HDPE probe. With glass, the PI film also was removed around the area of the wear track in addition to the destruction along the wear track; due to the film loss, it was not possible to quantify the actual wear track. For the HDPE probe, the overall film damage was less. The wear track width increased with velocity, suggesting the film deforms more at higher speeds.

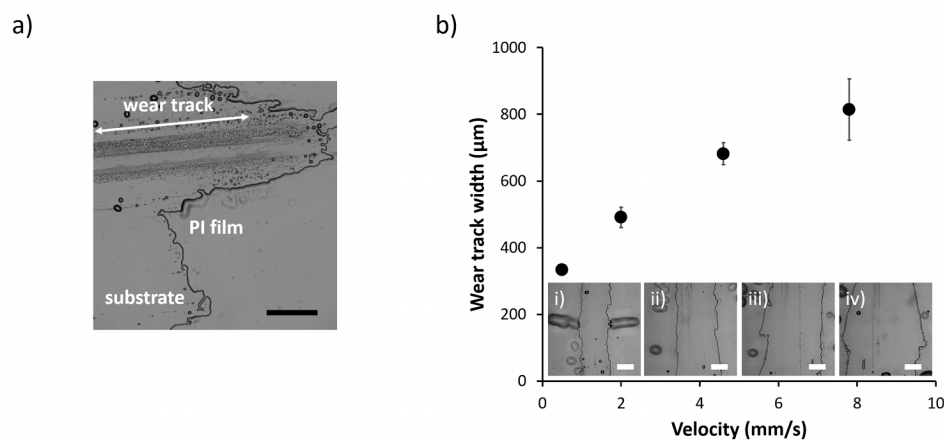


Figure 5-9. a) Wear through of a PI film with a glass probe at 0.5 mm/s and 5 mN for 100 cycles. b) Wear track widths for PI films after rastering across the film for 100 cycles at a 5 mN load with the HDPE probe at different velocities. The optical micrographs of the wear tracks at i) 0.5 mm/s, ii) 2.0 mm/s, iii) 4.6 mm/s, and iv) 7.8 mm/s are inset. The scale bars represent 200 μm.

The differences between the neat polymer friction coefficient behaviors with the two probes is related to the probe-polymer interactions, which was determined by the adhesion. $\mu_{PS-glass}$ showed no dependence on velocity, whereas $\mu_{PI-glass}$ increased with velocity. In comparison to these trends using glass probes, both friction coefficients measured with the HDPE probe ($\mu_{PS-HDPE}$ and $\mu_{PI-HDPE}$) increased with velocity. The adhesion of PS and PI was measured with both probes; these results are shown in Figure 5-10c and Figure 5-10d for the glass and HDPE probes, respectively. Probe-film adhesion was characterized by the pull-off forces measured upon immediate retraction. PI had higher pull-off force than PS with both probes. The glass pull-off forces for PS typically were within the noise level of the approach. However, the adhesion between PS and HDPE was statistically significant from the baseline.

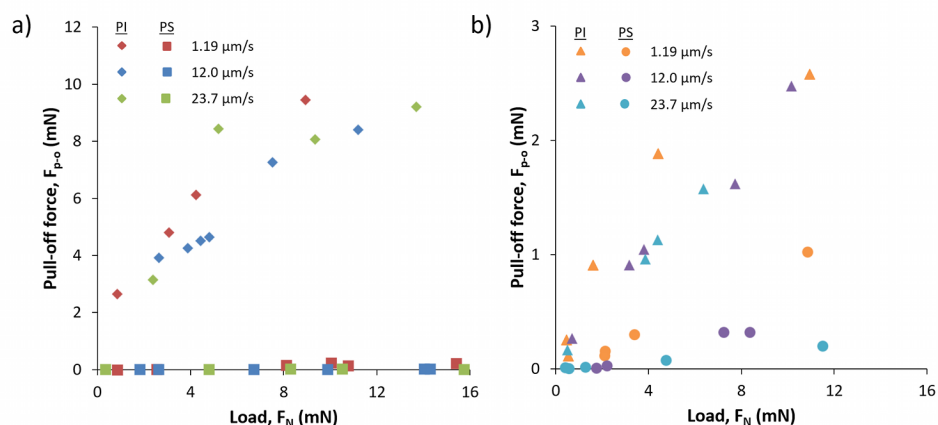


Figure 5-10. Adhesion of PS and PI with a) glass and b) HDPE probes. Adhesion is characterized by the pull-off force upon immediate retraction from the set load. PS has a lower adhesion than PI with both probes. The pull-off force for PS with glass is within the noise of the measurement, whereas it is statistically significant with HDPE. The HDPE-PI pull-off force is lower than the glass-PI pull-off forces, suggesting lower adhesion. There was no strong trend between the approach/retraction velocity and the adhesion.

The differences in the adhesion between the probe and homopolymer films help to elucidate the relationship between microstructure and friction coefficient. In general, PI had the highest friction coefficients, which is partially due to the larger contact radius, a , of the probes with PI than PS ($a_{\text{JKR,PS-g}} = 37 \mu\text{m}$; $a_{\text{JKR,PI-g}} = 287 \mu\text{m}$; $a_{\text{JKR,PS-HDPE}} = 22 \mu\text{m}$; $a_{\text{JKR,PI-HDPE}} = 300 \mu\text{m}$) and the adhesion between the probe and film. Additionally, the lack of change in friction coefficient measured with glass for $x_{\text{PS}} \leq 0.85$ likely is due to the low adhesion between the glass and PS along with the reduction in the PI domain size. At these compositions, the PI domain size is $\sim 10 \mu\text{m}$. Because PI is the shorter domain and the contact radius with neat PS is $37 \mu\text{m}$, the probe likely does not touch the PI domains (the PI wetting layer would be worn through prior to reaching the steady-state friction coefficient), producing a film that

mimics the neat PS behavior. The insensitivity of the HDPE-film friction coefficient to the composition for $0.00 < x_{PS} < 0.50$ could be due to the more similar adhesion of PS and PI with HDPE in comparison to the homopolymer adhesion with glass. However, despite the differences in the neat PS and PI adhesion, both probes measured a minimum in friction coefficient around $x_{PS} = 0.75$. Thus, it is of interest to study the microstructure in the blend films to determine the effect of composition and domain size on friction coefficient.

5.3.2 Structure of As-cast Films

The structure of the as-cast films, characterized by the domain assignment, domain size, and film thickness, was determined using optical microscopy and atomic force microscopy (AFM). The mass fraction PS, x_{PS} , was varied from 0 (pure PI) to 1 (pure PS). First, the domain assignments were made using height differences in the as-cast film, modulus differences in the atomic force micrographs, and domain removal *via* selective washing, as shown in Figure 5-11. Due to the higher relative T_g of PS compared to PI, PS will solidify first during casting. This earlier solidification results in a taller domain.²⁴ From the optical micrographs, in particular $x_{PS} = 0.50$, there is a visible contrast difference, suggesting a height difference in the domain. However, it is apparent by the reduced domain contrast (Figure 5-6a and Figure 5-6c) and the surface breakthrough of domains (Figure 5-6b) that these samples contain a wetting layer. PI has a lower surface energy and preferentially wets the free surface.²⁵ This wetting layer obscures the domain structure and hinders assignment based on height alone. Atomic force micrographs also were collected for the as-cast samples. The domain structures were confirmed using selective washing in *n*-hexane, which is a good solvent for PI and a poor solvent for PS. These washes remove the PI phase and

leave the PS film. For $x_{PS} = 0.50$ and $x_{PS} = 0.25$, the droplet phase is PS, whereas for $x_{PS} = 0.75$, the droplet phase is PI. Atomic force micrographs on the washed films supported the domain assignments from the optical micrographs.

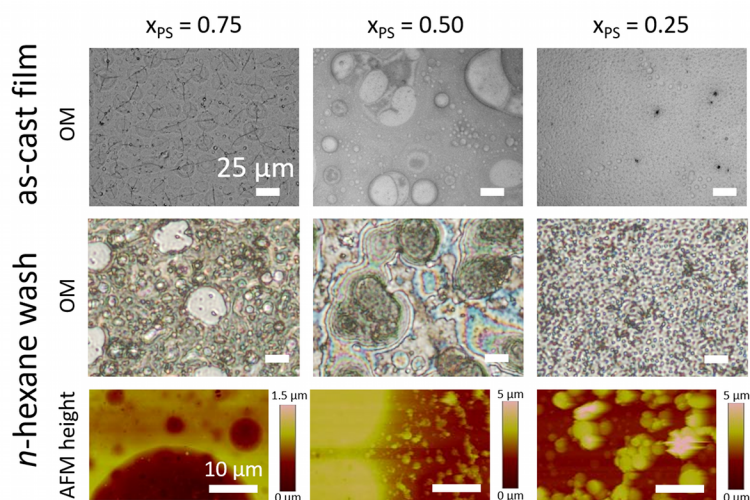


Figure 5-11. Domain assignment of PS/PI blend films. For $x_{PS} = 0.75$, the droplet phase was removed after washing with *n*-hexane; thus, the droplets are PI and the matrix is PS. Both $x_{PS} = 0.50$ and $x_{PS} = 0.25$ have a PI matrix with droplets of PI. The scale bars on the optical micrographs (reflection mode) represent 25 μm , and the scale bars on the atomic force micrographs (tapping mode) represent 10 μm .

It is also of interest to characterize the average domain size as a function of composition. Optical micrographs for the various compositions are shown in Figure 5-12a-h. The domain size was characterized by the area-weighted chord length, for which the chord length is given by $\pi A/p$; the area, *A*, and perimeter, *p*, of the droplet phase were determined using ImageJ's "Analyze Particle" routine. The area-weighted chord length as a function of composition is given in Figure 5-12i. As expected, the

droplet size increased and then decreased with increasing x_{PS} , with a maximum domain size near the critical point of the polymer blend ($x_{PS} \sim 0.57$).²⁶

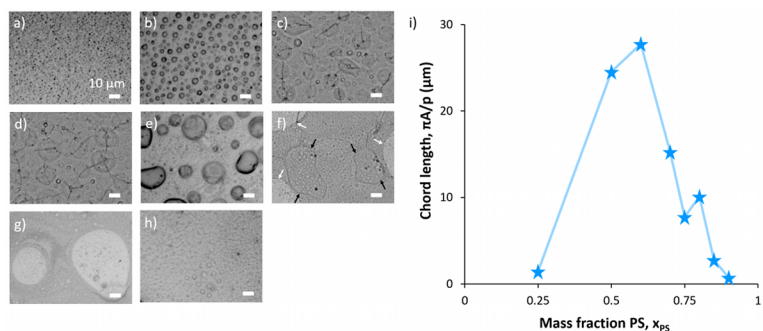


Figure 5-12. Optical micrographs of PS/PI films for x_{PS} values of a) 0.9, b) 0.85, c) 0.8, d) 0.75, e) 0.7, f) 0.6, g) 0.5, and h) 0.25. The brightness and contrast have been artificially enhanced and the scale bars represent 10 μm . In some of the films, a full (c, d) or partial (f) wetting layer decreased the natural contrast at the domain interfaces. In f) the white arrows point to holes in the wetting layer, whereas the black arrows highlight the edge of the underlying domain. The domain size was characterized by the area-weighted chord length ($\pi A/p$). The droplet domain size as a function of x_{PS} is shown in i). The droplet size increases with x_{PS} , reaches a maximum value near the critical point, and then decreases with additional increases in x_{PS} .

Finally, the film thickness and relative domain heights were determined. Using AFM, the film thicknesses were measured by the scratch test method. The relative height of each domain to the substrate was measured for $x_{PS} = 0.00, 0.25, 0.50, 0.75,$ and 1.00 . In addition to the thickness of the domains in the as-cast films, the blend films were washed to measure the height of the PS domain in the absence of PI. The resulting domain heights for the two-component and the PI removed films are shown in Figure 5-13.

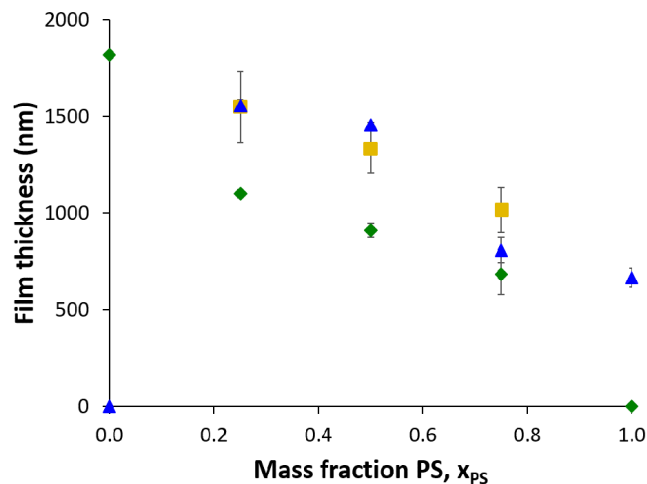


Figure 5-13. Effect of the mass fraction of PS on the film thickness. The domain height is shown for PS (▲) and PI (◆) in the two component system and for PS height in the films, for which the PI domains have been removed by washing with *n*-hexane (■). The film thickness was measured by atomic force microscopy using the scratch test method. In all cases, the PS domain is higher than the PI domain. The total film thicknesses increased with decreasing PS mass fraction due to the higher viscosity of the PI film. In the *n*-hexane washed films, the height of the PS agreed well with the two-component film heights.

Overall film thickness decreased with increasing x_{PS} . This trend is likely due to the higher viscosity of PI in comparison to PS; thus, the viscosity of the solution decreased with increasing PS content. At higher viscosities, more fluid is pushed under the blade, which produces a thicker solution layer,²⁷⁻²⁸ at the same polymer concentration, increasing the deposited liquid layer produces a thicker film. At the velocities accessed (10 mm/s – 20 mm/s), the Landau-Levich regime applies, during which the films are first drawn out by viscous forces followed by evaporation.²⁷

5.3.3 Effect of Microstructure on Friction Coefficient

To determine the effect of microstructure on friction coefficient, the friction coefficients reported in Figure 5-10 were replotted as a function of the area-weighted chord length in Figure 5-14 for the glass and HDPE probes. It is important to note that the domain size (Figure 5-12) is smaller than the contact radius of the neat homopolymers in all cases; therefore, the probe should be measuring the friction coefficient of the composite film and not of a single domain at all points along the path. For both probes, there is not a clear trend in the friction coefficient with chord length. However, for these films, the domain size is influenced by the composition. The composition also affects the modulus; the modulus varies linearly with composition far from the critical point, whereas the modulus changes non-linearly near the critical point with an inflection point at the critical point (phase inversion).²⁹ Thus, the modulus of the blend varies with the probe-film adhesion, which changes the contact radius.

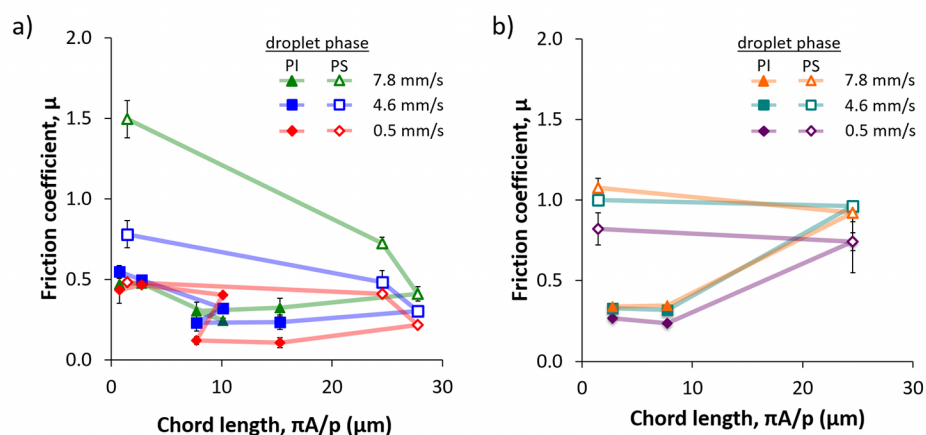


Figure 5-14. Effect of the domain size on the friction coefficient for friction coefficients measured with the a) glass or b) HDPE probe. The domain size is represented by the average area-weighted chord length. The open symbols represent films for which the droplet phase is PI and the closed symbols represent films for which the droplet phase is PS. There is no direct correlation between domain size and friction coefficient in these composition-controlled films. The lines are to guide the eye and connect the data points in order of increasing or decreasing x_{PS} . The highest blend film friction coefficient occurred at the $x_{PS} = 0.25$, whereas the lowest blend film friction coefficient was measured for $0.60 > x_{PS} > 0.75$ (glass) or 0.85 (HDPE).

To support the change in contact radius with composition, the wear tracks of the blend films can be studied, as shown for the glass probe in Figure 5-15. The blend films show an intermediate behavior in comparison to the PI wear tracks, which show breakthrough to the substrate (see also Figure 5-9), and the PS wear tracks, which are undetectable under optical microscopy after 100 cycles at 5 mN.

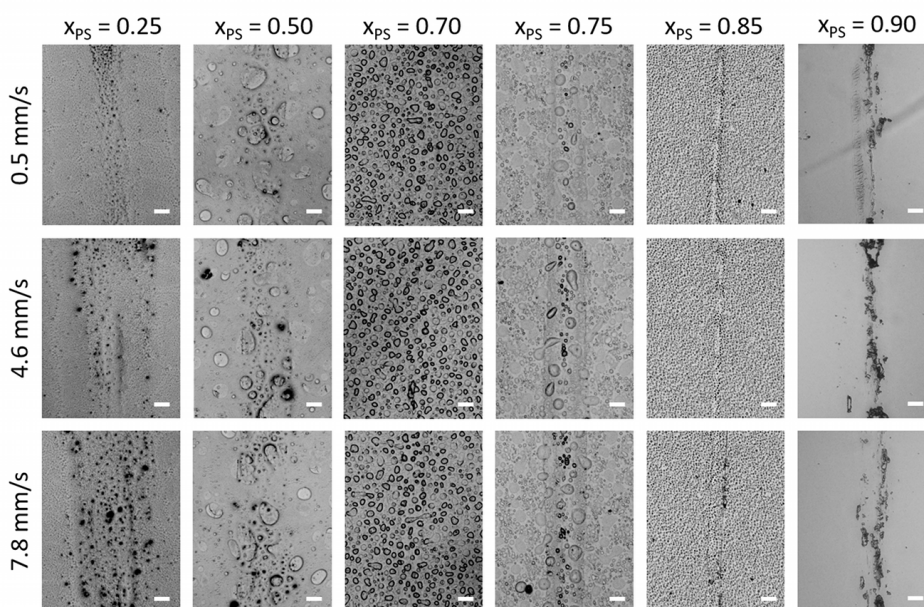


Figure 5-15. Wear tracks for various composition films with the glass probe. As the PS content increases, the wear track width decreases, suggesting that a combination of reduced wear and contact radius exists for these samples. The scale bar represents 50 μm .

From the optical micrographs, the wear track widths decrease with increasing x_{PS} , suggesting a reduction in modulus with increasing PS content. Even at high PS content, the wear tracks are still visible, which likely results from the wear of the PI wetting layer. This effect is further elucidated through AFM. The AFM height and phase micrographs for $x_{PS} = 0.25$, $x_{PS} = 0.50$, and $x_{PS} = 0.75$ after friction coefficient tests are shown in Figure 5-16.

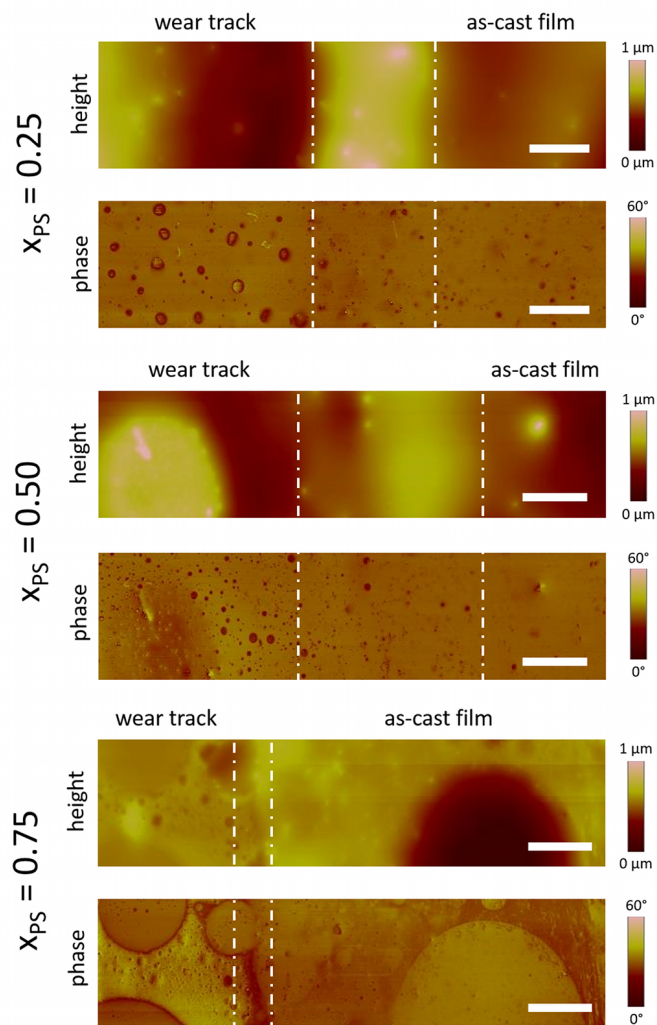


Figure 5-16. Atomic force micrographs of wear tracks on films after friction coefficient measurements with a 5 mN load after 100 cycles. For all micrographs, the phase image has higher contrast on the film that was exposed to the probe. The scale bars represent 10 μm .

The film over which the probe was rastered shows a loss of thickness, as evidenced by the darker color in the height images. In these lower regions of the film, the phase contrast is enhanced, suggesting a loss of the surface wetting layer. As discussed previously, this wetting layer is PI-rich due to the lower surface energy of PI

compared to PS. The results in this section demonstrate the complex relationship between microstructure and friction coefficient, but they do not help to explain the cause of the low friction coefficient seen with both probes in Figure 5-6. The probe-film adhesion was able to explain differences in the friction coefficients of the neat homopolymers. Because the adhesion influences the friction coefficient, it is of interest to measure the adhesion between the probe and blend films.

5.3.4 Adhesion Break-up in PS/PI Blend Films

The pull-off forces of HDPE were measured for $x_{PS} = 0.25$ and $x_{PS} = 0.75$, as shown in Figure 5-17. These values were compared to the neat PS and PI pull-off forces upon immediate retraction. To better match the conditions of the friction coefficient experiments with the blend films, additional experiments during which the probe was rastered across the film at 4.6 mm/s for 5, 20, or 100 cycles were performed to measure the adhesion. Furthermore, the probe was left in contact with the films for 4 s, 16s, or 80 s, which corresponds to the contact time during the rastering experiments from the previous tests. The results of these experiments showed similar pull-off forces to the immediate retraction studies. The $x_{PS} = 0.75$ films had a reduction in pull-off force compared to the neat PS at similar loads.

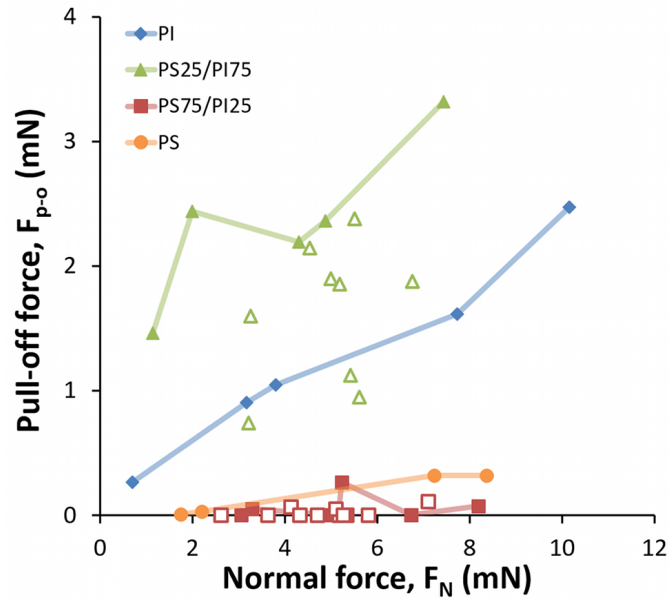


Figure 5-17. Comparison of HDPE adhesion with PS, PI and blend films. The approach and retraction speed were $12.0 \mu\text{m/s}$. The closed symbols represent immediate retraction, and open symbols represent results from experiments during which the probe was left in contact with the film (4 s, 16 s, or 80 s) or rastered across the film (5 mm/s for 5, 20, or 100 cycles). The $x_{PS} = 0.75$ blend film had lower pull-off forces than the neat PS.

The lower pull-off forces for the $x_{PS} = 0.75$ film are caused by adhesion break-up in the film, which contributes to producing a lower friction coefficient. To further elucidate the effect of PI in the adhesion break-up, PI was removed in $x_{PS} = 0.75$ both as-cast and after 24 h annealing in *o*-xylene by washing the films with *n*-hexane. The ratio of the friction coefficient of the films with PI removed (μ') to the two component films (μ) is shown as a function of velocity in Figure 5-18.

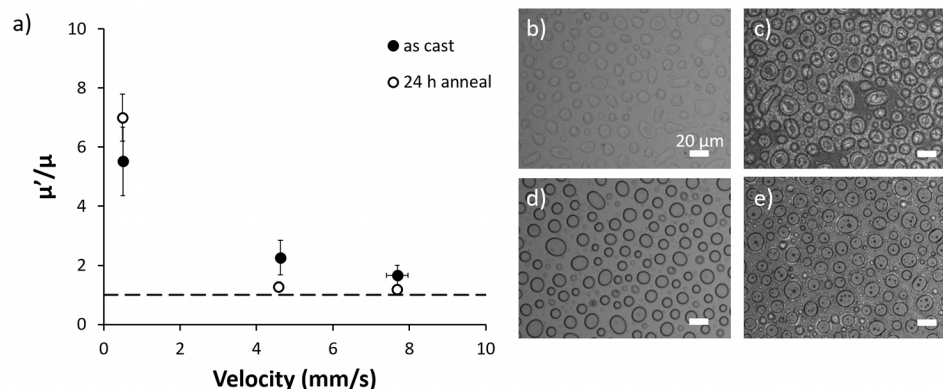


Figure 5-18. Ratio of the friction coefficient films for which the PI phase was removed (μ') to the friction coefficient of the neat polymer blend film (μ) produced under the same conditions. All films had an initial $x_{PS} = 0.75$. Optical micrographs of the b) as-cast film, c) as-cast film without the PI phase, d) film annealed for 24 h in *o*-xylene and d) 24 h annealed film without the PI phase. The PI was removed by soaking the films in *n*-hexane overnight. Compared to the friction coefficient of the film containing both PS and PI, the friction coefficients of the PI-removed films were always higher. Of particular interest was the spike in friction coefficient at 0.5 mm/s for both the as-cast and 24 h annealed films upon PI removal. This increase is likely due to the loss of the adhesion break-up in the film.

At low velocities (0.5 mm/s), the friction coefficient of the PI removed film was ~ 6 times higher than the two component film for both the as-cast structure and the annealed film; the ratio of the neat PS friction coefficient to the friction coefficient for $x_{PS} = 0.75$ ($\mu_{PS}/\mu_{x_{PS} = 0.75}$) is 4.3 at the same speed. These two values are comparable and suggest that the adhesion break-up is partially due to the PI and not just the film structure. Similarly, at higher velocities, the ratio of the PI-removed to the two component film ($\mu/\mu' = 1.2 - 2.3$) is comparable to the ratio of the neat PS film to the two-component film ($\mu_{PS}/\mu_{x_{PS} = 0.75} = 1.3 - 2.0$). To further probe the difference

between the PI removed and the two-component films, the wear tracks were compared under the same conditions, as shown in Figure 5-19.

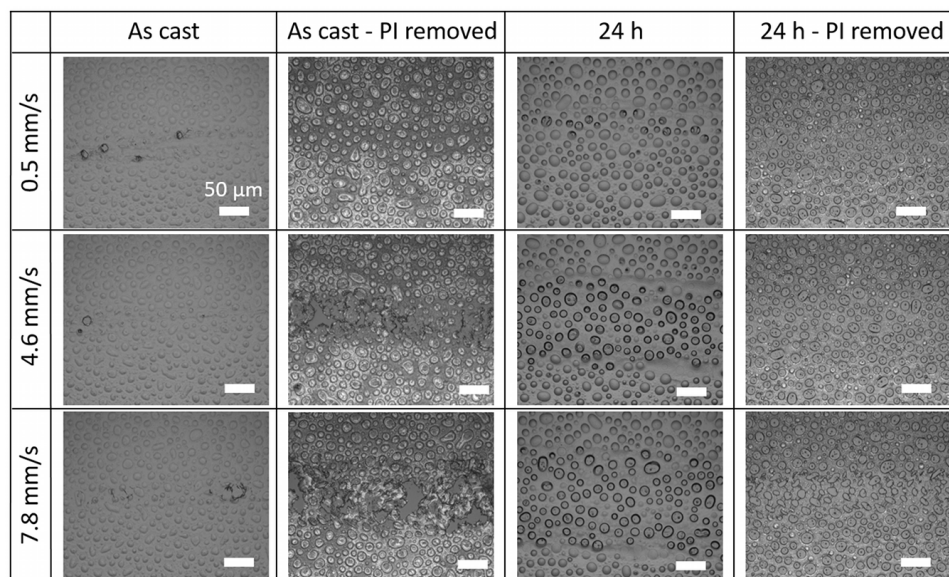


Figure 5-19. Wear tracks in PI-removed films (casting $x_{PS} = 0.75$). The as-cast film with PI phase removed showed higher wear than the two-component as-cast film. In the 24 h anneal samples, the increase in wear upon PI removal is less pronounced due to the enhanced de-mixing of the PS and PI under the annealing conditions.

The wear of the PI removed films is more significant than the PI-containing films. The higher wear in the PI removed films could result from the increased roughness after selectively removing the PI domain with *n*-hexane. The as-cast films also showed higher wear than the annealed films after the *n*-hexane wash; this effect is likely due to enhanced de-mixing of the PS and PI upon annealing. Thus, the structural integrity of the film was less affected upon washing with *n*-hexane after annealing.

5.3.5 Effect of Domain Size on Friction Coefficient

From the results discussed in the previous sections, it is evident that the composition affects the domain size, contact radius (modulus), and adhesion, which then change the friction coefficient. The domain size can also influence the friction coefficient, which has been documented previously in the literature.^{15-16, 19} Thus, changing the domain size independently of composition is key to understanding the effect of film microstructure on the blend friction coefficient. The film structure can be altered by changing the solution thermodynamics (compatibilizer, polymer choice, solvent choice), manipulating the processing (temperature, drying behavior), or post-casting modifications (thermal or solvent annealing). The first option can also affect the friction coefficient independent of either composition or domain size. Thus, the second two methods were implemented to change the film morphology.

Post-production processing procedures are useful, as they do not require modifications to the casting equipment. Though thermal annealing can be used, solvent vapor annealing is more widely applicable, as it can be used to tune the selectivity of the free surface for polymers with dissimilar surface energies or to anneal polymers that are susceptible to thermal degradation.³⁰ As such, we used solvent to modify the domains in $x_{PS} = 0.75$ films. The domain sizes were tuned on cast films using solvent vapor annealing. The effect of annealing on domain size is summarized in Figure 5-20. The optical micrographs (a-i) illustrate the increase in domain size with annealing time. The domain size of the droplet phase was also determined as described in Section 5.3.2. The area weighted chord length is plotted in Figure 5-20j. The chord length increased with increasing annealing times, except between 10 h and 16 h. The 14 h annealed film, for which the optical micrograph is shown in Figure 5-20e, has a smaller domain size. This decrease in domain size is due

to processing variability, most notably temperature differences, over the course of the various annealing experiments. Longer annealing times produced macroscopic structures that were larger than the contact radius. These films could not be studied under the same conditions and provide friction coefficients that were representative of the composite film. Thus, there is a limit to the domain sizes that could be probed in this study. Annealing times that were 48 h or shorter produced domain sizes that were smaller than the contact radius.

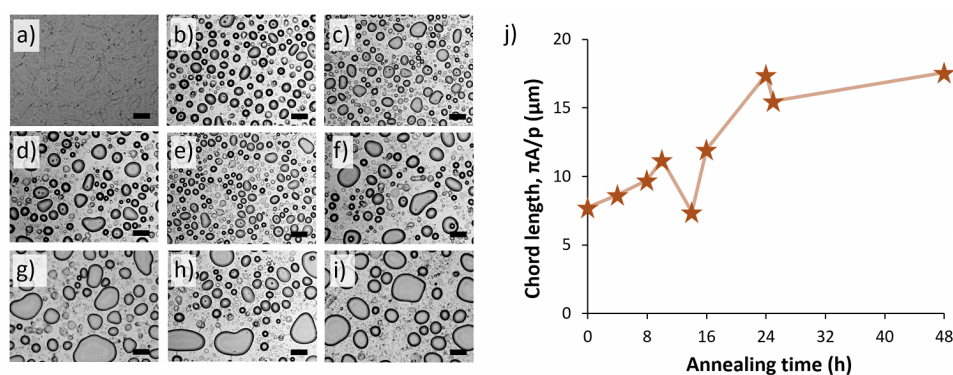


Figure 5-20. a)-i) optical micrographs of annealed $x_{PS} = 0.75$ films. Films were annealed in *o*-xylene for a) 0 h (as-cast) b) 4 h, c) 8 h, d) 10 h, e) 14 h, f) 16 h, g) 24 h, h) 25 h, i) 48 h. The resulting increase in domain size with increasing annealing time is shown in j). Note: due to processing variabilities, there is not a strictly linear increase in domain size with annealing time. The scale bars represent 25 μm .

The friction coefficient for the annealed films is shown in Figure 5-21a. At velocities of 4.6 mm/s and 7.8 mm/s, the friction coefficient increased with increasing annealing time (domain size), as shown in Figure 5-21b. However, at 0.5 mm/s, the friction coefficient was independent of domain size. This effect is likely the result of PI relaxation.

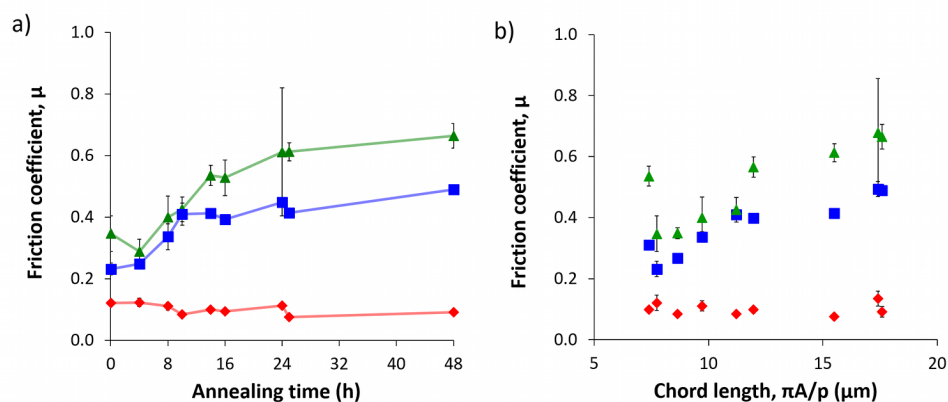


Figure 5-21. a) Friction coefficient of $x_{PS} = 0.75$ films with the glass probe measured at 0.5 mm/s (◆), 4.6 mm/s (■), and 7.8 mm/s (▲). Re-plotting of the friction coefficient with chord length, b) shows a correlation between the domain size and friction coefficient at a constant composition for the two higher speeds. The lowest speed shows no dependence of friction coefficient on annealing time; this effect is likely due to the relaxation of PI during these experiments.

The Deborah number (De) can be used to provide insight into the material flow relative to the timescale of deformation and is given by the ratio of the relaxation time to the characteristic timescale of deformation ($De = \tau/t_{exp}$). $De \leq 1$ indicates the material behaves as a fluid and flows under the experimental conditions. Higher De means that the polymer will not relax within the characteristic time scale of the applied stress, behaving more as a solid. In these friction coefficient measurements, the probe reciprocates linearly across the sample. Thus, there are two timescales of interest: (1) deformation during each pass and (2) relaxation between passes. The deformation during each pass can be characterized by the Deborah number, for which the deformation timescale is given by the ratio of the probe radius to the velocity. Thus, the deformation timescales for PI, are 0.57 s, 0.06 s, and 0.04 s at 0.5 mm/s, 4.6 mm/s, and 7.8 mm/s, respectively. These timescales are order of magnitude smaller

for PS, given that the contact radius is 10 times smaller between PS and either probe than the contact radius of PI with the probe. These times are much faster than the relaxation of either polymer.³¹⁻³³

The second timescale is related to relaxation between deformations. At 0.5 mm/s, the time during which the polymer can relax between deformations is of order 4 s. PI has a relaxation time of ~ 31 s,³¹⁻³³ which produces a De of 7.8 at 0.5 mm/s. In comparison to the De at 0.5 mm/s, the De is 71 and 121 at 4.6 mm/s and 7.8 mm/s, respectively. Thus, the material has improved flow at the lowest speed. The low De at 0.5 mm/s could allow the PI to relax, even as it adheres to the probe. At higher velocities (increased De), because PI has the same adhesion interaction but can no longer relax between deformations, the films are torn more quickly, which produces debris in the wear track. As debris can increase the friction coefficient in the sample, higher De value corresponds to more wear and friction in the film. Therefore, the PI fluidity plays a role in decreasing the friction coefficient at 0.5 mm/s, irrespective of domain size.

In addition to the friction coefficient of annealed films, the effect of annealing time and probe velocity on the wear track was studied. Figure 5-22 shows the wear tracks for the various films. At all velocities, the visibility of the wear track is reduced with increasing annealing time. As discussed in Section 5.3.1, there is a PI wetting layer at the free surface. During the annealing process, the films are exposed to a solvent-rich atmosphere. Because *o*-xylene is a nearly neutral solvent for PS and PI, the selectivity of the free surface is changed from PI-preferential to neutral. Thus, annealing also reduces the PI wetting.

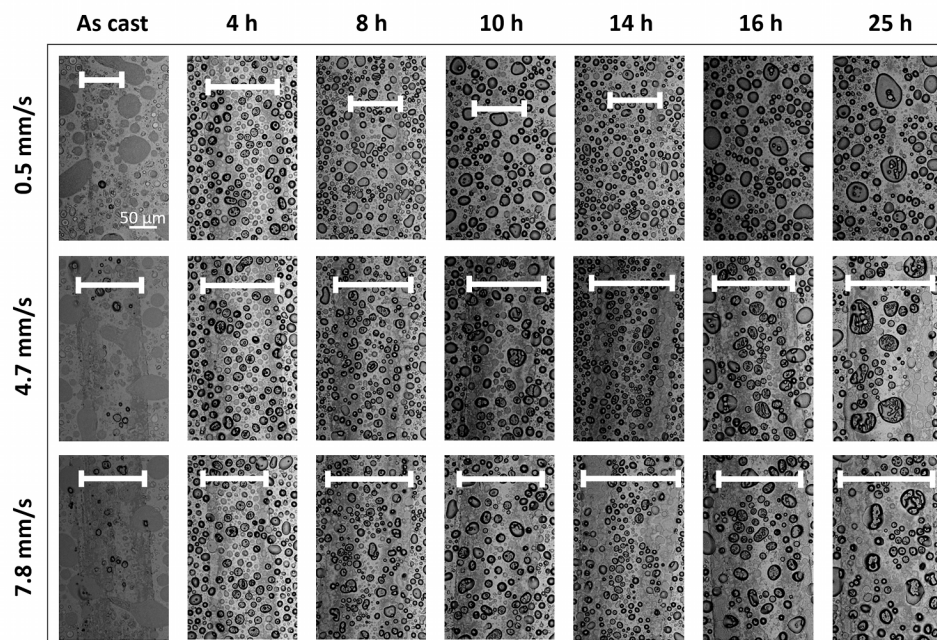


Figure 5-22. Wear tracks for annealed $x_{PS} = 0.75$ films. Wear tracks are shown for 0.5 mm/s, 4.6 mm/s, and 7.8 mm/s for an as-cast film as well as films annealed in *o*-xylene for 4 h, 8 h, 10 h, 14 h, 16 h, and 25 h.

For the varied composition films, the width of wear tracks (Figure 5-15) were notably different at the same velocity. The wear tracks for the constant composition, annealed films (Figure 5-22) are more similar in size at the same velocity, suggesting that the contact radius is not significantly changed for these blends. Thus, the annealing likely does not affect the material modulus significantly. Overall, these studies provide insight into the effect of domain size on friction; the friction coefficient increases with increasing domain size.

In addition to the post-casting annealing, *in situ* annealing during casting also can be used to control the film structure. The drying behavior was modified by introducing a radiative heat source during casting. This heat source was used to increase the temperature above the wafer to improve the compatibility of the

polymers, thereby increasing the domain size. As shown in Figure 5-23, the domain size increased with increasing temperature.

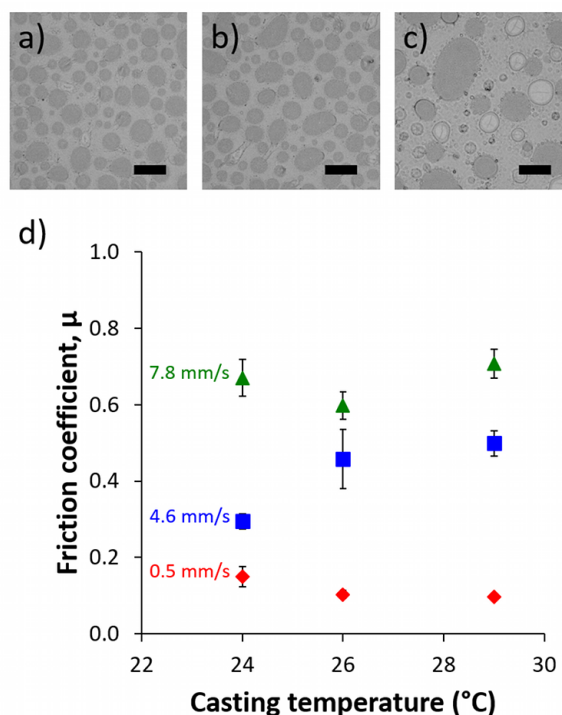


Figure 5-23. Tuning domain size during casting with combined radiation and convection. Optical micrographs of films cast onto substrates at a) 24 °C, b) 26 °C, and c) 29 °C. The apparent domain size increased with increasing temperature. The brightness and contrast of the optical micrographs were artificially enhanced. The scale bars represent 50 μm. d) The friction coefficient as a function of substrate temperature during casting. Increases in temperature, which produced larger domain sizes, resulted in higher friction coefficients at 7.8 mm/s and 4.6 mm/s. At 0.5 mm/s, the friction coefficient remained independent of casting temperature, which is likely due to the lower De of the film under these experimental conditions.

The friction coefficient for these materials were also measured, as shown in Figure 5-23d. The domain size increased with temperature, which lead to higher friction coefficients at 4.6 mm/s and 7.8 mm/s. At 0.5 mm/s, the friction coefficient was independent of temperature. As discussed previously, this effect likely is due to the low Deborah number in these films. Provided that the domain size is smaller than the contact radius of the probe with the film, the friction coefficient increases with domain size at a constant composition, regardless of the method used to control the film structure.

5.4 Conclusions

As demonstrated in this chapter, the microstructure of polymer blend films can significantly impact the material properties for coatings applications. Studying the relationship between the domain size, composition, and friction and wear of polymer blend films can inform the development of novel functional coatings. With a model PS/PI blend film, the friction coefficient was controlled by tuning the domain size and composition, as shown in Figure 5-24, measured at a velocity of 4.6 mm/s. The blend modulus (contact radius) and domain size both influenced the friction coefficient, producing a non-monotonic trend in friction coefficient with domain size. Additionally, the friction coefficient was strongly impacted by probe-film adhesion, which varied with the chemical make-up of the surface. Thus, decoupling the domain size with composition can afford new insights into the friction coefficient of multicomponent films. At a constant composition, μ increased with increasing domain size.

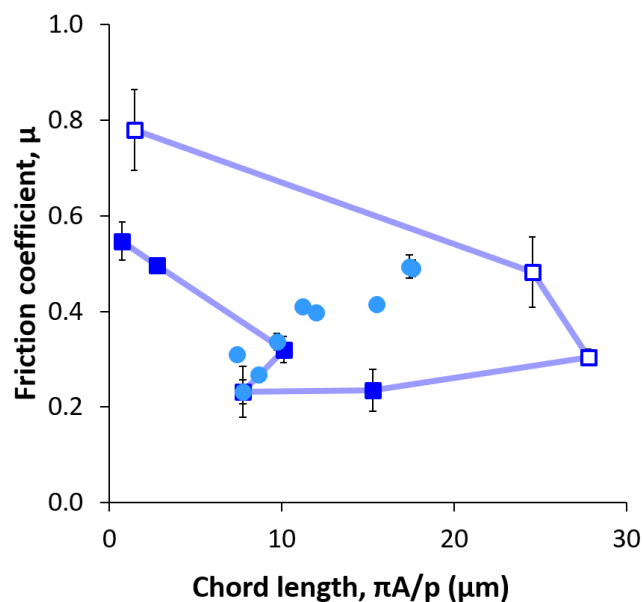


Figure 5-24. Effect of domain size on friction coefficient for varied composition films ($x_{PS} > 0.6$: ■, $x_{PS} \leq 0.6$: □) and annealed constant composition films (●). At a constant composition, the friction coefficient increases with domain size. For the varied composition films, the friction coefficient depends on both the composition and domain size.

The procedures and analysis developed herein provide a robust method to independently determine the effect of domain size on the friction coefficient, which can be applied towards in line, high-throughput screening of polymer blend films for tribology applications.

The wear of the polymer blend films was not explicitly studied in this chapter; the polymer blend wear can also impact the friction coefficient. Thus, a more detailed study on the wear of polymer blends can afford new insights into the effect of composition on the friction coefficient. Additionally, it would be of interest to extract the effect of modulus on the contact radius by both measuring the modulus and determining the effect of contact area experimentally. Finally, the wear resistance in

these films was low; low loads and slower speeds was required to improve the stability of these films under the experimental conditions. To afford enhanced wear resistance, other polymers can be employed or nanofillers can be added.

REFERENCES

1. Fabiano, S.; Himmelberger, S.; Drees, M.; Chen, Z.; Altamimi, R. M.; Salleo, A.; Loi, M. A.; Facchetti, A. C., Charge transport orthogonality in all-polymer blend transistors, diodes, and solar cells. *Adv. Energy Mater.* **2014**, *4*, 1301409.
2. Yu, G.; Nishino, H.; Heeger, A. J.; Chen, T. A.; Rieke, R. D., Enhanced electroluminescence from semiconducting polymer blends. *Synth. Met.* **1995**, *72*, 249-252.
3. Javier, A. E.; Patel, S. N.; Hallinan, D. T.; Srinivasan, V.; Balsara, N. P., Simultaneous electronic and ionic conduction in a block copolymer: application in lithium battery electrodes. *Angew. Chem. Int. Ed.* **2011**, *50*, 9848-9851.
4. Müller-Buschbaum, P.; Ittner, T.; Maurer, E.; Körstgens, V.; Petry, W., Pressure-sensitive adhesive blend films for low-tack applications. *Macromol. Mater. Eng.* **2007**, *292*, 825-834.
5. Nunes-Pereira, J.; Costa, C. M.; Lanceros-Mendez, S., Polymer composites and blends for battery separators: state of the art, challenges and future trends. *J. Power Sources* **2015**, *281*, 378 - 398.
6. Colaneri, N. F.; Schacklette, L. W., EMI shielding measurements of conductive polymer blends. *IEEE Trans. Instrum. Meas.* **1992**, *41*, 291-297.
7. Walheim, S.; Schäffer, E.; Mlynek, J.; Steiner, U., Nanophase-separated polymer films as high-performance antireflection coatings. *Science* **1999**, *283*, 520.
8. Paul, D. R., *Polymer Blends*. Elsevier Science: 2012.
9. Utracki, L. A., *Polymer Blends Handbook*. Springer Netherlands: 2003.
10. Hussain, F.; Hojjati, M.; Okamoto, M.; Gorga, R. E., Review article: polymer-matrix nanocomposites, processing, manufacturing, and application: an overview. *J. Compos. Mater.* **2006**, *40*, 1511-1575.

11. Chen, Z.; Li, T.; Yang, Y.; Liu, X.; Lv, R., Mechanical and tribological properties of PA/PPS blends. *Wear* **2004**, *257*, 696 - 707.
12. Chen, Z.-B.; Li, T.-S.; Yang, Y.-L.; Zhang, Y.; Lai, S.-Q., The effect of phase structure on the tribological properties of PA66/HDPE blends. *Macromol. Mater. Eng.* **2004**, *289*, 662-671.
13. Chen, Z.; Liu, X.; Li, T.; Lü, R., Mechanical and tribological properties of PA66/PPS blend. II. Filled with PTFE. *J. Appl. Polym. Sci.* **2006**, *101*, 969-977.
14. Brostow, W. a. D. T. a. H. B., Tribological properties of blends of melamine-formaldehyde resin with low density polyethylene. *Polymer Engineering & Science* **2008**, *48*, 292--296.
15. Bijwe, J.; Sen, S.; Ghosh, A., Influence of PTFE content in PEEK–PTFE blends on mechanical properties and tribo-performance in various wear modes. *Wear* **2005**, *258*, 1536 - 1542.
16. Burris, D. L.; Sawyer, W. G., A low friction and ultra low wear rate PEEK/PTFE composite. *Wear* **2006**, *261*, 410 - 418.
17. Stuart, B. H., Tribological studies of poly(ether ether ketone) blends. *Tribol. Int.* **1998**, *31*, 647 - 651.
18. Lu, Z. P.; Friedrich, K., On sliding friction and wear of PEEK and its composites. *Wear* **1995**, *181*, 624 - 631.
19. Briscoe, B. J.; Yao, L. H.; Stolarski, T. A., The friction and wear of poly(tetrafluoroethylene)-poly (etheretherketone) composites: An initial appraisal of the optimum composition. *Wear* **1986**, *108*, 357 - 374.
20. McLaren, K. G.; Tabor, D., Visco-elastic properties and the friction of solids: friction of polymers: influence of speed and temperature. *Nature* **1963**, *197*, 856-858.
21. Grosch, K. A., Visco-elastic properties and the friction of solids: relation between the friction and visco-elastic properties of rubber. *Nature* **1963**, *197*, 858-859.
22. Stafford, C. M.; Roskov, K. E.; Epps, T. H., III; Fasolka, M. J., Generating thickness gradients of thin polymer films via flow coating. *Rev. Sci. Instrum.* **2006**, *77*, 023908.

23. Ferreira, T.; Rashband, W., Image J User Guide - IJ 1.46. 2010-2012, imagej.nih.gov/ij/docs/guide/.
24. Walheim, S.; Boltau, M.; Mlynek, J.; Krausch, G.; Steiner, U., Structure formation via polymer demixing in spin-cast films. *Macromolecules* **1997**, *30*, 4995-5003.
25. Wu, S., *Polymer Interface and Adhesion*. Taylor & Francis: 1982.
26. Scott, R. L., The thermodynamics of high polymer solutions. V. Phase equilibria in the ternary system: polymer 1 – polymer 2 – solvent. *J. Chem. Phys.* **1949**, *17*, 279-284.
27. Le Berre, M.; Chen, Y.; Baigl, D., From convective assembly to Landau–Levich deposition of multilayered phospholipid films of controlled thickness. *Langmuir* **2009**, *25*, 2554-2557.
28. Davis, R. L.; Jayaraman, S.; Chaikin, P. M.; Register, R. A., Creating controlled thickness gradients in polymer thin films via flowcoating. *Langmuir* **2014**, *30*, 5637-5644.
29. Leclair, A.; Favis, B. D., The role of interfacial contact in immiscible binary polymer blends and its influence on mechanical properties. *Polymer* **1996**, *37*, 4723-4728.
30. Albert, J. N. L.; Epps, T. H., III, Self-assembly of block copolymer thin films. *Mater. Today* **2010**, *13*, 24-33.
31. Bero, C. A.; Roland, C. M., Terminal relaxations in linear and three-arm star polyisoprenes. *Macromolecules* **1996**, *29*, 1562-1568.
32. Santangelo, P. G.; Roland, C. M., Temperature dependence of mechanical and dielectric relaxation in cis-1,4-polyisoprene. *Macromolecules* **1998**, *31*, 3715-3719.
33. Roland, C. M.; Bero, C. A., Normal mode relaxation in linear and branched polyisoprene. *Macromolecules* **1996**, *29*, 7521-7526.

Chapter 6

CHEMICAL AND FRICTION PROPERTIES OF SUSTAINABLE POLYMERS

6.1 Introduction

Polymers sourced from renewable and cost-competitive feedstocks have gained increasing interest in the past decade to the polymers community. Many feedstock types have emerged as promising sources of monomer units for green polymer synthesis, such as lignin, cellulose, vegetable oils, chitin/chitosan, and starches.¹ In particular, polymers with comparable material properties to polystyrene [PS] or poly(methyl methacrylate) [PMMA] are desirable, as these polymers can be utilized in a variety of applications. Lignin is a promising feedstock as it has substantial aromatic character, which would provide higher glass transition temperatures comparable to those of PS and PMMA.² Additionally, lignin is abundant, inexpensive, and renewable; currently it is produced as a waste product from the paper and pulping industry in ~70 million tons/year.³ The total annual plastic production globally is ~300 million tons.⁴ Thus, utilizing lignin as a feedstock produces a viable pathway to significantly reduce dependence on fossil fuels.

However, lignin is a complex macromolecule and is compositionally different depending on the feedstock.^{1, 3, 5-7} Thus, to produce sustainable polymers with reproducible structures, it is of interest to fragment the lignin macromolecule into monomeric structures that are then polymerized. Using Kraft pyrolysis, lignin can be broken down into a variety of subunits including guaiacols and syringols.⁵⁻⁷ Of

particular interest is studying new bio-based polymers in thin films towards generation of novel coatings.⁸

For coatings applications, the properties of interest include the solubility, surface energy, and friction coefficient. Solubility influences the ability to process the polymers in solution and also determines the resistance of the material to various solvents in application. Predictions of solubility parameters by group contribution theory utilize the chemical constituents, suggesting that the solubility is controlled by the chemical nature of the material.⁹ The surface energy plays a role in the wettability of polymer on various substrates, as well as the wetting of other fluids on the polymer film.¹⁰⁻¹³ Shelton and coworkers recently demonstrated that the surface energy components can be used to accurately describe the wetting behavior in block polymer films.¹¹ Finally, the friction coefficient affords characterization of the interactions between two surfaces.¹⁴ The friction coefficient is influenced by the adhesion between the probe and the film, which is controlled by the chemical composition and interfacial energy of the two materials.¹⁵ For example, the friction coefficient of a polyethylene film is 5 times smaller than that of a polystyrene film measured under the same conditions.¹⁶ Thus, the solubility, surface energy, and friction coefficient of polymers depend strongly on the material structure.¹⁵⁻¹⁷

However, due to the variation in lignin composition from different feedstocks, understanding the effect of the functional groups on material properties is vital towards utilizing lignin-derived methacrylates. To this end, a library of sustainable methacrylate polymers was selected with various functionality in the *ortho* or *para* positions relative to the polymer backbone. These functional groups were selected as they represent the majority components in lignin pyrolysis products.⁵⁻⁷ This series of

polymers then represents the most common structures that could be produced from lignin pyrolysis products. The polymer structures are given in Table 6-1.

Table 6-1. Sustainable polymer library. Chemical structures of sustainable polymers. All polymers share the same general backbone and repeat unit structures; each polymer differs at the functional groups *ortho* (R_1 , R_3) and *para* (R_2) to the methacrylate backbone.

General structure	Polymer	Abbrev.	R_1	R_2	R_3
	poly(phenyl methacrylate)	PPM	H	H	H
	poly(guaiacyl methacrylate)	PGM	OCH ₃	H	H
	poly(creosyl methacrylate)	PCM	OCH ₃	CH ₃	H
	poly(4-ethyl guaiacyl methacrylate)	PEM	OCH ₃	CH ₂ CH ₃	H
	poly(vanillin methacrylate)	PVM	OCH ₃	CHO	H
	poly(syringyl methacrylate)	PSM	OCH ₃	H	OCH ₃
	poly(syringaldehyde methacrylate)	PSAM	OCH ₃	CHO	OCH ₃

Previous work in the group focused on synthesizing this library of lignin-derived polymers and characterizing the bulk properties, such as the glass transition temperature (T_g), elastic shear modulus (G'), complex and zero shear viscosity (η^* , η_0), and the onset and peak degradation temperatures (T_o , T_p).¹⁸⁻¹⁹ The differences in the bulk properties were related back to the functional group. For example, the T_g of poly(syringyl methacrylate) [PSM] is ~ 100 K higher than the T_g of poly(guaiacyl methacrylate) [PGM]. The two polymers differ by a methoxy group *ortho* to the polymer backbone, of which PSM has 2 and PGM has 1. The drastically higher T_g of PSM in comparison to PGM was attributed to the reduction in rotation freedom due to interactions between the carbonyl ester and the bulky *ortho* groups.¹⁹ Despite the advances made in generating and characterizing lignin-based polymers, the material properties of these sustainable polymers have not been fully elucidated. Using the library of polymers shown in Table 6-1, the solubility, surface energy, and friction

coefficient of each polymer was related to the pendant group functionality to develop *a priori* insight into the material properties based on feedstock composition.

6.2 Materials & Methods

6.2.1 Solvents

Tetrahydrofuran [THF] (optima), chloroform [CHCl₃] (certified ACS), dichloromethane [DCM] (certified ACS), and acetone (certified ACS) were purchased from Fisher Scientific. Anisole (anhydrous, 99.7%) and 2-butanone [MEK] (> 99%) were obtained from Sigma-Aldrich, and dimethylformamide [DMF] (HPLC grade) was procured from Acros Organics. All solvents were used as received.

6.2.2 Polymer Synthesis and Characterization

Sustainable polymers were synthesized using reversible addition–fragmentation chain-transfer [RAFT] polymerization as described elsewhere.^{2, 18-21} The polymers were synthesized by Dr. A. L. Holmberg, Dr. S. Wang, and M. Karavolias. The molecular weight and dispersities of the polymers were determined from light scattering in THF, except PSM and PSAM, for which the molecular weight distribution was calculated relative to polystyrene standards *via* SEC with refractive index detectors in chloroform.^{2, 18-21}

6.2.3 Glass Transition Temperature

The glass transition temperature of each polymer was determined from DSC using a TA Instruments Discovery DSC. For PGM, PCM, PEM, PVM, and PSM, the T_g was calculated from the second DSC trace on heating at 2 °C/min in N₂.¹⁸⁻²⁰ T_g for

PSAM and PPM were taken from the second DSC trace on heating at 5 °C/min in N₂, shown in Appendix D.

6.2.4 Film Casting

A flow coating apparatus was used to cast solutions onto cleaned silicon wafers.²² All substrates were triple rinsed with toluene before and after cleaning with ultraviolet-ozone (Jelight, Model 342). For films on silicon wafers (solvent vapor swelling, contact angle), solutions of 2 wt.% polymer in anisole were prepared gravimetrically. The flow coating apparatus was operated with a velocity of 17 mm/s, acceleration of 0.4 mm/s², gap height of 70 μm, and a blade width of 15 mm. 70 μL of solution were deposited under the blade. Due to the high boiling point of anisole, solubility limits of the sustainable polymers, and requisite film thickness > 100 nm, the solvent evaporation did not follow a directional drying front induced by the blade motion. Thus, additional convection was applied during casting to induce directional drying (shown schematically in Figure 3-1), which produced more uniform films

To produce thicker films for tribology experiments on silicon wafers, 10 wt.% solutions were prepared in DCM. These films were cast at a velocity of 12 mm/s, acceleration of 0.8 mm/s², and a blade width of 20 mm. The gap height was 70 μm, and the solution volume was 50 μL. These films did not require the forced convection to induce directional drying.

6.2.5 Solvent Vapor Swelling

Solvent vapor swelling was used to determine the solvent-polymer interaction parameter for the sustainable polymers in THF and CHCl₃, as described in Chapter 2 and Chapter 4. The total flow rate was maintained at 25 mL/min, and the solvent

concentration was tuned by changing the relative flow rate between the solvent-rich stream and the nitrogen diluent.

6.2.6 Atomic Force Microscopy

A Veeco Nanoscope V Dimension 3100 atomic force microscopy [AFM] operated in tapping mode was used to capture the atomic force micrographs. Silicon probes (tap150) with a force constant of 5 N/m and resonant frequencies between 120 kHz and 180 kHz were used to image the films. The thickness of the films was measured using a scratch test method, in which a scratch is made in the film to measure the relative height between the substrate and film surface. The roughness was characterized using AFM height images.

6.2.7 Contact Angle

Static sessile contact angle measurements were performed using a First Ten Ångströms FTÅ 125 contact angle device. Diiodomethane (99%, stabilized, Acros Organics) and water (purified with a Milli-Q reagent water purification system) were selected as the probe liquids, and 2 μL of liquid was dispensed onto the film surface using a DISTRIMAN pipet. The static contact angles were recorded after the drop shape stabilized (4 s for both diiodomethane and water). The contact angles were calculated from the images using the manual points fitting algorithm in the ImageJ contact angle plugin.

Advancing and receding contact angles were measured with a Kruss EasyDrop contact angle goniometer and analyzed using the same ImageJ plugin as the static sessile contact angle measurements. For the advancing contact angle measurements, $\sim 0.84 \mu\text{L}$ increments were added and imaged after 10 s. 5 measurements were taken on

the same spot with the same volume, spaced out every 2 s, to ensure the droplet was not changing in time after the first 10 s. The maximum total volume was ~12.5 μL . The contact angle was measured from the images using the ImageJ contact angle plugin. Receding contact angles were measured using the same protocol with the same volumetric increments.

6.3 Results & Discussion

To systematically study the effect of functional group on the solubility, surface energy, and friction coefficient, two sets of chemically identical polymers were utilized in this work. The first set, which typically had a higher molecular weight, were studied using solvent vapor swelling and contact angle tests. The higher molecular weight polymers provided enhanced solvent stability to probe the interactions over a wider solvent concentration range.²³ The second set was used in the tribology tests. The molecular weight, dispersity, and glass transition temperature of the polymers are given in Table 6-2.

Table 6-2. Molecular weight and glass transition temperature of sustainable polymers used in the solvent vapor swelling experiments and the friction coefficient measurements.

Polymer	Solvent vapor swelling			Friction coefficient		
	M_n^a kDa	\bar{D}^a	T_g^d K	M_n^a kDa	\bar{D}^a	T_g^d K
PPM	41 ^c	1.2 ^c	392 ^e	41 ^c	1.2 ^c	392 ^e
PGM	38	1.3	388	26	1.2	385
PCM	34	1.4	394	29	1.2	398
PEM	35	1.3	384	26	1.2	381
PVM	36	1.4	402	24	1.5	398
PSM	24 ^b	1.7 ^b	478	21	1.5	476
PSAM	29 ^c	1.5 ^c	474 ^e	--	--	--

^aMolecular weight and dispersities determined from light scattering unless noted otherwise. Molecular weight and dispersities determined *via* SEC with refractive index detectors relative to polystyrene standards from ^breferences ¹⁸⁻²⁰ and ^cunpublished work (see Appendix D). ^d T_g from second DSC trace on heating at 2 °C/min in N₂, data from references ¹⁸⁻²⁰. ^eUnpublished T_g from second DSC trace on heating at 5 °C/min in N₂ (see Appendix D).

In addition to sustainable homopolymers, the solvent vapor swelling was studied for heteropolymers. Four heteropolymers were studied: poly(bio-oil methacrylate) [PBOM], PVES, PCES, and PES. The chemical constituents and molecular characterization of the heteropolymers are given in Table 6-3, as reported elsewhere.¹⁹⁻²¹

Table 6-3. Characterization data for the sustainable heteropolymers.

Polymer	Chemical constituents ^a					Characterization		
	GM	CM	EM	VM	SM	M_n^b kDa	\bar{D}^b	T_g^c K
PBOM	0.25	0.23	0.27	0.25	0.00	40.5	1.33	392
PVES	0.00	0.00	0.23	0.22	0.55	34.9	1.50	432
PCES	0.00	0.18	0.34	0.00	0.48	35.3	1.32	427
PES	0.00	0.00	0.95	0.00	0.05	35.8	1.30	387

^aWeight fraction of the base components with in the heteropolymers. ^bMolecular weight and dispersities determined from light scattering from ^breferences ¹⁹⁻²¹. ^c T_g from second DSC trace on heating at 2 °C/min in N₂, data from references ¹⁹⁻²¹.

6.3.1 Solvent Vapor Swelling

Solvent vapor swelling experiments were performed on the sustainable polymers with a total flow rate of 25 mL/min. These experiments are started at the highest concentration to avoid start-up effects.²⁴ At each composition of solvent, an equilibrium value was reached, after which the polymer volume fraction did not change in time. After equilibration, the relative flow rates of the solvent-rich vapor stream to the nitrogen diluent stream was changed to reduce the solvent concentration within the chamber. Example swelling curves for the sustainable polymers in THF are shown in Figure 6-1.

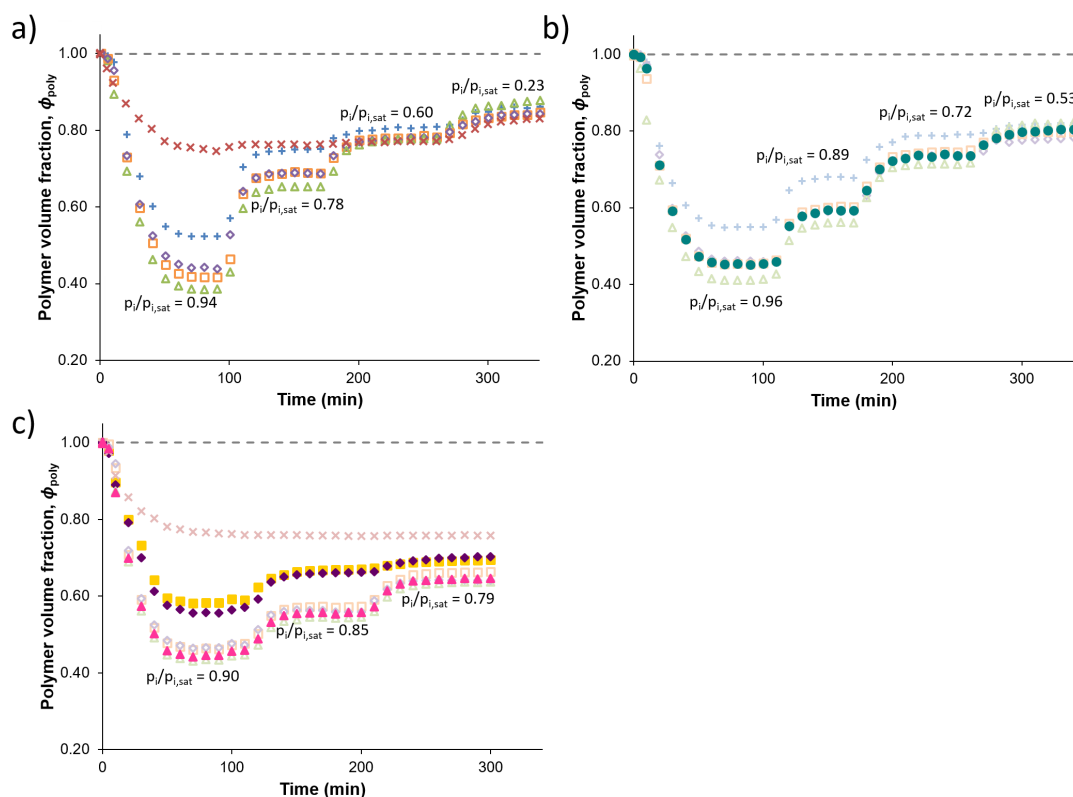


Figure 6-1. Sample swelling curves for polymers in THF. Increased compatibility occurs with decreasing polymer volume fraction. The solvent concentration is given by the ratio of the partial pressure to the saturated partial pressure, $p_i/p_{i,sat}$, for which the values are listed on the plots. The dashed line represents the non-swollen polymer (initial polymer volume fraction). a) Swelling of PSM (\times), PGM ($+$), PCM (\square), PVM (\diamond), PEM (\triangle). PSM had reduced swelling compared to the other polymers. This lack of swelling is likely due to the higher T_g of the material, which limits the mobility at insufficient solvent concentrations. b) Swelling of [PBOM] (\bullet) and c) PES (\blacktriangle), PCES (\blacksquare), PVES (\blacklozenge) in comparison to their homopolymer constituents.

For the homopolymers, PSM swelled the least, and PEM swelled the most. The PSM did not deswell upon solvent removal, which suggested the polymer film was in a non-equilibrium state. PSM had the highest T_g of the polymers used.

Therefore, the lack of equilibration could result from limited chain mobility under the experimental conditions. Historically, T_g reduction of a polymer upon solvent addition was studied using dynamic scanning calorimetry (DSC).²⁵ However, the solvent can destroy the electronic components of the DSC equipment. A variety of other methods have been utilized to examine the glass transition temperature in polymer systems.²⁶⁻²⁸ The refractive index,²⁶ film thickness,²⁶⁻²⁷ and self-diffusion coefficients²⁸ can inform the glass transition temperature. A change in slope of these parameters with temperature²⁶⁻²⁷ or solvent concentration²⁸ occurs at the glass transition temperature. The volume fraction of polymer in a swollen film is a measure of the change in film thickness, and the pressure ratio is used to characterize the solvent concentration. Thus, plotting the volume fraction data with solvent concentration can provide insight into the glass transition temperature of the polymers in a solvent-swollen state.

To test whether the other polymers had sufficient mobility to equilibrate with the solvent, the polymer volume fraction was plotted as a function of the solvent concentration, $p_i/p_{i,sat}$, as shown for PEM in Figure 6-2 (see Figure C-3 in Appendix D for the other polymers in THF). The intersection of the two lines, or the crossover point, occurs at the effective glass transition temperature under the experimental solvent concentration and temperature. The volume fraction corresponding to the maximum polymer volume fraction that still has chain mobility is the crossover volume fraction, ϕ_c . The solvent concentration at which ϕ_c occurs is $p_{i,c}/p_{i,sat}$.

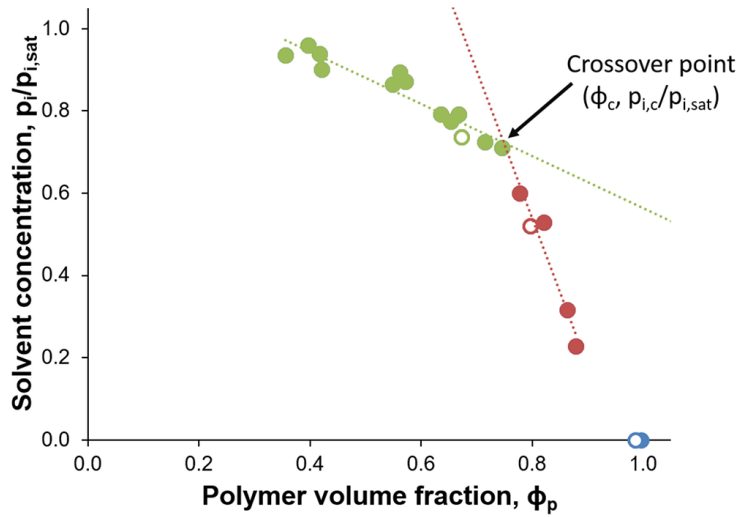


Figure 6-2. Effect of THF concentration on PEM mobility. The “rubbery” regime (●), in which the polymers have mobility, has a different slope than the “glassy” regime (●), in which the polymer is kinetically trapped. The closed symbols represent data from flow solvent vapor swelling experiments, whereas the open symbols represent data from THF/water bell jar experiments.

The crossover volume fraction, ϕ_c , for each polymer with THF is given in Figure 6-3a. ϕ_c of solvent/polymer mixtures also can be estimated from mixing rules between the glass transition temperatures of the neat polymer and solvent using eq. 6.1,²⁹

$$\frac{1}{T_{g,m}} = \frac{m_p}{T_{g,p}} + \frac{m_s}{T_{g,s}} \quad \text{eq. 6.1}$$

for which m_i is the weight or volume fraction of component i and $T_{g,i}$ is the glass transition temperature of i . Literature values were used for the solvent T_g 's. The resulting ranges of polymer volume fraction using eq. 6.1 with THF are represented by the shaded region in Figure 6-3a. The corresponding solvent concentration required to

reach ϕ_c in these experiments, $p_{i,c}/p_{i,sat}$, is shown in Figure 6-3b. $p_{i,c}/p_{i,sat}$ typically was between 0.70 and 0.75.

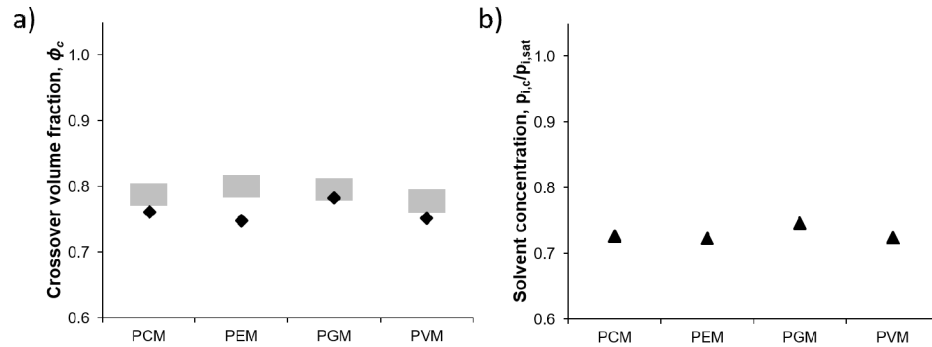


Figure 6-3. a) Data points represent crossover polymer volume fraction for sustainable polymers. Shaded regions represent the estimated crossover from eq. 6.1 for each polymer. b) Crossover solvent concentration ($p_{i,c}/p_{i,sat}$) required to access the minimum polymer volume fraction for chain mobility.

Excluding swelling data that is within the glassy regime ($\phi_c < 0.75$, $p_{i,c}/p_{i,sat} < 0.70$), the Flory-Huggins solvent-polymer interaction parameter can be calculated.

Rearranging the swelling equation yields eq. 6.2, described previously in Chapter 4:

$$\ln\left(\frac{p}{p_{sat}}\right) - \ln(1 - \phi_p) - \left(1 - \frac{V_s}{V_p}\right)\phi_p = \chi_{s-p}\phi_p^2 \quad \text{eq. 6.2}$$

Thus, by plotting the LHS of eq. 6.2 as a function of ϕ_p^2 , the slope of the linear fit to the data is the Flory-Huggins solvent-polymer interaction parameter.

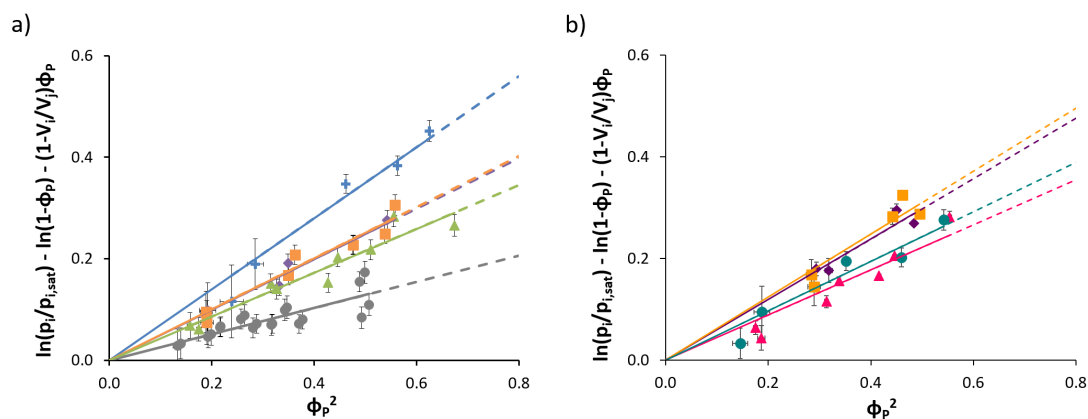


Figure 6-4. Replotting equilibrium swelling data for lignin-derived a) homopolymers and b) heteropolymers in THF. The solid lines represent the linear fit to the data, and the dashed lines represent the extrapolation of the fits. The homopolymers shown in a) in order of increasing compatibility with THF are PGM (+), PCM (■), PVM (◆), PEM (▲), PPM (●). The solubility of the heteropolymers in b) increases as expected based on the constituent make-up of the polymers: PCES (■) ~ PVES (◆) < PBOM (●) < PES (▲). The Flory-Huggins solvent-polymer interaction parameters are given in Table 6-4.

In comparison to PGM, which has a methoxy group in the *ortho* position, polymers containing functional constituents *para* to the backbone have increased solubility. PPM has the highest compatibility with THF; the methoxy group on PGM reduces the solubility of the polymer. The resulting Flory-Huggins solvent-polymer interaction parameters are shown in Table 6-4. These data suggest that THF is a good solvent ($\chi < 0.5$) for PPM and PEM, a theta solvent ($\chi = 0.5$) for PCM and PVM, and a poor solvent ($\chi > 0.5$) for PGM.

The THF-polymer interaction parameters for heteropolymers, which contain different functional groups, fall between the values for the homopolymers comprised of the constituent monomers. PES has the highest solubility, as it contains majority EM, but it is slightly less soluble than PEM due to the small fraction of SM. PCES

and PVES have the same interaction parameter within error, largely due to their similar compositions of EM and SM, as PCM and PVM have nearly identical interactions with THF. PBOM, which contains almost equivalent mass fractions of EM, GM, VM, and CM has a solubility parameter close to PVM, PCM, and PEM and lower than PGM. Thus, the relative solubility of the sustainable polymers can be tuned by incorporating monomers with different *ortho* and *para* constituents. This effect may be of interest to improve the solubility of higher T_g materials (e.g. PSM) or to increase the solvent resistance of other polymers, such as PEM.

Table 6-4. Flory-Huggins solvent-polymer interaction parameters for the homopolymers and heteropolymers with THF. As expected, the values of the heteropolymers fall between the interaction parameters of the homopolymers based on the same monomer constituents.

<u>homopolymer</u>		<u>heteropolymer</u>	
polymer	$\chi_{\text{THF-p}}$	polymer	$\chi_{\text{THF-p}}$
PGM	0.70 ± 0.03	PCES	0.56 ± 0.04
PVM	0.50 ± 0.02	PVES	0.52 ± 0.05
PCM	0.50 ± 0.02	PBOM	0.49 ± 0.03
PEM	0.43 ± 0.02	PES	0.43 ± 0.03
PPM	0.26 ± 0.02		

As discussed previously PSM had a higher solvent resistance to THF due to its higher T_g . However, the PSM did not swell sufficiently in THF to reach an equilibrium state, which is required to accurately capture the interaction parameter. In order to calculate solvent-PSM interaction parameters, there must be sufficient solvent to provide chain mobility. The maximum swelling of PSM in various solvents was studied using a bell jar annealing set-up, for which $p_i/p_{i,sat} = 1$. These solvents had a wide range of solubility parameters (see Figure 6-5), which allowed screening of a variety of solvent-polymer interaction parameters to produce the most swelling. For

the solvents tested, the critical PSM concentration, estimated using eq. 6.1, is ~ 0.60 to ~ 0.70 .

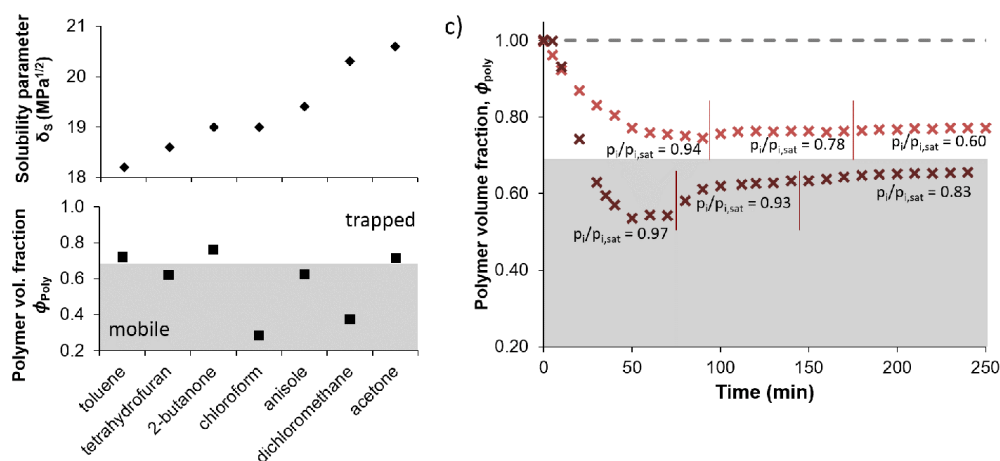


Figure 6-5. T_g and solvent quality for PSM. a) Polymer volume fractions of PSM swollen in saturated solvents. The gray shaded region represents the polymer volume fraction regime in which PSM has mobility, from eq. 6.1. b) Solubility parameters for solvents tested. PSM had the highest swelling (lowest polymer volume fraction) in chlorinated solvents (CHCl₃, DCM). Due to the greater solvent uptake compared to the other solvents tested, CHCl₃ was selected for further experiments. c) Flow SVA of PSM in THF (top, \times) and CHCl₃ (bottom, \times). At similar solvent concentrations ($p_i/p_{i,sat}$), CHCl₃ swelled PSM more than THF. Additionally, the rubbery regime was accessible in the flow set-up with CHCl₃ (see Appendix D, Figure D-4)

The swelling behavior of the polymers were tested in CHCl₃. PEM, PGM, and PCM dewet at the highest solvent concentrations. This effect likely is due to destabilization by short-range polar forces.³⁰⁻³¹ Reducing the concentration of CHCl₃ sufficiently to prevent dewetting did not provide adequate polymer mobility in these films to achieve an equilibrium structure. Thus, it was not possible to capture the

CHCl₃-polymer interaction parameters for these polymers; a higher molecular weight polymer could be used to produce a more stable film and provide these interaction parameters. Due to its higher solubility in THF, PPM was not tested in CHCl₃, as it likely would dewet more readily than the other polymers. Future tests could be performed to probe the solubility of these polymers in CHCl₃, provided that higher molecular weight polymers were used. Increasing the molecular weight provides enhanced stability from dewetting.²³ In comparison to the other polymers, PVM, PSM, and PSAM were stable to the high solvent concentrations due to their higher T_g and lower solubility with chloroform. Sample swelling curves for these polymers is shown in Figure 6-6a. From these data, PVM has the highest compatibility with CHCl₃. PSAM is less compatible than PVM and has slightly more favorable interactions than PSM with CHCl₃.

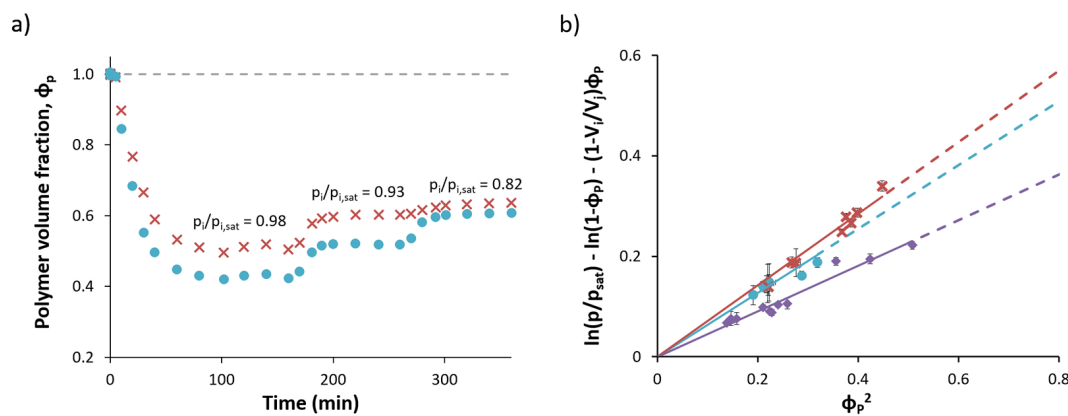


Figure 6-6. a) Sample swelling curves for PSM (×) and PSAM (●) in CHCl₃. b) Replotted swelling data for PSM (×), PSAM (●), and PVM (◆) in chloroform. PSM had the highest interaction parameter, whereas PVM had the lowest interaction parameter in CHCl₃.

For these polymers, PSM had the lowest compatibility. Thus, two *ortho* methoxy groups detract from the polymer solubility (comparing PSM and PGM). Additionally, a polymer containing an aldehyde *para* to the backbone have higher solubility (comparing PSM and PSAM; PGM and PVM). The difference in swelling for PVM and PGM at the same composition is shown in Appendix DD, Figure D-4. The solvent-polymer interaction parameters extracted from the slope of the lines in Figure 6-6 are given in Table 6-5. PSM had the lowest compatibility with CHCl₃, whereas PVM had the highest compatibility. The value for PSAM was between PSM and PVM.

Table 6-5. Flory-Huggins solvent-polymer interaction parameters for the homopolymers with CHCl₃.

homopolymer	
polymer	$\chi_{\text{CHCl}_3\text{-p}}$
PSM	0.71 ± 0.01
PSAM	0.64 ± 0.01
PVM	0.45 ± 0.01

6.3.2 Surface Energy

In addition to solubility, the surface energy is an important parameter to quantify for functional coatings. The surface energy impacts film stability,³² adhesion,¹⁷ and wettability. The surface energy was characterized with contact angle.

6.3.2.1 Sessile Contact Angle

The sessile contact angle was used as a starting point to measure the surface energy of the sustainable polymers. If sufficient volume is used, the sessile contact

angle is equivalent to the advancing contact angle and can be used to calculate the surface energy. From the two-fluid method, the surface energy is given by eq. 6.3

$$(1 + \cos(\theta))\gamma_L = 2\left(\sqrt{\gamma_S^D \gamma_L^D} + \sqrt{\gamma_S^P \gamma_L^P}\right) \quad \text{eq. 6.3}$$

For which θ is the contact angle, γ_L is the surface energy of the liquid, γ_S is surface energy of the solid, and the superscripts D and P represent dispersive and polar component, respectively. The contact angle fluids used in this study were water ($\gamma_{water} = 72.8$ mN/m, $\gamma_{water}^D = 21.8$ mN/m, $\gamma_{water}^P = 50$ mN/m) and diiodomethane ($\gamma_{diio} = 50.8$ mN/m, $\gamma_{diio}^D = 50.8$ mN/m, $\gamma_{diio}^P = 0$ mN/m).³³⁻³⁴ The contact angles with water and diiodomethane are shown in Figure 6-7a. The surface energies, calculated with eq. 6.3, are given in Figure 6-7b.

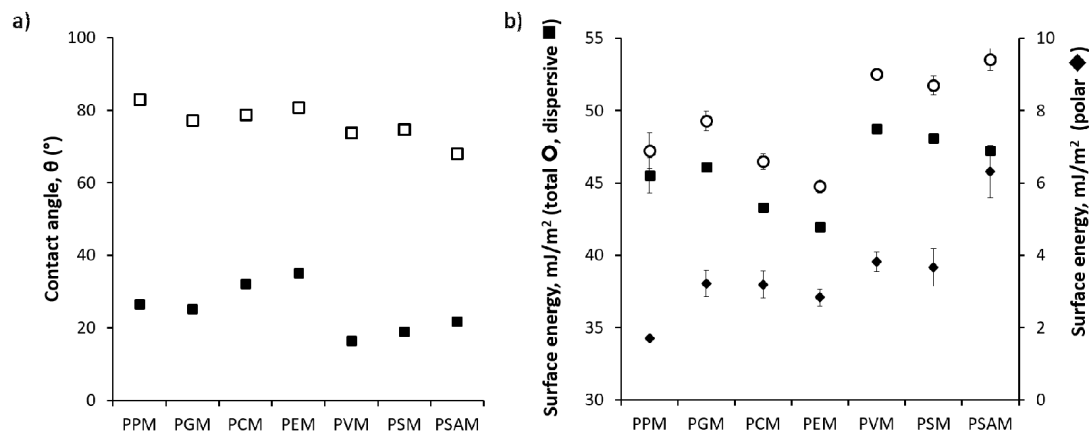


Figure 6-7. a) Contact angle with water (□) and diiodomethane (■). The water contact angle decreased with increasing oxygen content, whereas the diiodomethane contact angle increased slightly with aliphatic content and oxygen moieties. b) Calculated total (○), dispersive (■), and polar (◆) surface energy using the two-fluid contact angle method described in Chapter 2 as well as elsewhere.³³⁻³⁴ The PEM surface energy is the lowest, at 45 mJ/m^2 , which is higher than both polystyrene [40 mJ/m^2] and poly(methyl methacrylate) [41 mJ/m^2].³⁵ Aliphatic character decreased the polymer surface energy, whereas additional oxygen groups increased the surface energy.

The surface energy of the polymer decreased with aliphatic nature, but increased with number of oxygen groups on the molecule. However, the static sessile contact angle does not provide accurate surface energy results, as it is biased by surface heterogeneities.³⁶⁻³⁷ Thus, measuring the contact angle hysteresis will provide more robust surface energy values.

6.3.2.2 Contact Angle Hysteresis

Advancing and receding contact angles were measured on the polymer films to get insight into the equilibrium contact angle (Young's contact angle). The Young's

contact angle provides the most accurate surface energy measurements.³⁶⁻³⁷ As discussed in Chapter 2, the measured contact angle should decrease with increasing volume and reach a constant value, which is the advancing contact angle. Upon volume removal, the droplet should decrease initially, followed by a plateau regime (receding contact angle), and, finally, become distorted and loses its shape.³⁸ The values for advancing and receding contact angle, the contact angle hysteresis, and the equilibrium contact angle are given in Table 6-6, along with the sessile droplet contact angle.

Table 6-6. Sessile contact angle measurements for the sustainable polymers with water. The static sessile contact angle (θ_s) is comparable to the advancing sessile contact angle (θ_A). The difference between the advancing and receding (θ_R) sessile contact angle is the contact angle hysteresis ($\Delta\theta$). The equilibrium contact angle (θ_0) is used to calculate the surface energy of the material.

Polymer	θ_s	θ_A	θ_R	$\Delta\theta$	θ_0
PPM	83.0° ± 0.2°	82.5° ± 0.4°	63.0° ± 0.7°	19.4° ± 0.8°	72.2° ± 0.6°
PGM	77.2° ± 1.2°	76.7° ± 0.5°	59.0° ± 0.6°	17.7° ± 0.8°	67.5° ± 0.5°
PCM	78.8° ± 1.2°	78.8° ± 0.1°	63.4° ± 0.6°	15.4° ± 0.6°	70.8° ± 0.3°
PEM	80.8° ± 0.8°	79.6° ± 0.8°	67.1° ± 0.3°	12.5° ± 0.8°	73.2° ± 0.5°
PVM	73.8° ± 0.8°	84.0° ± 0.9°	62.1° ± 0.4°	21.9° ± 0.9°	72.4° ± 0.6°
PSM	74.7° ± 1.6°	68.0° ± 0.4°	50.6° ± 0.3°	17.5° ± 0.5°	59.1° ± 0.3°
PSAM	68.1° ± 1.8°	64.5° ± 0.41	44.3° ± 0.5°	20.2° ± 0.6°	54.2° ± 0.4°

The static sessile contact angle measurement matched well with the advancing contact angle measurements, suggesting that there was sufficient volume in the static sessile experiments to generate the advancing contact angle, with the exception of PVM. The PVM film had a slightly higher advancing contact angle than the sessile contact angle, which could indicate surface heterogeneity plays a more significant role in this sample. The equilibrium contact angle should fall between the advancing and

receding contact angle; thus, the surface energies calculated with the advancing contact angle will be slightly lower than with the equilibrium contact angle. A comparison of the total surface energy calculated from the Owens-Wendt method (two-fluid static sessile contact angle) or the Good-Girifalco equation (one-fluid contact angle hysteresis) is shown in Figure 6-8. The equilibrium contact angle produced a lower surface energy for all polymers using one fluid in comparison to the two-fluid static sessile contact angle method. However, the changes in surface energy with functional group were similar for both methods. Polymers with additional oxygen groups (PPM *vs.* PGM, PGM *vs.* PSM or PVM, PSM or PSAM *vs.* PSAM) had higher surface energies. Additionally, the surface energy for polymers containing longer aliphatic chains was lower (PGM *vs.* PCM *vs.* PEM) than polymers containing shorter or no aliphatic chains.

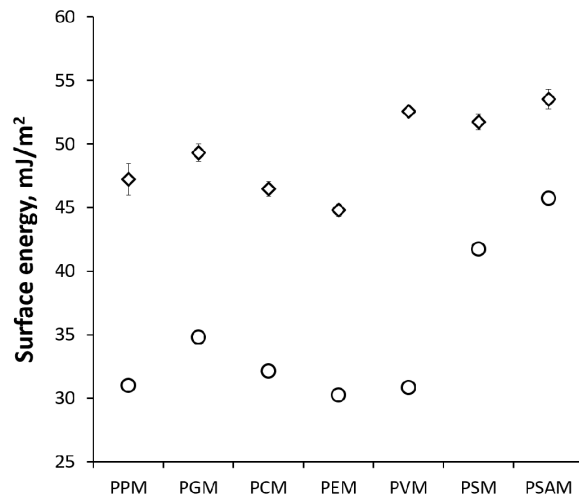


Figure 6-8. Comparison of surface energy calculated with static sessile contact angle measurements (◇) and advancing/receding contact angle measurements (○). The contact angles determined by the two-fluid static sessile method were higher than the angles calculated with the one-fluid equilibrium contact angle. The two-fluid Owens-Wendt formalism was used to calculate γ from θ for the static contact angle, whereas the Good-Girifalco method was used to calculate γ from θ_0 . It is worth noting that the trend in the surface energies is consistent for all of the polymers, which suggests that the static sessile method provides useful relative information about the polymer surface energies.

The surface energy calculated using the Good-Girifalco method can be low for low surface energy materials, such as polymers. Thus, in order to better determine the surface energy for the sustainable polymers, the Young's contact angle should be used for more than one fluid. Diiodomethane had a very low contact angle with the sustainable polymers; therefore, measuring the contact angle hysteresis with diiodomethane is not feasible. It has been detailed in literature that the contact angle hysteresis of diiodomethane can be very small; thus, the advancing (static sessile) contact angle was assumed to be the equilibrium value.^{37, 39} As a result, the total surface energy could be determined using both dispersive (diiodomethane, water) and

polar (water) contributions from the equilibrium contact angle data and is reported in Figure 6-9.

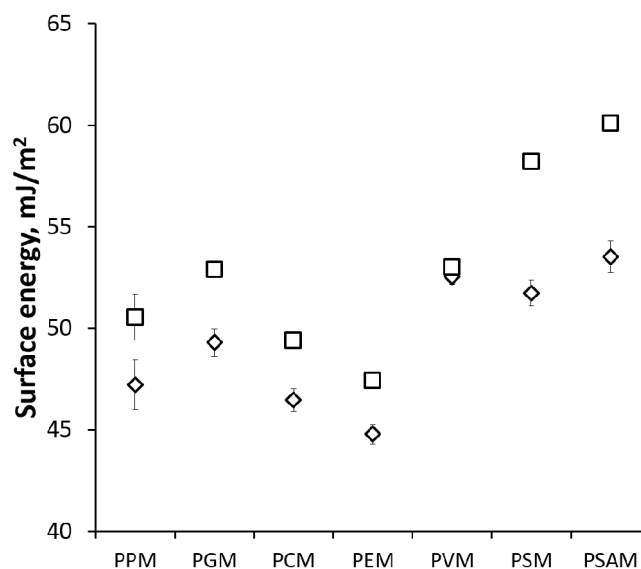


Figure 6-9. Comparison of surface energy calculated using the two-fluid Owens-Wendt formula for static sessile contact angle measurements (◇) and Young's water contact angle measurements in conjunction with the static sessile diiodomethane contact angle measurements (□). The two surface energies were in reasonable agreement; however, the surface energies calculated with the equilibrium contact angle were slightly higher than the static sessile method, as expected.

The surface energies calculated from the Young's water contact angle and the static sessile diiodomethane contact angle are in good agreement with the surface energies from both static sessile contact angles. Regardless of the specific contact angle value, the relative changes in surface energy are consistent for each of the polymers, suggesting that the sessile method is sufficient to infer trends relating to surface energy differences.

6.3.3 Tribology

In addition to solubility and surface energy, the friction coefficient of the sustainable polymers can inform the potential use in various applications. The set-up and experimental conditions as described in Chapter 3 for the friction coefficient test. Both the glass and HDPE probes were used to measure the friction coefficient at 4.6 mm/s. The time-dependent friction coefficient data is shown in Figure 6-11 for the glass and HDPE probes.

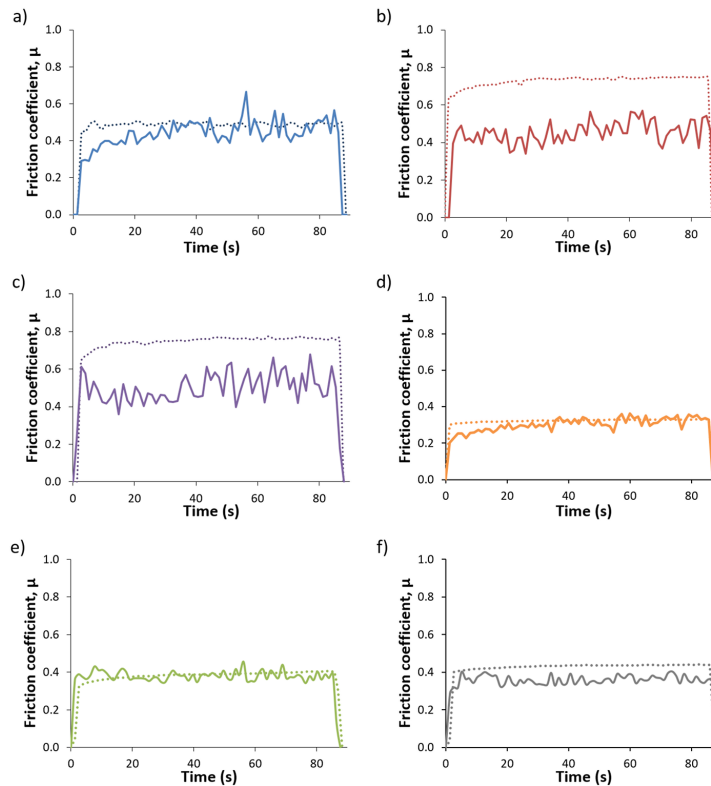


Figure 6-10. Friction coefficient for a) PGM, b) PSM, c) PVM, d) PCM, e) PEM, and f) PPM with the glass (solid line) and HDPE (dotted line) probe. The friction coefficient was higher with HDPE than with glass for all polymers except PCM, likely owing to the higher adhesion between the neat materials and HDPE.

The average friction coefficients were extracted from the time-dependent data using the protocol outlined in Chapter 5. Figure 6-11 includes a summary of the average friction coefficients for the sustainable polymers.

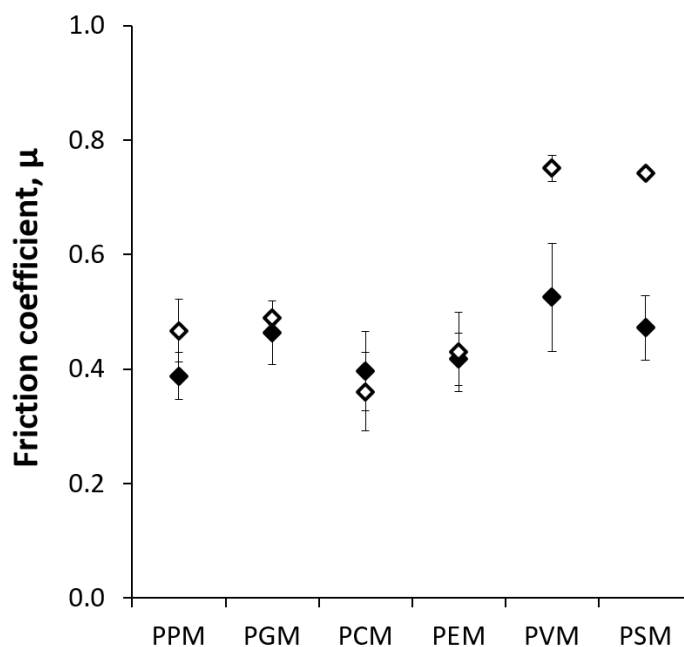


Figure 6-11. Time-averages of sustainable polymer friction coefficients with the HDPE (\diamond) and glass (\blacklozenge) probes. The glass-polymer friction coefficient was within error for PGM, PSM, and PVM. PEM and PPM had similar glass-polymer friction coefficient, which was slightly smaller than the value for PGM, PSM, and PVM. PCM had a higher glass-polymer friction coefficient. The HDPE-polymer friction coefficient increased with oxygen content and decreased with aliphatic character. The error bars represent the standard deviation of the friction coefficient in time.

The friction coefficient was nearly independent of polymer structure when measured with the glass bead. However, when measured with HDPE, the friction coefficient increased with oxygen content. Though oxygen content both increased

(PGM → PSM) and decreased (PGM → PVM) the polymer-solvent interaction parameter (see Figure 6-4 and Figure 6-6), depending on the position of the oxygen group, the polymers containing more oxygen generally were less soluble. These differences in solubility can influence the film roughness during casting, which can affect the friction coefficient. For example, Menezes and Kailas reported that the roughness of the steel plate influenced the friction coefficient with ultra-high molecular weight polyethylene (UHMWPE).⁴¹ The UHMWPE-steel friction coefficient increased with roughness, which was varied from ~ 0.05 μm to 0.30 μm. The increase in friction coefficient was attributed to the hysteresis rather than the adhesion friction component.⁴¹ As such, measuring the film roughness may provide insight into the mechanism of the friction coefficient of the polymer films. The root mean squared roughness, R_{RMS} , is given by

$$R_{RMS} = \sqrt{\frac{1}{n} \sum d_i^2}$$

for which n is the number of points in the micrograph and d_i height difference between point i and the mean. The film roughness was measured using AFM, as shown in Figure 6-12.

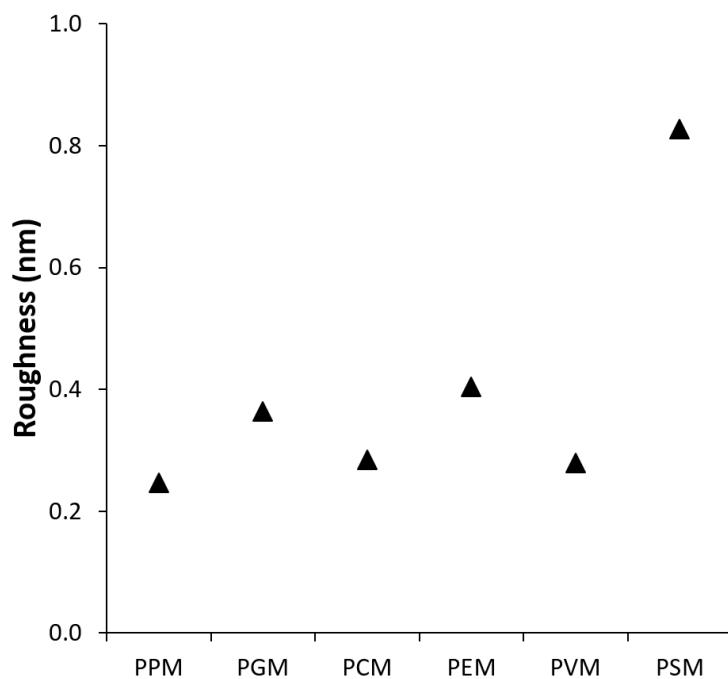


Figure 6-12. Root mean squared roughness of sustainable polymer films measured using AFM.

With the exception of PSM, the films had similar roughness. Additionally, the trends in the roughness do not match the differences in friction coefficient (see also Figure 6-11). For example, PSM and PVM had similar friction coefficients with glass and HDPE, but the roughness values were the most dissimilar of all of the polymers. These results suggest there is not a significant contribution from the surface roughness to the friction coefficient.

Thus, other factors must be explored to understand the differences in friction coefficient of the sustainable polymers. An increase in friction coefficient can be caused by an increase in adhesion between the film and probe. The adhesion between

two surfaces can be estimated from the differences in the material surface energies upon contact.¹⁷

$$W_{ad} = \gamma_1 + \gamma_2 - \gamma_{12} \quad \text{eq. 6.4}$$

γ_i is the surface energy of material i and γ_{ij} is the interfacial tension between materials i and j . The interfacial tension can be determined from the geometric mean of the dispersive (γ^D) and polar (γ^P) surface energy contributions.^{10,40}

$$\gamma_{12} = \gamma_1 + \gamma_2 - 2\sqrt{\gamma_1^D \gamma_2^D} - 2\sqrt{\gamma_1^P \gamma_2^P} \quad \text{eq. 6.5}$$

Using the surface energies calculated from the sessile contact angles in Table 6-6, the probe-film adhesion can be calculated. The results of this calculation is shown in Table 6-7.

Table 6-7. Calculated probe-film adhesion for sustainable polymers.

Polymer	W_{glass-poly} mJ/m²	W_{HDPE-poly} mJ/m²
PPM	99.7	80.6
PGM	108.9	81.1
PCM	106.4	78.6
PEM	103.4	77.4
PVM	113.9	83.4
PSM	112.7	82.9

The glass ($\gamma^P = 80 \text{ mJ/m}^2$, $\gamma^D = 32 \text{ mJ/m}^2$) and HDPE ($\gamma^P = 0 \text{ mJ/m}^2$, $\gamma^D = 35.3 \text{ mJ/m}^2$) surface energy contributions are used to calculate the work of adhesion from the sustainable polymer surface energies determined from the static sessile contact angles with the Owens-Wendt equation.

Despite the greater theoretical adhesion between the glass probe and the films, the contact area with the glass probe will be lower than the HDPE probe, due to the

smaller modulus of HDPE (see also Chapter 5). Thus, the glass-film adhesion likely is difficult to measure, which was discussed in Chapter 5 for glass-PS adhesion.

Additionally, the glass-polymer friction coefficient did not change significantly with the different chemical structure, suggesting adhesion does not factor significantly into the friction coefficient. Thus, studying the HDPE-polymer adhesion can provide more useful insights than the glass-polymer adhesion. The pull-off forces were measured with HDPE for the sustainable polymers using the immediate retraction method described in Chapter 5.

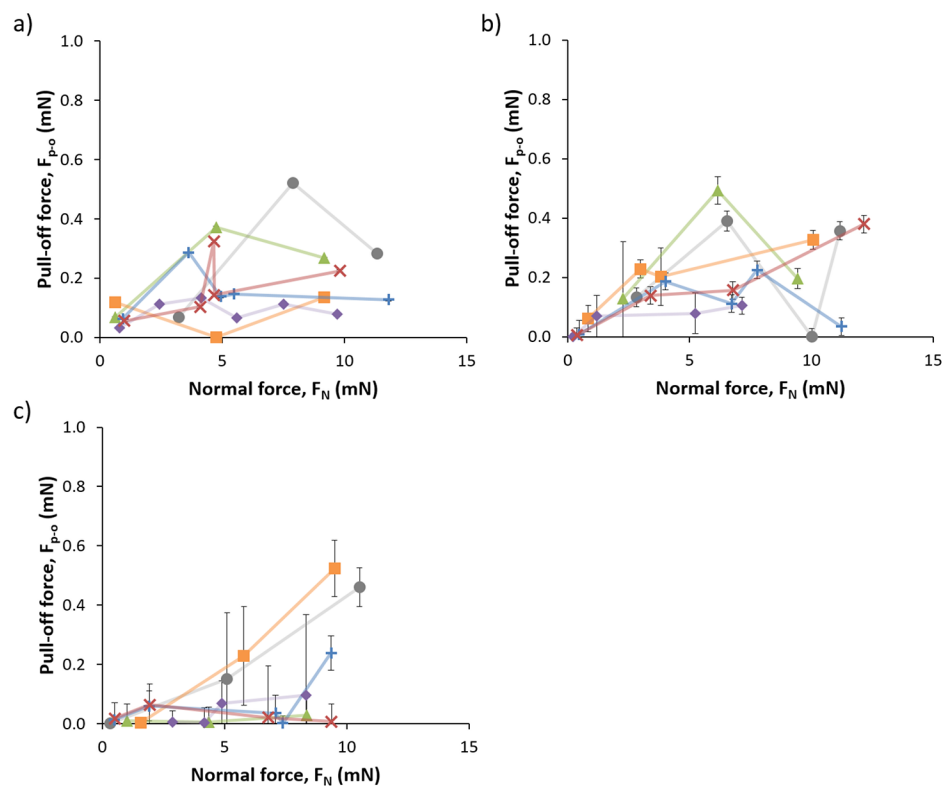


Figure 6-13. Pull-off forces for PSM (×), PGM (+), PVM (◆), PCM (■), PEM (▲), and PPM (●) upon immediate retraction with approach and retraction velocities of a) 1.3 $\mu\text{m/s}$, b) 13 $\mu\text{m/s}$, and c) 26 $\mu\text{m/s}$. The pull-off forces for all of the polymers were low (< 0.5 mN), and there were no apparent trends with polymer structure. Thus, the adhesion alone cannot be causing the major shift in friction coefficient.

The adhesion for all polymers with HDPE was very similar and small in magnitude. As such, these results cannot provide direct insight into the differences in friction coefficient for the glassy, sustainable polymers. Due to the high noise level in the adhesion data and the small adhesion values, it is difficult to determine the effect of adhesion on friction coefficient. A more sensitive tribometer, such as a

nanotribometer, may provide additional insight into the adhesion for each of the films with the probes, which is discussed in more detail in Chapter 7.

6.4 Conclusions

Sustainable polymers can be utilized in next-generation hierarchical coatings. However, sustainable materials often suffer from feedstock diversity. Thus, understanding the effect of functional groups on the material properties remains a key challenge to utilizing sustainable polymers in new materials. In this chapter, the effect of *ortho* and *para* constituents on the solubility, surface energy, and friction coefficient was measured for sustainable polymer films.

Polymers containing more aliphatic character in the *para* position to the polymer backbone had better the solubility and lower surface energy. The polymers containing aliphatic functional groups (PGM, PCM, and PEM) all have similar glass transition temperatures, but different solubilities in THF. Thus, at the same glass transition temperature, the solvent resistance or solvent quality can be selected through careful consideration of the functional group at the *para* position to the polymer backbone. The surface energy also decreased with increasing aliphatic chain length, which is consistent with the trend in the solubility.

Aldehyde functional groups were found to afford additional solubility (PVM vs. PGM or PSAM vs. PSM) in the sustainable polymer films. Furthermore, the additional oxygen group increased the surface energy of the polymer film and produced an increase in friction coefficient. Thus, in addition to the length of the functional group *para* to the backbone, the chemical nature provides another handle to tune the material properties.

Changing the number of methoxy groups *ortho* to the polymer backbone also affects the material properties in films. Polymers with two methoxy groups (PSM, PSAM) have drastically different from the polymers with the same *para* functional groups and one methoxy group (PGM, PVM). Additionally, the solvent resistance is significantly increased through the addition of the second methoxy group, due to the increased glass transition temperature. Incorporating additional oxygen moieties (PGM vs PSM, PVM, or PSAM) increases the surface energy and friction coefficient with HDPE. Thus, the friction and adhesion properties can be modified through feedstock selection.

Heteropolymers comprised of the same functional monomers had intermediate properties in comparison to their homopolymer counterparts. Not only do these heteropolymers afford additional material tunability, but they also allow for reduced separations cost. Thus, this systematic study of the material properties illustrates the effect of *para* and *ortho* function group nature on the material properties of the resulting polymer. These insights can inform development of novel sustainable coatings.

REFERENCES

1. Gandini, A.; Lacerda, T. M., From monomers to polymers from renewable resources: Recent advances. *Prog. Polym. Sci.* **2015**, *48*, 1-39.
2. Holmberg, A. L.; Stanzione, J. F.; Wool, R. P.; Epps, T. H., III, A facile method for generating designer block copolymers from functionalized lignin model compounds. *ACS Sustainable Chem. Eng.* **2014**, *2*, 569-573.
3. Gandini, A., The irruption of polymers from renewable resources on the scene of macromolecular science and technology. *Green Chemistry* **2011**, *13*, 1061-1083.
4. PlasticsEurope Plastics – the Facts 2014/2015.
http://www.plasticseurope.org/documents/document/20150227150049-final_plastics_the_facts_2014_2015_260215.pdf (accessed 10/20/2016).
5. Asmadi, M.; Kawamoto, H.; Saka, S., Gas- and solid/liquid-phase reactions during pyrolysis of softwood and hardwood lignins. *J. Anal. Appl. Pyrolysis* **2011**, *92*, 417-425.
6. Jegers, H. E.; Klein, M. T., Primary and secondary lignin pyrolysis reaction pathways. *Ind. Eng. Chem. Process Des. Dev.* **1985**, *24*, 173-183.
7. Brodin, I.; Sjöholm, E.; Gellerstedt, G., The behavior of kraft lignin during thermal treatment. *J. Anal. Appl. Pyrolysis* **2010**, *87*, 70-77.
8. Plackett, D., *Biopolymers – New Materials for Sustainable Films and Coatings*. John Wiley & Sons, Ltd: 2011, 10.1002/9781119994312.
9. van Krevelen, D. W.; Nijenhuis, K. T., *Properties of Polymers - Their Correlation with Chemical Structure; Their Numerical Estimation and Prediction from Additive Group Contributions*. 4 ed.; Elsevier: Amsterdam, 2009.
10. Fowkes, F. M., Attractive forces at interfaces. *Ind. Eng. Chem.* **1964**, *56*, 40-52.

11. Shelton, C. K.; Epps Iii, T. H., Decoupling substrate surface interactions in block polymer thin film self-assembly. *Macromolecules* **2015**, *48*, 4572-4580.
12. Shelton, C. K.; Epps Iii, T. H., Mapping substrate surface field propagation in block polymer thin films. *Macromolecules* **2016**, *49*, 574-580.
13. Geoghegan, M.; Krausch, G., Wetting at polymer surfaces and interfaces. *Prog. Polym. Sci.* **2003**, *28*, 261-302.
14. Burris, D. L.; Sawyer, W. G., Addressing practical challenges of low friction coefficient measurements. *Tribol. Lett.* **2009**, *35*, 17-23.
15. Abdelbary, A., *Wear of Polymers and Composites*. Elsevier Science: 2015.
16. Satyanarayana, N.; Sinha, S. K.; Shen, L., Effect of molecular structure on friction and wear of polymer thin films deposited on Si surface. *Tribol. Lett.* **2007**, *28*, 71-80.
17. Israelachvili, J. N., *Intermolecular and Surface Forces*. 3rd ed.; Academic Press: San Diego, 2011, p 415-467.
18. Holmberg, A. L.; Nguyen, N. A.; Karavolias, M. G.; Reno, K. H.; Wool, R. P.; Epps, T. H., III, Softwood lignin-based methacrylate polymers with tunable thermal and viscoelastic properties. *Macromolecules* **2016**, *49*, 1286-1295.
19. Holmberg, A. L.; Reno, K. H.; Nguyen, N. A.; Wool, R. P.; Epps, T. H., III, Syringyl methacrylate, a hardwood lignin-based monomer for high-Tg polymeric materials. *ACS Macro Lett.* **2016**, *5*, 574-578.
20. Holmberg, A. L. Bottom-up designs and syntheses of sustainable block polymers. University of Delaware, 2016.
21. Holmberg, A. L.; Karavolias, M. G.; Epps, T. H., III, RAFT polymerization and associated reactivity ratios of methacrylate-functionalized mixed bio-oil constituents. *Polym. Chem.* **2015**, *6*, 5728-5739.
22. Stafford, C. M.; Roskov, K. E.; Epps, T. H., III; Fasolka, M. J., Generating thickness gradients of thin polymer films via flow coating. *Rev. Sci. Instrum.* **2006**, *77*, 023908.
23. Miller-Chou, B. A.; Koenig, J. L., A review of polymer dissolution. *Prog. Polym. Sci.* **2003**, *28*, 1223-1270.

24. Emerson, J. A.; Toolan, D. T. W.; Howse, J. R.; Furst, E. M.; Epps, T. H., III, Determination of solvent–polymer and polymer–polymer Flory–Huggins interaction parameters for poly(3-hexylthiophene) via solvent vapor swelling. *Macromolecules* **2013**, *46*, 6533-6540.
25. Mark, J.; Ngai, K.; Graessley, W.; Mandelkern, L.; Samulski, E.; Koenig, J.; Wignall, G., *Physical Properties of Polymers*. 3 ed.; Cambridge University Press: Cambridge, 2003.
26. Bock, H.; Christian, S.; Knoll, W.; Vydra, J., Determination of the glass transition temperature of nonlinear optical planar polymer waveguides by attenuated total reflection spectroscopy. *Appl. Phys. Lett.* **1997**, *71*, 3643.
27. Kim, J. H.; Jang, J.; Zin, W.-C., Thickness dependence of the glass transition temperature in thin polymer films. *Langmuir* **2001**, *17*, 2703-2710.
28. Vrentas, J. S.; Vrentas, C. M., Effect of glass transition on the concentration dependence of self-diffusion coefficients. *J. Appl. Polym. Sci.* **2003**, *89*, 1682-1684.
29. Pochan, J. M.; Beatty, C. L.; Pochan, D. F., Different approach for the correlation of the Tg of mixed amorphous systems. *Polymer* **1979**, *20*, 879-886.
30. Lee, S. H.; Yoo, P. J.; Kwon, S. J.; Lee, H. H., Solvent-driven dewetting and rim instability. *J. Chem. Phys.* **2004**, *121*, 4346.
31. Xu, L.; Shi, T.; Dutta, P. K.; An, L., Rim instability by solvent-induced dewetting. *J. Chem. Phys.* **2007**, *127*, 144704.
32. Ashley, K. M.; Raghavan, D.; Douglas, J. F.; Karim, A., Wetting–dewetting transition line in thin polymer films. *Langmuir* **2005**, *21*, 9518-9523.
33. Albert, J. N. L.; Baney, M. J.; Stafford, C. M.; Kelly, J. Y.; Epps, T. H., III, Generation of monolayer gradients in surface energy and surface chemistry for block copolymer thin film studies. *ACS Nano* **2009**, *3*, 3977-3986.
34. Jańczuk, B.; Wójcik, W.; Zdziennicka, A., Determination of the components of the surface tension of some liquids from interfacial liquid-liquid tension measurements. *J. Colloid Interface Sci.* **1993**, *157*, 384-393.
35. Brandrup, J.; Immergut, E. H.; Grulke, E. A., *Polymer Handbook*. 4th ed.; Wiley: New York, 1999.

36. Tadmor, R., Line energy and the relation between advancing, receding, and Young contact angles. *Langmuir* **2004**, *20*, 7659-7664.
37. Chibowski, E.; Terpilowski, K., Surface free energy of sulfur—Revisited: I. Yellow and orange samples solidified against glass surface. *J. Colloid Interface Sci.* **2008**, *319*, 505-513.
38. Korhonen, J. T.; Huhtamäki, T.; Ikkala, O.; Ras, R. H. A., Reliable measurement of the receding contact angle. *Langmuir* **2013**, *29*, 3858-3863.
39. Biresaw, G.; Mittal, K. L., *Surfactants in Tribology*. Taylor & Francis: 2014.
40. Wu, S., Calculation of interfacial tension in polymer systems. *J. Polym. Sci., Part C: Polym. Symp.* **1971**, *34*, 19-30.
41. Menezes, P. L.; Kailas, S. V., Role of surface texture and roughness parameters on friction and transfer film formation when UHMWPE sliding against steel. *Biosurface and Biotribology* **2016**, *2*, 1-10.

Chapter 7

CONCLUSION & FUTURE DIRECTIONS

7.1 Dissertation Summary

Multi-component polymer systems, such as polymer blends and polymer blend nanocomposites, can be utilized in a variety of applications including functional coatings, optoelectronics, and membranes. For each of these applications, a particular material structure produces optimal device properties. For instance in organic photovoltaics comprised of polymer blends, a co-continuous structure with small domain sizes had a higher device efficiency than the same structure with larger domains and the bilayer phase separated structure.¹ Thus, understanding the relationship between the structure of the polymer films and the performance is key to producing optimal composite materials. Furthermore, the thermodynamics and processing effects must be understood, as these factors determine the morphology of the film. Overall, the efforts described herein enable enhanced control over the morphology and properties, providing a foundation towards producing novel hierarchical materials.

7.1.1 Interplay Between Phase Behavior, Casting, and Film Morphology in Polymer Blends

The first aim of Chapter 3 was to understand the solution thermodynamics of polymers and polymer blends. The polymers studied in this chapter were polystyrene [PS], poly(3-hexylthiophene) [P3HT], polyisoprene [PI], and poly(methyl

methacrylate) [PMMA]. A robust methodology was developed to characterize solvent-polymer interactions using solvent vapor swelling of polymer films. The resulting solvent-polymer interactions were utilized to calculate polymer-polymer interactions for PS/P3HT, PS/PI, and PS/PMMA; theoretical phase diagrams were produced for each of the three polymer blend combinations in *o*-xylene. These phase diagrams were validated experimentally using transmission experiments (for PS/P3HT) and proton nuclear magnetic resonance (^1H NMR, for PS/PI). Good agreement existed between the theoretical phase diagrams and experimental results.

The second aim of Chapter 3 was to elucidate the effect of quenching through the phase diagram (processing) on the polymer morphology. Spin coating was used to generate the films. To better understand the effect of processing (casting) on morphology, *in situ* techniques were applied to visualize the phase separation during casting. Early stages of phase separation were measured by comparing the experimental drying behavior to the theoretical film thinning. In low molecular weight (more compatible) $^{17\text{k}}\text{PS}/^{33\text{k}}\text{PMMA}$ blends, there was no difference in the measured and predicted drying behaviors; increasing the molecular weight (reduce compatibility) of the blend ($^{110\text{k}}\text{PS}/^{100\text{k}}\text{PMMA}$) produced deviations from the drying model, suggesting that the development of structure increased the viscosity. Similarly, for PS/P3HT, deviations between the model and data occurred due to significant increases in viscosity, which was the result of structure formation in these solutions. However, the deviations in PS/P3HT blends occurred at much earlier time scales than expected, which was attributed to P3HT gelation. Though P3HT forms a gel in *o*-xylene, the time scales of gelation in this system typically are much slower than the casting of the polymer film. Thus, the processing of the film significantly affects the

gelation of P3HT, causing a drastic increase in viscosity. As such, viscosity can be a useful parameter to infer structural development from deviations between the theoretical and experimental drying curves, because the theoretical drying curves are calculated assuming the viscosity follows a homogenous solution behavior.

The effect of solvent removal during casting was studied in relation to the phase diagrams for PS/PMMA and PS/P3HT using stroboscopic illumination. Though the visible onset of phase separation occurred deep within the two-phase region, the formed structures corresponded to later stages of phase separation. Suggestions for future studies involving enhanced understanding of this process *via* scattering techniques can be found in Section 7.2.1.2.

The results presented in Chapter 3 highlight the interplay between the phase behavior, casting, and final film morphology in polymer blends. Of particular importance is the robust methodology that was developed to determine the solvent-polymer interaction parameters and relate them to the phase behavior and casting of polymer blends.

7.1.2 Effect of Particles on Polymer Blend Morphology

A natural extension of polymer blends towards application involves incorporating nanoparticles to impart additional thermal, mechanical, electrical, optical, or catalytic properties. Polymer blend nanocomposites (PBNCs) have potential applications in organic optoelectronics, membranes, and functional coatings. In Chapter 4, the effect of PS-capped nanorod (aspect ratio: 3) addition on processing (casting) and film morphology was studied. In a PS-Selective solvent, nanorods, which were loaded at 1 vol.% and 2 vol.% with respect to total polymer content, assembled at/near the polymer/polymer interface and produced a ~30 % decrease in

the average domain size. Incorporating a high loading of nanoparticles (~10 vol.%) significantly decreased the blend viscosity and produced larger domain sizes than the 1 vol.% or 2 vol.% mixtures. In a PI-selective solvent, the addition of nanorods did not change the drying behavior or the film morphology. These results suggest that the solvent choice also can play a role in the nanoparticle location. In PBNCs, it has been reported that the graft molecular weight and composition control dispersion and partitioning; however, little attention has been paid to the processing effects. Extension of PBNCs to new functional materials will be discussed in Section 7.2.2.1.

7.1.3 Structure-property Relationships for Tribology

The tribology (friction and wear) of polymer blend films can be readily tuned by controlling the composition and morphology. Chapter 5 focused on understanding the relationship between friction coefficient, composition, and domain size. The friction coefficient was measured as a function of domain size, which was controlled by varying the relative polymer composition in solution or annealing the blend films in solvent. These results demonstrated the friction coefficient was not solely related to the composition; the friction coefficient was non-monotonic with the coupled domain size-composition and increased with the domain size at a constant composition. The mechanism for differences in the friction coefficient was found to come from the adhesion of the polymer blend films.

7.1.4 Chemical and Friction Properties of Sustainable Polymers

In Chapter 6, the solvent-polymer interaction parameters are studied for a library of sustainable polymers from both softwood and hardwood feedstocks. The relationship between the functional groups and the solubility was explored. In

general, materials containing functionality *para* to the polymer backbone had enhanced solvent compatibility with only small changes in the glass transition temperature (T_g). The polymers with functional groups *ortho* to the backbone were more solvent resistant and had higher T_g 's.

The surface energy of the sustainable polymers were studied; polymers with more oxygen-containing moieties had higher surface energies than those with fewer oxygen groups. Additionally, the friction coefficient of the sustainable polymers was studied. The friction coefficient increased slightly for the higher surface energy polymers, which was attributed to higher adhesion between the probe and film. This work highlights the relationship between the constituents of the polymers and their properties. Thus, targeted material properties can be achieved from careful selection of feedstock and composition of these lignin-derived polymers.

7.2 Recommendations for Future Work

7.2.1 Additional Considerations in Processing Effects

In Chapter 3 and Chapter 4, a variety of processing factors were discussed, including solvent choice, polymer selection, and addition of particles. There are additional parameters that were not explored and could be of interest to better understand including the effect of glass transition temperature, relationship between early and late stages of phase separation, translation from batch to continuous processing techniques, and the influence of external fields.

7.2.1.1 Glass Transition Temperatures.

A focus of this dissertation has been on solvent-polymer interactions including swelling behavior, casting, and solvent selectivity. However, we did not consider the

effect of polymer glass transition temperatures on the casting behavior. The T_g 's of polymers used in this dissertation span over 100 °C from polyisoprene [PI] (-73 °C) to polystyrene [PS] (104 °C) to poly(syringyl methacrylate) [PSM] (205 °C). In addition to differences in interactions, differences in T_g can affect the morphology of the polymer blend films. Steiner and coworkers found for a PS/poly(methyl methacrylate) [PMMA] blend, the solvent selectivity played a role in the relative domain height; the polymer that had the least favorable interactions with the solvent solidified first during the drying process and produced taller domains.² However, PS and PMMA have similar T_g 's. We found that the PS domains were always taller than the PI domains, regardless of the solvent selectivity, as highlighted in Figure 7-1 for a PI-selective (decalin), nearly neutral (*o*-xylene), and PS-selective (phenetole) solvent.

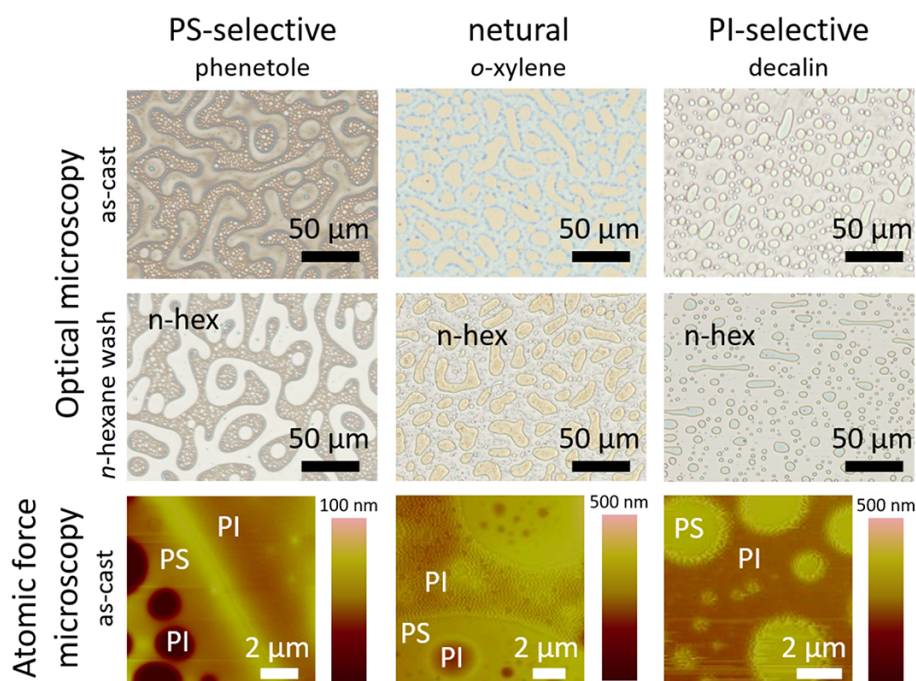


Figure 7-1. Effect of casting solvent selectivity on height differences in polymer blend films. Phenetole is PS selective, *o*-xylene is nearly neutral for both PS and PI, and decalin is selective for PI. Atomic force microscopy height images are shown at the bottom; brighter colors represent higher regions. For all three solvents, the PS phase (which remains after *n*-hexane washes) is taller than the PI phase.

The discrepancy between the predicted relative height difference and the actual relative height difference is due to the low T_g of PI. Although PI is less compatible with the PS-selective solvent, neat PI still can flow at room temperature, whereas the PS loses mobility at much higher solvent concentrations. Thus, it is important to understand the effect of the effective T_g on casting behavior and relate it to the polymer-polymer-solvent phase diagram to understand the solidification point. Thus, the formation of ideal structures can be promoted in new materials, such as sustainable polymers, for which the T_g can change drastically based on feedstock.³⁻⁶ To further

probe the effect of T_g , the library of sustainable polymers provides a compelling model system. The sustainable polymers discussed in this dissertation differ in the *ortho* and *para* positions relative to the polymer backbone and have a range of accessible glass transition temperatures. Given the knowledge developed on these new materials (Chapter 6) along with the understanding of processing as it relates to phase separation (Chapter 3), the solubility can be related to the solidification during casting.

7.2.1.2 Macro-micro Phase Separation Connection.

Connecting macrophase separation with microphase separation during casting via stroboscopic illumination and other techniques is desirable to better understand the relationship between the processing and morphology. One of the challenges discussed in Chapter 3 is related to accessing nanoscale sizes during processing. *In situ* techniques have been developed for spin and flow coating processes that can access smaller size scales than stroboscopic illumination, which has a resolution on the order of microns.

In situ grazing-incidence small-angle X-ray scattering (GISAXS),⁷⁻⁹ grazing-incidence wide-angle X-ray scattering (GIWAXS),¹⁰⁻¹¹ and combinations of the two techniques¹²⁻¹⁴ have been used to probe phase separation and crystallization upon solvent removal. These techniques have been demonstrated during both spin coating,¹⁰⁻¹² flow coating,^{7-9, 14} and other coating processes.¹³ Though these studies have been focused on organic photovoltaic applications (solvent/small molecule/polymer blends), this technique could be extended to other polymer/polymer systems of interest.

Utilizing *in situ* GISAXS to probe the onset of phase separation and the evolution of structure for polymer blends, which could further inform the

thermodynamics/processing relationships for all polymer blends discussed in Chapter 3. Furthermore, by combining GISAXS with GIWAXS, the crystallization of P3HT could be studied in conjunction with the phase separation in the PS/P3HT blends. Despite the promise of *in situ* GISAXS/GIWAXS, the time resolution ~ 1 s.^{7-10, 12-14} For high boiling point solvents and long drying times, GISAXS/GIWAXS can be very useful, which makes it applicable to many organic photovoltaic formulations. As technology develops, this technique will continue to be able to resolve structures during fast drying times.

7.2.1.3 Transitioning from Batch to Continuous Processes.

Many researchers are studying the transition from batch casting techniques (spin coating) to roll-to-roll processing. Flow coating provides a functional intermediate method between spin coating and roll-to-roll processing. Although flow coating is a batch process for most uses, it can be extended readily to continuous processing. Different casting techniques on the same or similar initial solutions produced different morphologies and structures for polymer blends and block polymers.¹⁵⁻¹⁶ One of the differences between spin coating and flow coating is the solvent evaporation rate.

As discussed in Chapter 3 and Chapter 4, the evaporation rate is a key parameter in controlling the morphology. To translate morphologies produced from spin coating to flow coating (and continuous processing techniques), better understanding of the effect of evaporation rate is required. For all techniques, the solvent evaporation is controlled by solvent choice, experimental temperature, and solvent concentration in the atmosphere. In spin coating, the evaporation rate is also influenced by the spin speed. The accessible spin speed range is limited by the spin

coater motor. Although a variety of solvents can be chosen, the interaction between the polymers and solvents should be maintained to better understand the effect of solvent evaporation on morphology. To this end, a series of solvents with similar structures (solubility parameters) with varying evaporation rates should be utilized to relate morphologies in flow coating to spin coating. One such series is reported in Table 7-1

Table 7-1. Properties of organic solvents

Solvent	Boiling point ^a (°C)	Evaporation rate ^a	Solubility parameter ^b (MPa ^{1/2})
benzene	80.09	5.1	18.6
toluene	110.6	1.9	18.2
ethylbenzene	136.19	0.89	18
<i>o</i> -xylene	144.4	1	18
mesitylene ^c	165	--	18

^aBoiling points and evaporation rates (relative to butyl acetate) from reference 17.

^bSolubility parameters from reference 18. ^cThough the evaporation rate is not reported for mesitylene, solvents with higher boiling points typically have slower evaporation rates.

Films that had the same drying time produced similar structures regardless of the particular solvent and casting rate, whereas films with dissimilar drying times produced different morphologies when cast from the same concentration and composition.¹⁵ For both spin coating and flow coating, concentration can be a factor in the evaporation rate as well as in determining the composition at which phase separation occurs; however, maintaining the same concentration across both techniques should minimize the effect of concentration. Because different concentrations were used in these studies, the resulting morphologies cannot be directly compared. Nevertheless, this work provides insight into the effect of solvent

evaporation, which should be further probed to allow reproducible morphology production across processing methods towards continuous production.

7.2.1.4 Effect of external fields on casting.

In addition to the processing parameters discussed previously, the morphology phase space can be expanded through the addition of external fields. Electric fields have been used in literature studies to affect the alignment and crystallization of polymer blends during casting or post-casting processing steps.¹⁹⁻²³ For polymers with dissimilar dielectric constants, electric fields can induce anisotropic assemblies in the blends.²⁰ Thus, electric fields provide a tool to further manipulate the morphology of polymer blend structures. In addition to promoting anisotropic assembly in blends, electric fields facilitate polymer chain alignment, which can promote crystallization.^{22,}²⁴ Finally, electric fields can influence the assembly of particles within a polymer matrix during casting.²⁵

Applying electric fields during casting can provide an additional tunable handle towards developing new hierarchical structures. However, the effect of this processing route on morphology has not been systematically studied from a casting-structure relationship. Thus, it is of interest to better understand the effect of electric fields on polymer blend films to expand the library of morphologies these systems can produce. The methodologies outlined in this dissertation to relate the equilibrium phase behavior to processing and final film morphology can be applied to new structure-direction parameters.

7.2.2 Functional Materials Generation

7.2.2.1 Pressure Sensitive Adhesives

A simple extension to the work presented in Chapter 5 is to tribologically-relevant materials, such as pressure sensitive adhesives (PSAs). Low-tack PSAs can be produced from polymer blends. For example, Müller-Buschbaum and coworkers demonstrated a PSA made from a rubbery and glassy polymer blend; they found that the domain size (tuned by composition) in these poly(*n*-butyl acrylate) [PnBA]/polystyrene [PS] films affected the tack.²⁶ However, they did not decouple the domain size from the composition, as discussed for our work in Chapter 5, to determine the more significant factor. Thus, it is of interest to systematically study the tack in rubbery/glassy polymer blends as a function of both domain size and composition towards producing structure-function relationship in these materials.

As part of this work, improved understanding of the adhesion of the polymer blend is required. In Chapter 5, we discussed the friction, wear, and adhesion of polymer blend films. However, through our analysis, we were unable to fully elucidate the underlying factors related to reduction in adhesion at PS mass fractions between 0.6 and 0.8. The specific molecular mechanism of friction is unknown; however, the friction coefficient is related to the adhesion, contact area, and surface structure. Complementary techniques, such as nanotribology, should be performed on the polymer blends. Nanotribology will provide a direct measure of the friction coefficient of the neat materials within the domains. Due to the disparate size scales of the tips used in nanotribology and macrotribology, the difference in contact area also must be explored to relate the friction coefficient results. As such, the contact area of the probe with the films should be determined along with the modulus of the

polymer blends. The contact area effects can be probed indirectly by varying the probe size on the same instrument; in the absence of adhesion, the contact radius grows with (probe radius)^{1/3}. Determination of the polymer blend modulus will also allow for understanding of the effect of composition on the friction coefficient, in particular, within the context of changes in contact area. These insights will inform the changes in contact area with the film structure as well as the effect of modulus on the contact area, which can then be applied to the measured differences in adhesion and friction coefficients of the hierarchical films.

7.2.2.2 Hierarchical Assemblies for Membranes

Biporous polymeric materials are of particular interest for membranes and hybrid catalytic supports.²⁷⁻³⁰ In typical biporous polymer membranes, hierarchical assemblies including co-solvent evaporation and particle templating are used to induce the micro- (~10 nm – 1 μm) and macro- (~100 μm) pores.²⁷ One of the key challenges is understanding the parameters that affect the pore size. The macro-phase separation produced by polymer blends in combination to nanoscale structures inherent in self-assembled block polymers can be leveraged to produce biporous membranes.

Blends of homopolymer A with diblock copolymer B-C (A/B-C blends) for which A, B, and C are immiscible, can be used to produce hierarchical structures for applications like porous membranes.³¹ In comparison to other homopolymer/block polymer blends (A/A-B), the A/B-C blend system has higher tunability in that one or two domains may be selectively removed. These systems utilize the macrophase separation of the immiscible homopolymer blend along with the nanoscale phase separation within the block polymer domain. To date, there have only been a few studies on A/B-C blends.³¹⁻³² The interactions between the A, B, and C block can be

tuned to produce different assemblies. For example, Park *et al.* used PS-P2VP/PMMA mixtures to produce multi-scale surface patterns.³²

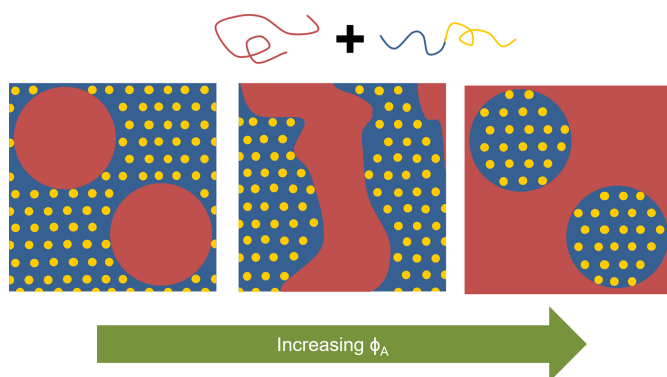


Figure 7-2: Schematic of A/B-C polymer blends. The homopolymer, A, is shown in red, and the block polymer, B-C, is shown in blue and yellow, respectively. With increasing volume fraction A, the domain should shift from droplets of A in a B-C matrix to co-continuous A/B-C structures to matrix of A with droplets of B-C.

The work presented in Chapter 3 can provide direction to control the macrophase separation of the polymer blend (A and B-C). Once the desired morphology is achieved, the structure and orientation of the block polymer can be controlled. The nanostructure of the block polymer is determined by the composition and segregation strength,³³⁻³⁴ whereas the orientation and ordering can be controlled *via* annealing techniques.³⁵⁻³⁷ Thus, from the expertise developed within the Epps group, it is feasible to produce these hierarchical materials.

7.2.2.3 Hierarchical Assemblies for OPV Materials.

Organic photovoltaic devices composed of polymers blended with nanoparticles have been reported, in which the nanoparticles act as the acceptor and

transport the charge to the electrodes.³⁸⁻⁵⁴ In these devices, the nanoparticle dispersion within the active layer is key towards enhancing the efficiency by increasing the interfacial area between the inorganic particle and polymer.³⁹ Furthermore, particles with higher aspect ratios better facilitate charge transport between the electrodes.⁴¹ Additionally, nanoparticles have been incorporated to improve the efficiency of devices by scattering light or plasmonic effects.⁵⁵⁻⁵⁷ In these plasmonic nanoparticle/polymer donor/small molecule acceptor blends, the location of the nanoparticle affects different efficiencies; for instance, nanoparticles at the interface between the hole transport layer and the anode improve efficiency by reducing exciton quenching.⁵⁵ Despite these advantages, inorganic nanoparticle-polymer OPVs, the processing of these materials can be challenging and the absorbance spectrum of the device is limited by the polymer selection.

Polymer blends have also been used in organic photovoltaics; though polymer blends have lower device efficiency compared to block polymer OPVs due to the larger domain sizes, they have additional tunability and require fewer synthetic steps.⁵⁸⁻⁶⁰ Herein, I will discuss only polymer blend devices. All polymer solar cells, which consist of donor/acceptor polymer blends are more easily processed than the polymer/small molecule OPVs.^{1, 61-65} In these systems, the morphology of the resulting devices is key.¹ Thus, being able to control the morphology is vital towards producing higher efficiency polymer blends. To capitalize on a larger portion of the solar spectrum, donor/donor/small molecule acceptor polymer blends have been generated.⁶⁶⁻⁶⁸ In addition to the structure of these active layers, the domain size is also important. Thus, reducing the domain size will also increase the efficiency.

I propose using donor polymer/donor polymer/acceptor nanoparticle blends to generate more efficient OPVs. The donor polymer pair can afford increased absorption of the solar spectrum. Additionally, incorporating plasmonic nanoparticles will contribute surface plasmon resonance effects in addition to acting as the electron acceptor material. These improvements should further enhance the device efficiency. Finally, driving the particles to the interface during phase separation can reduce the domain size. The resulting hierarchical multi-component solar cell device proposed is shown schematically in Figure 7-3.

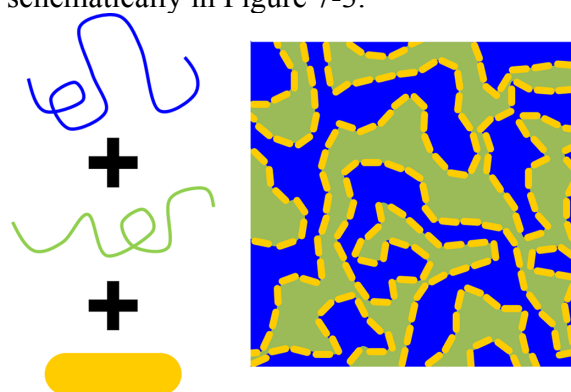


Figure 7-3. Hierarchical organic photovoltaic (OPV) structure. Blue and green represent the two polymers and the gold capsules represent gold nanorods.

The device proposed herein can be produced from extension of the knowledge developed and discussed in previous sections, including effect of crystallization on polymer blend phase separation (Chapter 3) and the partitioning of nanoparticles within a polymer blend (Chapter 4). However, further understanding must be gained before achieving these structures. In particular, the connection between the onset of phase separation, driven by thermodynamic incompatibility upon solvent removal, and the kinetic trapping of the phase evolution, which occurs due to jamming of the

interfaces by the particles and the loss of chain mobility due to solvent evaporation, must be elucidated. To probe these relationships, the application of new *in situ* techniques, such as the methods suggested in Section 7.2.1.2, is required.

7.3 Summary of Future Directions

The future directions proposed in the previous sections involve furthering the understanding of additional factors on processing and leveraging the insights gained from this work to create new functional materials.

In Section 7.2.1, additional processing factors and relationships that were beyond the scope of this dissertation but that are relevant towards producing new materials were highlighted. One such effect is the glass transition temperature; in our studies of renewable polymers (Chapter 6), the T_g 's spanned a range of 100 K. Utilizing these materials in applications requires knowledge of the effect of T_g on processing (Section 7.2.1.1). One of the limitations in the study described in Chapter 4 on the interplay between kinetics and thermodynamics was the difficulty in measuring the early stage phase separation. Utilization of *in situ* techniques, such as GISAXS/GIWAXS, during casting (Section 7.2.1.2) can greatly improve the understanding of the effect of the phase behavior on the morphology. These insights will provide better relationships between the equilibrium thermodynamics and the processing factors, which affords the generation of targeted structures for batch and continuous processes. Towards producing coatings on a large scale, directly translating morphologies from batch to continuous processes can be desirable. Thus, exploring factors that differ between batch and continuous casting processes, such as the solvent evaporation rate and drying time (Section 7.2.1.3) can provide useful insight to target desirable morphologies. Other processing manipulations, in particular

the addition of an external electric field, were suggested to expand the morphology parameter space towards controlling and generating new hierarchical structures (Section 7.2.1.4).

In Section 7.2.2, three applications of multi-component polymer systems which can benefit from the structure-property relationships described in Chapter 5, along with the knowledge gained on controlling the morphology, as discussed in Chapter 3 and Chapter 4 are proposed. The development of structure-property relationships in pressure sensitive adhesives (Section 7.2.2.1) can promote new structures or widen the range of applications of polymer blends. For membranes (Section 7.2.2.2) and organic photovoltaics (Section 7.2.2.3), hierarchical structures can be leveraged to greatly enhance their properties and extend their use to other materials systems of interest. However, there are other processing factors that need to be explored to implement these new material systems.

Overall, the future directions target further knowledge on controlling the production of hierarchical structures from multicomponent polymer solutions and improved understanding of structure-property relationships in functional coatings

REFERENCES

1. Fabiano, S.; Himmelberger, S.; Drees, M.; Chen, Z.; Altamimi, R. M.; Salleo, A.; Loi, M. A.; Facchetti, A. C., Charge transport orthogonality in all-polymer blend transistors, diodes, and solar cells. *Adv. Energy Mater.* **2014**, *4*, 1301409.
2. Walheim, S.; Boltau, M.; Mlynek, J.; Krausch, G.; Steiner, U., Structure formation via polymer demixing in spin-cast films. *Macromolecules* **1997**, *30*, 4995-5003.
3. Holmberg, A. L.; Stanzione, J. F.; Wool, R. P.; Epps, T. H., III, A facile method for generating designer block copolymers from functionalized lignin model compounds. *ACS Sustainable Chem. Eng.* **2014**, *2*, 569-573.
4. Holmberg, A. L.; Karavolias, M. G.; Epps, T. H., III, RAFT polymerization and associated reactivity ratios of methacrylate-functionalized mixed bio-oil constituents. *Polym. Chem.* **2015**, *6*, 5728-5739.
5. Holmberg, A. L.; Nguyen, N. A.; Karavolias, M. G.; Reno, K. H.; Wool, R. P.; Epps, T. H., III, Softwood lignin-based methacrylate polymers with tunable thermal and viscoelastic properties. *Macromolecules* **2016**, *49*, 1286-1295.
6. Holmberg, A. L.; Reno, K. H.; Nguyen, N. A.; Wool, R. P.; Epps, T. H., III, Syringyl methacrylate, a hardwood lignin-based monomer for high-Tg polymeric materials. *ACS Macro Lett.* **2016**, *5*, 574-578.
7. Sanyal, M.; Schmidt-Hansberg, B.; Klein, M. F. G.; Colsmann, A.; Munuera, C.; Vorobiev, A.; Lemmer, U.; Schabel, W.; Dosch, H.; Barrena, E., In situ X-ray study of drying-temperature influence on the structural evolution of bulk-heterojunction polymer–fullerene solar cells processed by doctor-blading. *Adv. Energy Mater.* **2011**, *1*, 363-367.
8. Schmidt-Hansberg, B.; Sanyal, M.; Klein, M. F. G.; Pfaff, M.; Schnabel, N.; Jaiser, S.; Vorobiev, A.; Müller, E.; Colsmann, A.; Scharfer, P.; Gerthsen, D.; Lemmer, U.; Barrena, E.; Schabel, W., Moving through the phase diagram: morphology formation in solution cast polymer–fullerene blend films for organic solar cells. *ACS Nano* **2011**, *5*, 8579-8590.

9. Sanyal, M.; Schmidt-Hansberg, B.; Klein, M. F. G.; Munuera, C.; Vorobiev, A.; Colsmann, A.; Scharfer, P.; Lemmer, U.; Schabel, W.; Dosch, H.; Barrena, E., Effect of photovoltaic polymer/fullerene blend composition ratio on microstructure evolution during film solidification investigated in real time by X-ray diffraction. *Macromolecules* **2011**, *44*, 3795-3800.
10. Perez, L. A.; Chou, K. W.; Love, J. A.; van der Poll, T. S.; Smilgies, D.-M.; Nguyen, T.-Q.; Kramer, E. J.; Amassian, A.; Bazan, G. C., Solvent additive effects on small molecule crystallization in bulk heterojunction solar cells probed during spin casting. *Adv. Mater.* **2013**, *25*, 6380-6384.
11. Toolan, D. T. W.; Isakova, A.; Hodgkinson, R.; Reeves-McLaren, N.; Hammond, O. S.; Edler, K. J.; Briscoe, W. H.; Arnold, T.; Gough, T.; Topham, P. D.; Howse, J. R., Insights into the influence of solvent polarity on the crystallization of poly(ethylene oxide) spin-coated thin films via in situ grazing incidence wide-angle X-ray scattering. *Macromolecules* **2016**, *49*, 4579-4586.
12. Chou, K. W.; Yan, B.; Li, R.; Li, E. Q.; Zhao, K.; Anjum, D. H.; Alvarez, S.; Gassaway, R.; Biocca, A.; Thoroddsen, S. T.; Hexemer, A.; Amassian, A., Spin-cast bulk heterojunction solar cells: a dynamical investigation. *Adv. Mater.* **2013**, *25*, 1923-1929.
13. Pröllner, S.; Liu, F.; Zhu, C.; Wang, C.; Russell, T. P.; Hexemer, A.; Müller-Buschbaum, P.; Herzig, E. M., Following the morphology formation in situ in printed active layers for organic solar cells. *Adv. Energy Mater.* **2016**, *6*, 1501580-n/a.
14. Wang, T.; Dunbar, A. D. F.; Staniec, P. A.; Pearson, A. J.; Hopkinson, P. E.; MacDonald, J. E.; Lilliu, S.; Pizzey, C.; Terrill, N. J.; Donald, A. M.; Ryan, A. J.; Jones, R. A. L.; Lidzey, D. G., The development of nanoscale morphology in polymer:fullerene photovoltaic blends during solvent casting. *Soft Matter* **2010**, *6*, 4128-4134.
15. Haq, E. U.; Toolan, D. T. W.; Emerson, J. A.; Epps, T. H., III; Howse, J. R.; Dunbar, A. D. F.; Ebbens, S. J., Real time laser interference microscopy for bar-spread polystyrene/poly(methyl methacrylate) blends. *J. Polym. Sci., Part B: Polym. Phys.* **2014**, *52*, 985-992.
16. Zhang, X.; Douglas, J. F.; Jones, R. L., Influence of film casting method on block copolymer ordering in thin films. *Soft Matter* **2012**, *8*, 4980-4987.
17. Wypych, G., Knovel Solvents - A Properties Database. ChemTec Publishing.

18. Brandrup, J.; Immergut, E. H.; Grulke, E. A., *Polymer Handbook*. 4th ed.; Wiley: New York, 1999.
19. Venugopal, G.; Krause, S.; Wnek, G. E., Modification of polymer blend morphology using electric fields. *J. Polym. Sci., Part C: Polym. Lett.* **1989**, *27*, 497-501.
20. Venugopal, G.; Krause, S.; Wnek, G. E., Morphological variations in polymer blends made in electric fields. *Chem. Mater.* **1992**, *4*, 1334-1343.
21. Hori, H.; Urakawa, O.; Yano, O.; Tran-Cong-Miyata, Q., Phase separation of binary polymer mixtures under an electric field. *Macromolecules* **2007**, *40*, 389-394.
22. Lee, J. S.; Prabu, A. A.; Kim, K. J., UCST-type phase separation and crystallization behavior in poly(vinylidene fluoride)/poly(methyl methacrylate) blends under an external electric field. *Macromolecules* **2009**, *42*, 5660-5669.
23. Wang, C.-H.; Chen, P.; Lu, C. Y. D., Phase separation of thin-film polymer mixtures under in-plane electric fields. *Phys. Rev. E* **2010**, *81*, 061501.
24. Padinger, F.; Rittberger, R. S.; Sariciftci, N. S., Effects of postproduction treatment on plastic solar cells. *Adv. Funct. Mater.* **2003**, *13*, 85-88.
25. Guo, Y.; Batra, S.; Chen, Y.; Wang, E.; Cakmak, M., Roll to roll electric field “Z” alignment of nanoparticles from polymer solutions for manufacturing multifunctional capacitor films. *ACS Appl. Mater. Interfaces* **2016**, *8*, 18471-18480.
26. Müller-Buschbaum, P.; Ittner, T.; Maurer, E.; Körstgens, V.; Petry, W., Pressure-sensitive adhesive blend films for low-tack applications. *Macromol. Mater. Eng.* **2007**, *292*, 825-834.
27. Grande, D., Crossing porosity scales in functional polymer materials: from design to application. In *Polymer science: research advances, practical applications and educational aspects*, Méndez-Vilas, A.; Solano-Martín, A., Eds. Formatex Research Center: Spain, 2016.
28. Ly, H. B.; Le Droumaguet, B.; Monchiet, V.; Grande, D., Designing and modeling doubly porous polymeric materials. *Eur. Phys. J.: Spec. Top.* **2015**, *224*, 1689-1706.

29. Ly, H. B.; Le Droumaguet, B.; Monchiet, V.; Grande, D., Facile fabrication of doubly porous polymeric materials with controlled nano- and macro-porosity. *Polymer* **2015**, *78*, 13-21.
30. Ly, H. B.; Le Droumaguet, B.; Monchiet, V.; Grande, D., Tailoring doubly porous poly(2-hydroxyethyl methacrylate)-based materials via thermally induced phase separation. *Polymer* **2016**, *86*, 138-146.
31. Millett, P. C., Mesoscopic simulations of coarsening kinetics within block-copolymer/homopolymer thin films. *Comput. Mater. Sci.* **2016**, *125*, 20-27.
32. Park, H.; Kim, J.-U.; Park, S., High-throughput preparation of complex multi-scale patterns from block copolymer/homopolymer blend films. *Nanoscale* **2012**, *4*, 1362-1367.
33. Bates, F. S., Polymer-polymer phase behavior. *Science* **1991**, *251*, 898.
34. Matsen, M. W., Effect of architecture on the phase behavior of AB-type block copolymer melts. *Macromolecules* **2012**, *45*, 2161-2165.
35. Albert, J. N. L.; Epps, T. H., III, Self-assembly of block copolymer thin films. *Mater. Today* **2010**, *13*, 24-33.
36. Luo, M.; Epps, T. H., III, Directed block copolymer thin film self-assembly: emerging trends in nanopattern fabrication. *Macromolecules* **2013**, *46*, 7567-7579.
37. Mastroianni, S. E.; Epps, T. H., III, Interfacial manipulations: controlling nanoscale assembly in bulk, thin film, and solution block copolymer systems. *Langmuir* **2013**, *29*, 3864-3878.
38. Huynh, W. U.; Dittmer, J. J.; Alivisatos, A. P., Hybrid nanorod-polymer solar cells. *Science* **2002**, *295*, 2425.
39. Huynh, W. U.; Dittmer, J. J.; Libby, W. C.; Whiting, G. L.; Alivisatos, A. P., Controlling the morphology of nanocrystal-polymer composites for solar cells. *Adv. Funct. Mater.* **2003**, *13*, 73-79.
40. Sun, Z.; Li, J.; Liu, C.; Yang, S.; Yan, F., Enhancement of hole mobility of poly(3-hexylthiophene) induced by titania nanorods in composite films. *Adv. Mater.* **2011**, *23*, 3648-3652.

41. Bouclé, J.; Chyla, S.; Shaffer, M. S. P.; Durrant, J. R.; Bradley, D. D. C.; Nelson, J., Hybrid solar cells from a blend of poly(3-hexylthiophene) and ligand-capped TiO₂ nanorods. *Adv. Funct. Mater.* **2008**, *18*, 622-633.
42. Wu, S.; Tai, Q.; Yan, F., Hybrid photovoltaic devices based on poly(3-hexylthiophene) and ordered electrospun ZnO nanofibers. *J. Phys. Chem. C* **2010**, *114*, 6197-6200.
43. Tai, Q.; Zhao, X.; Yan, F., Hybrid solar cells based on poly(3-hexylthiophene) and electrospun TiO₂ nanofibers with effective interface modification. *J. Mater. Chem.* **2010**, *20*, 7366-7371.
44. Lin, Y.-Y.; Chu, T.-H.; Li, S.-S.; Chuang, C.-H.; Chang, C.-H.; Su, W.-F.; Chang, C.-P.; Chu, M.-W.; Chen, C.-W., Interfacial nanostructuring on the performance of polymer/TiO₂ nanorod bulk heterojunction solar cells. *J. Am. Chem. Soc.* **2009**, *131*, 3644-3649.
45. Kwong, C. Y.; Choy, W. C. H.; Djurišić, A. B.; Chui, P. C.; Cheng, K. W.; Chan, W. K., Poly (3-hexylthiophene): TiO₂ nanocomposites for solar cell applications. *Nanotechnology* **2004**, *15*, 1156.
46. Wu, M.-C.; Lo, H.-H.; Liao, H.-C.; Chen, S.; Lin, Y.-Y.; Yen, W.-C.; Zeng, T.-W.; Chen, Y.-F.; Chen, C.-W.; Su, W.-F., Using scanning probe microscopy to study the effect of molecular weight of poly(3-hexylthiophene) on the performance of poly(3-hexylthiophene):TiO₂ nanorod photovoltaic devices. *Sol. Energy Mater. Sol. Cells* **2009**, *93*, 869-873.
47. Ravirajan, P.; Haque, S. A.; Durrant, J. R.; Bradley, D. D. C.; Nelson, J., The effect of polymer optoelectronic properties on the performance of multilayer hybrid polymer/TiO₂ solar cells. *Adv. Funct. Mater.* **2005**, *15*, 609-618.
48. Lu, M.-D.; Yang, S.-M., Synthesis of poly(3-hexylthiophene) grafted TiO₂ nanotube composite. *J. Colloid Interface Sci.* **2009**, *333*, 128-134.
49. Zeng, T.-W.; Lo, H.-H.; Chang, C.-H.; Lin, Y.-Y.; Chen, C.-W.; Su, W.-F., Hybrid poly (3-hexylthiophene)/titanium dioxide nanorods material for solar cell applications. *Sol. Energy Mater. Sol. Cells* **2009**, *93*, 952-957.
50. Lin, Y.-Y.; Chu, T.-H.; Chen, C.-W.; Su, W.-F., Improved performance of polymer/TiO₂ nanorod bulk heterojunction photovoltaic devices by interface modification. *Appl. Phys. Lett.* **2008**, *92*, 053312.

51. Xi, D.; Zhang, H.; Furst, S.; Chen, B.; Pei, Q., Electrochemical synthesis and photovoltaic property of cadmium sulfide–polybithiophene interdigitated nanohybrid thin films. *J. Phys. Chem. C* **2008**, *112*, 19765-19769.
52. Beek, W. J. E.; Wienk, M. M.; Janssen, R. A. J., Hybrid solar cells from regioregular polythiophene and ZnO nanoparticles. *Adv. Funct. Mater.* **2006**, *16*, 1112-1116.
53. Liu, J. S.; Kadnikova, E. N.; Liu, Y. X.; McGehee, M. D.; Frechet, J. M. J., Polythiophene containing thermally removable solubilizing groups enhances the interface and the performance of polymer-titania hybrid solar cells. *J. Am. Chem. Soc.* **2004**, *126*, 9486–9487.
54. Liu, R., Hybrid organic/inorganic nanocomposites for photovoltaic cells. *Materials* **2014**, *7*, 2747-2771.
55. Stratakis, E.; Kymakis, E., Nanoparticle-based plasmonic organic photovoltaic devices. *Mater. Today* **2013**, *16*, 133-146.
56. Jiang, W. J.; Salvador, M.; Dunham, S. T., Combined three-dimensional electromagnetic and device modeling of surface plasmon-enhanced organic solar cells incorporating low aspect ratio silver nanoprisms. *Appl. Phys. Lett.* **2013**, *103*, 5.
57. Wang, D. H.; Kim, D. Y.; Choi, K. W.; Seo, J. H.; Im, S. H.; Park, J. H.; Park, O. O.; Heeger, A. J., Enhancement of donor–acceptor polymer bulk heterojunction solar cell power conversion efficiencies by addition of Au nanoparticles. *Angew. Chem. Int. Ed.* **2011**, *50*, 5519-5523.
58. Guo, C.; Lin, Y.-H.; Witman, M. D.; Smith, K. A.; Wang, C.; Hexemer, A.; Strzalka, J.; Gomez, E. D.; Verduzco, R., Conjugated block copolymer photovoltaics with near 3% efficiency through microphase separation. *Nano Lett.* **2013**, *13*, 2957-2963.
59. McNeill, C. R.; Halls, J. J. M.; Wilson, R.; Whiting, G. L.; Berkebile, S.; Ramsey, M. G.; Friend, R. H.; Greenham, N. C., Efficient polythiophene/polyfluorene copolymer bulk heterojunction photovoltaic devices: device physics and annealing effects. *Adv. Funct. Mater.* **2008**, *18*, 2309-2321.
60. McNeill, C. R.; Abrusci, A.; Zaumseil, J.; Wilson, R.; McKiernan, M. J.; Burroughes, J. H.; Halls, J. J. M.; Greenham, N. C.; Friend, R. H., Dual electron donor/electron acceptor character of a conjugated polymer in efficient photovoltaic diodes. *Appl. Phys. Lett.* **2007**, *90*, 193506.

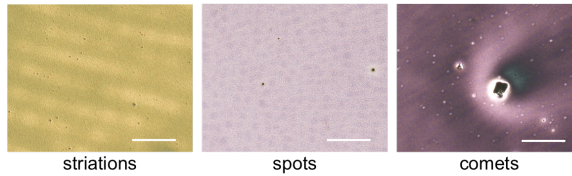
61. Zhou, Y.; Kurosawa, T.; Ma, W.; Guo, Y.; Fang, L.; Vandewal, K.; Diao, Y.; Wang, C.; Yan, Q.; Reinspach, J.; Mei, J.; Appleton, A. L.; Koleilat, G. I.; Gao, Y.; Mannsfeld, S. C. B.; Salleo, A.; Ade, H.; Zhao, D.; Bao, Z., High performance all-polymer solar cell via polymer side-chain engineering. *Adv. Mater.* **2014**, *26*, 3767-3772.
62. Liu, Y.; Larsen-Olsen, T. T.; Zhao, X.; Andreasen, B.; Søndergaard, R. R.; Helgesen, M.; Norrman, K.; Jørgensen, M.; Krebs, F. C.; Zhan, X., All polymer photovoltaics: from small inverted devices to large roll-to-roll coated and printed solar cells. *Sol. Energy Mater. Sol. Cells* **2013**, *112*, 157-162.
63. Facchetti, A., Polymer donor–polymer acceptor (all-polymer) solar cells. *Mater. Today* **2013**, *16*, 123-132.
64. Falzon, M.-F.; Wienk, M. M.; Janssen, R. A. J., Designing acceptor polymers for organic photovoltaic devices. *J. Phys. Chem. C* **2011**, *115*, 3178-3187.
65. Mu, C.; Liu, P.; Ma, W.; Jiang, K.; Zhao, J.; Zhang, K.; Chen, Z.; Wei, Z.; Yi, Y.; Wang, J.; Yang, S.; Huang, F.; Facchetti, A.; Ade, H.; Yan, H., High-efficiency all-polymer solar cells based on a pair of crystalline low-bandgap polymers. *Adv. Mater.* **2014**, *26*, 7224-7230.
66. Li, N.; Machui, F.; Waller, D.; Koppe, M.; Brabec, C. J., Determination of phase diagrams of binary and ternary organic semiconductor blends for organic photovoltaic devices. *Sol. Energy Mater. Sol. Cells* **2011**, *95*, 3465-3471.
67. Koppe, M.; Egelhaaf, H.-J.; Dennler, G.; Scharber, M. C.; Brabec, C. J.; Schilinsky, P.; Hoth, C. N., Near IR sensitization of organic bulk heterojunction solar cells: towards optimization of the spectral response of organic solar cells. *Adv. Funct. Mater.* **2010**, *20*, 338-346.
68. Park, S. J.; Cho, J. M.; Byun, W.-B.; Lee, J.-C.; Shin, W. S.; Kang, I.-N.; Moon, S.-J.; Lee, S. K., Bulk heterojunction polymer solar cells based on binary and ternary blend systems. *J. Polym. Sci., Part A: Polym. Chem.* **2011**, *49*, 4416-4424.

Appendix A

CASTING FROM POLYMER SOLUTIONS

During casting, a number of defects can occur that influence the final film. Common defects for spin cast films are shown in Figure A-1. Striations and spots occur as the result of instabilities at the film surface, such as Marangoni instabilities. Comets occur due to dust, dirt, or particles that are found on the wafer surface or in the solution.. Depending on the size of the particulates, comets may also be seen macroscopically. Pin-holes are also caused by particles on the surface or in the solution. Dewetting can occur in films if the substrate-solution interaction is unfavorable. Corner effects occur when using non-circular substrates. If the solution viscosity is too high, swirl patterns may develop, resulting in a variety of thicknesses across the film. Finally, if not enough solution is dispensed onto the substrate, the film may only partially coat the surface.

Microscopic defects



Macroscopic defects

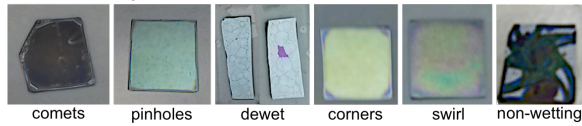


Figure A-1. Common spin coating defects. The scale bar is 100 μm .

During flow coating from concentrated or viscous solutions, such as those in Chapter 5 and 6, a number of casting artifacts can occur. In these films, the drying front is not induced immediately after casting. Thus, in order to produce a more uniform film, a drying front must propagate from one direction.

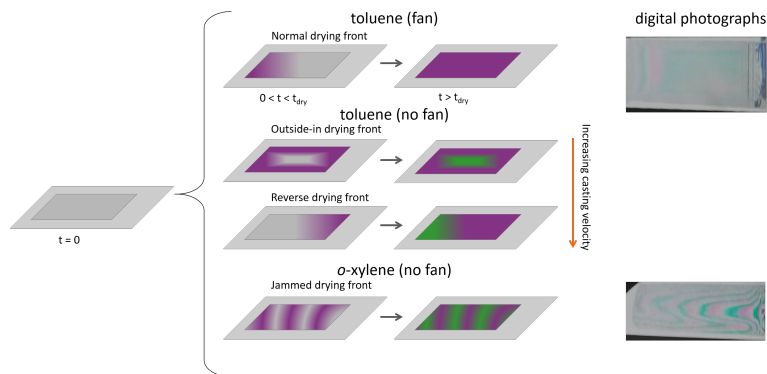


Figure A-2. Non-uniformities in flow coated films.

Appendix B

SOLVENT VAPOR SWELLING OF POLYMER FILMS

B.1 Solvent Vapor Swelling

In this dissertation, solvent vapor swelling is used for two purposes: (1) producing solvent-polymer interaction parameters, which is discussed in Chapter 3 and Chapter 6, and (2) annealing the structure in polymer blend films, which is demonstrated in Chapter 5. For these experiments, either a bell jar annealing (closed system) or flow solvent vapor annealing (open system) set-up can be accessed.

B.2 Bell Jar Solvent Vapor Swelling

The first type of solvent vapor swelling/solvent annealing is the bell jar solvent vapor swelling method. The set-up for a bell jar experiment is shown in Figure B-1. Whole films or segments of films are placed in a chamber alongside a solvent reservoir. The chamber is then sealed, which allows the solvent to saturate the atmosphere. The main parameters that can be controlled in a bell jar solvent vapor swelling test are solvent, solvent concentration, temperature, and time. With a single solvent reservoir containing only one solvent, the solvent concentration reaches saturation. However, the solvent concentration can be tuned by incorporating a second solvent, typically a non-solvent for the polymers of interest. In these solvent mixtures, the vapor phase composition can be predicted using vapor liquid equilibrium with software such as ASPEN. The temperature of the chamber can also be controlled using a thermal stage. Finally, the amount of time the films are exposed to the solvent

can be used to change the morphology or orientation in the case of polymer blends or block polymers.

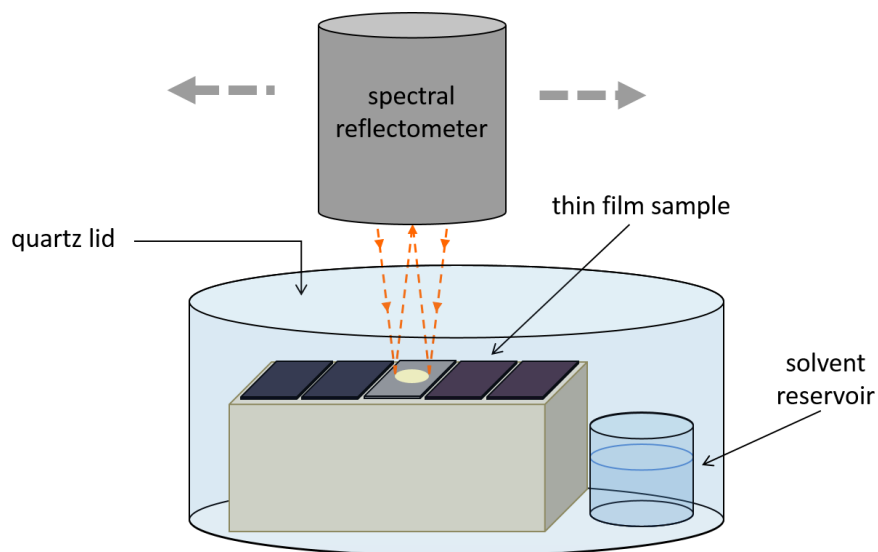


Figure B-1. Schematic of bell jar solvent vapor swelling setup. The films are placed in a chamber alongside a solvent reservoir. The solvent evaporates and produces a saturated solvent atmosphere inside the sealed chamber. The film thickness can be measured *in situ* using the spectral reflectometer through the quartz lid.

B.3 Flow Solvent Vapor Swelling

The second type of solvent vapor swelling experiment is flow solvent vapor annealing (flow SVA). The flow SVA system is shown in Figure B-2.

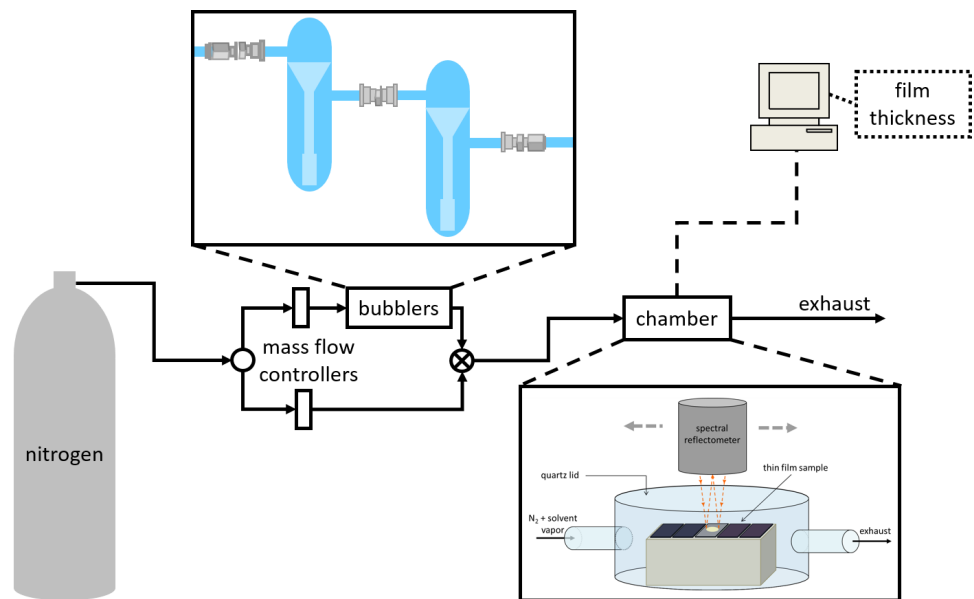


Figure B-2. Flow solvent vapor annealing/swelling set-up. The nitrogen carrier gas is split into two streams; the first stream flows through the solvent bubblers, and the second stream acts as a diluent. The relative flow rates are controlled using mass flow controllers. Then, the solvent-rich vapor is delivered to the chamber, which is shown larger in Figure B-3. Changes in film thickness are monitored using a spectral reflectometer that is connected to a computer.

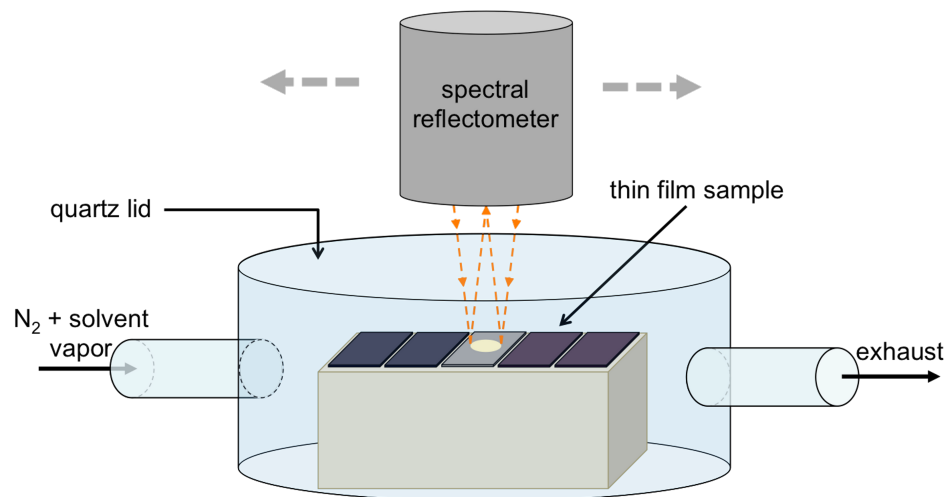


Figure B-3. Schematic of solvent vapor swelling chamber (not to scale). Solvent rich vapor in a nitrogen carrier gas is delivered to the sealed glass chamber. The quartz lid enables *in situ* film thickness measurements with a spectral reflectometer, which is moved using a motorized stage. The solvent vapor and N₂ gas exit the chamber *via* the exhaust port. Reprinted with permission from Emerson, J. A., *et al. Macromolecules* 2013, 46 (16), 6533-6540. Copyright 2013 American Chemical Society.

B.4 Solvent Collection

In order to determine the composition of solvent in the vapor phase, solvent collection experiments were implemented. For solvent quantification, the vapor is condensed using a dry ice/isopropanol bath, as shown in Figure B-4.

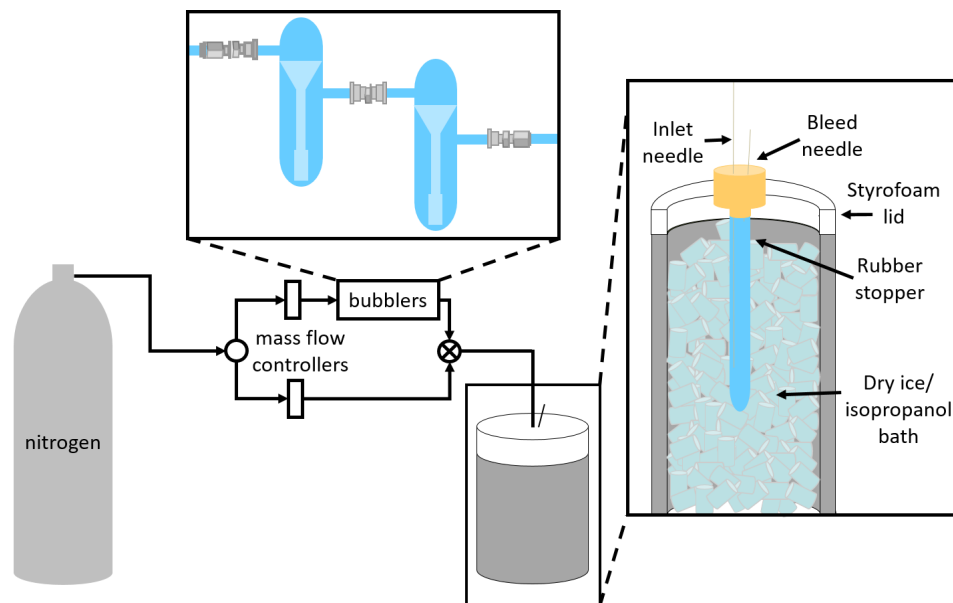


Figure B-4. Schematic of solvent collection experiments. After the N_2 passes through the solvent bubblers, the solvent rich vapor is condensed in a dry ice/isopropanol bath. The solvent condenses, and the N_2 is allowed to escape through the bleed needle to prevent pressurization.

Typical uptake curves determined using the solvent collection set-up (see Figure B-4) are shown in Figure B-5. The key parameters in choosing a solvent for swelling or annealing tests are: (1) the solvent swells the polymer sufficiently to provide chain mobility within the accessible solvent concentration range (moderate to good solvent) and (2) there is a measurable amount of solvent to be collected (lower boiling point)

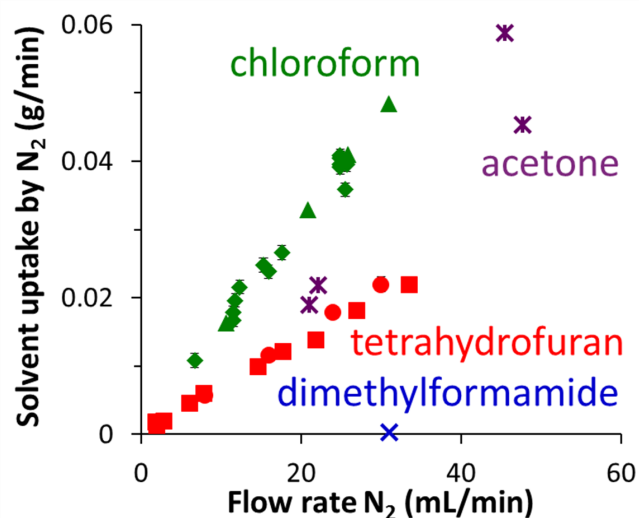


Figure B-5. Solvent uptake curves for chloroform (◆,▲), acetone (*), tetrahydrofuran (■,●), dimethylformamide (×). Manual (◆,*,■) and automated (▲,●,×) flow controllers were used to flow N₂ through the solvent bubblers; there was not a significant difference between the two controller types with respect to the solvent uptake. The linear relationship between flow rate and solvent uptake suggests that the solvent-rich stream is saturated with respect to nitrogen.

The temperature also can play a significant role in the solvent vapor swelling experiments. Using the same flow rates, the solvent uptake varied as much as 30% over a 4 °C temperature range, as demonstrated in Figure B-6. Within this temperature range, the uptake was nearly linear with temperature.

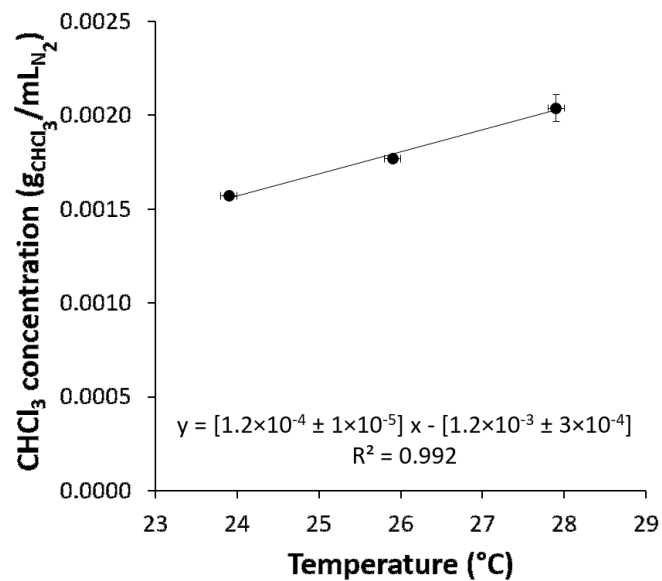


Figure B-6. Chloroform uptake with concentration. Between 24 °C and 28 °C, the solvent uptake is roughly linear with temperature. This 4 °C region has a ~30% difference in uptake values.

Appendix C

SUPPORTING INFORMATION FOR CHAPTER 3

C.1 Drying Curves – Selecting $t = 0$ s

Setting $t = 0$ s in the drying curves was important to comparing the drying times. Depending on the lag between starting the spectra capturing program (SpinCoating.py) and the spin coater, the drying times vary for the same material. Thus, a method was developed to determine the beginning of spinning (the spectra acquisition program was always started first). Measuring the same spot with no significant differences should not produce a change in the spectra. Thus, any changes from the previous spectra initially is due to the start of the motor. This effect is illustrated in Figure C-1 for a 0.9 wt.% PS in *o*-xylene solution cast at 1500 rpm. At 0.867 s, the spectra deviates from the previously recorded profiles. Thus, for this experiment, the time is shifted by 0.867 s.

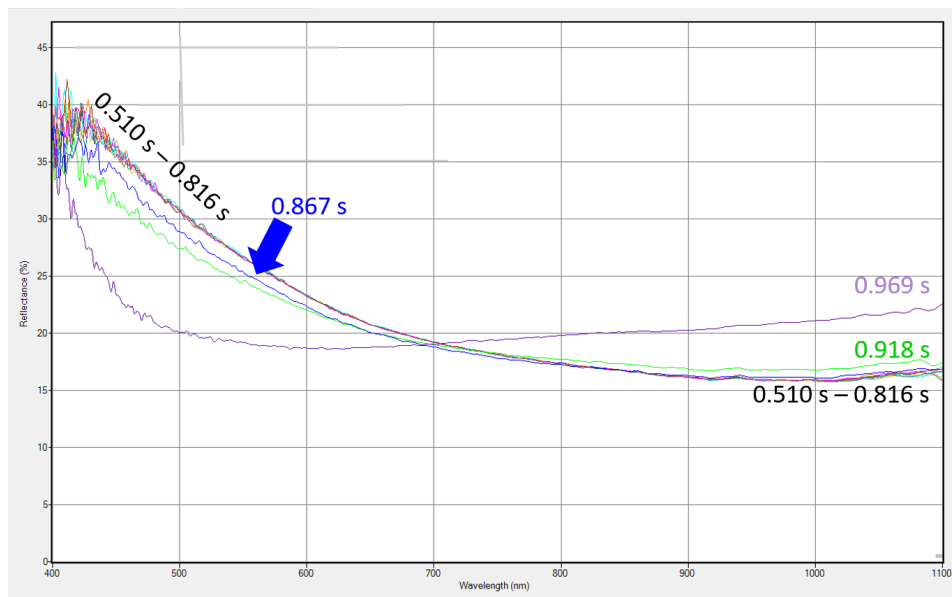


Figure C-1. Time stamped spectra (reflectance [%] vs. wavelength [nm]) for drying curve experiments with 0.9 wt.% PS in *o*-xylene cast at 1500 rpm.

C.2 P3HT Refractive Index

One limitation of solvent vapor swelling is that the refractive index profile must be known. The refractive indices for the common polymers (PS, PI, PMMA) were from literature (1.59, 1.52, 1.49).¹ For polymers that absorb, such as P3HT, determining the refractive index profile is challenging. Though the refractive index profile for P3HT has been reported in literature, it did not provide good fits for the experimental data profile. *Ex situ* experiments were performed to refine the P3HT refractive index from literature.

The refractive index profile for poly(3-hexylthiophene) [P3HT] was determined with assistance from Jim Elman at Filmetrics, Inc. Campoy-Quiles *et al.* determined a refractive index profile for P3HT.² However, this P3HT profile did not

accurately capture the spectra of the P3HT films. Neat P3HT films were cast at the same conditions on fused silica and silicon wafers. The thickness of the films deposited on silicon wafers was determined by scratch test using AFM. The films on fused silica were sent to Jim Elman, who analyzed the complex refractive index profile by measuring the reflection and transmission through the film. This profile was confirmed with ellipsometry. The resulting refractive index profile is shown in Figure C-2.

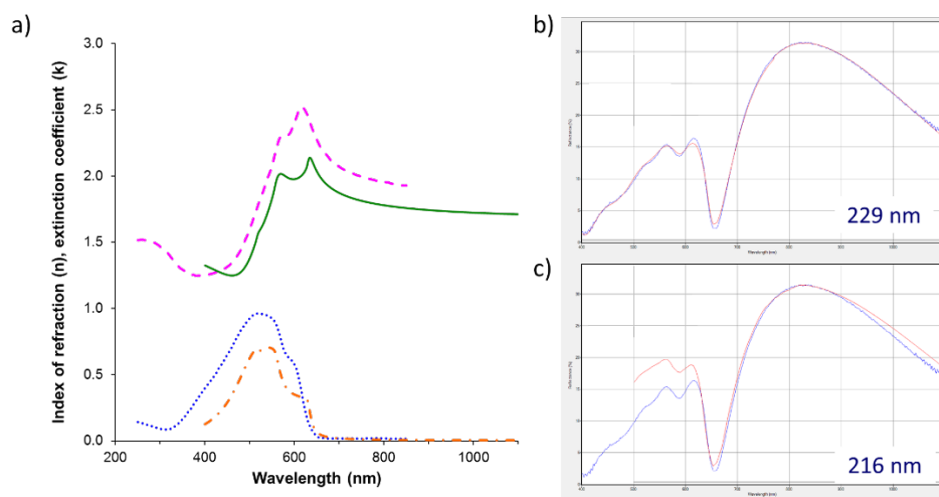


Figure C-2. a) Refractive index (n) and extinction coefficient (k) as a function of wavelength from Filmetrics (n: solid, k: dash dot) and literature (n: dash, k: dot).² b) Reflectance spectra (blue) fit for thickness using the Filmetrics model (red) produces a film thickness of 229 nm. c) The same spectra (blue) fit with the Campoy-Quiles refractive index profile (red) has a thickness of 216 nm. The thickness of this film from AFM was 222 nm \pm 8 nm. Though both fits provide thicknesses within error of the AFM value, the Filmetrics fit is visually improved (lower residuals).

However, this approach is not always accessible. An alternative work-around would be to utilize an ellipsometer instead of the spectral reflectometer. Though the

analysis is more challenging, the ellipsometer can extract information about both the refractive index and thickness.³ For other polymers, the refractive index was estimated, which is described in more detail in Appendix D.

C.3 Mathematica Code for Phase Diagram Calculation

The spinodal curve was generated using Mathematica. The code was implemented based on the Gibbs free energy relationships developed by R. L. Scott.⁴⁻⁵

Example code:

The input parameters are defined in the Mathematica code as follows:

```

(*dispersity*)
PSD = 105/100; (*dispersity of the PS*)
PSM = 111/100;(*dispersity of the PMMA*)

(*molecular weights*)
Mnps = 892000/PSD; (*number-average molecular weight of PS*)
Mnppmma = 100000/PSM;(*number-average molecular weight of
PMMA*)
Mnoxyl = 10616/100; (*molecular weight of o-xylene*)
MWs = 10415/100; (*molecular weight of the styrene monomer*)
MWmma = 10012/100; (*molecular weight of the methyl
methacrylate monomer*)

(*density*)
pps = 105/100; (*density of PS in g/cm3*)
ppmma = 119/100; (*density of PMMA in g/cm3*)
poxyl = 880/1000; (*density of o-xylene in g/cm3*)

(*molar volume*)
Vps = Mnps/pps;(*molar volume of PS*)
Vpmma = Mnppmma/ppmma;(*molar volume of PMMA*)
Voxy = Mnoxyl/poxyl;(*molar volume of o-xylene*)

(*volume ratio*)
mpmma = Vpmma/Voxy;(*ratio of molar volumes of PMMA to o-
xylene*)
mps = Vps/Voxy;(*ratio of molar volumes of PS to o-xylene*)

(*interaction parameters for polymer-polymer and polymer-solvent*)
upspmma = 97/1000; (*F-H interaction parameter for PS and
PMMA*)
uoxylps = 341/1000; (*F-H interaction parameter for o-xylene and
PS*)
uoxylpmma = 465/1000; (*F-H interaction parameter for o-xylene and
PMMA*)

```

The Gibbs free energy relationships described in Eq. D-1 are then written in the code, and the solving routine is set up. The spinodal curve is calculated as described by R. L. Scott.⁴⁻⁵ We note that the volume fraction of component i with respect to the total solution volume, ϕ_i , is denoted as x_i in the code.

```

(*the partial molar free energies of the components*)
Gs[xs_, xps_, xpmma_] := (Log[xs] + (1 - (1/mps))*xps + (1 -
(1/mpmma))*xpmma + uoxylps*xps^2 + uoxylpmma*xpmma^2 +
(uoxylps + uoxylpmma - upspmma)*xps*xpmma);
Gps[xs_, xps_, xpmma_] := (Log[xps] + (1 - mps)*xs + (1 -
(mps/mpmma))*xpmma + mps*(uoxylps*xs^2 + upspmma*xpmma^2
+ (uoxylps + upspmma - uoxylpmma)*xs*xpmma));
Gpmma[xs_, xps_, xpmma_] := (Log[xpmma] + (1 - mpmma)*xs + (1 -
(mpmma/mps))*xps + mpmma*(uoxylpmma*xs^2 +
upspmma*xps^2 + (uoxylpmma + upspmma - uoxylps)*xs*xps));

(* Does the as prepared solution phase separate? *)
Jac = {{Voxy1*D[Gs[xs, xps, xpmma], xs], Vps*D[Gs[xs, xps,
xpmma], xps], Vpmma*D[Gs[xs, xps, xpmma], xpmma]},
{Voxy1*D[Gps[xs, xps, xpmma], xs], Vps*D[Gps[xs, xps, xpmma],
xps], Vpmma*D[Gps[xs, xps, xpmma], xpmma]},
{Voxy1*D[Gpmma[xs, xps, xpmma], xs], Vps*D[Gpmma[xs, xps,
xpmma], xps], Vpmma*D[Gpmma[xs, xps, xpmma], xpmma]}};

sol = Solve[(Det[Jac] /. {xs -> 1 - xpmma - xps}) == 0, xpmma];

```

The solution is produced in this step. ϕ_{PS} is the input and ϕ_{PMMA} is the output.

The solvent volume fraction is given by $1 - \phi_{PS} - \phi_{PMMA}$. Both the third and fourth column of the resulting matrix provide valid values for the PMMA volume fraction.

```

(*the solution*)
n = 90000/100000; (*input a value for xps here*)
sln = N[xpmma /. sol /. {xps -> n}, 8](*this is xpmma*)

```

C.4 Transmission Data

For PS/P3HT blends, the onset of phase separation was determined using transmission experiments. The relative transmission of the sample with respect to the transmission of the pure solvent was measured. The cloud point curves are shown in

Figure C-3. The deviation from 100% transmission indicates the onset of phase separation in these systems.

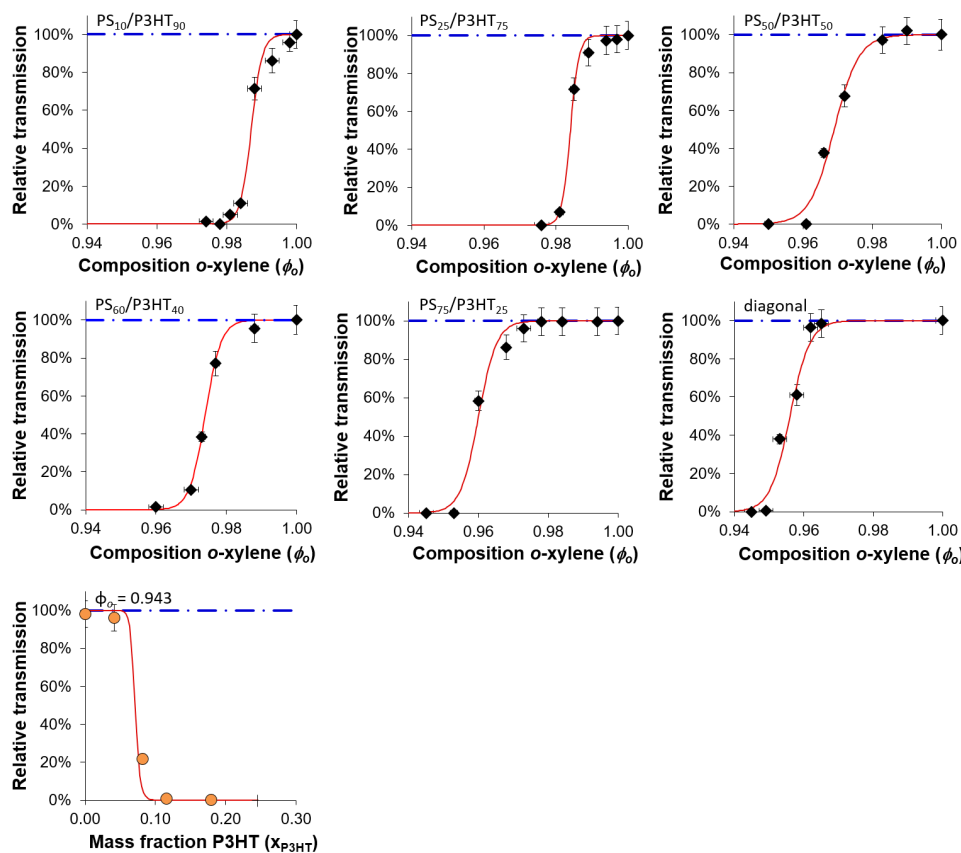


Figure C-3. Transmission experiment data at varying compositions of *o*-xylene (\blacklozenge) and at varying mass fraction of P3HT (\bullet). The dotted dashed line represents 100 % transmission (no phase separation). The solid red lines represent the spinodal fit to the data. The binodal region was determined by the deviation from 100 % transmission.

Digital photographs of the solutions through which transmission was measured are shown in Figure C-4. Solutions through which the background grid was visible were classified as transparent. These solutions had relative transmissions higher than

greater than These solutions had relative transmissions of 6.8 vol.% *o*-xylene. Starting with the highest concentration of solvent, the relative transmission decreased with solvent concentration relative to the transmission through *o*-xylene. The deviation (within error) of the transmission value from 100% transmission indicated the onset of phase separation in the polymer blend solution.⁶⁻⁸ With increasing polymer concentration (decreasing solvent content), the transmission decreased until the solutions became turbid, for which, the relative transmission was 0%.

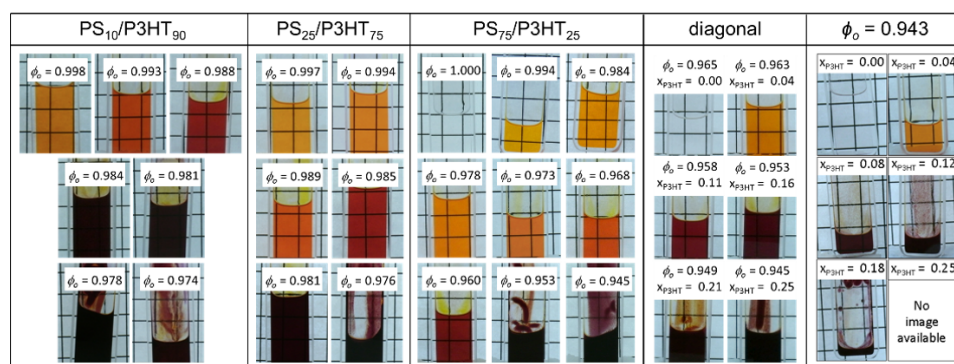


Figure C-4. Digital photographs of PS/P3HT/*o*-xylene solutions in the transmission cell. The volume fraction of each sample is indicated on the image. With increasing solvent concentration, the solutions change from opaque to optically transparent. Samples with higher P3HT content require more solvent to transition from the one phase (100% transmission) to the two phase (< 100% transmission) region.

C.5 Gelation of P3HT in *o*-Xylene

The gelation of P3HT occurred in *o*-xylene at sufficiently high polymer concentration. Digital photographs of gelled samples are shown in Figure C-5.

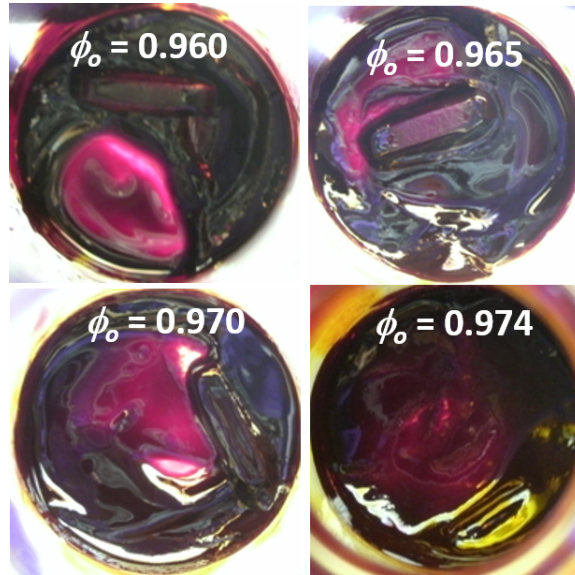


Figure C-5. Tilted vials containing PS₉₀/P3HT₁₀ in *o*-xylene. For solution volume fractions less than or equal to 0.97, the mixture formed a gel-like state that was capable of suspending a stir bar when the vial was tilted 90°. Increasing the solvent concentration to 0.974 produced more liquid-like behavior; during the tilt test for this solution, the stir bar fell to the bottom of the vial.

C.6 Matlab Code for Fitting Spin Coating Data

The code for solving the spin coating equation derived by Meyerhofer⁹ was developed using the Runge-Kutta 4th-5th order method outlined by Dormand and Prince.¹⁰ The majority of the code is given below for the constant viscosity solution.

```
%Here I use a Runge-Kutta 45 method (manually) to solve
the Meyerhofer spin casting model
```

```
clear; clc; close all; format LongG; pause on
```

```

%Reading in data
Experiment = csvread('5wtPSPMMAoxyl.csv');
nwt = length(Experiment);
Exptime = Experiment(1:nwt,1)/1000;
Expheight = Experiment(1:nwt,2)/10^9;

%Parameters of interest
    %Spin speed, rotations per minute
    rpm = 1500;
    %Angular velocity, 1/s
    w = rpm/60*2*pi;
    %Kinematic viscosity (constant), m2/s
    v = 1.4477*10^(-6);
    %Evaporation rate (constant), m/s
    evap = 4.453*10^(-7);
    %Initial concentration
    x0 = 0.05;
    %Relative ratio of PS to PMMA
    xPS = 0.5;
    xPMMA = 1 - xPS;
    %Polymer densities, g/m3
    pPS = 1.05*100^3;
    pPMMA = 1.19*100^3;
    %Volume fraction of PS relative ratio to polymer
    vPS = xPS./pPS./(xPS./pPS+xPMMA./pPMMA);
    %Volume fraction of PI relative ratio to polymer
    vPMMA = 1-vPS;
    %Solvent density, g/m3
    poxyl = 0.88*100^3;
    pfilm = vPMMA*pPMMA+vPS*pPS;
    %Final thickness, m
    hfinal = 182*10^(-9);
    %Final polymer mass per area, g/m2
    mp = hfinal.*pfilm;
    %Dynamic viscosity of solvent, g/(m s) [=] mPa s
    doxyl = 0.8794;

%RK45 Parameters based on nomenclature from Dormand and
Prince RK5(4)7M
%Journal of computational and applied mathematics, v6,
1980 19-26.
    c0 = 0;
    c1 = 1./5.;

```

```

c2 = 3./10.;
c3 = 4./5.;
c4 = 8./9.;
c5 = 1.;
c6 = 1.;
a10 = 1./5.;
a20 = 3./40.;
a21 = 9./40.;
a30 = 44./45.;
a31 = -56./15.;
a32 = 32./9.;
a40 = 19372./6561.;
a41 = -25360./2187.;
a42 = 64448./6561.;
a43 = -212/729.;
a50 = 9017./3168.;
a51 = -355./33.;
a52 = 46732./5247.;
a53 = 49./176.;
a54 = -5103./18656.;
a60 = 35./384;
a61 = 0.;
a62 = 500./1113.;
a63 = 125./192.;
a64 = -2187./6784.;
a65 = 11./84.;
%4th order coefficients
b0 = 5179./57600.;
b1 = 0.;
b2 = 7571./16695.;
b3 = 393./640.;
b4 = -92097./339200.;
b5 = 187./2100.;
b6 = 1./40.;
%5th order coefficients
B0 = 35./384.;
B1 = 0;
B2 = 500./1113.;
B3 = 125./192.;
B4 = -2187./6784.;
B5 = 11./84.;
B6 = 0;
%Time coeff
tnc0 = -71/57600;
tnc1 = 0;

```

```

tnc2 = 71/16695;
tnc3 = -71/1920;
tnc4 = 17253/339200;
tnc5 = -22/525;
tnc6 = 1/40;

Tottime = 9.6; %time to calculate model
h = 0.001; %step size
Steps = floor( (Tottime-Exptime(1,1))/h)+1;

%Here I define the loop of the RK45 method
for i=1:Steps
    if i==1
        time(i,1) = Exptime(1,1);
        height(i,1) = Expheight(1,1);
        vtime(i,1) = Exptime(1,1);
        vheight(i,1) = Expheight(1,1);

    else
        %Time step variables
        tJ0 = vtime(i-1,1) + c0*h;
        tJ1 = vtime(i-1,1) + c1*h;
        tJ2 = vtime(i-1,1) + c2*h;
        tJ3 = vtime(i-1,1) + c3*h;
        tJ4 = vtime(i-1,1) + c4*h;
        tJ5 = vtime(i-1,1) + c5*h;
        tJ6 = vtime(i-1,1) + c6*h;

        tJl0(i,1) = tJ0;

        %Weight fraction polymers during casting
        xp0 = mp./(mp./x0-tJ0.*evap.*poxy1);
        xp1 = mp./(mp./x0-tJ1.*evap.*poxy1);
        xp2 = mp./(mp./x0-tJ2.*evap.*poxy1);
        xp3 = mp./(mp./x0-tJ3.*evap.*poxy1);
        xp4 = mp./(mp./x0-tJ4.*evap.*poxy1);
        xp5 = mp./(mp./x0-tJ5.*evap.*poxy1);
        xp6 = mp./(mp./x0-tJ6.*evap.*poxy1);

        %PS
        cps0 = xPS*xp0/(xPMMA*xp0/pPMMA+xPS*xp0/pPS+(1-xp0)/poxy1);
        cps1 = xPS*xp1/(xPMMA*xp1/pPMMA+xPS*xp1/pPS+(1-xp1)/poxy1);

```

```

cps2 = xPS*xp2/(xPMMA*xp2/pPMMA+xPS*xp2/pPS+(1-
xp2)/poxy1);
cps3 = xPS*xp3/(xPMMA*xp3/pPMMA+xPS*xp3/pPS+(1-
xp3)/poxy1);
cps4 = xPS*xp4/(xPMMA*xp4/pPMMA+xPS*xp4/pPS+(1-
xp4)/poxy1);
cps5 = xPS*xp5/(xPMMA*xp5/pPMMA+xPS*xp5/pPS+(1-
xp5)/poxy1);
cps6 = xPS*xp6/(xPMMA*xp6/pPMMA+xPS*xp6/pPS+(1-
xp6)/poxy1);

%PMMA
cpmma0 = xPMMA*xp0/(xPMMA*xp0/pPMMA+xPS*xp0/pPS+(1-
xp0)/poxy1);
cpmma1 = xPMMA*xp1/(xPMMA*xp1/pPMMA+xPS*xp1/pPS+(1-
xp1)/poxy1);
cpmma2 = xPMMA*xp2/(xPMMA*xp2/pPMMA+xPS*xp2/pPS+(1-
xp2)/poxy1);
cpmma3 = xPMMA*xp3/(xPMMA*xp3/pPMMA+xPS*xp3/pPS+(1-
xp3)/poxy1);
cpmma4 = xPMMA*xp4/(xPMMA*xp4/pPMMA+xPS*xp4/pPS+(1-
xp4)/poxy1);
cpmma5 = xPMMA*xp5/(xPMMA*xp5/pPMMA+xPS*xp5/pPS+(1-
xp5)/poxy1);
cpmma6 = xPMMA*xp6/(xPMMA*xp6/pPMMA+xPS*xp6/pPS+(1-
xp6)/poxy1);

%Constant viscosity solution
K0 = h*( (-2*w^2*(height(i-1,1))^3)/(3*v)-evap);
K1 = h*( (-2*w^2*(height(i-1,1)+a10*K0)^3)/(3*v)-evap);
K2 = h*( (-2*w^2*(height(i-1,1)+a20*K0+a21*K1)^3)/(3*v)-
evap);
K3 = h*( (-2*w^2*(height(i-
1,1)+a30*K0+a31*K1+a32*K2)^3)/(3*v)-evap);
K4 = h*( (-2*w^2*(height(i-
1,1)+a40*K0+a41*K1+a42*K2+a43*K3)^3)/(3*v)-evap);
K5 = h*( (-2*w^2*(height(i-
1,1)+a50*K0+a51*K1+a52*K2+a53*K3+a54*K4)^3)/(3*v)-evap);
K6 = h*( (-2*w^2*(height(i-
1,1)+a60*K0+a61*K1+a62*K2+a63*K3+a64*K4+a65*K5)^3)/(3*v)-
evap);

time(i,1) = time(i-1,1) + h;
vtime(i,1) = vtime(i-1,1) + h;

```

```

height(i,1) = height(i-1,1) + B0*K0 + B1*K1 + B2*K2 +
B3*K3 + B4*K4 + B5*K5 + B6*K6;
height2 = height(i-1,1) + b0*K0 + b1*K1 + b2*K2 + b3*K3 +
b4*K4 + b5*K5 + b6*K6;

error(i,1) = abs(height2-height(i,1));

truncerror(i,1) =
tnc0*K0+tnc1*K1+tnc2*K2+tnc3*K3+tnc4*K4+tnc5*K5+tnc6*K6;
end
end

xtime = mp./(mp./x0-time.*evap.*poxyl);
cps =
xPS.*xtime./(xPMMA.*xtime./pPMMA+xPS.*xtime./pPS+(1-
xtime)./poxyl);
cpmma =
xPMMA.*xtime./(xPMMA.*xtime./pPMMA+xPS.*xtime./pPS+(1-
xtime)./poxyl);

vfrac = hfinal./Expheight;
mfrac = vfrac.*pfilm./(vfrac.*pfilm+(1-vfrac).*poxyl);

solution(:,1) = time(:,1);
solution(:,2) = height(:,1);
solution(1,3) = v;
solution(2,3) = evap;
solution(3,3) = x0;
solution(4,3) = hfinal;

hmod = solution;
csvwrite('5wt17kPSPMMAoxylRK.csv',hmod);

figure
plot(Expptime, Expheight,'ro', time,
height,'k:','MarkerSize',8,'LineWidth',1.5), axis([0 14 0
2e-5]);
set(gca,'fontsize',12, 'fontweight','bold');
xlabel('Time (s)','FontWeight','bold','Color','k');
ylabel('Height(m)','FontWeight','bold','Color','k');
title('Height vs. Time (explicit RK45)');
hleg=legend('Exp. Data','Model Pred. ');
set(hleg,'Location','NorthEast')
set(hleg,'box','off');

```

```

figure
plot(Exptime,mfrac,'o','Color',[0 0.75 0])
hold all
plot(time,xtime,'b')
ylim([0 1])
xlim([0 12])

%Error:
figure
plot(time, error, 'r:', time,
truncerror, 'b:', 'MarkerSize',8, 'LineWidth',1.5);
set(gca, 'fontsize',12, 'fontweight', 'bold');
xlabel('Time (s)', 'FontWeight', 'bold', 'Color', 'k');
ylabel('Error', 'FontWeight', 'bold', 'Color', 'k');
title('Error');
hleg=legend('Error', 'Trunc. Error');
set(hleg, 'Location', 'NorthEast')
set(hleg, 'box', 'off');

```

C.7 PS/PMMA Film Characterization

The morphology of the $^{17}\text{k}/^{33}\text{k}$ PMMA films was confirmed by selective washing. The PMMA phase was removed with acetic acid, whereas the PS was removed with cyclohexane. For 0.9 wt.%, the film morphology is comprised of small droplets of PMMA in a PS matrix, which was seen in the atomic force and optical micrographs. Films cast from a 5.0 wt.% or 9.0 wt.% polymer solution had a bilayer, or stratified, structure. The PMMA segregated to the substrate surface, whereas the polystyrene remained at the free surface due to the preference of PMMA for the silicon.¹¹

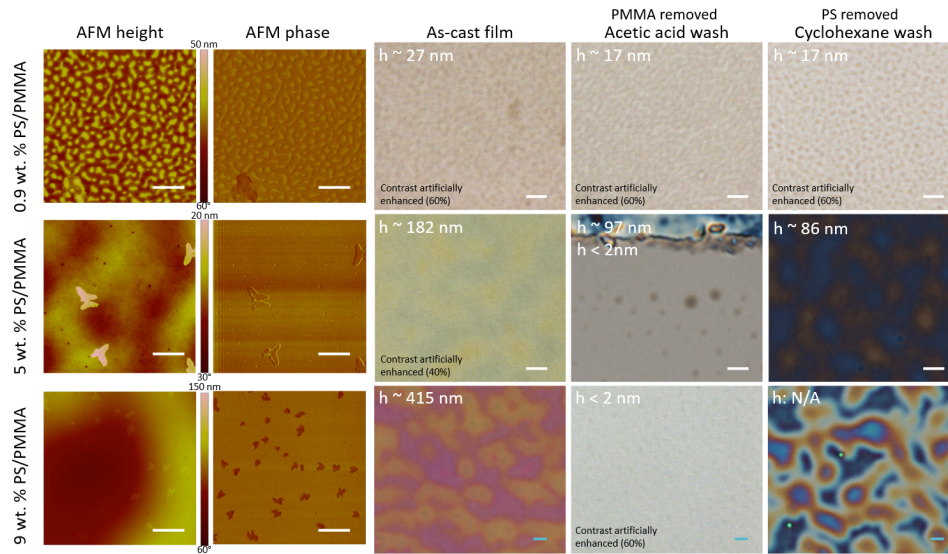


Figure C-6. Morphology of 17k PS/ 33k PMMA films cast from *o*-xylene. The scale bar represents $2\ \mu\text{m}$ in all images, except for the bottom row of the optical micrographs, for which the scale bar is $5\ \mu\text{m}$. Although 0.9 wt.% 1:1 17k PS/ 33k PMMA in *o*-xylene cast into a film with microstructure, 5.0 wt.% and 9.0 wt.% solutions produced bilayer structure films. The color in the top row comes from height differences in the PS vs. PMMA domains, whereas it comes from thickness differences within a single polymer domain in the bottom rows.

C.8 Substituted Polystyrenes

Another set of materials that was studied in collaboration with the University of Sheffield included blends of polyfluorene (PFO) with substituted polystyrenes. The two substituted polystyrenes used were poly(4-vinyl veratrole) [P4VV] and poly(4-vinyl catechol) [P4VC], which were synthesized by reversible addition–fragmentation chain-transfer polymerization [RAFT]. The solvent concentration was tuned by changing the relative flow rate between the solvent-rich stream and the nitrogen diluent, and the total nitrogen flow rate was maintained at 25 mL/min.

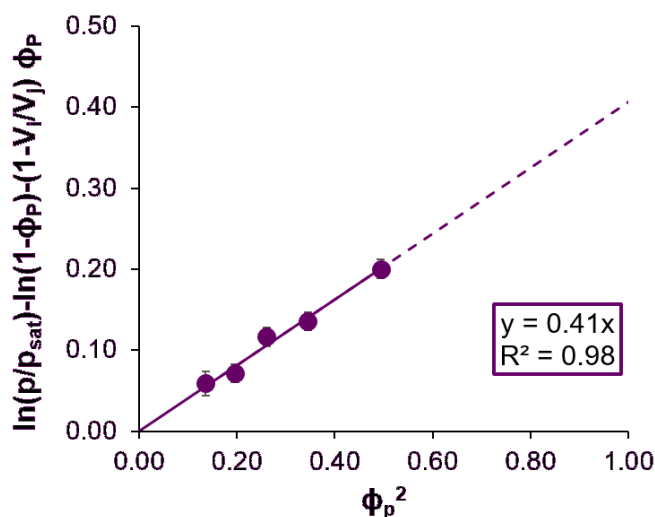


Figure C-7. Replotting Eq. 3.2 for P4VV (●) in THF. The dashed line represents an extrapolation of the interaction parameter to higher polymer volume fractions.

In THF, PS and P4VV have similar interactions, suggesting their solubility parameters are offset by the same amount from THF. A constant χ_{s-p} fits the film

swelling data for P3HT with both THF and CHCl₃ as well as PS and P4VV with THF. The interaction parameter for P4VV with THF ($\chi_{\text{THF-poly}} = 0.41$) was comparable to that of PS and higher with CHCl₃ than PS, which suggests the solubility parameter is higher than THF or CHCl₃. In addition to polymers for which there exist some literature data, new polymers, such as P4VV can also be studied using solvent vapor swelling. One limitation to the solvent vapor swelling technique discussed previously is that the analysis utilizes Flory-Huggins theory. As such, the solubility parameters of materials that hydrogen bond, such as P4VC, cannot be determined. Group contribution theory can be used to determine the solubility of these materials. The calculated group contribution theory values are given in Table C-1.

Table C-1. Solubility parameters from literature, solvent vapor swelling, and group contribution theory.

Polymer	Literature	Solubility parameter, δ (MPa ^{1/2})	
		Solvent vapor swelling ^b	Group contribution theory ^c
PS	18.2 ^{a,1}	17.9 ± 0.2*	18.0
P4VV	N/A	~ 21.0*	22.6
P4VC	N/A	N/A	30.6*
PFO	18.6 – 19.1 ^{*,12-14}	N/A	17.2

*Value used to calculate $\chi_{\text{solv-poly}}$ and $\chi_{\text{poly-poly}}$. ^aSolubility parameters represent an average over the range of reported values for PS (17.4 MPa^{1/2} – 19.8 MPa^{1/2}). ^bSolubility parameters (δ) were determined from regular solution theory calculations with solvent–polymer Flory–Huggins interaction parameters measured by solvent vapor swelling experiments with THF and CHCl₃. Error propagated from the uncertainties in the calculated Flory-Huggins interaction parameters. ^cSolubility parameters estimated from the van Krevelen and Hoftyzer group contribution method.¹⁵

For PS and P4VV, the group contribution theory solubility parameters are in good agreement with the calculated solubility parameters. PFO does not match well, which could be the result of the intramolecular interactions of PFO with itself (similar to P3HT). Ongoing work is in progress to quantify differences in the casting behavior of PFO with the three substituted polystyrenes (PS, P4VV, P4VC).

REFERENCES

1. Brandrup, J.; Immergut, E. H.; Grulke, E. A., *Polymer Handbook*. 4th ed.; Wiley: New York, 1999.
2. Campoy-Quiles, M.; Ferenczi, T.; Agostinelli, T.; Etchegoin, P. G.; Kim, Y.; Anthopoulos, T. D.; Stavrinou, P. N.; Bradley, D. D. C.; Nelson, J., Morphology evolution via self-organization and lateral and vertical diffusion in polymer:fullerene solar cell blends. *Nat. Mater.* **2008**, *7*, 158-164.
3. McCrackin, F. L.; Passaglia, E.; Stromberg, R. R.; Steinberg, H. L., Measurement of the thickness and refractive index of very thin films and the optical properties of surfaces by ellipsometry. *J. Res. Natl. Bur. Stand., Sect. A* **1963**, *67A*, 363-377.
4. Scott, R. L., The thermodynamics of high polymer solutions. V. Phase equilibria in the ternary system: polymer 1 – polymer 2 – solvent. *J. Chem. Phys.* **1949**, *17*, 279-284.
5. Scott, R. L., Thermodynamics of high polymer solutions. VI. The compatibility of copolymers. *J. Polym. Sci.* **1952**, *9*, 423-432.
6. Kapnistos, M.; Hinrichs, A.; Vlassopoulos, D.; Anastasiadis, S. H.; Stammer, A.; Wolf, B. A., Rheology of a lower critical solution temperature binary polymer blend in the homogeneous, phase-separated, and transitional regimes. *Macromolecules* **1996**, *29*, 7155-7163.
7. Bae, Y. C.; Lambert, S. M.; Soane, D. S.; Prausnitz, J. M., Cloud-point curves of polymer solutions from thermo-optic measurements. *Macromolecules* **1991**, *24*, 4403-4407.
8. Boutris, C.; Chatzi, E. G.; Kiparissides, C., Characterization of the LCST behaviour of aqueous poly(N-isopropylacrylamide) solutions by thermal and cloud point techniques. *Polymer* **1997**, *38*, 2567-2570.
9. Meyerhofer, D., Characteristics of resist films produced by spinning. *J. Appl. Phys.* **1978**, *49*, 3993-3997.

10. Dormand, J. R.; Prince, P. J., A family of embedded Runge-Kutta formulae. *Journal of Computational and Applied Mathematics* **1980**, *6*, 19-26.
11. Albert, J. N. L.; Baney, M. J.; Stafford, C. M.; Kelly, J. Y.; Epps, T. H., III, Generation of monolayer gradients in surface energy and surface chemistry for block copolymer thin film studies. *ACS Nano* **2009**, *3*, 3977-3986.
12. Nilsson, S.; Bernasik, A.; Budkowski, A.; Moons, E., Morphology and phase segregation of spin-casted films of polyfluorene/PCBM blends. *Macromolecules* **2007**, *40*, 8291-8301.
13. Björström, C. M.; Nilsson, S.; Bernasik, A.; Budkowski, A.; Andersson, M.; Magnusson, K. O.; Moons, E., Vertical phase separation in spin-coated films of a low bandgap polyfluorene/PCBM blend—Effects of specific substrate interaction. *Appl. Surf. Sci.* **2007**, *253*, 3906-3912.
14. Grell, M.; Bradley, D. D. C.; Long, X.; Chamberlain, T.; Inbasekaran, M.; Woo, E. P.; Soliman, M., Chain geometry, solution aggregation and enhanced dichroism in the liquidcrystalline conjugated polymer poly(9,9-dioctylfluorene). *Acta Polym.* **1998**, *49*, 439-444.
15. van Krevelen, D. W.; Nijenhuis, K. T., *Properties of Polymers - Their Correlation with Chemical Structure; Their Numerical Estimation and Prediction from Additive Group Contributions*. 4 ed.; Elsevier: Amsterdam, 2009.

Appendix D

SUPPORTING INFORMATION FOR CHAPTER 6

D.1 Characterization of PSAM and PPM

The polymers were characterized using size exclusion chromatography (SEC) and differential scanning calorimetry (DSC). The molecular weight and dispersity was measured using SEC, and the glass transition temperature (T_g) was captured from the DSC data.

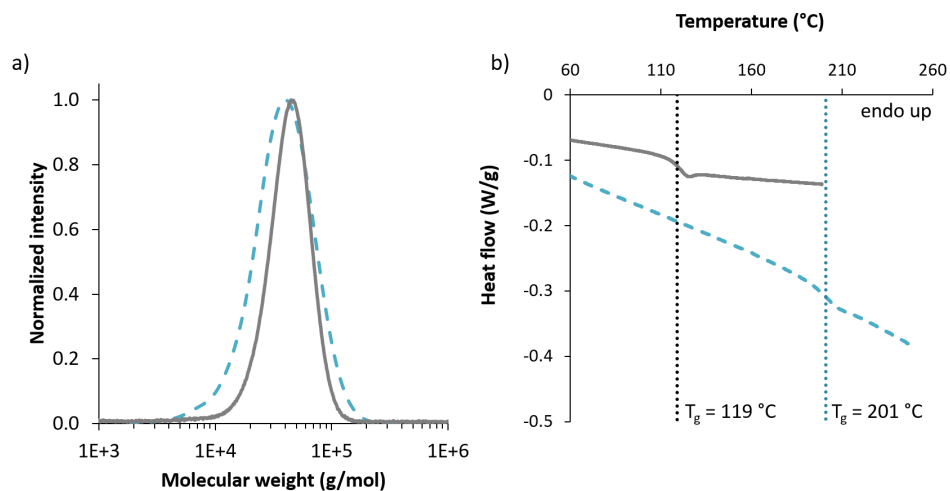


Figure D-1. a) SEC of PPM (gray, solid) and PSAM (teal, dashed) in THF and CHCl_3 , respectively. b) Second DSC trace on heating (endo up) of PPM (gray, solid) and PSAM (teal, dashed). The heating rate was $5\text{ }^\circ\text{C}/\text{min}$ in N_2 .

D.2 Estimation of Polymer Refractive Index

The refractive index of the sustainable polymers was estimated using the following protocol. First, the film thickness was measured using the spectral reflectometer. Next, the films were scratched near the locations at which the normal reflectance curves were captured. Then, the relative height difference between the film surface and the substrate was determined by atomic force microscopy (AFM) (see also Chapter 2, Section 2.2.4). Finally, the spectral reflectance curve was fit for refractive index at a constant film thickness, which was taken as the height difference from the scratch test. The refractive index that provides the best fit (and had a reasonable value) was taken to be the refractive index of the film.

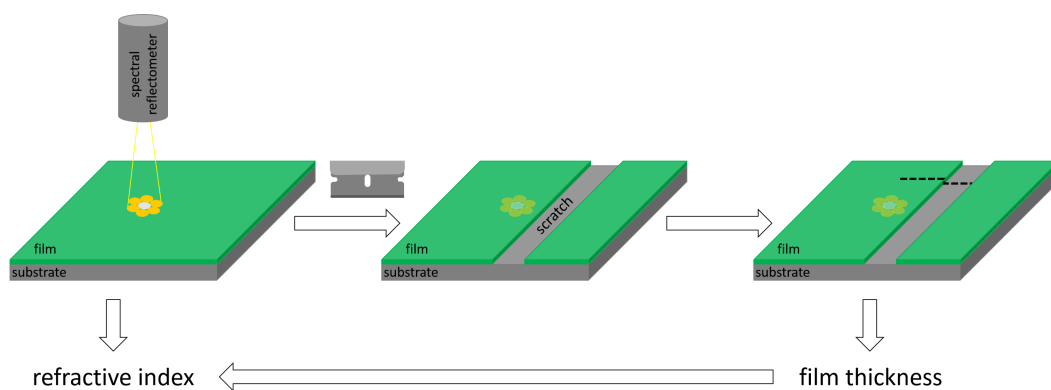


Figure D-2. Schematic of refractive index determination. First the reflectance spectrum is measured on the thin film. The position at which the spectra reflectance was captured is illustrated by the faded light spot. Note: the light spot does not burn in to the film. The film is then scratched using a razor blade, which does not damage the substrate surface at light loads. Atomic force microscopy is then used to measure the height of the scratch along a path shown schematically as the dashed black line. The resulting film thickness is then input into the fitting model for the spectrum, and the refractive index is varied until a good fit is achieved.

D.3 Glass Transition Temperature Effects

The transition between rubbery and glassy regimes was probed using the solvent vapor swelling data, shown in Figure D-3. The intersection of the glassy and rubbery regime fits provided a critical polymer concentration, below which the polymer lacked mobility to achieve equilibrium structures.

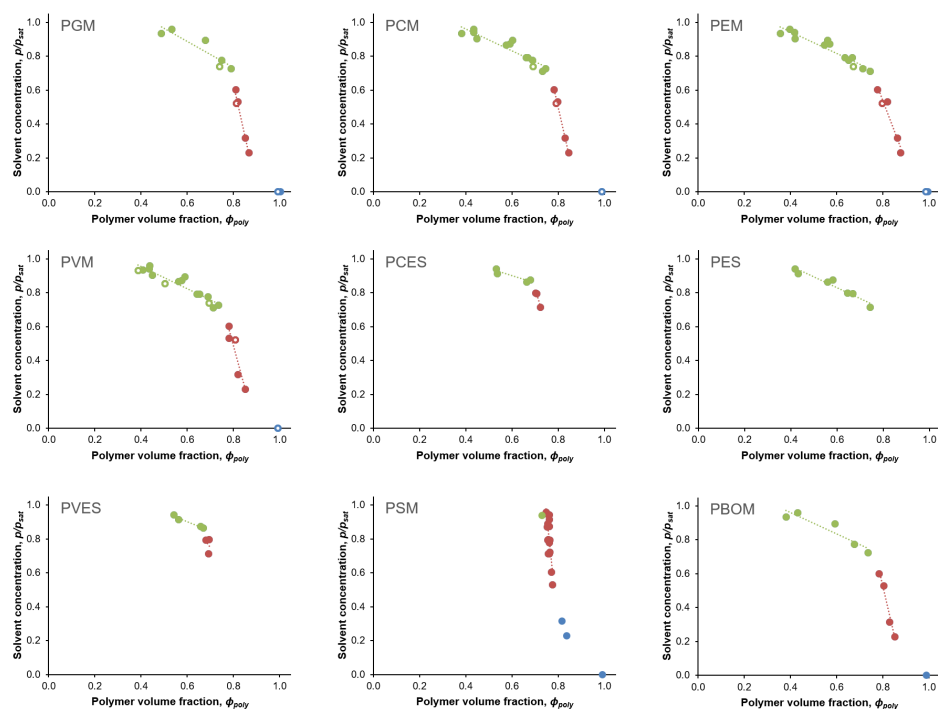


Figure D-3. Effect of THF content on polymer mobility. The “rubbery” regime (\bullet), in which the polymers have mobility, has a different slope than the “glassy” regime (\bullet), in which the polymer is kinetically trapped. The closed symbols represent data from flow solvent vapor swelling experiments, whereas the open symbols represent data from THF/water bell jar experiments. For PES, the polymer remains rubbery across the THF content explored. PSM is glassy for the entirety of the experiments. The intersection of the glassy and rubbery lines provides the minimum polymer swelling to provide the polymer chains with sufficient mobility, called the crossover volume fraction, ϕ_c .

The same analysis can be performed for polymers in CHCl_3 . Of particular interest is PSM in CHCl_3 . Though limited data are available for PSM, a number of experimental conditions fell within the rubbery regime, as evidenced in Figure D-4, below.

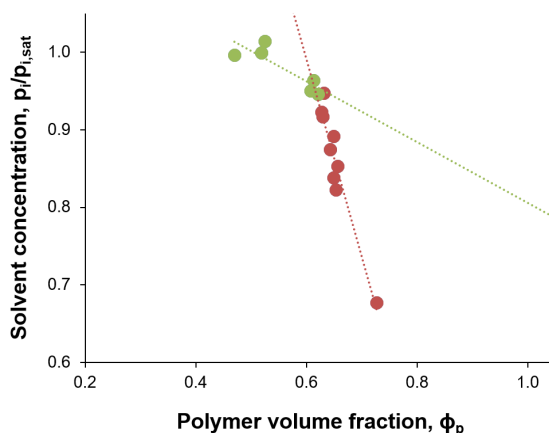


Figure D-4. Effect of CHCl_3 on PSM T_g . In comparison to THF (shown in Figure D-3), CHCl_3 had a crossover between the glassy and rubbery regimes.

D.4 Comparison of Swelling – PVM vs. PGM

Though PGM was not stable enough to extract interaction parameters in CHCl_3 , the relative swelling behavior can be used to qualitatively determine differences in compatibility. In comparison to PVM, PGM had less solvent uptake (higher polymer volume fraction). This effect indicates that PGM has less favorable interactions with CHCl_3 than PVM (lower solubility).

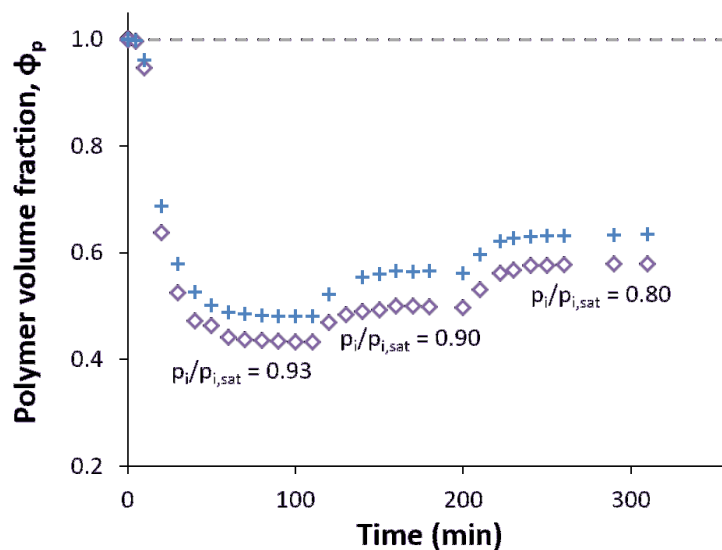


Figure D-5. Comparison of swelling of PGM (+) and PVM (◇) at the same CHCl₃ concentration. PGM swelled less than PVM at all CHCl₃ compositions, which suggests that CHCl₃ is a better solvent for PVM than PGM.

Appendix E

SOLVENT SELECTIVITY AND POLYMER DISSOLUTION

E.1 PS/PI Selective Solvents

Solvent selectivity was determined by bell jar annealing of PS and PI films. The polymer film that had the greatest solvent uptake (highest polymer volume fraction) was the polymer for which the solvent was preferential. The selectivity of toluene, *o*-xylene, *cis*-decalin, and anisole are shown in Figure E-1.

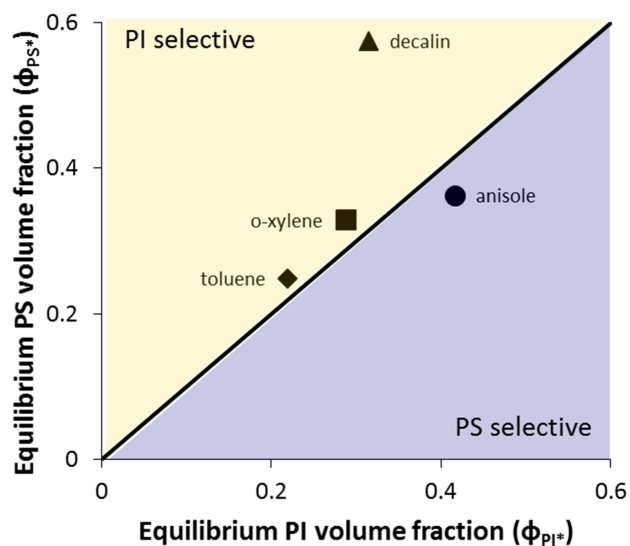


Figure E-1. Solvent selectivity for PS/PI mixtures. The $\phi_{PS} = \phi_{PI}$ line represents equal swelling under the same solvent conditions (neutral solvent). A solvent that falls below the line is PS selective, whereas a solvent that produces more swelling in PI is PI selective. *o*-Xylene and toluene are nearly neutral solvents for PS and PI. *cis*-Decalin is PI selective, and anisole is slightly PS selective.

In addition to swelling experiments, simple dissolution tests combined with solubility parameters of the solvents (and/or literature solvent-interaction parameters) were used to predict the selectivity of various solvents, shown in Table E-1.

Table E-1. Solvent selectivity for PS and PI. The selectivity was determined by literature values, experimentally, or solubility parameters. The color map indicates whether the solvent dissolved (blue) or didn't dissolve (red) the indicated component. Yellow boxes are placed for clear solutions that produced unstable films (films that partially dewet), which suggests solvent choice issues.

Solvent	PS	PI	Selectivity
o-xylene	Blue	Blue	PI
toluene	Blue	Blue	PI
THF	Blue	Blue	PS
n-hexane	Red	Blue	PI
cyclohexane	Red	Blue	PI
decalin	Blue	Blue	PI
anisole	Blue	Yellow	PS
acetone	Blue	Red	PS
isopropyl acetate	Blue	Red	PS
ethyl acetate	Blue	Red	PS
2-butanone (MEK)	Blue	Red	PS
PGMEA	Blue	Red	PS
cyclohexylbromide	Blue	Red	PS
acetonitrile	Red	Red	N.D.
dimethylformamide	Blue	Red	PS
dimethylsulfoxide	Red	Red	N.D.
3-methyl cyclohexanone	Blue	Yellow	PS
phenetole	Blue	Yellow	PS

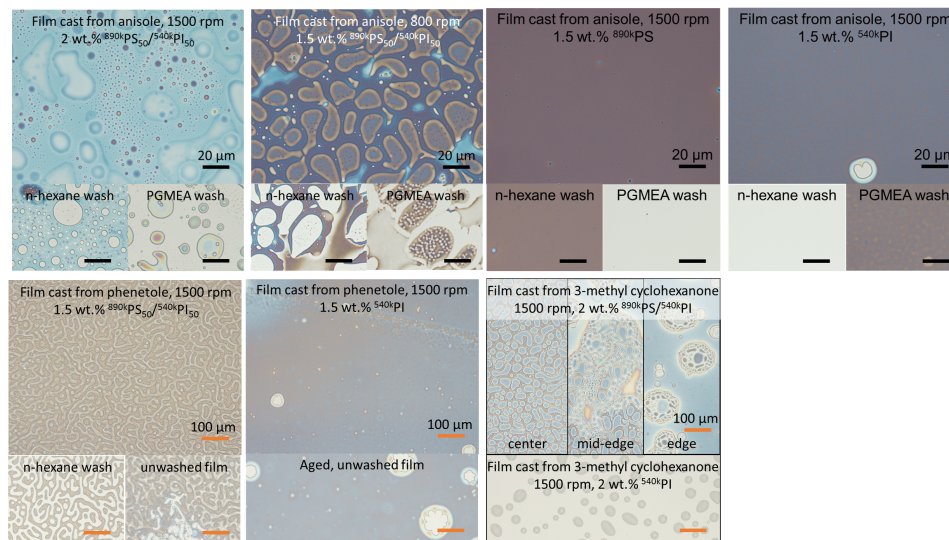


Figure E-2. Various film instabilities formed during and after casting from initially clear solutions. In all cases, the PI films had evidence of dewetting (unstable).

E.2 PS/PMMA Selective Solvents

The same dissolution test was performed with PS and PMMA.

Table E-2. Solvent selectivity for PS and PMMA. The selectivity was determined using literature values, experimentally, or solubility parameters. The color map indicates whether the polymer dissolved (blue) or partially dissolved (purple) in the solvent.

Solvent	PS	PMMA	Selectivity
o-xylene	Blue	Purple	PS
anisole	Blue	Blue	PS/neutral
2-butanone (MEK)	Blue	Blue	PMMA
PGMEA	Blue	Blue	PMMA
dimethylformamide	Blue	Blue	unknown
3-methyl cyclohexanone	Blue	Purple	PS

Appendix F
PERMISSIONS

**JOHN WILEY AND SONS LICENSE
TERMS AND CONDITIONS**

Nov 29, 2016

This Agreement between Jillian A Emerson ("You") and John Wiley and Sons ("John Wiley and Sons") consists of your license details and the terms and conditions provided by John Wiley and Sons and Copyright Clearance Center.

License Number	3998390695251
License date	Nov 29, 2016
Licensed Content Publisher	John Wiley and Sons
Licensed Content Publication	Macromolecular Symposia
Licensed Content Title	Morphology development and control in immiscible polymer blends
Licensed Content Author	Christopher W. Macosko
Licensed Content Date	Nov 14, 2000
Licensed Content Pages	14
Type of use	Dissertation/Thesis
Requestor type	University/Academic
Format	Print and electronic
Portion	Figure/table
Number of figures/tables	1
Original Wiley figure/table number(s)	Figure 1
Will you be translating?	No
Title of your thesis / dissertation	Thermodynamics of polymer mixtures in solution and their applications in functional, microstructured films
Expected completion date	Jan 2017
Expected size (number of pages)	300
Requestor Location	Jillian A Emerson 150 Academy St NEWARK, DE 19716 United States Attn: Jillian A Emerson
Publisher Tax ID	EU826007151
Billing Type	Invoice
Billing Address	Jillian A Emerson 150 Academy St NEWARK, DE 19716 United States Attn: Jillian A Emerson
Total	0.00 USD
Terms and Conditions	

TERMS AND CONDITIONS

This copyrighted material is owned by or exclusively licensed to John Wiley & Sons, Inc. or one of its group companies (each a "Wiley Company") or handled on behalf of a society with which a Wiley Company has exclusive publishing rights in relation to a particular work (collectively "WILEY"). By clicking "accept" in connection with completing this licensing transaction, you agree that the following terms and conditions apply to this transaction (along with the billing and payment terms and conditions established by the Copyright Clearance Center Inc., ("CCC's Billing and Payment terms and conditions"), at the time that you opened your RightsLink account (these are available at any time at <http://myaccount.copyright.com>).

Terms and Conditions

- The materials you have requested permission to reproduce or reuse (the "Wiley Materials") are protected by copyright.
- You are hereby granted a personal, non-exclusive, non-sub licensable (on a stand-alone basis), non-transferable, worldwide, limited license to reproduce the Wiley Materials for the purpose specified in the licensing process. This license, **and any CONTENT (PDF or image file) purchased as part of your order**, is for a one-time use only and limited to any maximum distribution number specified in the license. The first instance of republication or reuse granted by this license must be completed within two years of the date of the grant of this license (although copies prepared before the end date may be distributed thereafter). The Wiley Materials shall not be used in any other manner or for any other purpose, beyond what is granted in the license. Permission is granted subject to an appropriate acknowledgement given to the author, title of the material/book/journal and the publisher. You shall also duplicate the copyright notice that appears in the Wiley publication in your use of the Wiley Material. Permission is also granted on the understanding that nowhere in the text is a previously published source acknowledged for all or part of this Wiley Material. Any third party content is expressly excluded from this permission.
- With respect to the Wiley Materials, all rights are reserved. Except as expressly granted by the terms of the license, no part of the Wiley Materials may be copied, modified, adapted (except for minor reformatting required by the new Publication), translated, reproduced, transferred or distributed, in any form or by any means, and no derivative works may be made based on the Wiley Materials without the prior permission of the respective copyright owner. **For STM Signatory Publishers clearing permission under the terms of the [STM Permissions Guidelines](#) only, the terms of the license are extended to include subsequent editions and for editions in other languages, provided such editions are for the work as a whole in situ and does not involve the separate exploitation of the permitted figures or extracts**, You may not alter, remove or suppress in any manner any copyright, trademark or other notices displayed by the Wiley Materials. You may not license, rent, sell, loan, lease, pledge, offer as security, transfer or assign the Wiley Materials on a stand-alone basis, or any of the rights granted to you hereunder to any other person.
- The Wiley Materials and all of the intellectual property rights therein shall at all times remain the exclusive property of John Wiley & Sons Inc, the Wiley Companies, or their respective licensors, and your interest therein is only that of having possession of and the right to reproduce the Wiley Materials pursuant to Section 2 herein during the continuance of this Agreement. You agree that you own no right, title or interest in or to the Wiley Materials or any of the intellectual property rights therein. You shall have no rights hereunder other than the license as provided for above in Section 2. No right,

license or interest to any trademark, trade name, service mark or other branding ("Marks") of WILEY or its licensors is granted hereunder, and you agree that you shall not assert any such right, license or interest with respect thereto

- NEITHER WILEY NOR ITS LICENSORS MAKES ANY WARRANTY OR REPRESENTATION OF ANY KIND TO YOU OR ANY THIRD PARTY, EXPRESS, IMPLIED OR STATUTORY, WITH RESPECT TO THE MATERIALS OR THE ACCURACY OF ANY INFORMATION CONTAINED IN THE MATERIALS, INCLUDING, WITHOUT LIMITATION, ANY IMPLIED WARRANTY OF MERCHANTABILITY, ACCURACY, SATISFACTORY QUALITY, FITNESS FOR A PARTICULAR PURPOSE, USABILITY, INTEGRATION OR NON-INFRINGEMENT AND ALL SUCH WARRANTIES ARE HEREBY EXCLUDED BY WILEY AND ITS LICENSORS AND WAIVED BY YOU.
- WILEY shall have the right to terminate this Agreement immediately upon breach of this Agreement by you.
- You shall indemnify, defend and hold harmless WILEY, its Licensors and their respective directors, officers, agents and employees, from and against any actual or threatened claims, demands, causes of action or proceedings arising from any breach of this Agreement by you.
- IN NO EVENT SHALL WILEY OR ITS LICENSORS BE LIABLE TO YOU OR ANY OTHER PARTY OR ANY OTHER PERSON OR ENTITY FOR ANY SPECIAL, CONSEQUENTIAL, INCIDENTAL, INDIRECT, EXEMPLARY OR PUNITIVE DAMAGES, HOWEVER CAUSED, ARISING OUT OF OR IN CONNECTION WITH THE DOWNLOADING, PROVISIONING, VIEWING OR USE OF THE MATERIALS REGARDLESS OF THE FORM OF ACTION, WHETHER FOR BREACH OF CONTRACT, BREACH OF WARRANTY, TORT, NEGLIGENCE, INFRINGEMENT OR OTHERWISE (INCLUDING, WITHOUT LIMITATION, DAMAGES BASED ON LOSS OF PROFITS, DATA, FILES, USE, BUSINESS OPPORTUNITY OR CLAIMS OF THIRD PARTIES), AND WHETHER OR NOT THE PARTY HAS BEEN ADVISED OF THE POSSIBILITY OF SUCH DAMAGES. THIS LIMITATION SHALL APPLY NOTWITHSTANDING ANY FAILURE OF ESSENTIAL PURPOSE OF ANY LIMITED REMEDY PROVIDED HEREIN.
- Should any provision of this Agreement be held by a court of competent jurisdiction to be illegal, invalid, or unenforceable, that provision shall be deemed amended to achieve as nearly as possible the same economic effect as the original provision, and the legality, validity and enforceability of the remaining provisions of this Agreement shall not be affected or impaired thereby.
- The failure of either party to enforce any term or condition of this Agreement shall not constitute a waiver of either party's right to enforce each and every term and condition of this Agreement. No breach under this agreement shall be deemed waived or excused by either party unless such waiver or consent is in writing signed by the party granting such waiver or consent. The waiver by or consent of a party to a breach of any provision of this Agreement shall not operate or be construed as a waiver of or consent to any other or subsequent breach by such other party.
- This Agreement may not be assigned (including by operation of law or otherwise) by you without WILEY's prior written consent.

- Any fee required for this permission shall be non-refundable after thirty (30) days from receipt by the CCC.
- These terms and conditions together with CCC's Billing and Payment terms and conditions (which are incorporated herein) form the entire agreement between you and WILEY concerning this licensing transaction and (in the absence of fraud) supersedes all prior agreements and representations of the parties, oral or written. This Agreement may not be amended except in writing signed by both parties. This Agreement shall be binding upon and inure to the benefit of the parties' successors, legal representatives, and authorized assigns.
- In the event of any conflict between your obligations established by these terms and conditions and those established by CCC's Billing and Payment terms and conditions, these terms and conditions shall prevail.
- WILEY expressly reserves all rights not specifically granted in the combination of (i) the license details provided by you and accepted in the course of this licensing transaction, (ii) these terms and conditions and (iii) CCC's Billing and Payment terms and conditions.
- This Agreement will be void if the Type of Use, Format, Circulation, or Requestor Type was misrepresented during the licensing process.
- This Agreement shall be governed by and construed in accordance with the laws of the State of New York, USA, without regards to such state's conflict of law rules. Any legal action, suit or proceeding arising out of or relating to these Terms and Conditions or the breach thereof shall be instituted in a court of competent jurisdiction in New York County in the State of New York in the United States of America and each party hereby consents and submits to the personal jurisdiction of such court, waives any objection to venue in such court and consents to service of process by registered or certified mail, return receipt requested, at the last known address of such party.

WILEY OPEN ACCESS TERMS AND CONDITIONS

Wiley Publishes Open Access Articles in fully Open Access Journals and in Subscription journals offering Online Open. Although most of the fully Open Access journals publish open access articles under the terms of the Creative Commons Attribution (CC BY) License only, the subscription journals and a few of the Open Access Journals offer a choice of Creative Commons Licenses. The license type is clearly identified on the article.

The Creative Commons Attribution License

The [Creative Commons Attribution License \(CC-BY\)](#) allows users to copy, distribute and transmit an article, adapt the article and make commercial use of the article. The CC-BY license permits commercial and non-

Creative Commons Attribution Non-Commercial License

The [Creative Commons Attribution Non-Commercial \(CC-BY-NC\) License](#) permits use, distribution and reproduction in any medium, provided the original work is properly cited and is not used for commercial purposes.(see below)

Creative Commons Attribution-Non-Commercial-NoDerivs License

The [Creative Commons Attribution Non-Commercial-NoDerivs License](#) (CC-BY-NC-ND) permits use, distribution and reproduction in any medium, provided the original work is properly cited, is not used for commercial purposes and no modifications or adaptations are made. (see below)

Use by commercial "for-profit" organizations

Use of Wiley Open Access articles for commercial, promotional, or marketing purposes requires further explicit permission from Wiley and will be subject to a fee.

Further details can be found on Wiley Online Library

<http://olabout.wiley.com/WileyCDA/Section/id-410895.html>

Other Terms and Conditions:

v1.10 Last updated September 2015

Questions? customercare@copyright.com or +1-855-239-3415 (toll free in the US) or +1-978-646-2777.

**THE AMERICAN ASSOCIATION FOR THE ADVANCEMENT OF SCIENCE LICENSE
TERMS AND CONDITIONS**

Nov 22, 2016

This Agreement between Jillian A Emerson ("You") and The American Association for the Advancement of Science ("The American Association for the Advancement of Science") consists of your license details and the terms and conditions provided by The American Association for the Advancement of Science and Copyright Clearance Center.

License Number	3994290250193
License date	Nov 22, 2016
Licensed Content Publisher	The American Association for the Advancement of Science
Licensed Content Publication	Science
Licensed Content Title	Polymer-Polymer Phase Behavior
Licensed Content Author	FRANK S. BATES
Licensed Content Date	Feb 22, 1991
Licensed Content Volume Number	251
Licensed Content Issue Number	4996
Volume number	251
Issue number	4996
Type of Use	Thesis / Dissertation
Requestor type	Scientist/individual at a research institution
Format	Print and electronic
Portion	Figure
Number of figures/tables	2
Order reference number	
Title of your thesis / dissertation	Thermodynamics of polymer mixtures in solution and their applications in functional, microstructured films
Expected completion date	Jan 2017
Estimated size(pages)	300
Requestor Location	Jillian A Emerson 150 Academy St NEWARK, DE 19716 United States Attn: Jillian A Emerson
Billing Type	Invoice
Billing Address	Jillian A Emerson 150 Academy St NEWARK, DE 19716 United States Attn: Jillian A Emerson

Total

0.00 USD

Terms and Conditions

American Association for the Advancement of Science TERMS AND CONDITIONS

Regarding your request, we are pleased to grant you non-exclusive, non-transferable permission, to republish the AAAS material identified above in your work identified above, subject to the terms and conditions herein. We must be contacted for permission for any uses other than those specifically identified in your request above.

The following credit line must be printed along with the AAAS material: "From [Full Reference Citation]. Reprinted with permission from AAAS."

All required credit lines and notices must be visible any time a user accesses any part of the AAAS material and must appear on any printed copies and authorized user might make.

This permission does not apply to figures / photos / artwork or any other content or materials included in your work that are credited to non-AAAS sources. If the requested material is sourced to or references non-AAAS sources, you must obtain authorization from that source as well before using that material. You agree to hold harmless and indemnify AAAS against any claims arising from your use of any content in your work that is credited to non-AAAS sources.

If the AAAS material covered by this permission was published in Science during the years 1974 - 1994, you must also obtain permission from the author, who may grant or withhold permission, and who may or may not charge a fee if permission is granted. See original article for author's address. This condition does not apply to news articles.

The AAAS material may not be modified or altered except that figures and tables may be modified with permission from the author. Author permission for any such changes must be secured prior to your use.

Whenever possible, we ask that electronic uses of the AAAS material permitted herein include a hyperlink to the original work on AAAS's website (hyperlink may be embedded in the reference citation).

AAAS material reproduced in your work identified herein must not account for more than 30% of the total contents of that work.

AAAS must publish the full paper prior to use of any text.

AAAS material must not imply any endorsement by the American Association for the Advancement of Science.

This permission is not valid for the use of the AAAS and/or Science logos.

AAAS makes no representations or warranties as to the accuracy of any information contained in the AAAS material covered by this permission, including any warranties of merchantability or fitness for a particular purpose.

If permission fees for this use are waived, please note that AAAS reserves the right to charge for reproduction of this material in the future.

Permission is not valid unless payment is received within sixty (60) days of the issuance of this permission. If payment is not received within this time period then all rights granted herein shall be revoked and this permission will be considered null and void.

In the event of breach of any of the terms and conditions herein or any of CCC's Billing and Payment terms and conditions, all rights granted herein shall be revoked and this permission will be considered null and void.

AAAS reserves the right to terminate this permission and all rights granted herein at its discretion, for any purpose, at any time. In the event that AAAS elects to terminate this permission, you will have no further right to publish, publicly perform, publicly display, distribute or otherwise use any matter in which the AAAS content had been included, and all fees paid hereunder shall be fully refunded to you. Notification of termination will be sent to the contact information as supplied by you during the request process and termination shall be immediate upon sending the notice. Neither AAAS nor CCC shall be liable for any costs, expenses, or damages you may incur as a result of the termination of this permission, beyond the refund noted above.

This Permission may not be amended except by written document signed by both parties. The terms above are applicable to all permissions granted for the use of AAAS material. Below you will find additional conditions that apply to your particular type of use.

FOR A THESIS OR DISSERTATION

If you are using figure(s)/table(s), permission is granted for use in print and electronic versions of your dissertation or thesis. A full text article may be used in print versions only of a dissertation or thesis.

Permission covers the distribution of your dissertation or thesis on demand by ProQuest / UMI, provided the AAAS material covered by this permission remains in situ.

If you are an Original Author on the AAAS article being reproduced, please refer to your License to Publish for rules on reproducing your paper in a dissertation or thesis.

FOR JOURNALS:

Permission covers both print and electronic versions of your journal article, however the AAAS material may not be used in any manner other than within the context of your article.

FOR BOOKS/TEXTBOOKS:

If this license is to reuse figures/tables, then permission is granted for non-exclusive world rights in all languages in both print and electronic formats (electronic formats are defined below).

If this license is to reuse a text excerpt or a full text article, then permission is granted for non-exclusive world rights in English only. You have the option of securing either print or electronic rights or both, but electronic rights are not automatically granted and do garner additional fees. Permission for translations of text excerpts or full text articles into other languages must be obtained separately.

Licenses granted for use of AAAS material in electronic format books/textbooks are valid only in cases where the electronic version is equivalent to or substitutes for the print version of the book/textbook. The AAAS material reproduced as permitted herein must remain in situ and must not be exploited separately (for example, if permission covers the use of a full text article, the article may not be offered for access or for purchase as a stand-alone unit), except in the case of permitted textbook companions as noted below.

You must include the following notice in any electronic versions, either adjacent to the reprinted AAAS material or in the terms and conditions for use of your electronic products: "Readers may view, browse, and/or download material for temporary copying purposes only, provided these uses are for noncommercial personal purposes. Except as provided by law, this material may not be further reproduced, distributed, transmitted, modified, adapted, performed, displayed, published, or sold in whole or in part, without prior written permission from the publisher."

If your book is an academic textbook, permission covers the following companions to your textbook, provided such companions are distributed only in conjunction with your textbook at no additional cost to the user:

- Password-protected website
- Instructor's image CD/DVD and/or PowerPoint resource
- Student CD/DVD

All companions must contain instructions to users that the AAAS material may be used for non-commercial, classroom purposes only. Any other uses require the prior written permission from AAAS.

If your license is for the use of AAAS Figures/Tables, then the electronic rights granted herein permit use of the Licensed Material in any Custom Databases that you distribute the electronic versions of your textbook through, so long as the Licensed Material remains within the context of a chapter of the title identified in your request and cannot be downloaded by a user as an independent image file.

Rights also extend to copies/files of your Work (as described above) that you are required to provide for use by the visually and/or print disabled in compliance with state and federal laws.

This permission only covers a single edition of your work as identified in your request.

FOR NEWSLETTERS:

Permission covers print and/or electronic versions, provided the AAAS material reproduced as permitted herein remains in situ and is not exploited separately (for example, if permission covers the use of a full text article, the article may not be offered for access or for purchase as a stand-alone unit)

FOR ANNUAL REPORTS:

Permission covers print and electronic versions provided the AAAS material reproduced as permitted herein remains in situ and is not exploited separately (for example, if permission covers the use of a full text article, the article may not be offered for access or for purchase as a stand-alone unit)

FOR PROMOTIONAL/MARKETING USES:

Permission covers the use of AAAS material in promotional or marketing pieces such as information packets, media kits, product slide kits, brochures, or flyers limited to a single print run. The AAAS Material may not be used in any manner which implies endorsement or promotion by the American Association for the Advancement of Science (AAAS) or Science of any product or service. AAAS does not permit the reproduction of its name, logo or text on promotional literature.

If permission to use a full text article is permitted, The Science article covered by this permission must not be altered in any way. No additional printing may be set onto an article copy other than the copyright credit line required above. Any alterations must be approved in advance and in writing by AAAS. This includes, but is not limited to, the placement of sponsorship identifiers, trademarks, logos, rubber stamping or self-adhesive stickers onto the article copies.

Additionally, article copies must be a freestanding part of any information package (i.e. media kit) into which they are inserted. They may not be physically attached to anything, such as an advertising insert, or have anything attached to them, such as a sample product. Article copies must be easily removable from any kits or informational packages in which they are used. The only exception is that article copies may be inserted into three-ring binders.

FOR CORPORATE INTERNAL USE:

The AAAS material covered by this permission may not be altered in any way. No additional printing may be set onto an article copy other than the required credit line. Any alterations must be approved in advance and in writing by AAAS. This includes, but is not limited to the placement of sponsorship identifiers, trademarks, logos, rubber stamping or self-adhesive stickers onto article copies.

If you are making article copies, copies are restricted to the number indicated in your request and must be distributed only to internal employees for internal use.

If you are using AAAS Material in Presentation Slides, the required credit line must be visible on the slide where the AAAS material will be reprinted

If you are using AAAS Material on a CD, DVD, Flash Drive, or the World Wide Web, you must include the following notice in any electronic versions, either adjacent to the reprinted AAAS material or in the terms and conditions for use of your electronic products: "Readers may view, browse, and/or download material for temporary copying purposes only, provided these uses are for noncommercial personal purposes. Except as provided by law, this material may not be further reproduced, distributed, transmitted, modified, adapted, performed, displayed, published, or sold in whole or in part, without prior written permission from the publisher." Access to any such CD, DVD, Flash Drive or Web page must be restricted to your organization's employees only.

FOR CME COURSE and SCIENTIFIC SOCIETY MEETINGS:

Permission is restricted to the particular Course, Seminar, Conference, or Meeting indicated in your request. If this license covers a text excerpt or a Full Text Article, access to the reprinted AAAS material must be restricted to attendees of your event only (if you have been granted electronic rights for use of a full text article on your website, your website must

be password protected, or access restricted so that only attendees can access the content on your site).

If you are using AAAS Material on a CD, DVD, Flash Drive, or the World Wide Web, you must include the following notice in any electronic versions, either adjacent to the reprinted AAAS material or in the terms and conditions for use of your electronic products: "Readers may view, browse, and/or download material for temporary copying purposes only, provided these uses are for noncommercial personal purposes. Except as provided by law, this material may not be further reproduced, distributed, transmitted, modified, adapted, performed, displayed, published, or sold in whole or in part, without prior written permission from the publisher."

FOR POLICY REPORTS:

These rights are granted only to non-profit organizations and/or government agencies. Permission covers print and electronic versions of a report, provided the required credit line appears in both versions and provided the AAAS material reproduced as permitted herein remains in situ and is not exploited separately.

FOR CLASSROOM PHOTOCOPIES:

Permission covers distribution in print copy format only. Article copies must be freestanding and not part of a course pack. They may not be physically attached to anything or have anything attached to them.

FOR COURSEPACKS OR COURSE WEBSITES:

These rights cover use of the AAAS material in one class at one institution. Permission is valid only for a single semester after which the AAAS material must be removed from the Electronic Course website, unless new permission is obtained for an additional semester. If the material is to be distributed online, access must be restricted to students and instructors enrolled in that particular course by some means of password or access control.

FOR WEBSITES:

You must include the following notice in any electronic versions, either adjacent to the reprinted AAAS material or in the terms and conditions for use of your electronic products: "Readers may view, browse, and/or download material for temporary copying purposes only, provided these uses are for noncommercial personal purposes. Except as provided by law, this material may not be further reproduced, distributed, transmitted, modified, adapted, performed, displayed, published, or sold in whole or in part, without prior written permission from the publisher."

Permissions for the use of Full Text articles on third party websites are granted on a case by case basis and only in cases where access to the AAAS Material is restricted by some means of password or access control. Alternately, an E-Print may be purchased through our reprints department (brocheleau@rockwaterinc.com).

REGARDING FULL TEXT ARTICLE USE ON THE WORLD WIDE WEB IF YOU ARE AN 'ORIGINAL AUTHOR' OF A SCIENCE PAPER

If you chose "Original Author" as the Requestor Type, you are warranting that you are one of authors listed on the License Agreement as a "Licensed content author" or that you are acting on that author's behalf to use the Licensed content in a new work that one of the authors listed on the License Agreement as a "Licensed content author" has written.

Original Authors may post the 'Accepted Version' of their full text article on their personal or on their University website and not on any other website. The 'Accepted Version' is the version of the paper accepted for publication by AAAS including changes resulting from peer review but prior to AAAS's copy editing and production (in other words not the AAAS published version).

FOR MOVIES / FILM / TELEVISION:

Permission is granted to use, record, film, photograph, and/or tape the AAAS material in connection with your program/film and in any medium your program/film may be shown or heard, including but not limited to broadcast and cable television, radio, print, world wide web, and videocassette.

The required credit line should run in the program/film's end credits.

FOR MUSEUM EXHIBITIONS:

Permission is granted to use the AAAS material as part of a single exhibition for the duration of that exhibit. Permission for use of the material in promotional materials for the exhibit must be cleared separately with AAAS (please contact us at permissions@aaas.org).

FOR TRANSLATIONS:

Translation rights apply only to the language identified in your request summary above. The following disclaimer must appear with your translation, on the first page of the article, after the credit line: "This translation is not an official translation by AAAS staff, nor is it endorsed by AAAS as accurate. In crucial matters, please refer to the official English-language version originally published by AAAS."

FOR USE ON A COVER:

Permission is granted to use the AAAS material on the cover of a journal issue, newsletter issue, book, textbook, or annual report in print and electronic formats provided the AAAS material reproduced as permitted herein remains in situ and is not exploited separately. By using the AAAS Material identified in your request, you agree to abide by all the terms and conditions herein.

Questions about these terms can be directed to the AAAS Permissions department permissions@aaas.org.

Other Terms and Conditions:

v 2

Questions? customer care@copyright.com or +1-855-239-3415 (toll free in the US) or +1-978-646-2777.

**AIP PUBLISHING LLC LICENSE
TERMS AND CONDITIONS**

Nov 22, 2016

This Agreement between Jillian A Emerson ("You") and AIP Publishing LLC ("AIP Publishing LLC") consists of your license details and the terms and conditions provided by AIP Publishing LLC and Copyright Clearance Center.

License Number	3994290651074
License date	Nov 22, 2016
Licensed Content Publisher	AIP Publishing LLC
Licensed Content Publication	Journal of Chemical Physics
Licensed Content Title	The Thermodynamics of High Polymer Solutions. V. Phase Equilibria in the Ternary System: Polymer 1—Polymer 2—Solvent
Licensed Content Author	Robert L. Scott
Licensed Content Date	Dec 22, 2004
Licensed Content Volume Number	17
Licensed Content Issue Number	3
Type of Use	Thesis/Dissertation
Requestor type	Student
Format	Print and electronic
Portion	Photograph/Image
Title of your thesis / dissertation	Thermodynamics of polymer mixtures in solution and their applications in functional, microstructured films
Expected completion date	Jan 2017
Estimated size (number of pages)	300
Requestor Location	Jillian A Emerson 150 Academy St NEWARK, DE 19716 United States Attn: Jillian A Emerson
Billing Type	Invoice
Billing Address	Jillian A Emerson 150 Academy St NEWARK, DE 19716 United States Attn: Jillian A Emerson
Total	0.00 USD

Terms and Conditions

AIP Publishing LLC -- Terms and Conditions: Permissions Uses

AIP Publishing hereby grants to you the non-exclusive right and license to use and/or distribute the Material according to the use specified in your order, on a one-time basis, for the specified term, with a maximum distribution equal to the number that you have ordered. Any links or other content accompanying the Material are not the subject of this license.

1. You agree to include the following copyright and permission notice with the reproduction of the Material: "Reprinted from [FULL CITATION], with the permission of AIP Publishing." For an article, the credit line and permission notice must be printed on the first page of the article or book chapter. For photographs, covers, or tables, the notice may appear with the Material, in a footnote, or in the reference list.
2. If you have licensed reuse of a figure, photograph, cover, or table, it is your responsibility to ensure that the material is original to AIP Publishing and does not contain the copyright of another entity, and that the copyright notice of the figure, photograph, cover, or table does not indicate that it was reprinted by AIP Publishing, with permission, from another source. Under no circumstances does AIP Publishing purport or intend to grant permission to reuse material to which it does not hold appropriate rights.
You may not alter or modify the Material in any manner. You may translate the Material into another language only if you have licensed translation rights. You may not use the Material for promotional purposes.
3. The foregoing license shall not take effect unless and until AIP Publishing or its agent, Copyright Clearance Center, receives the Payment in accordance with Copyright Clearance Center Billing and Payment Terms and Conditions, which are incorporated herein by reference.
4. AIP Publishing or Copyright Clearance Center may, within two business days of granting this license, revoke the license for any reason whatsoever, with a full refund payable to you. Should you violate the terms of this license at any time, AIP Publishing, or Copyright Clearance Center may revoke the license with no refund to you. Notice of such revocation will be made using the contact information provided by you. Failure to receive such notice will not nullify the revocation.
5. AIP Publishing makes no representations or warranties with respect to the Material. You agree to indemnify and hold harmless AIP Publishing, and their officers, directors, employees or agents from and against any and all claims arising out of your use of the Material other than as specifically authorized herein.
6. The permission granted herein is personal to you and is not transferable or assignable without the prior written permission of AIP Publishing. This license may not be amended except in a writing signed by the party to be charged.
7. If purchase orders, acknowledgments or check endorsements are issued on any forms containing terms and conditions which are inconsistent with these provisions, such inconsistent terms and conditions shall be of no force and effect. This document, including the CCC Billing and Payment Terms and Conditions, shall be the entire agreement between the parties relating to the subject matter hereof.

This Agreement shall be governed by and construed in accordance with the laws of the State of New York. Both parties hereby submit to the jurisdiction of the courts of New York County for purposes of resolving any disputes that may arise hereunder.

V1.1

Questions? customer care@copyright.com or +1-855-239-3415 (toll free in the US) or +1-978-646-2777.



Title: Influence of Nanoparticles on
Miscibility of Polymer Blends. A
Simple Theory

Author: Valeriy V. Ginzburg

Publication: Macromolecules

Publisher: American Chemical Society

Date: Mar 1, 2005

Copyright © 2005, American Chemical Society

Logged in as:
Jillian Emerson
Account #:
3001073337

LOGOUT

PERMISSION/LICENSE IS GRANTED FOR YOUR ORDER AT NO CHARGE

This type of permission/license, instead of the standard Terms & Conditions, is sent to you because no fee is being charged for your order. Please note the following:

- Permission is granted for your request in both print and electronic formats, and translations.
- If figures and/or tables were requested, they may be adapted or used in part.
- Please print this page for your records and send a copy of it to your publisher/graduate school.
- Appropriate credit for the requested material should be given as follows: "Reprinted (adapted) with permission from (COMPLETE REFERENCE CITATION). Copyright (YEAR) American Chemical Society." Insert appropriate information in place of the capitalized words.
- One-time permission is granted only for the use specified in your request. No additional uses are granted (such as derivative works or other editions). For any other uses, please submit a new request.

If credit is given to another source for the material you requested, permission must be obtained from that source.

BACK

CLOSE WINDOW

**JOHN WILEY AND SONS LICENSE
TERMS AND CONDITIONS**

Nov 22, 2016

This Agreement between Jillian A Emerson ("You") and John Wiley and Sons ("John Wiley and Sons") consists of your license details and the terms and conditions provided by John Wiley and Sons and Copyright Clearance Center.

License Number	3994300402028
License date	Nov 22, 2016
Licensed Content Publisher	John Wiley and Sons
Licensed Content Publication	Journal of Polymer Science Part B: Polymer Physics
Licensed Content Title	Determining the phase behavior of nanoparticle-filled binary blends
Licensed Content Author	Gang He,Valeriy V. Ginzburg,Anna C. Balazs
Licensed Content Date	Jul 25, 2006
Licensed Content Pages	15
Type of use	Dissertation/Thesis
Requestor type	University/Academic
Format	Print and electronic
Portion	Figure/table
Number of figures/tables	1
Original Wiley figure/table number(s)	Figure 4
Will you be translating?	No
Title of your thesis / dissertation	Thermodynamics of polymer mixtures in solution and their applications in functional, microstructured films
Expected completion date	Jan 2017
Expected size (number of pages)	300
Requestor Location	Jillian A Emerson 150 Academy St NEWARK, DE 19716 United States Attn: Jillian A Emerson
Publisher Tax ID	EU826007151
Billing Type	Invoice
Billing Address	Jillian A Emerson 150 Academy St NEWARK, DE 19716 United States Attn: Jillian A Emerson
Total	0.00 USD
Terms and Conditions	

TERMS AND CONDITIONS

This copyrighted material is owned by or exclusively licensed to John Wiley & Sons, Inc. or one of its group companies (each a "Wiley Company") or handled on behalf of a society with which a Wiley Company has exclusive publishing rights in relation to a particular work (collectively "WILEY"). By clicking "accept" in connection with completing this licensing transaction, you agree that the following terms and conditions apply to this transaction (along with the billing and payment terms and conditions established by the Copyright Clearance Center Inc., ("CCC's Billing and Payment terms and conditions"), at the time that you opened your RightsLink account (these are available at any time at <http://myaccount.copyright.com>).

Terms and Conditions

- The materials you have requested permission to reproduce or reuse (the "Wiley Materials") are protected by copyright.
- You are hereby granted a personal, non-exclusive, non-sub licensable (on a stand-alone basis), non-transferable, worldwide, limited license to reproduce the Wiley Materials for the purpose specified in the licensing process. This license, **and any CONTENT (PDF or image file) purchased as part of your order**, is for a one-time use only and limited to any maximum distribution number specified in the license. The first instance of republication or reuse granted by this license must be completed within two years of the date of the grant of this license (although copies prepared before the end date may be distributed thereafter). The Wiley Materials shall not be used in any other manner or for any other purpose, beyond what is granted in the license. Permission is granted subject to an appropriate acknowledgement given to the author, title of the material/book/journal and the publisher. You shall also duplicate the copyright notice that appears in the Wiley publication in your use of the Wiley Material. Permission is also granted on the understanding that nowhere in the text is a previously published source acknowledged for all or part of this Wiley Material. Any third party content is expressly excluded from this permission.
- With respect to the Wiley Materials, all rights are reserved. Except as expressly granted by the terms of the license, no part of the Wiley Materials may be copied, modified, adapted (except for minor reformatting required by the new Publication), translated, reproduced, transferred or distributed, in any form or by any means, and no derivative works may be made based on the Wiley Materials without the prior permission of the respective copyright owner. **For STM Signatory Publishers clearing permission under the terms of the [STM Permissions Guidelines](#) only, the terms of the license are extended to include subsequent editions and for editions in other languages, provided such editions are for the work as a whole in situ and does not involve the separate exploitation of the permitted figures or extracts**, You may not alter, remove or suppress in any manner any copyright, trademark or other notices displayed by the Wiley Materials. You may not license, rent, sell, loan, lease, pledge, offer as security, transfer or assign the Wiley Materials on a stand-alone basis, or any of the rights granted to you hereunder to any other person.
- The Wiley Materials and all of the intellectual property rights therein shall at all times remain the exclusive property of John Wiley & Sons Inc, the Wiley Companies, or their respective licensors, and your interest therein is only that of having possession of and the right to reproduce the Wiley Materials pursuant to Section 2 herein during the continuance of this Agreement. You agree that you own no right, title or interest in or to the Wiley Materials or any of the intellectual property rights therein. You shall have no rights hereunder other than the license as provided for above in Section 2. No right,

license or interest to any trademark, trade name, service mark or other branding ("Marks") of WILEY or its licensors is granted hereunder, and you agree that you shall not assert any such right, license or interest with respect thereto

- NEITHER WILEY NOR ITS LICENSORS MAKES ANY WARRANTY OR REPRESENTATION OF ANY KIND TO YOU OR ANY THIRD PARTY, EXPRESS, IMPLIED OR STATUTORY, WITH RESPECT TO THE MATERIALS OR THE ACCURACY OF ANY INFORMATION CONTAINED IN THE MATERIALS, INCLUDING, WITHOUT LIMITATION, ANY IMPLIED WARRANTY OF MERCHANTABILITY, ACCURACY, SATISFACTORY QUALITY, FITNESS FOR A PARTICULAR PURPOSE, USABILITY, INTEGRATION OR NON-INFRINGEMENT AND ALL SUCH WARRANTIES ARE HEREBY EXCLUDED BY WILEY AND ITS LICENSORS AND WAIVED BY YOU.
- WILEY shall have the right to terminate this Agreement immediately upon breach of this Agreement by you.
- You shall indemnify, defend and hold harmless WILEY, its Licensors and their respective directors, officers, agents and employees, from and against any actual or threatened claims, demands, causes of action or proceedings arising from any breach of this Agreement by you.
- IN NO EVENT SHALL WILEY OR ITS LICENSORS BE LIABLE TO YOU OR ANY OTHER PARTY OR ANY OTHER PERSON OR ENTITY FOR ANY SPECIAL, CONSEQUENTIAL, INCIDENTAL, INDIRECT, EXEMPLARY OR PUNITIVE DAMAGES, HOWEVER CAUSED, ARISING OUT OF OR IN CONNECTION WITH THE DOWNLOADING, PROVISIONING, VIEWING OR USE OF THE MATERIALS REGARDLESS OF THE FORM OF ACTION, WHETHER FOR BREACH OF CONTRACT, BREACH OF WARRANTY, TORT, NEGLIGENCE, INFRINGEMENT OR OTHERWISE (INCLUDING, WITHOUT LIMITATION, DAMAGES BASED ON LOSS OF PROFITS, DATA, FILES, USE, BUSINESS OPPORTUNITY OR CLAIMS OF THIRD PARTIES), AND WHETHER OR NOT THE PARTY HAS BEEN ADVISED OF THE POSSIBILITY OF SUCH DAMAGES. THIS LIMITATION SHALL APPLY NOTWITHSTANDING ANY FAILURE OF ESSENTIAL PURPOSE OF ANY LIMITED REMEDY PROVIDED HEREIN.
- Should any provision of this Agreement be held by a court of competent jurisdiction to be illegal, invalid, or unenforceable, that provision shall be deemed amended to achieve as nearly as possible the same economic effect as the original provision, and the legality, validity and enforceability of the remaining provisions of this Agreement shall not be affected or impaired thereby.
- The failure of either party to enforce any term or condition of this Agreement shall not constitute a waiver of either party's right to enforce each and every term and condition of this Agreement. No breach under this agreement shall be deemed waived or excused by either party unless such waiver or consent is in writing signed by the party granting such waiver or consent. The waiver by or consent of a party to a breach of any provision of this Agreement shall not operate or be construed as a waiver of or consent to any other or subsequent breach by such other party.
- This Agreement may not be assigned (including by operation of law or otherwise) by you without WILEY's prior written consent.

- Any fee required for this permission shall be non-refundable after thirty (30) days from receipt by the CCC.
- These terms and conditions together with CCC's Billing and Payment terms and conditions (which are incorporated herein) form the entire agreement between you and WILEY concerning this licensing transaction and (in the absence of fraud) supersedes all prior agreements and representations of the parties, oral or written. This Agreement may not be amended except in writing signed by both parties. This Agreement shall be binding upon and inure to the benefit of the parties' successors, legal representatives, and authorized assigns.
- In the event of any conflict between your obligations established by these terms and conditions and those established by CCC's Billing and Payment terms and conditions, these terms and conditions shall prevail.
- WILEY expressly reserves all rights not specifically granted in the combination of (i) the license details provided by you and accepted in the course of this licensing transaction, (ii) these terms and conditions and (iii) CCC's Billing and Payment terms and conditions.
- This Agreement will be void if the Type of Use, Format, Circulation, or Requestor Type was misrepresented during the licensing process.
- This Agreement shall be governed by and construed in accordance with the laws of the State of New York, USA, without regards to such state's conflict of law rules. Any legal action, suit or proceeding arising out of or relating to these Terms and Conditions or the breach thereof shall be instituted in a court of competent jurisdiction in New York County in the State of New York in the United States of America and each party hereby consents and submits to the personal jurisdiction of such court, waives any objection to venue in such court and consents to service of process by registered or certified mail, return receipt requested, at the last known address of such party.

WILEY OPEN ACCESS TERMS AND CONDITIONS

Wiley Publishes Open Access Articles in fully Open Access Journals and in Subscription journals offering Online Open. Although most of the fully Open Access journals publish open access articles under the terms of the Creative Commons Attribution (CC BY) License only, the subscription journals and a few of the Open Access Journals offer a choice of Creative Commons Licenses. The license type is clearly identified on the article.

The Creative Commons Attribution License

The [Creative Commons Attribution License \(CC-BY\)](#) allows users to copy, distribute and transmit an article, adapt the article and make commercial use of the article. The CC-BY license permits commercial and non-

Creative Commons Attribution Non-Commercial License

The [Creative Commons Attribution Non-Commercial \(CC-BY-NC\) License](#) permits use, distribution and reproduction in any medium, provided the original work is properly cited and is not used for commercial purposes.(see below)

Creative Commons Attribution-Non-Commercial-NoDerivs License

The [Creative Commons Attribution Non-Commercial-NoDerivs License](#) (CC-BY-NC-ND) permits use, distribution and reproduction in any medium, provided the original work is properly cited, is not used for commercial purposes and no modifications or adaptations are made. (see below)

Use by commercial "for-profit" organizations

Use of Wiley Open Access articles for commercial, promotional, or marketing purposes requires further explicit permission from Wiley and will be subject to a fee.

Further details can be found on Wiley Online Library

<http://olabout.wiley.com/WileyCDA/Section/id-410895.html>

Other Terms and Conditions:

v1.10 Last updated September 2015

Questions? customercare@copyright.com or +1-855-239-3415 (toll free in the US) or +1-978-646-2777.

Title: Determination of Solvent-Polymer and Polymer-Polymer Flory-Huggins Interaction Parameters for Poly(3-hexylthiophene) via Solvent Vapor Swelling

Author: Jillian A. Emerson, Daniel T. W. Toolan, Jonathan R. Howse, et al

Publication: Macromolecules

Publisher: American Chemical Society

Date: Aug 1, 2013

Copyright © 2013, American Chemical Society

Logged in as:
Jillian Emerson

LOGOUT

PERMISSION/LICENSE IS GRANTED FOR YOUR ORDER AT NO CHARGE

This type of permission/license, instead of the standard Terms & Conditions, is sent to you because no fee is being charged for your order. Please note the following:

- Permission is granted for your request in both print and electronic formats, and translations.
- If figures and/or tables were requested, they may be adapted or used in part.
- Please print this page for your records and send a copy of it to your publisher/graduate school.
- Appropriate credit for the requested material should be given as follows: "Reprinted (adapted) with permission from (COMPLETE REFERENCE CITATION). Copyright (YEAR) American Chemical Society." Insert appropriate information in place of the capitalized words.
- One-time permission is granted only for the use specified in your request. No additional uses are granted (such as derivative works or other editions). For any other uses, please submit a new request.

BACK

CLOSE WINDOW

**JOHN WILEY AND SONS LICENSE
TERMS AND CONDITIONS**

Oct 21, 2016

This Agreement between Jillian A Emerson ("You") and John Wiley and Sons ("John Wiley and Sons") consists of your license details and the terms and conditions provided by John Wiley and Sons and Copyright Clearance Center.

License Number	3973711415559
License date	Oct 21, 2016
Licensed Content Publisher	John Wiley and Sons
Licensed Content Publication	Journal of Polymer Science Part B: Polymer Physics
Licensed Content Title	Real time laser interference microscopy for bar-spread polystyrene/poly(methyl methacrylate) blends
Licensed Content Author	Ehtsham Ul Haq, Daniel T. W. Toolan, Jillian A. Emerson, Thomas H. Epps, Jonathan R. Howse, Alan D. F. Dunbar, Stephen J. Ebbens
Licensed Content Date	Jun 6, 2014
Licensed Content Pages	8
Type of use	Dissertation/Thesis
Requestor type	Author of this Wiley article
Format	Print and electronic
Portion	Full article
Will you be translating?	No
Title of your thesis / dissertation	Thermodynamics of polymer mixtures in solution and their applications in functional, microstructured films
Expected completion date	Jan 2017
Expected size (number of pages)	300
Requestor Location	Jillian A Emerson 150 Academy St NEWARK, DE 19716 United States Attn: Jillian A Emerson
Publisher Tax ID	EU826007151
Billing Type	Invoice
Billing Address	Jillian A Emerson 150 Academy St NEWARK, DE 19716 United States Attn: Jillian A Emerson
Total	0.00 USD
Terms and Conditions	

TERMS AND CONDITIONS

This copyrighted material is owned by or exclusively licensed to John Wiley & Sons, Inc. or one of its group companies (each a "Wiley Company") or handled on behalf of a society with which a Wiley Company has exclusive publishing rights in relation to a particular work (collectively "WILEY"). By clicking "accept" in connection with completing this licensing transaction, you agree that the following terms and conditions apply to this transaction (along with the billing and payment terms and conditions established by the Copyright Clearance Center Inc., ("CCC's Billing and Payment terms and conditions"), at the time that you opened your RightsLink account (these are available at any time at <http://myaccount.copyright.com>).

Terms and Conditions

- The materials you have requested permission to reproduce or reuse (the "Wiley Materials") are protected by copyright.
- You are hereby granted a personal, non-exclusive, non-sub licensable (on a stand-alone basis), non-transferable, worldwide, limited license to reproduce the Wiley Materials for the purpose specified in the licensing process. This license, **and any CONTENT (PDF or image file) purchased as part of your order**, is for a one-time use only and limited to any maximum distribution number specified in the license. The first instance of republication or reuse granted by this license must be completed within two years of the date of the grant of this license (although copies prepared before the end date may be distributed thereafter). The Wiley Materials shall not be used in any other manner or for any other purpose, beyond what is granted in the license. Permission is granted subject to an appropriate acknowledgement given to the author, title of the material/book/journal and the publisher. You shall also duplicate the copyright notice that appears in the Wiley publication in your use of the Wiley Material. Permission is also granted on the understanding that nowhere in the text is a previously published source acknowledged for all or part of this Wiley Material. Any third party content is expressly excluded from this permission.
- With respect to the Wiley Materials, all rights are reserved. Except as expressly granted by the terms of the license, no part of the Wiley Materials may be copied, modified, adapted (except for minor reformatting required by the new Publication), translated, reproduced, transferred or distributed, in any form or by any means, and no derivative works may be made based on the Wiley Materials without the prior permission of the respective copyright owner. **For STM Signatory Publishers clearing permission under the terms of the [STM Permissions Guidelines](#) only, the terms of the license are extended to include subsequent editions and for editions in other languages, provided such editions are for the work as a whole in situ and does not involve the separate exploitation of the permitted figures or extracts**, You may not alter, remove or suppress in any manner any copyright, trademark or other notices displayed by the Wiley Materials. You may not license, rent, sell, loan, lease, pledge, offer as security, transfer or assign the Wiley Materials on a stand-alone basis, or any of the rights granted to you hereunder to any other person.
- The Wiley Materials and all of the intellectual property rights therein shall at all times remain the exclusive property of John Wiley & Sons Inc, the Wiley Companies, or their respective licensors, and your interest therein is only that of having possession of and the right to reproduce the Wiley Materials pursuant to Section 2 herein during the continuance of this Agreement. You agree that you own no right, title or interest in or to the Wiley Materials or any of the intellectual property rights therein. You shall have no rights hereunder other than the license as provided for above in Section 2. No right, license or interest to any trademark, trade name, service mark or other branding

("Marks") of WILEY or its licensors is granted hereunder, and you agree that you shall not assert any such right, license or interest with respect thereto

- NEITHER WILEY NOR ITS LICENSORS MAKES ANY WARRANTY OR REPRESENTATION OF ANY KIND TO YOU OR ANY THIRD PARTY, EXPRESS, IMPLIED OR STATUTORY, WITH RESPECT TO THE MATERIALS OR THE ACCURACY OF ANY INFORMATION CONTAINED IN THE MATERIALS, INCLUDING, WITHOUT LIMITATION, ANY IMPLIED WARRANTY OF MERCHANTABILITY, ACCURACY, SATISFACTORY QUALITY, FITNESS FOR A PARTICULAR PURPOSE, USABILITY, INTEGRATION OR NON-INFRINGEMENT AND ALL SUCH WARRANTIES ARE HEREBY EXCLUDED BY WILEY AND ITS LICENSORS AND WAIVED BY YOU.
- WILEY shall have the right to terminate this Agreement immediately upon breach of this Agreement by you.
- You shall indemnify, defend and hold harmless WILEY, its Licensors and their respective directors, officers, agents and employees, from and against any actual or threatened claims, demands, causes of action or proceedings arising from any breach of this Agreement by you.
- IN NO EVENT SHALL WILEY OR ITS LICENSORS BE LIABLE TO YOU OR ANY OTHER PARTY OR ANY OTHER PERSON OR ENTITY FOR ANY SPECIAL, CONSEQUENTIAL, INCIDENTAL, INDIRECT, EXEMPLARY OR PUNITIVE DAMAGES, HOWEVER CAUSED, ARISING OUT OF OR IN CONNECTION WITH THE DOWNLOADING, PROVISIONING, VIEWING OR USE OF THE MATERIALS REGARDLESS OF THE FORM OF ACTION, WHETHER FOR BREACH OF CONTRACT, BREACH OF WARRANTY, TORT, NEGLIGENCE, INFRINGEMENT OR OTHERWISE (INCLUDING, WITHOUT LIMITATION, DAMAGES BASED ON LOSS OF PROFITS, DATA, FILES, USE, BUSINESS OPPORTUNITY OR CLAIMS OF THIRD PARTIES), AND WHETHER OR NOT THE PARTY HAS BEEN ADVISED OF THE POSSIBILITY OF SUCH DAMAGES. THIS LIMITATION SHALL APPLY NOTWITHSTANDING ANY FAILURE OF ESSENTIAL PURPOSE OF ANY LIMITED REMEDY PROVIDED HEREIN.
- Should any provision of this Agreement be held by a court of competent jurisdiction to be illegal, invalid, or unenforceable, that provision shall be deemed amended to achieve as nearly as possible the same economic effect as the original provision, and the legality, validity and enforceability of the remaining provisions of this Agreement shall not be affected or impaired thereby.
- The failure of either party to enforce any term or condition of this Agreement shall not constitute a waiver of either party's right to enforce each and every term and condition of this Agreement. No breach under this agreement shall be deemed waived or excused by either party unless such waiver or consent is in writing signed by the party granting such waiver or consent. The waiver by or consent of a party to a breach of any provision of this Agreement shall not operate or be construed as a waiver of or consent to any other or subsequent breach by such other party.
- This Agreement may not be assigned (including by operation of law or otherwise) by you without WILEY's prior written consent.

- Any fee required for this permission shall be non-refundable after thirty (30) days from receipt by the CCC.
- These terms and conditions together with CCC's Billing and Payment terms and conditions (which are incorporated herein) form the entire agreement between you and WILEY concerning this licensing transaction and (in the absence of fraud) supersedes all prior agreements and representations of the parties, oral or written. This Agreement may not be amended except in writing signed by both parties. This Agreement shall be binding upon and inure to the benefit of the parties' successors, legal representatives, and authorized assigns.
- In the event of any conflict between your obligations established by these terms and conditions and those established by CCC's Billing and Payment terms and conditions, these terms and conditions shall prevail.
- WILEY expressly reserves all rights not specifically granted in the combination of (i) the license details provided by you and accepted in the course of this licensing transaction, (ii) these terms and conditions and (iii) CCC's Billing and Payment terms and conditions.
- This Agreement will be void if the Type of Use, Format, Circulation, or Requestor Type was misrepresented during the licensing process.
- This Agreement shall be governed by and construed in accordance with the laws of the State of New York, USA, without regards to such state's conflict of law rules. Any legal action, suit or proceeding arising out of or relating to these Terms and Conditions or the breach thereof shall be instituted in a court of competent jurisdiction in New York County in the State of New York in the United States of America and each party hereby consents and submits to the personal jurisdiction of such court, waives any objection to venue in such court and consents to service of process by registered or certified mail, return receipt requested, at the last known address of such party.

WILEY OPEN ACCESS TERMS AND CONDITIONS

Wiley Publishes Open Access Articles in fully Open Access Journals and in Subscription journals offering Online Open. Although most of the fully Open Access journals publish open access articles under the terms of the Creative Commons Attribution (CC BY) License only, the subscription journals and a few of the Open Access Journals offer a choice of Creative Commons Licenses. The license type is clearly identified on the article.

The Creative Commons Attribution License

The [Creative Commons Attribution License \(CC-BY\)](#) allows users to copy, distribute and transmit an article, adapt the article and make commercial use of the article. The CC-BY license permits commercial and non-

Creative Commons Attribution Non-Commercial License

The [Creative Commons Attribution Non-Commercial \(CC-BY-NC\) License](#) permits use, distribution and reproduction in any medium, provided the original work is properly cited and is not used for commercial purposes.(see below)

Creative Commons Attribution-Non-Commercial-NoDerivs License

The [Creative Commons Attribution Non-Commercial-NoDerivs License](#) (CC-BY-NC-ND) permits use, distribution and reproduction in any medium, provided the original work is properly cited, is not used for commercial purposes and no modifications or adaptations are made. (see below)

Use by commercial "for-profit" organizations

Use of Wiley Open Access articles for commercial, promotional, or marketing purposes requires further explicit permission from Wiley and will be subject to a fee.

Further details can be found on Wiley Online Library

<http://olabout.wiley.com/WileyCDA/Section/id-410895.html>

Other Terms and Conditions:

v1.10 Last updated September 2015

Questions? customercare@copyright.com or +1-855-239-3415 (toll free in the US) or +1-978-646-2777.

**ELSEVIER LICENSE
TERMS AND CONDITIONS**

Nov 22, 2016

This Agreement between Jillian A Emerson ("You") and Elsevier ("Elsevier") consists of your license details and the terms and conditions provided by Elsevier and Copyright Clearance Center.

License Number	3994460172011
License date	Nov 22, 2016
Licensed Content Publisher	Elsevier
Licensed Content Publication	Wear
Licensed Content Title	A low friction and ultra low wear rate PEEK/PTFE composite
Licensed Content Author	David L. Burriss,W. Gregory Sawyer
Licensed Content Date	30 August 2006
Licensed Content Volume Number	261
Licensed Content Issue Number	3-4
Licensed Content Pages	9
Start Page	410
End Page	418
Type of Use	reuse in a thesis/dissertation
Intended publisher of new work	other
Portion	figures/tables/illustrations
Number of figures/tables/illustrations	1
Format	both print and electronic
Are you the author of this Elsevier article?	No
Will you be translating?	No
Order reference number	
Original figure numbers	Figure 6
Title of your thesis/dissertation	Thermodynamics of polymer mixtures in solution and their applications in functional, microstructured films
Expected completion date	Jan 2017
Estimated size (number of pages)	300
Elsevier VAT number	GB 494 6272 12
Requestor Location	Jillian A Emerson 150 Academy St

NEWARK, DE 19716

United States
Attn: Jillian A Emerson

Total 0.00 USD

[Terms and Conditions](#)

INTRODUCTION

1. The publisher for this copyrighted material is Elsevier. By clicking "accept" in connection with completing this licensing transaction, you agree that the following terms and conditions apply to this transaction (along with the Billing and Payment terms and conditions established by Copyright Clearance Center, Inc. ("CCC"), at the time that you opened your Rightslink account and that are available at any time at <http://myaccount.copyright.com>).

GENERAL TERMS

2. Elsevier hereby grants you permission to reproduce the aforementioned material subject to the terms and conditions indicated.

3. Acknowledgement: If any part of the material to be used (for example, figures) has appeared in our publication with credit or acknowledgement to another source, permission must also be sought from that source. If such permission is not obtained then that material may not be included in your publication/copies. Suitable acknowledgement to the source must be made, either as a footnote or in a reference list at the end of your publication, as follows:

"Reprinted from Publication title, Vol /edition number, Author(s), Title of article / title of chapter, Pages No., Copyright (Year), with permission from Elsevier [OR APPLICABLE SOCIETY COPYRIGHT OWNER]." Also Lancet special credit - "Reprinted from The Lancet, Vol. number, Author(s), Title of article, Pages No., Copyright (Year), with permission from Elsevier."

4. Reproduction of this material is confined to the purpose and/or media for which permission is hereby given.

5. Altering/Modifying Material: Not Permitted. However figures and illustrations may be altered/adapted minimally to serve your work. Any other abbreviations, additions, deletions and/or any other alterations shall be made only with prior written authorization of Elsevier Ltd. (Please contact Elsevier at permissions@elsevier.com)

6. If the permission fee for the requested use of our material is waived in this instance, please be advised that your future requests for Elsevier materials may attract a fee.

7. Reservation of Rights: Publisher reserves all rights not specifically granted in the combination of (i) the license details provided by you and accepted in the course of this licensing transaction, (ii) these terms and conditions and (iii) CCC's Billing and Payment terms and conditions.

8. License Contingent Upon Payment: While you may exercise the rights licensed immediately upon issuance of the license at the end of the licensing process for the transaction, provided that you have disclosed complete and accurate details of your proposed use, no license is finally effective unless and until full payment is received from you (either by publisher or by CCC) as provided in CCC's Billing and Payment terms and conditions. If full payment is not received on a timely basis, then any license preliminarily granted shall be deemed automatically revoked and shall be void as if never granted. Further, in the event that you breach any of these terms and conditions or any of CCC's Billing and Payment terms and conditions, the license is automatically revoked and shall be void as if never granted. Use of materials as described in a revoked license, as well as any use of the materials beyond the scope of an unrevoked license, may constitute copyright infringement and publisher reserves the right to take any and all action to protect its copyright in the materials.

9. Warranties: Publisher makes no representations or warranties with respect to the licensed material.

10. Indemnity: You hereby indemnify and agree to hold harmless publisher and CCC, and their respective officers, directors, employees and agents, from and against any and all

claims arising out of your use of the licensed material other than as specifically authorized pursuant to this license.

11. **No Transfer of License:** This license is personal to you and may not be sublicensed, assigned, or transferred by you to any other person without publisher's written permission.

12. **No Amendment Except in Writing:** This license may not be amended except in a writing signed by both parties (or, in the case of publisher, by CCC on publisher's behalf).

13. **Objection to Contrary Terms:** Publisher hereby objects to any terms contained in any purchase order, acknowledgment, check endorsement or other writing prepared by you, which terms are inconsistent with these terms and conditions or CCC's Billing and Payment terms and conditions. These terms and conditions, together with CCC's Billing and Payment terms and conditions (which are incorporated herein), comprise the entire agreement between you and publisher (and CCC) concerning this licensing transaction. In the event of any conflict between your obligations established by these terms and conditions and those established by CCC's Billing and Payment terms and conditions, these terms and conditions shall control.

14. **Revocation:** Elsevier or Copyright Clearance Center may deny the permissions described in this License at their sole discretion, for any reason or no reason, with a full refund payable to you. Notice of such denial will be made using the contact information provided by you. Failure to receive such notice will not alter or invalidate the denial. In no event will Elsevier or Copyright Clearance Center be responsible or liable for any costs, expenses or damage incurred by you as a result of a denial of your permission request, other than a refund of the amount(s) paid by you to Elsevier and/or Copyright Clearance Center for denied permissions.

LIMITED LICENSE

The following terms and conditions apply only to specific license types:

15. **Translation:** This permission is granted for non-exclusive world **English** rights only unless your license was granted for translation rights. If you licensed translation rights you may only translate this content into the languages you requested. A professional translator must perform all translations and reproduce the content word for word preserving the integrity of the article.

16. **Posting licensed content on any Website:** The following terms and conditions apply as follows: Licensing material from an Elsevier journal: All content posted to the web site must maintain the copyright information line on the bottom of each image; A hyper-text must be included to the Homepage of the journal from which you are licensing at <http://www.sciencedirect.com/science/journal/xxxxx> or the Elsevier homepage for books at <http://www.elsevier.com>; Central Storage: This license does not include permission for a scanned version of the material to be stored in a central repository such as that provided by Heron/XanEdu.

Licensing material from an Elsevier book: A hyper-text link must be included to the Elsevier homepage at <http://www.elsevier.com>. All content posted to the web site must maintain the copyright information line on the bottom of each image.

Posting licensed content on Electronic reserve: In addition to the above the following clauses are applicable: The web site must be password-protected and made available only to bona fide students registered on a relevant course. This permission is granted for 1 year only. You may obtain a new license for future website posting.

17. **For journal authors:** the following clauses are applicable in addition to the above:

Preprints:

A preprint is an author's own write-up of research results and analysis, it has not been peer-reviewed, nor has it had any other value added to it by a publisher (such as formatting, copyright, technical enhancement etc.).

Authors can share their preprints anywhere at any time. Preprints should not be added to or enhanced in any way in order to appear more like, or to substitute for, the final versions of

articles however authors can update their preprints on arXiv or RePEc with their Accepted Author Manuscript (see below).

If accepted for publication, we encourage authors to link from the preprint to their formal publication via its DOI. Millions of researchers have access to the formal publications on ScienceDirect, and so links will help users to find, access, cite and use the best available version. Please note that Cell Press, The Lancet and some society-owned have different preprint policies. Information on these policies is available on the journal homepage.

Accepted Author Manuscripts: An accepted author manuscript is the manuscript of an article that has been accepted for publication and which typically includes author-incorporated changes suggested during submission, peer review and editor-author communications.

Authors can share their accepted author manuscript:

- immediately
 - via their non-commercial person homepage or blog
 - by updating a preprint in arXiv or RePEc with the accepted manuscript
 - via their research institute or institutional repository for internal institutional uses or as part of an invitation-only research collaboration work-group
 - directly by providing copies to their students or to research collaborators for their personal use
 - for private scholarly sharing as part of an invitation-only work group on commercial sites with which Elsevier has an agreement
- after the embargo period
 - via non-commercial hosting platforms such as their institutional repository
 - via commercial sites with which Elsevier has an agreement

In all cases accepted manuscripts should:

- link to the formal publication via its DOI
- bear a CC-BY-NC-ND license - this is easy to do
- if aggregated with other manuscripts, for example in a repository or other site, be shared in alignment with our hosting policy not be added to or enhanced in any way to appear more like, or to substitute for, the published journal article.

Published journal article (JPA): A published journal article (PJA) is the definitive final record of published research that appears or will appear in the journal and embodies all value-adding publishing activities including peer review co-ordination, copy-editing, formatting, (if relevant) pagination and online enrichment.

Policies for sharing publishing journal articles differ for subscription and gold open access articles:

Subscription Articles: If you are an author, please share a link to your article rather than the full-text. Millions of researchers have access to the formal publications on ScienceDirect, and so links will help your users to find, access, cite, and use the best available version. Theses and dissertations which contain embedded PJAs as part of the formal submission can be posted publicly by the awarding institution with DOI links back to the formal publications on ScienceDirect.

If you are affiliated with a library that subscribes to ScienceDirect you have additional private sharing rights for others' research accessed under that agreement. This includes use for classroom teaching and internal training at the institution (including use in course packs and courseware programs), and inclusion of the article for grant funding purposes.

Gold Open Access Articles: May be shared according to the author-selected end-user license and should contain a [CrossMark logo](#), the end user license, and a DOI link to the formal publication on ScienceDirect.

Please refer to Elsevier's [posting policy](#) for further information.

18. **For book authors** the following clauses are applicable in addition to the above: Authors are permitted to place a brief summary of their work online only. You are not allowed to download and post the published electronic version of your chapter, nor may you scan the printed edition to create an electronic version. **Posting to a repository:** Authors are permitted to post a summary of their chapter only in their institution's repository.

19. **Thesis/Dissertation:** If your license is for use in a thesis/dissertation your thesis may be submitted to your institution in either print or electronic form. Should your thesis be published commercially, please reapply for permission. These requirements include permission for the Library and Archives of Canada to supply single copies, on demand, of the complete thesis and include permission for Proquest/UMI to supply single copies, on demand, of the complete thesis. Should your thesis be published commercially, please reapply for permission. Theses and dissertations which contain embedded PJAs as part of the formal submission can be posted publicly by the awarding institution with DOI links back to the formal publications on ScienceDirect.

Elsevier Open Access Terms and Conditions

You can publish open access with Elsevier in hundreds of open access journals or in nearly 2000 established subscription journals that support open access publishing. Permitted third party re-use of these open access articles is defined by the author's choice of Creative Commons user license. See our [open access license policy](#) for more information.

Terms & Conditions applicable to all Open Access articles published with Elsevier:

Any reuse of the article must not represent the author as endorsing the adaptation of the article nor should the article be modified in such a way as to damage the author's honour or reputation. If any changes have been made, such changes must be clearly indicated.

The author(s) must be appropriately credited and we ask that you include the end user license and a DOI link to the formal publication on ScienceDirect.

If any part of the material to be used (for example, figures) has appeared in our publication with credit or acknowledgement to another source it is the responsibility of the user to ensure their reuse complies with the terms and conditions determined by the rights holder.

Additional Terms & Conditions applicable to each Creative Commons user license:

CC BY: The CC-BY license allows users to copy, to create extracts, abstracts and new works from the Article, to alter and revise the Article and to make commercial use of the Article (including reuse and/or resale of the Article by commercial entities), provided the user gives appropriate credit (with a link to the formal publication through the relevant DOI), provides a link to the license, indicates if changes were made and the licensor is not represented as endorsing the use made of the work. The full details of the license are available at <http://creativecommons.org/licenses/by/4.0>.

CC BY NC SA: The CC BY-NC-SA license allows users to copy, to create extracts, abstracts and new works from the Article, to alter and revise the Article, provided this is not done for commercial purposes, and that the user gives appropriate credit (with a link to the formal publication through the relevant DOI), provides a link to the license, indicates if changes were made and the licensor is not represented as endorsing the use made of the work. Further, any new works must be made available on the same conditions. The full details of the license are available at <http://creativecommons.org/licenses/by-nc-sa/4.0>.

CC BY NC ND: The CC BY-NC-ND license allows users to copy and distribute the Article, provided this is not done for commercial purposes and further does not permit distribution of the Article if it is changed or edited in any way, and provided the user gives appropriate credit (with a link to the formal publication through the relevant DOI), provides a link to the license, and that the licensor is not represented as endorsing the use made of the work. The full details of the license are available at <http://creativecommons.org/licenses/by-nc-nd/4.0>.

Any commercial reuse of Open Access articles published with a CC BY NC SA or CC BY NC ND license requires permission from Elsevier and will be subject to a fee.

Commercial reuse includes:

**ELSEVIER LICENSE
TERMS AND CONDITIONS**

Nov 22, 2016

This Agreement between Jillian A Emerson ("You") and Elsevier ("Elsevier") consists of your license details and the terms and conditions provided by Elsevier and Copyright Clearance Center.

License Number	3994460609769
License date	Nov 22, 2016
Licensed Content Publisher	Elsevier
Licensed Content Publication	Wear
Licensed Content Title	The friction and wear of poly(tetrafluoroethylene)-poly(etheretherketone) composites: An initial appraisal of the optimum composition
Licensed Content Author	B.J. Briscoe, Lin Heng Yao,T.A. Stolarski
Licensed Content Date	15 April 1986
Licensed Content Volume Number	108
Licensed Content Issue Number	4
Licensed Content Pages	18
Start Page	357
End Page	374
Type of Use	reuse in a thesis/dissertation
Intended publisher of new work	other
Portion	figures/tables/illustrations
Number of figures/tables/illustrations	1
Format	both print and electronic
Are you the author of this Elsevier article?	No
Will you be translating?	No
Order reference number	
Original figure numbers	Figure 5
Title of your thesis/dissertation	Thermodynamics of polymer mixtures in solution and their applications in functional, microstructured films
Expected completion date	Jan 2017
Estimated size (number of pages)	300
Elsevier VAT number	GB 494 6272 12
Requestor Location	Jillian A Emerson 150 Academy St

NEWARK, DE 19716
United States
Attn: Jillian A Emerson

Total

0.00 USD

[Terms and Conditions](#)

INTRODUCTION

1. The publisher for this copyrighted material is Elsevier. By clicking "accept" in connection with completing this licensing transaction, you agree that the following terms and conditions apply to this transaction (along with the Billing and Payment terms and conditions established by Copyright Clearance Center, Inc. ("CCC"), at the time that you opened your Rightslink account and that are available at any time at <http://myaccount.copyright.com>).

GENERAL TERMS

2. Elsevier hereby grants you permission to reproduce the aforementioned material subject to the terms and conditions indicated.

3. Acknowledgement: If any part of the material to be used (for example, figures) has appeared in our publication with credit or acknowledgement to another source, permission must also be sought from that source. If such permission is not obtained then that material may not be included in your publication/copies. Suitable acknowledgement to the source must be made, either as a footnote or in a reference list at the end of your publication, as follows:

"Reprinted from Publication title, Vol /edition number, Author(s), Title of article / title of chapter, Pages No., Copyright (Year), with permission from Elsevier [OR APPLICABLE SOCIETY COPYRIGHT OWNER]." Also Lancet special credit - "Reprinted from The Lancet, Vol. number, Author(s), Title of article, Pages No., Copyright (Year), with permission from Elsevier."

4. Reproduction of this material is confined to the purpose and/or media for which permission is hereby given.

5. Altering/Modifying Material: Not Permitted. However figures and illustrations may be altered/adapted minimally to serve your work. Any other abbreviations, additions, deletions and/or any other alterations shall be made only with prior written authorization of Elsevier Ltd. (Please contact Elsevier at permissions@elsevier.com)

6. If the permission fee for the requested use of our material is waived in this instance, please be advised that your future requests for Elsevier materials may attract a fee.

7. Reservation of Rights: Publisher reserves all rights not specifically granted in the combination of (i) the license details provided by you and accepted in the course of this licensing transaction, (ii) these terms and conditions and (iii) CCC's Billing and Payment terms and conditions.

8. License Contingent Upon Payment: While you may exercise the rights licensed immediately upon issuance of the license at the end of the licensing process for the transaction, provided that you have disclosed complete and accurate details of your proposed use, no license is finally effective unless and until full payment is received from you (either by publisher or by CCC) as provided in CCC's Billing and Payment terms and conditions. If full payment is not received on a timely basis, then any license preliminarily granted shall be deemed automatically revoked and shall be void as if never granted. Further, in the event that you breach any of these terms and conditions or any of CCC's Billing and Payment terms and conditions, the license is automatically revoked and shall be void as if never granted. Use of materials as described in a revoked license, as well as any use of the materials beyond the scope of an unrevoked license, may constitute copyright infringement and publisher reserves the right to take any and all action to protect its copyright in the materials.

9. Warranties: Publisher makes no representations or warranties with respect to the licensed material.

10. Indemnity: You hereby indemnify and agree to hold harmless publisher and CCC, and their respective officers, directors, employees and agents, from and against any and all claims arising out of your use of the licensed material other than as specifically authorized pursuant to this license.

11. No Transfer of License: This license is personal to you and may not be sublicensed, assigned, or transferred by you to any other person without publisher's written permission.

12. No Amendment Except in Writing: This license may not be amended except in a writing signed by both parties (or, in the case of publisher, by CCC on publisher's behalf).

13. Objection to Contrary Terms: Publisher hereby objects to any terms contained in any purchase order, acknowledgment, check endorsement or other writing prepared by you, which terms are inconsistent with these terms and conditions or CCC's Billing and Payment terms and conditions. These terms and conditions, together with CCC's Billing and Payment terms and conditions (which are incorporated herein), comprise the entire agreement between you and publisher (and CCC) concerning this licensing transaction. In the event of any conflict between your obligations established by these terms and conditions and those established by CCC's Billing and Payment terms and conditions, these terms and conditions shall control.

14. Revocation: Elsevier or Copyright Clearance Center may deny the permissions described in this License at their sole discretion, for any reason or no reason, with a full refund payable to you. Notice of such denial will be made using the contact information provided by you. Failure to receive such notice will not alter or invalidate the denial. In no event will Elsevier or Copyright Clearance Center be responsible or liable for any costs, expenses or damage incurred by you as a result of a denial of your permission request, other than a refund of the amount(s) paid by you to Elsevier and/or Copyright Clearance Center for denied permissions.

LIMITED LICENSE

The following terms and conditions apply only to specific license types:

15. **Translation:** This permission is granted for non-exclusive world **English** rights only unless your license was granted for translation rights. If you licensed translation rights you may only translate this content into the languages you requested. A professional translator must perform all translations and reproduce the content word for word preserving the integrity of the article.

16. **Posting licensed content on any Website:** The following terms and conditions apply as follows: Licensing material from an Elsevier journal: All content posted to the web site must maintain the copyright information line on the bottom of each image; A hyper-text must be included to the Homepage of the journal from which you are licensing at <http://www.sciencedirect.com/science/journal/xxxxx> or the Elsevier homepage for books at <http://www.elsevier.com>; Central Storage: This license does not include permission for a scanned version of the material to be stored in a central repository such as that provided by Heron/XanEdu.

Licensing material from an Elsevier book: A hyper-text link must be included to the Elsevier homepage at <http://www.elsevier.com>. All content posted to the web site must maintain the copyright information line on the bottom of each image.

Posting licensed content on Electronic reserve: In addition to the above the following clauses are applicable: The web site must be password-protected and made available only to bona fide students registered on a relevant course. This permission is granted for 1 year only. You may obtain a new license for future website posting.

17. **For journal authors:** the following clauses are applicable in addition to the above:

Preprints:

A preprint is an author's own write-up of research results and analysis, it has not been peer-reviewed, nor has it had any other value added to it by a publisher (such as formatting, copyright, technical enhancement etc.).

Authors can share their preprints anywhere at any time. Preprints should not be added to or enhanced in any way in order to appear more like, or to substitute for, the final versions of articles however authors can update their preprints on arXiv or RePEc with their Accepted Author Manuscript (see below).

If accepted for publication, we encourage authors to link from the preprint to their formal publication via its DOI. Millions of researchers have access to the formal publications on ScienceDirect, and so links will help users to find, access, cite and use the best available version. Please note that Cell Press, The Lancet and some society-owned have different preprint policies. Information on these policies is available on the journal homepage.

Accepted Author Manuscripts: An accepted author manuscript is the manuscript of an article that has been accepted for publication and which typically includes author-incorporated changes suggested during submission, peer review and editor-author communications.

Authors can share their accepted author manuscript:

- immediately
 - via their non-commercial person homepage or blog
 - by updating a preprint in arXiv or RePEc with the accepted manuscript
 - via their research institute or institutional repository for internal institutional uses or as part of an invitation-only research collaboration work-group
 - directly by providing copies to their students or to research collaborators for their personal use
 - for private scholarly sharing as part of an invitation-only work group on commercial sites with which Elsevier has an agreement
- after the embargo period
 - via non-commercial hosting platforms such as their institutional repository
 - via commercial sites with which Elsevier has an agreement

In all cases accepted manuscripts should:

- link to the formal publication via its DOI
- bear a CC-BY-NC-ND license - this is easy to do
- if aggregated with other manuscripts, for example in a repository or other site, be shared in alignment with our hosting policy not be added to or enhanced in any way to appear more like, or to substitute for, the published journal article.

Published journal article (JPA): A published journal article (PJA) is the definitive final record of published research that appears or will appear in the journal and embodies all value-adding publishing activities including peer review co-ordination, copy-editing, formatting, (if relevant) pagination and online enrichment.

Policies for sharing publishing journal articles differ for subscription and gold open access articles:

Subscription Articles: If you are an author, please share a link to your article rather than the full-text. Millions of researchers have access to the formal publications on ScienceDirect, and so links will help your users to find, access, cite, and use the best available version.

Theses and dissertations which contain embedded PJAs as part of the formal submission can be posted publicly by the awarding institution with DOI links back to the formal publications on ScienceDirect.

If you are affiliated with a library that subscribes to ScienceDirect you have additional private sharing rights for others' research accessed under that agreement. This includes use for classroom teaching and internal training at the institution (including use in course packs and courseware programs), and inclusion of the article for grant funding purposes.

Gold Open Access Articles: May be shared according to the author-selected end-user license and should contain a [CrossMark logo](#), the end user license, and a DOI link to the

formal publication on ScienceDirect.

Please refer to Elsevier's [posting policy](#) for further information.

18. **For book authors** the following clauses are applicable in addition to the above:

Authors are permitted to place a brief summary of their work online only. You are not allowed to download and post the published electronic version of your chapter, nor may you scan the printed edition to create an electronic version. **Posting to a repository:** Authors are permitted to post a summary of their chapter only in their institution's repository.

19. **Thesis/Dissertation:** If your license is for use in a thesis/dissertation your thesis may be submitted to your institution in either print or electronic form. Should your thesis be published commercially, please reapply for permission. These requirements include permission for the Library and Archives of Canada to supply single copies, on demand, of the complete thesis and include permission for Proquest/UMI to supply single copies, on demand, of the complete thesis. Should your thesis be published commercially, please reapply for permission. Theses and dissertations which contain embedded PJAs as part of the formal submission can be posted publicly by the awarding institution with DOI links back to the formal publications on ScienceDirect.

Elsevier Open Access Terms and Conditions

You can publish open access with Elsevier in hundreds of open access journals or in nearly 2000 established subscription journals that support open access publishing. Permitted third party re-use of these open access articles is defined by the author's choice of Creative Commons user license. See our [open access license policy](#) for more information.

Terms & Conditions applicable to all Open Access articles published with Elsevier:

Any reuse of the article must not represent the author as endorsing the adaptation of the article nor should the article be modified in such a way as to damage the author's honour or reputation. If any changes have been made, such changes must be clearly indicated.

The author(s) must be appropriately credited and we ask that you include the end user license and a DOI link to the formal publication on ScienceDirect.

If any part of the material to be used (for example, figures) has appeared in our publication with credit or acknowledgement to another source it is the responsibility of the user to ensure their reuse complies with the terms and conditions determined by the rights holder.

Additional Terms & Conditions applicable to each Creative Commons user license:

CC BY: The CC-BY license allows users to copy, to create extracts, abstracts and new works from the Article, to alter and revise the Article and to make commercial use of the Article (including reuse and/or resale of the Article by commercial entities), provided the user gives appropriate credit (with a link to the formal publication through the relevant DOI), provides a link to the license, indicates if changes were made and the licensor is not represented as endorsing the use made of the work. The full details of the license are available at <http://creativecommons.org/licenses/by/4.0>.

CC BY NC SA: The CC BY-NC-SA license allows users to copy, to create extracts, abstracts and new works from the Article, to alter and revise the Article, provided this is not done for commercial purposes, and that the user gives appropriate credit (with a link to the formal publication through the relevant DOI), provides a link to the license, indicates if changes were made and the licensor is not represented as endorsing the use made of the work. Further, any new works must be made available on the same conditions. The full details of the license are available at <http://creativecommons.org/licenses/by-nc-sa/4.0>.

CC BY NC ND: The CC BY-NC-ND license allows users to copy and distribute the Article, provided this is not done for commercial purposes and further does not permit distribution of the Article if it is changed or edited in any way, and provided the user gives appropriate credit (with a link to the formal publication through the relevant DOI), provides a link to the license, and that the licensor is not represented as endorsing the use made of the work. The full details of the license are available at <http://creativecommons.org/licenses/by-nc-nd/4.0>.

Any commercial reuse of Open Access articles published with a CC BY NC SA or CC BY NC ND license requires permission from Elsevier and will be subject to a fee.

Commercial reuse includes:

- Associating advertising with the full text of the Article
- Charging fees for document delivery or access
- Article aggregation
- Systematic distribution via e-mail lists or share buttons

Posting or linking by commercial companies for use by customers of those companies.

20. Other Conditions:

v1.8

Questions? customercare@copyright.com or +1-855-239-3415 (toll free in the US) or +1-978-646-2777.
